

**Approaches to Industry 4.0
implementation for electron
beam quality assurance using
BeamAssure™**



Norbert Sieczkiewicz

**This dissertation is submitted for the degree of
Doctor of Philosophy**

January 2024

Department of Engineering

To my wife

Declaration

This thesis has not been submitted in support of an application for another degree at this or any other university. It is the result of my own work and includes nothing that is the outcome of work done in collaboration except where specifically indicated. Many of the ideas in this thesis were the product of discussion with my supervisor Professor Andrew Kennedy.

Dr Yingtao Tian (Lancaster University) – conceptualisation and supervision of the work.

Dr Colin Ribton (TWI Ltd.) – revision of the thesis chapters and supervision of the experiments.

Excerpts of this thesis have been published in the following conference manuscripts and academic publications.

N. Siczekiewicz, C. Ribton, A. Kennedy, Y. Tian, D. Williams. "Electron beam characterisation using time series imaging and deep learning", 6th International Electron Beam Welding Conference, 2021

Abstract

Electron beam welding (EBW) is a complex process used in manufacturing high-value components in the aerospace and nuclear industries. The Fourth Industrial Revolution is a fusion of advances in artificial intelligence, sensing techniques, data science, and other technologies to improve productivity and competitiveness in fast-growing markets.

Although the EBW process can be monitored by characterisation of the electron beams before welding or using backscattered electron signals (BSE), the noise and lack of understanding of these signal patterns is a major obstacle to the development of a reliable, rapid and cost-effective process analysis and control methodology.

In this thesis a controlled experiment was designed to be relevant to those industries and improve understanding of the relationship between beam and weld quality. The welding quality control starts before welding, continue throughout the welding process, and is completed with examination after welding. The same workflow was followed in this thesis, focusing on aforementioned QC stages, starting with beam probing experiments, followed by monitoring weld pool stability using high dynamic range camera and BSE signals, and ending with metallographic inspection on sections.

The rapid development of computer vision methods brought an idea of classifying beam probing data before welding, which is first QC stage. Dataset of 3015 BeamAssure measurements was used in combination with deep learning, and various encoding methods such as Recurrence Plots (RP), Gramian Angular Fields (GAF), and Markov Transition Fields (MTF). The segmentation and classification results achieved a remarkable rate of 97.6% of accuracy in the classification task. This part of the work showed that use of time-series images enabled identification of the beam focus location before welding and providing recommended focus adjustment value.

To replicate in-process QC step, titanium alloy (Ti-6Al-4V) plates were welded with a gap opened in a stepwise manner, to simulate gap defects and introduce weld pool instability. Experiments were conducted to monitor the weld pool stability with a HDR camera and BSE detector designed for the need of this experiment. Signal and image analysis revealed occurrence of the weld defects and their locations, which was reflected by last QC stage, metallographic inspection on sections. This final part of the work proved that whatever method is used for gap defects monitoring, those joint misalignments can be easily registered by both methods. More interestingly, BSE monitoring allowed porosity and humping detection, which shapes and location were projected onto the BSE signal amplitude.

Presented three stage QC method can contribute to a better understanding of beam probing and BSE signals patterns, providing a promising approach for quality assurance in EBW and could lead to higher weld integrity by improved process monitoring.

Acknowledgements

This PhD research was made possible by the sponsorship and support of the Lloyd's Register Foundation. The Lloyd's Register Foundation helps to protect life and property by supporting engineering-related education, public engagement and the application of research. The work was enabled through, and undertaken at, the National Structural Integrity Research Centre (NSIRC), a postgraduate engineering facility for industry-led research into structural integrity established and managed by TWI through a network of both national and international Universities. This work was also supported by NVIDIA Corp. All experimental studies were performed on a TITAN V graphic card donated by NVIDIA.

I am deeply grateful to my supervisors, Prof Andrew Kennedy and Dr Yingtao Tian, who guided, instructed, and motivated me. Their feedback allowed me to deepen and refine my research, and the results presented in my thesis would be impossible without their careful supervision. AK in particular has been a fantastic primary supervisor, who helped me shape this thesis.

I would like to thank my industrial supervisor Dr Colin Ribton for his support which was influential in shaping my experimental methods and my daily life. I also would like to thank our technician Vitalijs Jefimovs for the help during my experiments and Diane Shaw for the scrupulous processing of my samples.

I would like to thank my friends – Yi Yin, Bowei Li and Anurag Niranjana for the cherished time spent together in the lab, and in social settings. My appreciation also goes out to my family and friends for their encouragement and support throughout my studies. I would like to thank my parents, Monika and Andrzej, for helping me with relocation and their best life advice tips. It is their kindness, help and support that have made my study and life in the UK a wonderful time.

I would like to thank Charles Weir, Kayla Friedman and Malcolm Morgan for the Microsoft Word thesis template used as a basis for the document.

Lastly, an immense thank you to my wife, Dr Beatriz Costa Gomes, for her love and support throughout these past few months. I am immensely thankful for the late nights and early mornings she has spent by my side and for the invaluable role she has played in keeping me grounded. I am truly indebted to her as my source of inspiration. Above all, I want to extend my deepest appreciation for being my closest companion and best friend.

Contents

1 RESEARCH BACKGROUND.....	1
1.1 Introduction.....	1
1.2 Electron beam welding.....	2
1.3 Welding in the Age of Industry 4.0.....	3
1.4 Aim and Specific objectives.....	6
1.5 Summary of Methodology.....	8
1.6 Thesis structure.....	8
1.7 Contribution to Knowledge.....	9
1.8 Summary.....	10
2 LITERATURE REVIEW.....	11
2.1 Electron beam welding parameters.....	11
2.2 Beam quality.....	13
2.3 Beam focus.....	15
2.4 Beam focus supporting systems.....	16
2.5 Beam probing.....	18
2.6 4-slit beam probe (BeamAssure).....	21
2.7 Beam width definitions.....	22
2.8 Multi-slit probing.....	24
2.9 Radon transform.....	25
2.10 Melt pool dynamics.....	26
2.10.1 "Rosenthal" regime.....	27
2.10.2 "Single wave" regime.....	27
2.10.3 "Elongated keyhole" regime.....	28
2.10.4 "Pre-humping" regime.....	28
2.10.5 "Humping" regime.....	29
2.11 Electron beam welding related standards.....	32
2.12 Vision systems used in EBW.....	34
2.13 Imaging devices including welding cameras.....	35
2.14 Electron beam imaging using backscattered electrons.....	37
2.15 Backscatter electron monitoring.....	38
2.16 Design considerations for the BSE collector.....	40
2.17 Time series imaging.....	41
2.18 Encoding to GAF.....	41
2.19 Encoding to MTF.....	43
2.20 Encoding to RP.....	44
2.21 Encoding to MIX.....	44
2.22 Deep learning for time series images classification.....	45
2.23 Residual Networks.....	46
2.24 Related works.....	48
2.24.1 Vision system process monitoring.....	48
2.24.2 Electron-optical process monitoring.....	49
2.24.3 Backscatter electron monitoring.....	49
2.24.4 Neural network assisted EBW.....	50
2.25 Knowledge gap.....	51

3 EXPERIMENTAL METHODS.....	53
3.1 EBW machine	53
3.2 PLC data.....	54
3.3 BSE collector plate.....	55
3.4 Welding cameras.....	57
3.5 8-bit and 12-bit image encoding.....	59
3.6 Welding data monitoring triggering control.....	61
3.7 Data post-processing pipeline	62
3.8 Design of the samples.....	64
3.9 Sources of errors	66
3.9.1 <i>The charge build-up on the surface of the plastic liner.....</i>	<i>66</i>
3.9.2 <i>Size of the samples.....</i>	<i>67</i>
3.9.3 <i>Welding parameters (PLC).....</i>	<i>67</i>
3.9.4 <i>Digital oscilloscope error</i>	<i>68</i>
3.9.5 <i>Trigger delay</i>	<i>68</i>
3.9.6 <i>Sources of uncontrolled errors.....</i>	<i>68</i>
3.10 Workstation.....	68
4 BEAM PROBING EXPERIMENTAL RESULTS AND DISCUSSION.....	70
4.1 BeamAssure signal processing	72
4.2 BeamAssure dataset	74
4.3 Multi-slit probe data processing.....	76
4.4 Encoding BeamAssure signals to images.....	77
4.5 Three-classes neural network model.....	78
4.5.1 <i>Three-classes neural network model with data augmentation.....</i>	<i>81</i>
4.6 Seventeen-classes neural network model.....	83
4.6.1 <i>Seventeen-classes neural network model with data augmentation.....</i>	<i>85</i>
4.7 Multi-slit beam probing results.....	86
4.7.1 <i>Three-classes neural network model with 17-slit probe.....</i>	<i>88</i>
4.8 Summary	90
5 BSE COLLECTOR PLATE EXPERIMENTAL RESULTS AND DISCUSSION	91
5.1 BSE collector plate signal.....	92
5.2 HDR camera	97
5.3 Time series imaging.....	101
5.4 Summary	106
6 CONCLUSIONS.....	107
7 FUTURE WORK	110
8 BIBLIOGRAPHY.....	112

List of Tables

Table 1: Factors contributing to high electron beam weld integrity – adapted from [9].	6
Table 2: Weld quality control stages covered in the research.	7
Table 3: Differences between high- and low-voltage EBW machines [10].	12
Table 4: Differences between beam probing techniques including their advantages (+) and disadvantages (-). Adapted from [28].	19
Table 5: Selected standards and guidelines related to electron beam welding and quality.	33
Table 6: Architectures for ResNet34, ResNet50 and ResNet101. Adapted from [107].	48
Table 7: Difference between target and measured values for each welding parameter.	67
Table 8: Python packages installed on workstation and their usage.	69
Table 9: Dataset distribution for training, validation and test sets.	79
Table 10: The training time in seconds for one epoch.	79
Table 11: The K-fold cross-validation classification accuracy on unseen data for ResNet-34, ResNet-50, ResNet-101 architectures and four encoding methods.	80
Table 12: The K-fold cross-validation classification accuracy on unseen data for the ResNet-34 architecture. Training done with MIX-based dataset and various data augmentation techniques.	81
Table 13: Dataset distribution for training, validation and test sets.	83
Table 14: The train time in seconds for one epoch.	84
Table 15: The K-fold cross-validation classification accuracy on unseen data for ResNet-34 architecture and four encoding methods.	84
Table 16: The K-fold cross-validation classification accuracy on unseen data for the ResNet-34 architecture. Training done with MIX-based dataset and various data augmentation techniques.	85
Table 17: Reconstruction time in seconds for different reconstruction kernels. ..	88

List of Figures

Figure 1: Simplified representation of electron beam gun column. Adapted from [1].	2
Figure 2: Stages of the joint formation. a) joint before welding, b) material melted on the surface, c) formation of keyhole, d) beam penetrated the workpiece, e) formed weld seam. Adapted from [1].	3
Figure 3: Thesis layout.....	8
Figure 4: Schematic showing beam probe signal with corresponding heatmap (side view) and their location on the plan view of the 3D beam cross-section. The highest intensity part of the beam is emitted from a core and it is surrounded by low-intensity fringe. Adapted from [12].	14
Figure 5: Schematic diagram of the EB machine generated beam showing the difference between core and fringe caustics. Adapted from [14].	14
Figure 6: Schematic diagram of the beam caustic created from multiple beam diameter measurements. The images illustrate the beam shape change, registered with the camera, on the top surface of the workpiece.....	16
Figure 7: Slit probe design. The slit is in a molybdenum casing, the beam passes through the slit (at the position 2) and it is collected by an electrical pickup. The beam should be lined up with the slit so that the apparent width is no less than the actual width, which translates into accuracy. Courtesy of TWI Ltd.	17
Figure 8: The BeamAssure probe design. Courtesy of TWI Ltd.....	18
Figure 9: Different setup scenarios in terms of accuracy and precision. The chart is based on centring and stigmatising parameters and their possible error areas. Cross represents the target value. Adapted from [26].	19
Figure 10: The BeamAssure probe schematic. The red lines mark electron beam path. Courtesy of TWI Ltd.	21
Figure 11: Schematic of the BeamAssure signal.	22
Figure 12: Comparison of the slit voltage for 2nd slit as a function of beam radius for the defocused, focused and overfocused beam obtained from the BeamAssure probe. The shape of the curves complies with Elmer (2001) [31].	22
Figure 13: Beam width definitions. a) FWHM, $D4\sigma$, $1/e^2$, b) 20/80, $D86$, 10/90, FWHP. Adapted from [29].....	23
Figure 14: The multi-slit (17 slits) probe design. The small circle between slits is used as a signal reference.	24

Figure 15: Typical multi-slit probe signal. Orange arrows (highest peaks) point to the centres of the signal references. As the beam is swept multiple times over the slits, the signal of interest is located between two signal references. 24

Figure 16: Signal processing applied to 17-slit probe measurements required to obtain sinogram. The process starts with extracting the signal between signal reference peaks (1), signal segmentation for each slit (2), extracting each signal (3), encoding each signal as a heatmap (4), rotating the heatmaps by a 21.18° angle (5), creating the sinogram from the rotated heatmaps (6). 25

Figure 17: Reconstructed image using SART technique..... 26

Figure 18: Typical cross-section of the “Rosenthal” regime weld. Adapted from [39]..... 27

Figure 19: Typical cross-section of the “Single wave” regime weld. Adapted from [39]..... 28

Figure 20: Typical cross-section of the “elongated” regime weld. Adapted from [39]..... 28

Figure 21: Typical cross-section of the “pre-humping” regime weld. Adapted from [39]..... 29

Figure 22: The hump weld bead in electron beam welding (focusing current 330 mA, beam current 18 mA, accelerating voltage 60 kV, welding speed 500mm/min, working distance 330 mm). 29

Figure 23: Typical cross-section of the “humping” regime weld. Adapted from [39]. 30

Figure 24: The ratio between the working distance to the focal distance and its impact on weld pool shape. Adapted from [41]. 31

Figure 25: Relationship between focus position a) normal focus, b) overfocus, c) defocus, and weld imperfections. Adapted from [26]. 32

Figure 26: Visualisation of the shrinkage groove based on the ISO 13919-2:2001 standard. Adapted from [47]. 33

Figure 27: Left: sacrificial windows made from polyester on rollers to protect the visual optics. Right: Clean and dirty films..... 36

Figure 28: Splash registered (marked in green) by the HDR camera Xiris XVC-1100. 36

Figure 29: Process emissions from the electron beam welding zone. Adapted from [19]..... 38

Figure 30: Electron beam imaging methods: a) light-optical systems and their non-collimated (rays are not parallel to the optical axis) illumination source b) BSE detector location.....	39
Figure 31: Transition process of the GAF conversion.	43
Figure 32: Transition process of the MTF conversion.	43
Figure 33: Transition process of the RP conversion.	44
Figure 34: Transition process of the MIX conversion. Each encoding method (GAF, RP, MTF) occupies one layer of the RGB image.....	45
Figure 35: CNN architecture based on the PyTorch implementation of ResNet 34 for MIX encoded BeamAssure signal as an input image. Adapted from [105].	47
Figure 36: Residual block. Orange line represents shortcut (skipped connection). Adapted from [107].....	47
Figure 37: Location of the camera and BSE detector.....	54
Figure 38: Schematic of the triggering and data collection process.	55
Figure 39: Emissions created during welding process. Adapted from [19].....	56
Figure 40: BSE plate design. a) 3D concept, b) machined plate and its main dimensions (4 mm thick), c) plate installed inside the EBW chamber with a deposited dust layer.....	57
Figure 41: Schematic of the detector assembly inside vacuum chamber and connection circuit between detector and data acquisition device (Picoscope 3203D).....	57
Figure 42: Custom-designed lens mounts prevents any environmental light leaks and provide stable support for the lens.	58
Figure 43: Image processing steps of the beam capillary registered by HDR camera, starting with camera raw images, converting them to grayscale, extracting background from weld pool image using Otsu's thresholding and calculating centre of mass of the segmented.....	59
Figure 44: Interpolated output obtained through debayering process, by which image gets decoded from a colour matrix into a full resolution colour image. Adapted from [130].....	60
Figure 45: Differences in camera output between packed and unpacked pixel formats. Adapted from [131].....	60

Figure 46: Time delay between Picoscope (blue) and RS PRO arbitrary function generator (red) introduced an additional 0.001 ms delay between triggering pulses (shifted signals).	62
Figure 47: System architecture.	63
Figure 48: Image processing. The same raw image (.dat) was decoded in Xiris WeldStudio and custom Python code.....	64
Figure 49: Stepwise opening gap sample design (t=10mm). The welding direction is from the beginning of the zero gap until the end of the 1 mm gap.	65
Figure 50: Setup and clamping of welded materials.....	66
Figure 51: White cable sleeving (marked with the red arrow) made of silicone impregnated braided fibreglass – positioned closer to the roof of the chamber to avoid charge build-up.....	67
Figure 52: Code schematics of BeamAssure signal processing and encoding it as time-series images. Each step is colour coded according to the level of contribution and marked with circular markers to highlight the Python packages used, as per the legend.	71
Figure 53: Code schematics of neural network training pipeline. Each step is colour coded according to the level of contribution and marked with circular markers to highlight the Python packages used, as per the legend.....	71
Figure 54: Code visualisation of CT reconstruction of 17-slit probe signal. Each step is colour coded according to the level of contribution and marked with circular markers to highlight the Python packages used, as per the legend.	72
Figure 55: Enlarged part of the probe signal. PAA 10x (left) and PAA 20x (right) were applied to beam probe signals to reduce data and at the same time to preserve features.	73
Figure 52: Graphical representation of the BeamAssure dataset.....	74
Figure 57: GAFs generated for defocused, focused and overfocused beam conditions. These images were used to train a neural network, but a human can also easily spot focus-based patterns in the beam caustic. Labels based on [150].....	75
Figure 58: Class distributions for original (unbalanced) and augmented data.....	75
Figure 59: BeamAssure signal segmentation steps.....	77
Figure 60: Different encoding methods revealed distinguishable patterns of the BeamAssure signal.....	78
Figure 61: False focus labels for different normalized focus current values obtained from Resnet-34 model trained with concatenated images.....	81

Figure 62: Confusion matrix obtained from seventeen-classes Resnet-34 model trained with concatenated images.	85
Figure 63: Selected raw signals for various focusing currents – 210, 350, 390 and 470 mA. Orange lines are drawn by the peak finding algorithm.	87
Figure 64: Reconstructed radial current density distributions in 2D and 3D with different reconstruction kernels (350 mA focusing current – sharp focus location).	88
Figure 65: Time series encoded data from a 17-slit probe for 270, 350 and 390 mA focus currents.	89
Figure 66: Code visualisation of data acquisition steps. Each step is colour coded according to the level of contribution and marked with circular markers to highlight the Python packages used, as per legend.	91
Figure 67: Code visualisation of data visualisation steps. Each step is colour coded according to the level of contribution and marked with circular markers to highlight the Python packages used, as per legend.	92
Figure 68: Example of BSE signal (raw and filtered) plotted against PLC signal (Appendix O). No changes were observed in the welding parameters such as focus current, beam current and accelerating voltage. Green double arrows marking three regions of interest.	93
Figure 69: Sample (number eight – Appendix N), weld bead, longitudinal cross-sections and corresponding BSE signal shape (time-shift corrected). Metal leak on the root side. Handwritten markings on the samples are unrelated to the numeration in the thesis.	94
Figure 70: Sample (number ten – Appendix P), weld bead, longitudinal cross-sections and corresponding BSE signal shape (time-shift corrected). Metal leak can be seen on the root side.	95
Figure 71: Sample (number five – Appendix K), weld bead, longitudinal cross-sections and corresponding BSE signal shape (time-shift corrected). Humping and visible pore which ejected metal droplet.	96
Figure 72: Three different welding behaviours. a) partially formed keyhole behaviour in the range 0-100 mm (area in pixels 3753), b) weld pool behaviour in 100-150 mm range (area in pixels 4197), c) weld pool behaviour in 150-200 mm range (area in pixels 4361).	97
Figure 73: Three different weld pools behaviours plotted as 3D surface plots. X and Y axis correspond to the resolution of the image in pixels, and Z is interpreted as height for the plot based on the luminance as 0-255 pixel value (grid size is 1024 pixels). From left to right are visualised the welding sections: 0-100 mm, 100-150 and 150-200 mm.	98

Figure 74: Different weld pool split locations. a) half-half split close to the edge, b) split by the gap, c) split close to the edge, most of the weld pool visible on the top surface of the workpiece, d) split between the gap, weld pool located between two edges and on the workpiece top surface. 98

Figure 75: Example comparison of the eccentricity, change of the total intensity, pixel area, centre of mass in transverse and longitudinal welding direction, and solidity. Locations of observed changes are marked with orange arrows. All welds can be found in Appendices G-P..... 99

Figure 76: Comparison between BSE signal and camera data for visible pore which ejected metal droplet. Purple circle mark the location of the defect.100

Figure 77: 4x3 matrix representing different encoding methods for different weld sections and their location corresponding to weld bead. The top of the image presents a filtered BSE collector plate signal.101

Figure 78: Region of interest, marked in red circles, in GAF encoded signal for rising and falling signal.102

Figure 79: Features of interest, marked in the red cross, in GAF encoded signal for the spike in the signal.102

Figure 80: Stable welding conditions. No apparent features in the image.....103

Figure 81: Weld pool travelling between two workpiece edges.....105

Figure 82: Weld pool split (marked green) visible on the signal and gaps (marked red) in the signal due to the code limitations.....105

List of Abbreviations and Acronyms

AMS	Aerospace Material Specifications
AWS	American Welding Society
BS	British Standards
BSE	Backscattered Electrons
CCD	Charge-coupled Device
CNC	Computerized Numerical Control
CNN	Convolutional Neural Network
CT	Computed Tomography
CWT	Continuous Wavelet Transform
DL	Deep Learning
DVS	Deutscher Verband für Schweißen und verwandte Verfahren e. V. ("German Welding Society")
EB	Electron Beam
EBAM	Electron Beam Additive Manufacturing
EBAZ	Electron Beam Active Zone
EBW	Electron Beam Welding
ELO	Electron-optical
FBP	Filtered Back Projection
FC	Faraday Cup
FPS	Frames Per Second
FWHM	Full Width at Half Maximum
FWHP	Full Width to Half Power
GAF	Gramian Angular Fields
GPU	Graphics Processing Unit
HDR	High Dynamic Range
HVEB	High-voltage Electron Beam
I/O	Input/Output
ISO	International Organization for Standardization
LVEB	Low-voltage Electron Beam
MIX	Mixed (blended) Images
ML	Machine Learning
MTF	Markov Transition Fields
ND	Neutral Density
NDT	Non-destructive Testing
PAA	Piecewise Aggregation Approximation
PI	Proportional-integral
PLC	Programmable Logic Controller
POE	Power over Ethernet
R&D	Research and Development
ResNet	Residual Network
RP	Recurrence Plots
SART	Simultaneous Algebraic Reconstruction Technique
SDK	Software Development Kit
TWI	The Welding Institute
QC	Quality Control

List of Appendices

Appendix A. PLC data dictionary	125
Appendix B. Image processing.....	126
Appendix C. Trigger control and data acquisition	127
Appendix D. Image debayering.....	133
Appendix E. Material test report	134
Appendix F. Time-series encoding.....	135
Appendix G. Weld 1.....	141
Appendix H. Weld 2.....	145
Appendix I. Weld 3.....	149
Appendix J. Weld 4.....	153
Appendix K. Weld 5.....	157
Appendix L. Weld 6.....	162
Appendix M. Weld 7	166
Appendix N. Weld 8.....	171
Appendix O. Weld 9	176
Appendix P. Weld 10	180

1 Research Background

The aim of the research work undertaken for this thesis was to explore quality assurance methods for electron beam welding using beam probing and electron beam monitoring. This work is the result of a project with the Lancaster University in collaboration with TWI (The welding Institute) Ltd. (Cambridge) focused on Industry 4.0 and its application to electron beam welding. The electron beam section of TWI, which has been active in electron beam technology research and development since the 1960s, is primarily focused on advancement of new capabilities for electron beam processing. One of such advanced quality assurance tools is BeamAssure, used in this thesis, which measures and quantifies electron beams to produce joints with excellent integrity in industries requiring the most exacting standards and quality. As Industry 4.0 is data-driven, this research was also supported by a NVIDIA GPU grant, providing deep learning computational capabilities to make better use of the collected data. This chapter describes the research background related to quality assurance of electron beam welding. It starts with a brief introduction to electron beam welding, followed by Industry 4.0 and market needs. Furthermore, it includes aims of the research and thesis layout.

1.1 Introduction

Welding is considered a “Special Process” by norm ISO 9001:the quality cannot be easily verified and as a consequence it requires great coordination of welding operations to achieve confidence in weld integrity for reliable and safe service performance. There are numerous welding technologies and which method to use depends on a triple constraint, which consists in time, cost and scope of the work. Welding processes in general can be classified in four ways, based on:

- Whether the base material is melting or not,
- Need and type of filler material,

- Heat source,
- Utilisation of automated system.

Based on the above, electron beam welding is a fusion welding process, where the electron beam provides a precise and narrow heat source. It produces high quality welds in single pass usually without the need of filler material. That makes the electron beam welding process appealing to industries such as aerospace and defence. Modern electron beam welding machines have only a certain level of automation, which include the seam tracking system, weld penetration monitoring system and control systems such as programmable logic controller (PLC) and computerized numerical control (CNC). On top of that, they are equipped with various control and safety systems to protect the operator from the radiation.

1.2 Electron beam welding

Electron beam welding (EBW) is a process that produces a joint between two materials with a concentrated beam. Electrons are generated in a vacuum chamber by heating the cathode, which starts to emit electrons until their maximum emission level is reached. This cloud of electrons is shaped into a beam, by passing through the bias cup, anode and focusing lens. The focusing lens uses electromagnetic coils below the anode to focus the beam of electrons. Deflection coils, which are located below the focus coil and supported by a function generator, are used to move the beam to predetermined locations. It is also possible to use high-speed deflection systems as heat treatment, including pre- and post-heating (cosmetic pass). The design of the electron beam gun is presented in Figure 1.

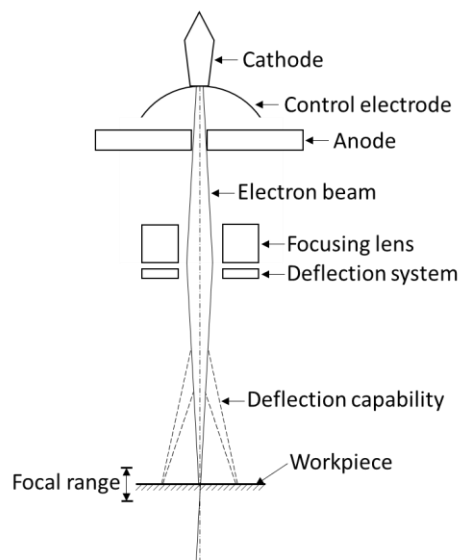


Figure 1: Simplified representation of electron beam gun column. Adapted from [1].

The main beam, once focused, is pointed at the workpiece and welding heat is obtained from the kinetic energy when high-velocity electrons hit the surface of the workpiece (Figure 2b). Some of the material is vaporized (Figure 2c), and if the

steady state condition between the pressure of expanding vapour and surface tension of the molten material is reached, the keyhole is formed (Figure 2d). This mode is called keyhole welding and results in the narrow heat-affected zone and low-distortion welds.

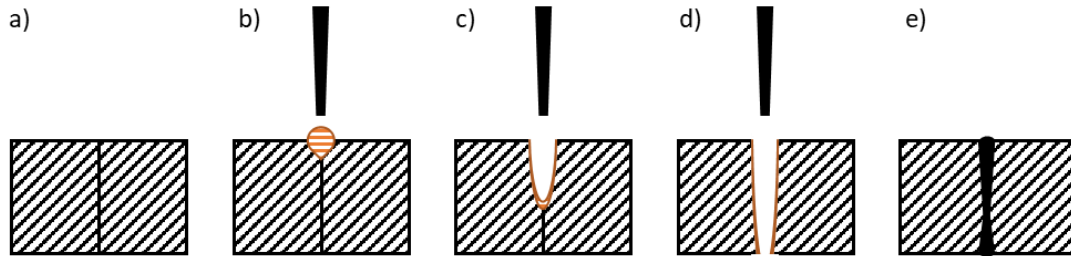


Figure 2: Stages of the joint formation. a) joint before welding, b) material melted on the surface, c) formation of keyhole, d) beam penetrated the workpiece, e) formed weld seam. Adapted from [1].

Shallower welds, which resemble arc welds, are created in the mode termed conduction welding (Figure 2b, no keyhole formed). As a result, bottom bead weld is smooth for applications where bead machining access is limited and workpiece material is thin (less than 6 mm). A condition between these two modes is called transition keyhole welding (Figure 2c, keyhole partially formed) and results in a deeper penetration than in the conduction mode. However, despite the presence of the keyhole, it still has shallow penetration.

Both control systems, focus and deflection, can be either manually or automatically controlled. These parameters can be observed using optical systems, which allow real-time adjustments to fine-tune the welding process. Visual feedback is useful when the formation of welding imperfections is observed and can reduce spatter, undercuts, pores and lack of fusion at the weld root. If a weld bead is considered, there is a possibility to accommodate joint fit-up tolerances and shrinkage and modify visual appearance.

1.3 Welding in the Age of Industry 4.0

When researching the market and industry needs, a study was carried out by Böhm (2014) [2], on behalf of the German Welding Society (DVS), with 70 interviewees including experts from the industry and research institutes. Part of the study was related to identifying fields of research and increasing the application of electron beam technology in the modern manufacturing environment. A requirement for future R&D activities has been defined as, including but not limited to, beam shaping (55% answers, 1st place out of 22), process control and quality assurance (45% answers, 5th place). From the evaluation of the German Welding Society research seminar, six requirements for future R&D activities were selected. One of them was related to the mitigation of “system fluctuations” because the electron beam weld quality was required to be more consistent.

Like any other welding technique, EBW process can be affected by welding defects that occur in welded parts and described in detail in the ISO 13919-1:2019 standard. Quality requirements imposed by standards set a specific quality level on imperfections in electron beam welded joints. This requires precise quality monitoring in order to meet the needs of stringent standards.

Industry 4.0 is a term that encompasses automation and intelligent adaptation through data analytics, and requires a change in approach, with emphasis on digitalisation, control systems, and data transfer. With regards to the welding quality and process control, there is currently a strong tendency on the user side to record and store the data with a resolution as high as possible. Welding data storage can be used for documentation and data analysis. These data can be later used for defects/material properties prediction and health-monitoring of equipment. Despite this, it has not yet been determined at which level of detail the data must be available in order to create appropriate algorithms.

There are increasing drives in the industry to maximize equipment uptime and to minimize maintenance and operating costs. Modern equipment has become essentially automated and involves minimal human intervention.

Basic training of personnel, according to DVS guideline 1199, requires 75 hours for basic training of an engineer, 60 hours for a work planer and 40 hours for an operator [3]. Today's manufacturing processes are forced to reduce production lead time and at the same time improve product quality. As a result, this puts cost and labour pressures. One possible solution is reducing the human factor during the electron beam welding process so the operator does not require special qualifications. On top of it all, an operator cannot easily notice that the welding process is not performed well, neither visually nor by monitoring parameters on the dashboard.

Until recently, the welding engineering sector focused on the development of welding machines and power sources but the adoption of Industry 4.0 will make welding equipment self-configurative and self-adaptive.

Electron beam welders are equipped with PLC and CNC systems, but the data output from them is not currently collected for the improvement of process control. Additionally, there aren't any new sensors on the market or algorithms to ensure high quality of the welding.

To avoid this problem, data collected from beam probing, backscattered electrons signals and industrial cameras can be used together to improve welding quality. Various beam probing systems based on different operating principles are available. The TWI BeamAssure probing system is based on slit method and it is used to characterise the electron beam prior to welding to ensure the quality of the beam, which has a direct impact on weld quality. During the welding, the process can be observed using welding cameras, which are equipped with high dynamic range sensors. Those sensors allow the recording of the darkest and brightest details of the weld pool simultaneously. Additionally, during the electron beam welding process, various electron emissions are generated, including, among others, backscattered electrons, secondary electrons, charged plasma and,

thermionic emission [4]. Any changes in the amount of induced current can be registered by the electron sensors.

During the welding, the beam parameters are defined within computer control systems, such as PLC and CNC, and maintained by them during welding. However, it is difficult to observe the welding process due to the remoteness of the part from the operator and possible line-of-sight obstructions.

Although welding parameters should be stable during the welding, there is still a noise element to them. There is variability of the beams generated by various electron beam welders, which is related to the source of free electrons (cathode). Current density distribution in different sections of the same beam can vary in shape and are also affected by accelerating voltage, beam current, cathode defects, changes in the pressure in the vacuum chamber, filament alignment and electron generator design. Any variation in these parameters influences the current density distribution of the beam and has an impact on weld penetration, weld width and defect formation [1, 5].

Additionally, there is a human factor involved during the focusing stage. Beam focus consistency is important in the electron beam welding process because it can directly impact welding quality. Beam focusing can be described either as “normal” or “optimum” as referred to by Schultz (1992) [1]. For welding operators, it is most useful to use the term “normal focusing” of the electron beam, which means that focus is set manually by observing and evaluating the brightness of the heated spot on the surface either of the workpiece or a refractory metal block (e.g. a tungsten focus block) [5,6]. This raises concerns regarding reproducibility and repeatability of the sharp focus setting. The difference in sharp focus setting varies between various experienced operators and different machines. As mentioned by Kaur (2015) [6] the methods of identifying the surface focus are very subjective. Elmer (2009) [7] suggested a benchmark to determine a sharp focus condition and compare it with the operator's sharp focus. Giedt (1988) [8] found that the variation in weld penetration is from 2 to 3 times more sensitive to inconsistency in beam focus current setting than to errors in beam voltage or current. Manual focus adjustment cannot guarantee optimum beam focus current settings. In contrast to “normal” focus set by operator, the “optimum” focus is the beam focus that produces the fewest defects in the weld. In that case, beam probing can be used as a method to set and maintain “optimum” focus.

Communication between human and welding machine plays an important role in Industry 4.0 and welding engineering. Currently, to produce welds with the highest specified quality levels, electron beam welding relies on trained personnel and operator skills. Those manual weld inefficiencies can lead to increased costs and failure in service with potentially catastrophic consequences economically, environmentally and to human life. The aerospace and defence industry, where high weld quality is essential, can benefit from high repeatability to ensure that welds do not deviate from the programmed parameters for high accuracy.

For example, if the shape of the beam changes, it will create dangerous imperfections for the reasons stated above. Further parameters contributing to

high electron beam weld integrity, including challenges described above, are summarised in Table 1.

Table 1: Factors contributing to high electron beam weld integrity - adapted from [9].

Pre-production	Material quality	Material dimensions	Surface condition	Production testing	Welding process
NDT	Correct grade	Thickness variations	Surface contamination	Limits of NDT	Gun filament condition
Tensile strength	Residual material	Eccentricity	Surface corrosion	Limit of batch testing	Vacuum quality and background gas
Fatigue strength		Geometric variations	Surface finish		
Hardness		Joint preparation			Machine selection and human elements
Corrosion					
Impact toughness					Welding parameters
Fracture toughness					

In general, electron beam welding process is carried out with fixed and PLC/CNC controlled welding parameters. The beam probing may be used to measure the beam intensity distribution to support focusing step and maintaining performance or transferring welding parameters between different machines. This research has been focused on reducing the human factor during electron beam focusing using a trained deep learning model capable of determining sharp focus location based on one BeamAssure measurement. Additionally, to solve issues with observing the welding process, backscattered electrons monitoring system has been developed and compared against a high dynamic range camera.

1.4 Aim and Specific objectives

The main aim of this research was to develop a multiple-input quality monitoring system for electron beam machines using a beam probing system (a system developed by TWI that measures electron beam characteristics), supported by images from a welding camera and data from a back-scattered electron collector signal. To achieve this objective, a neural network model was used to relate process inputs (including the shape of the weld pool) to indicators of weld quality (such as humping and spiking – in accordance with relevant standards). The output of the system was based on the occurrence of those imperfections and the

focus state of the beam. These outputs will alert the user that a post-weld inspection is required. All of the weld quality control stages are described and summarised in Table 2.

The specific objectives of this research are outlined as follows:

1. To review the existing methods and devices for monitoring the electron beam process and beam itself.
2. To develop a deep learning model capable of analysing beam probing data related to the focus position (pre-process quality control).
3. To design a backscattered electron detector plate and verify, through practical trials, that the welding process stability can be monitored (in-process quality control).
4. To improve backscattered electron detector signal analysis by understanding different weld imperfections and how they affect data collected (post-process quality control).

Table 2: Weld quality control stages covered in the research.

Quality control stage	Quality criteria	Data source	Approach	Aim
Pre-process	Current density distribution	Beam probing	Time series imaging combined with the deep neural network on existing datasets	Support beam focusing
In-process (manufacturing process)	Melt pool and keyhole dynamics	Welding camera, back-scattered electron collector plate	Designing back scattered electron (BSE) detector plate, signal analysis	Welding process stability monitoring, distinguish between weld imperfections
Post-process	Weld geometry	High-quality photos of the weld bead and root, longitudinal cross-sections	Combining BSE signal analysis with high photos to reveal distinguishable features	Support for BSE collector plate signal analysis

1.5 Summary of Methodology

The methodology developed for this thesis work includes review of literature on electron beam defects, beam probing, welding process monitoring, focusing methods and time series imaging. The research work on the problem of finding sharp focus location has been done using the dataset of 3015 BeamAssure measurements provided by TWI. For this reason, pre-process methodology focused on data analysis using deep learning algorithm has been presented. The relationship between BeamAssure signals and time series images created based on them has been identified. For the in-process stage, backscattered electron collector plates have been designed and the experimental trial has been carried out to collect BSE signal and HDR camera images. The samples used in the trial have been manufactured with simulated gap defect using titanium alloy Ti-6Al-4V, which is relevant to the aerospace industry. The welds carried out during the experimental phase are examined and the BSE signal is compared against longitudinal cross-sections. The same cross-sections have been also compared against camera data, which have been processed to reveal changes in the weld pool shape. The limits of the camera and BSE collector plate are identified based on the observed weld defects.

1.6 Thesis structure

This thesis is organized into seven chapters, including this introductory chapter. The layout of the thesis, addressing the objectives mentioned in the section before, is illustrated in figure 3.

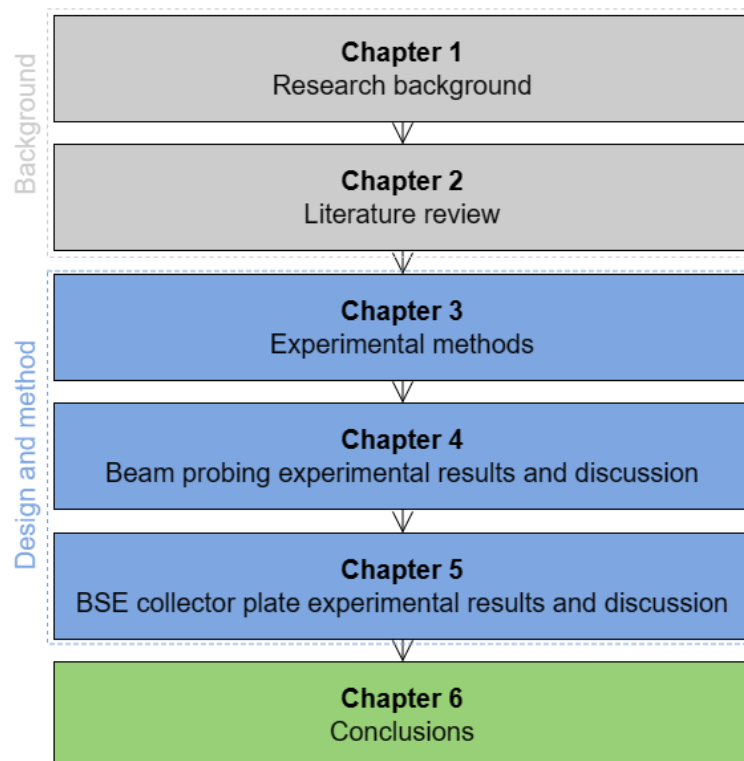


Figure 3: Thesis layout.

Chapter 2 includes the literature review of standards related to quality in EBW, weld pool behaviour, beam probing and focusing methods, backscattered electron monitoring and imaging.

Chapter 3 provides general details about the methodology and equipment used and introduces some technical limitations and methods to overcome them.

Chapter 4 describes research using beam probing and signal processing (time-series imaging) for training deep learning models.

Chapter 5 is focused on the backscattered electron monitoring and camera data, processing the obtained signals and detecting specific imperfections during welding.

Chapter 6 is finally concluding the research work and Chapter 7 discusses the future development of a multi-sensor fusion system for electron beam welding.

1.7 Contribution to Knowledge

Chapter 2: This chapter presents detailed literature review on the developments in the field of electron beam welding related to weld quality, beam probing, backscatter electron monitoring, vision systems and beam focusing methods. Time-series encoding methods and their applicability in other fields have been introduced.

Chapter 3: Detailed summary of encountered problems during beam probing and BSE monitoring including methods to solve them. The research in this field has been targeted on differentiating the signals features for sharp focus location, overfocused and defocused beams using beam probing. It was observed that encoding electron beam originated signals can be efficiently encoded as time series imaging for further processing using deep learning tools. Usage of sensors, such as HDR camera and BSE collector plate have been discussed. Main focus of this part is on design and retrofit of the BSE collector plate have been described. Additionally, proper selection of the camera and the way of decoding of the collected images have been presented.

Chapter 4: The dataset of 3015 probe signals have been encoded using time series encoding methods in order to predict sharp focus location based on one measurement. This work has applied signal pre-processing methods to segment signal and extract pulses related to the electron beam, compress it without losing its trend, and encode it as images. The deep learning model has been retrained and it has been observed that it was able to differentiate between beam with different focus levels with remarkable rate of 97.6% of accuracy in the classification task. The algorithm has been further fine-tuned to provide sharp focus adjustment value for the operator. Additionally, a method of 3D reconstruction and visualisation of beam probe signal from 17 slit probe has been presented for detailed analysis of the beam. Tomographic reconstruction and filters have been compared to highlight the most suitable approach for reconstructing electron beam.

Chapter 5: This research work is an effort to better understand BSE signals patterns and how they correspond to weld defects. Additionally, the HDR camera has been involved during this experiment as additional data source. The results of the experimental work carried out prove that BSE signal monitoring is powerful tool in detecting any weld pool instabilities, especially joint misalignment, porosity, humping and root defects. Detected defects corresponded to the longitudinal cross-sections and have been as small as 1 mm. Joint misalignment have also been recognized from the camera images, but with much greater size of the data.

1.8 Summary

This chapter includes research background and thesis structure. In order to get clearer understanding of the research problem, an exhaustive literature review is presented in the next chapter covering developments of beam and process quality monitoring methods used in electron beam welding.

2 Literature review

This chapter summarises primary electron beam welding parameters, the standards applicable to the quality of electron beam welded joints, beam probing and melt pool behaviour of power beam processes. Beam probing related subchapters consist of beam probing techniques, tomographic reconstruction and methods of estimating electron beam focus quality. Melt pool behaviour topics are enriched with monitoring methods, such as backscattered electrons, vision systems and welding cameras. Time-series encoding methods are elucidated closer to the end of this chapter. Additionally, this section also includes up-to-date review of the work carried out related to the problem of evaluating the surface focus and backscattered electron monitoring concerning weld quality. In view of the above, details about the machine learning approach and its comparison with other devices and systems has been described.

2.1 Electron beam welding parameters

The electron beam welding process can be fully controlled by electrical parameters. In order to produce welds with excellent characteristics, those parameters need to be within specified tolerances. Any variation in these parameters influences the current density distribution of the beam and has an impact on weld penetration, weld width and surface quality. Essential parameters, called primary in this section, are crucial as a starting point for setting welding variables. Meanwhile, secondary parameters are not normally used to adjust different welding results. However, they should be also controlled, as they contribute to the final quality of the weld.

Primary EBW parameters are beam voltage, beam current, focus current and welding speed. Secondary parameters include pressure (vacuum), working distance, and beam deflection. All of those primary and secondary parameters can be tuned and monitored with solid-state control units to maintain them within one percent of the set value [10].

Beam voltage has effect on beam power and beam power density, which greatly affects focus current and the ability to produce a minimum focus spot. EBW guns are supplied with various voltages and a suitable system must be selected so that the performance meets the requirements of the application. EBW machines with beam voltages below 60 kV are classified as low-voltage systems. Respectively, any machine above 60 kV is referred to as a high-voltage one [10]. Properties of the typical high-voltage electron beam (HVEB) and low-voltage electron beam (LVEB) machines are presented in Table 3.

Table 3: Differences between high- and low-voltage EBW machines [10].

High-voltage EBW machines	Low-voltage EBW machines
Used in non-vacuum EBW machines	Produce less energetic X-rays
Maximize the working distance	Compact electron beam guns
Can be focused to smaller spot sizes at equivalent power levels	Possible multi-axis control of the gun

Another primary parameter which affects focus current is the beam current. However, its effect on the focal spot is not as great as beam voltage. The most common application of varying beam current is during slope-in and slope-out control. Slope-in is used at the start of the weld to increase the depth of the keyhole from zero to full penetration as the beam power is increased (with time or rate controls). Similarly, slope-out is used at the end of the welding, but in a reversed sequence. Those controls are used to maintain smooth weld bead contour, in cases such as welds which overlap themselves. It allows for the avoidance of material build-up during the initiation of the keyhole and slows down the collapse of the keyhole at the end of the process (no crater formation) [11].

The aforementioned focus current has a primary effect on the beam focal spot. It changes beam size, shape and power density distribution. Focus current is measured in reference to the focal spot on a target at the closest possible working distance to the workpiece. Depending on the type of EB gun used, it can be set at the welding current or lower. With constant focus guns, it is possible to determine the focus current at a lower welding current, so the spot size can be observed more easily. The bottom line is that the actual focal point fluctuates with changes in beam current, so it is very important to record the beam current (alongside with focus current) used to determine the focal spot.

The final primary parameter is welding speed. It has an impact on power input per unit length of weld and it is linked to penetration depth. For the secondary parameters, beam deflection is the most complex parameter, which consists of oscillation frequency, amplitude, pattern and phase. From all of these component parameters, the oscillation pattern has the biggest effect on the weld, whereas amplitude and frequency variation have little effect. Beam deflection is commonly used to control the shape of the weld, but it may be used in heat treatment, electron optical imaging and seam tracking on small components.

Another secondary parameter is working distance, which affects focal spot size and shape. Short distances are not recommended for deep penetration welds due to the inaccurate weld shape and the spattering and evaporating of the material onto the EB gun. The final secondary parameter is vacuum, which has an effect on the weld penetration and bead shape. In high-vacuum welding, it can also change

the focal spot. The effect of the varying vacuum level will be more pronounced if the working distance is increased.

Besides the variables mentioned above, filament-related variability can also affect the welding process but not to a great extent. Starting with the filament current, it has negligible effect on the weld quality, as any variations in the current are mainly related to the excessive wear of the EB gun. Moving further, filament orientation also should not matter for weld quality, as machines use flat or ribbon filaments without obvious orientation. Only “hairpin” filaments made from wire produce elliptical spot shapes and may have any notable effect on the final weld. It is important to take filament current into consideration, but as a result of variability between filaments and over the length of use, rather than the value itself.

2.2 Beam quality

The main electrical parameters mentioned above can be easily recorded by parameter monitoring systems, which enable verification that correct welding parameters were followed. The data monitoring system can collect the values for parameters such as accelerating voltage, beam current, focus current, deflection current, oscillation frequency, among others. Collected data can be either streamed directly from sensors or cumulatively from programmable logic controllers (PLC).

It has been found to be more difficult to monitor variability in gun performance, which affects beam intensity and focus position. This task is more demanding as it can be done either by performing and evaluating trial welds or by examining the beam intensity distribution. The former method is a costly and time-consuming trial and error approach, whereas the latter can be done by assessing the beam shape from beam probing method. Welding test pieces seem to be a simple pass/fail check and cannot assess the state of the EB machine. Even if the test is successful, there is a lack of information about beam shape and its condition change.

The complex nature of an electron beam can be characterised as having a high-intensity core and low-intensity fringe, whose distribution may vary between the beams of the same diameter. Figure 4 a) illustrates beam profile and Figure 4 c) shows typical regions of outer ring of electrons (also called ‘halo’) and high electron density centre. One of the risks associated with the fringe is that it still has extreme power and may cause overheating of the workpiece surface without sufficient power for penetration. It also affects a weld fusion zone, producing a range of imperfections such as wide nailhead-shaped bead, asymmetric features and undercuts visible in cross-sections. Those differences between beam profiles are mainly caused by the EB machine and gun combination, but also come from electron gun alignment errors, cathode distortion and erosion, working distance changes, electrical parameter drift or simply by equipment failure. The frequency of beam quality changes may be as long as the frequency of maintenance checks, varying from batch to batch, or can be a consequence of unexpected cathode failures due to its wear [12,13]. Burgardt (2016) found that the difference between beam focused in the fringe and in the core can be as high as 16 mm and this effect

is more pronounced in low-voltage EBW machines rather than high-voltage ones [14]. Figure 5 illustrates the offset in heights of the sharp focus location in core and fringe.

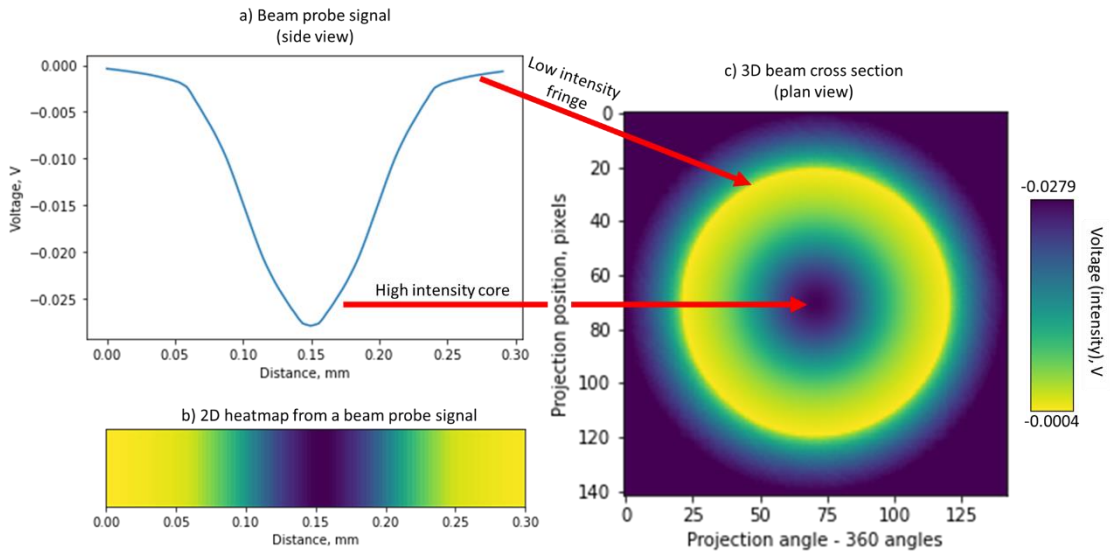


Figure 4: Schematic showing beam probe signal with corresponding heatmap (side view) and their location on the plan view of the 3D beam cross-section. The highest intensity part of the beam is emitted from a core and it is surrounded by low-intensity fringe. Adapted from [12].

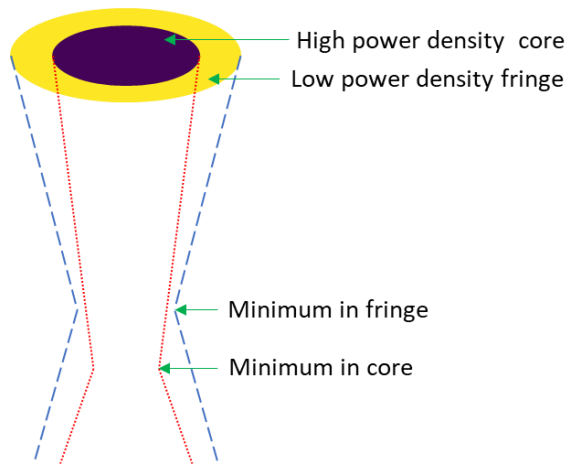


Figure 5: Schematic diagram of the EB machine generated beam showing the difference between core and fringe caustics. Adapted from [14].

Ideally, the beam probing data will follow a Gaussian shape pulse, which will be narrower and higher for intense beams. For electron beams with non-ideal beam quality, the pulse will be broader and asymmetric. For focus currents outside of

the range of sharp focus, power density distribution is described by non-Gaussian distribution. Additionally, as the resulting beam profile may be often irregular and can be oval-shaped, it cannot be easily described by a power density distribution. Energy density distribution refers to two directions of the beam, but may omit high-intensity patches inside the beam, caused by the type of filament used, focus condition and filament wear. Those complex non-symmetric beams can be measured using computerised tomography, utilising multiple scans taken around the beam [15].

The main purpose of monitoring the beam quality is to collect the data consistently to track the changes of the beam over time by comparing the pulse shapes. This leads to the detection of anomalies prior to welding and, with the correct intervention, can lead to increased reproducibility of the welding beam and improved weld quality.

In addition to the direct influence on weld quality, beam diameter monitoring is also important to obtain high-quality images using backscattered electron vision, as the smaller spot sizes offer better image quality [16].

2.3 Beam focus

Focus is a very important characteristic in the electron beam welding process because it can directly impact welding quality. Beam focusing can be described either as “normal” or “optimum” as referred to by Schultz (1992) [1]. For welding operators, it is most useful to use the term normal focusing of the electron beam, which means that focus is set manually by observing and evaluating the brightness of the heated spot on the surface either of the work piece or the refractory metal block (e.g. a tungsten focus block) [6, 17]. It is also referred to as surface focus. The difference between the shape and the brightness of the point of the beam impingement is presented in Figure 6.

The procedure of setting the focus current is described in the guideline developed by the American Welding Society. The AWS C7.1M/C7.1:2013 [10] standard divides methods into two different types: the first one is about determining focus current at the focal spot determined at the welding current, and the second one is related to constant focus guns. In the latter case, focus current is determined at lower welding currents, which gives a better view of the spot size. In the case of using a lower beam current to determine the focal spot, it is important to realise that the actual focal point changes with the adjustments in beam current. Thus, the beam current and focus current should be recorded [6]. The focus is considered as a “sharp” focus when the operator achieves the smallest possible focal spot diameter and the luminosity brightness becomes maximal. A further obstacle to effectively and accurately set the focus is caused by dirty optics and penetration of the surrogate block. If at least one of these conditions occurs, they will obscure the spot viewed [18].

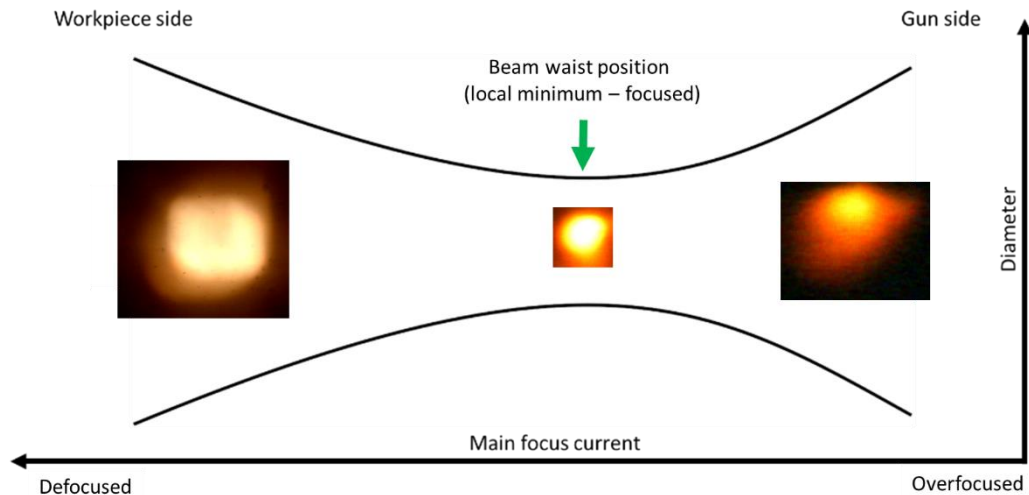


Figure 6: Schematic diagram of the beam caustic created from multiple beam diameter measurements. The images illustrate the beam shape change, registered with the camera, on the top surface of the workpiece.

In contrast to “normal” focus, the “optimum” focus refers to the beam focus that produces as few defects as possible in the weld. Under these requirements, the beam, irradiating the surface of the target material, is set to be defocused. It results in greater spot diameter than the actual focal diameter [6] at the workpiece surface.

2.4 Beam focus supporting systems

As described in previous chapters, focus can be set either manually using video systems or by utilising beam probing. It can be also controlled based on the parameters of secondary signals. During electron beam welding various electron emissions can be detected. These emissions can be used to detect the focal position of an electron beam. In 1991, Hiramoto [19] described monitoring the intensity distribution (collector current) of electrons emitted from the workpiece during welding and the frequency spectrum of the emitted charged particles. An automatic beam focus detecting system utilised thermoelectron detection. One slight disadvantage is that prior to detection, the electron beam needed to be turned on and consequently left a small flaw on the workpiece surface (0.2 mm in diameter). However, this defect was later covered by the bead after welding. The automatic beam focus detecting system described by Hiramoto can also be used for the correction of beam current. It is commonly known that if the beam current is varied it will affect the focal position, so a correction is recommended for the difference between the beam current at the time of detection and during welding. Using teaching/playback programming, the system allows welding with uniform penetration for materials with an irregular work distance [19].

Moving towards beam probing devices, Giedt and Campiotti (1993) [20] described a method to focus the beam so that its focal point is just at the surface. Using a plural slit-type Faraday beam trap, the diameter of an electron beam is measured. By measuring the current obtained from the beam, which is swept over at least

two narrow slits of the beam trap, it is possible to determine beam size. Then, using an automated loop, the focus coil current is changed until the focal point location passes through the elevation of a workpiece surface. Fitting the parabolic equation to the calculated beam sizes allows for determining the optimal focus coil current and optimal beam diameter.

Another automatic beam focus system consisting in using the Faraday cup, described by Elmer (2006) [21], includes the operation of sweeping a beam across a disk having a plurality of slits, which is arranged in a Faraday cup system and it is presented in Figure 7. This signal produced by the probe can be used in an automatic beam focus procedure. The process starts with setting an arbitrary sharp focus coil current. Then, using a feedback loop, the focus coil current was incremented above and below the arbitrary sharp focus current. Using Faraday cup measurements and computed tomography algorithms [22, 23] allowed to perform a 3D analysis of the beam density distribution. The last step involved determining a desired focus coil current based on calculated beam diameters [21].

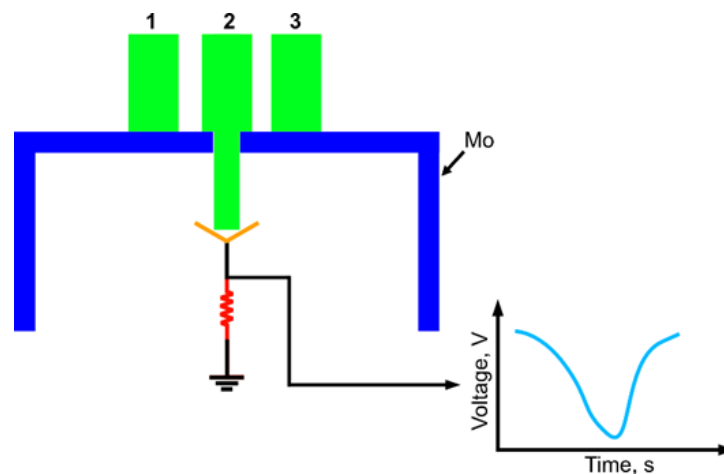


Figure 7: Slit probe design. The slit is in a molybdenum casing, the beam passes through the slit (at the position 2) and it is collected by an electrical pickup. The beam should be lined up with the slit so that the apparent width is no less than the actual width, which translates into accuracy.

Courtesy of TWI Ltd.

Commercially available systems to support beam focusing systems include beam probing devices such as Enhanced Modified Faraday Cup (EMFC), DIABEAM and two-slit probe (BeamAssure, Figure 8) [28]. Also, electron beam welding manufacturers like Pro Beam Group integrate automatic beam alignment systems into their machines.



Figure 8: The BeamAssure probe design. Courtesy of TWI Ltd.

2.5 Beam probing

Weld quality is in part determined by beam characteristics. These, in turn, are dependent upon parameters as well as other factors concerning mechanical alignment, proper functioning electron optics and wear of gun parts, particularly the cathode. Direct measurement of beam characteristics can be carried out by beam probing. Those measurements at various sections of the beam form beam caustics, which is useful information during beam focus adjustments.

In general, beam probing can be used in three ways:

- as a health monitoring device to ensure that the machine performance is maintained,
- as a good starting point for parameter development,
- as a record of beam parameters for a process and to provide a method of transferring them between different machines [25].

Volker (2011) [26] points out that the average operator during beam alignment will produce results with low accuracy and low precision. Experienced operators are much better at reproducing their alignment results with high accuracy, but still with low precision. The highest accuracy and highest precision are offered by automatic beam alignment, which is usually very close to the optimal alignment values. For this reason, the beam probes are used to ensure constant product quality through a reliable and reproducible beam setup. The relationship between the accuracy and precision of different setup scenarios is presented in Figure 9.

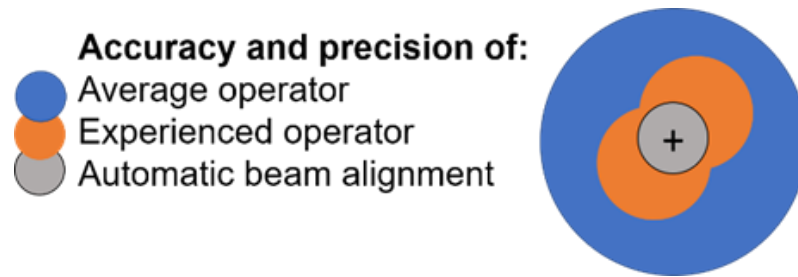
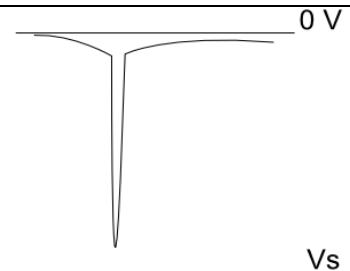
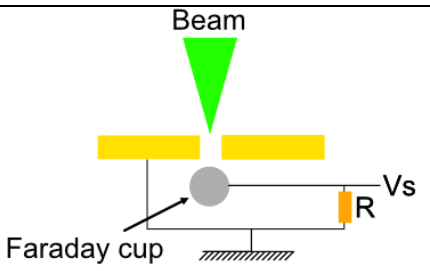
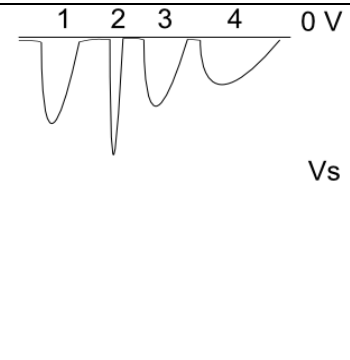
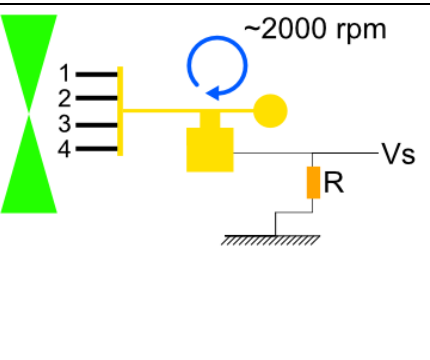


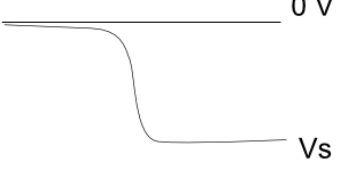
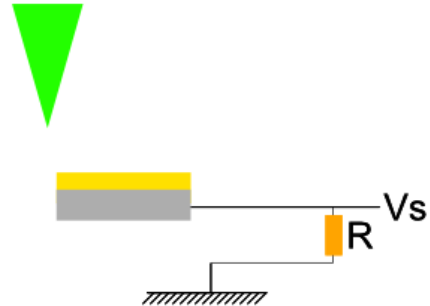
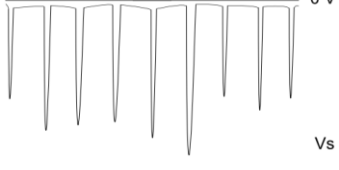
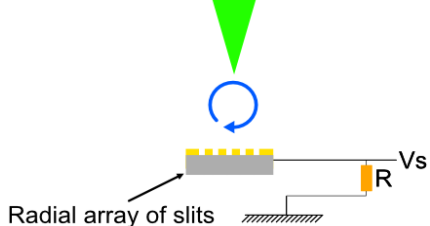
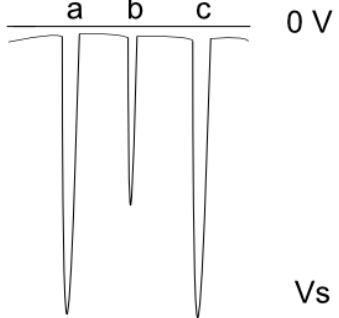
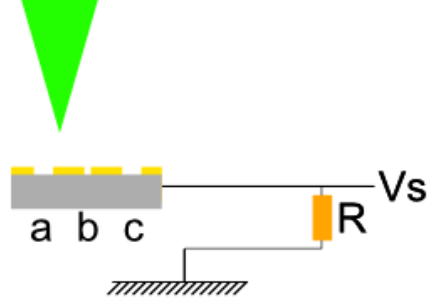
Figure 9: Different setup scenarios in terms of accuracy and precision. The chart is based on centring and stigmatising parameters and their possible error areas. Cross represents the target value. Adapted from [26].

As mentioned earlier, beam probing is used as a rapid interpretation of the beam and as a guide to the expected weld shapes in the X and Y axes [27], but it lacks 3D information of the beam power density distribution. In order to obtain the 3D image of the beam, the beam probe needs to be equipped with multiple slits. Once the data from multiple slits is collected, using tomographic reconstruction, it is also possible to obtain a 3D density distribution plot [15,23].

The slit probe discussed before is not the only possible beam probing configuration. All of the probing techniques were described by Dack (2011) [28], and are compared and summarised in Table 4 below.

Table 4: Differences between beam probing techniques including their advantages (+) and disadvantages (-). Adapted from [28].

Technique	Characteristics	Typical individual signal	Probe schematic
Slit	+high duty cycles -single axis analysis		
Rotary	+simple -delicate -low beam powers -large fixture -backscatter noise -several electrical feedthroughs		

Edge	<ul style="list-style-type: none"> +simple and robust hardware -backscatter noise -difficult data analysis 		
Multiple slit	<ul style="list-style-type: none"> +comprehensive beam analysis +easy to use -low power levels (<4kW), but could be extended to high power beams -difficult to process the data -all slits must be of the same width 		
Pinhole	<ul style="list-style-type: none"> +comprehensive beam analysis +high beam powers -difficult to align -difficult data processing -slow as the beam must be paused between raster scans and probe may require water cooling for high power beams 		
Two perpendicular slits	<ul style="list-style-type: none"> +high duty cycles +easy to set up and use -both slits needs to be same width 	As Figure 11	As Figure 7

2.6 4-slit beam probe (BeamAssure)

A BeamAssure probe head was used in the experimental part of this thesis to provide signals representing the beam current distribution over the beam spot. The probe head, which is manufactured from refractory metal, consists of two pairs of slits positioned perpendicularly to each other. The probe is mounted inside the vacuum chamber of the electron beam welding machine. The beam, initially placed in its free-fall position, is deflected over the probe in the form of a circular path represented as dashed red line in Figure 10 [29]. The beam firstly passes over two slits, then it crosses the Faraday cup and moves through the second pair of slits, where each has a smaller collector beneath. The beam speed is high, typically 450ms^{-1} , thus contact time with the probe is kept to a minimum and there is minimum damage to the probe caused by intense beam [29,30,31].

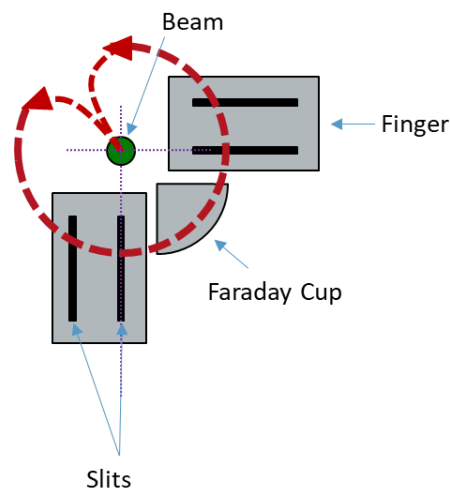


Figure 10: The BeamAssure probe schematic. The red lines mark electron beam path. Courtesy of TWI Ltd.

The voltage (shown in Figure 11), which is collected by the beam probe, forms a signal. It consists of 4 peaks that come from the slits in the fingers and 1 large peak from the Faraday cup (FC). From the probe signal, three main beam checks can be obtained. The position of the 2nd (Figure 11) and 4th pulses are used to verify the correctness of beam positioning. In the case of a correct position, the pulses will be apart by $\frac{1}{4}$ of the deflection period. This enables proper alignment between free-fall axis and the intersection of X and Y slits. This first check uses the shapes of these pulses to define the beam width in the X and Y directions.

The second check is based on the 1st and 5th pulses, which independently do not carry enough information. However, in combination with the 2nd and 4th pulses, they are used to calculate the beam deflection speed. This simple velocity check is useful for converting the time-based signal to a distance based one. The last check utilises the 3rd pulse, which is usually omitted during sophisticated beam analysis, because it is produced when all of the beam is passed into the Faraday cup and it only contains an amplitude of 70% of beam current. In such case, it is used to quickly verify the total beam current level [29].

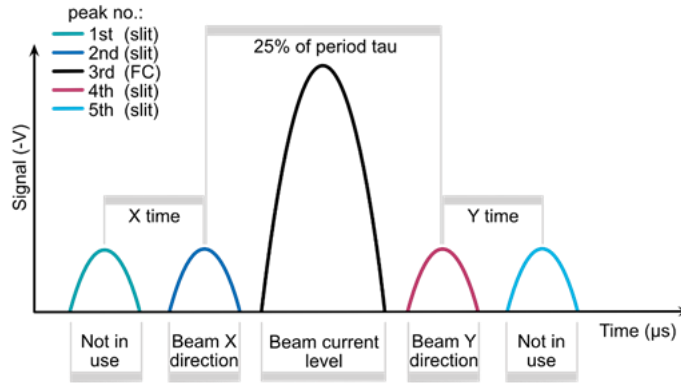


Figure 11: Schematic of the BeamAssure signal.

Depending on the focus current, the collected voltage from mutually perpendicular slits, can take different shapes. The difference between the various focus conditions for one of the slits, in X direction, is presented in Figure 12. Defocused beams can be characterized by sub-Gaussian (flat top) profiles as shown in Figure 12 by the blue line. Focused beams follow Gaussian distribution which is marked with orange line in Figure 12. Overfocused beams follow Laplace (super-Gaussian) signal distribution and highlighted by the green line in Figure 12.

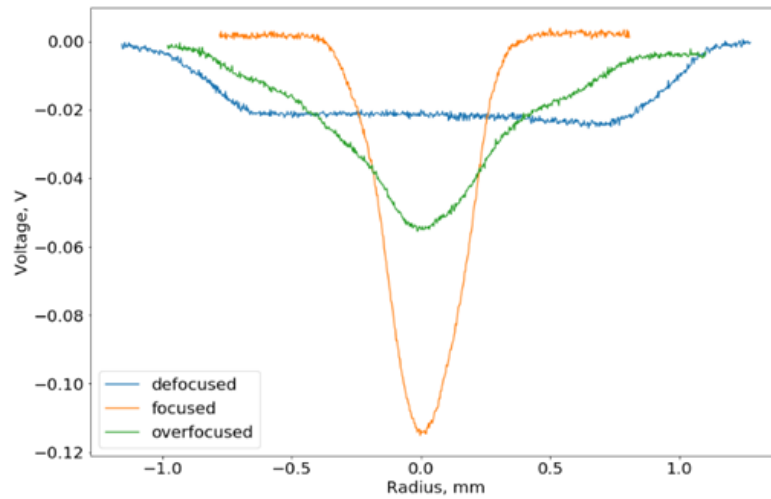


Figure 12: Comparison of the slit voltage for 2nd slit as a function of beam radius for the defocused, focused and overfocused beam obtained from the BeamAssure probe. The shape of the curves complies with Elmer (2001) [31].

2.7 Beam width definitions

Currently, beam width can be represented by one of the six common definitions such as $D4\sigma$, 10/90 or 20/80 knife-edge, $1/e^2$, full width at half maximum (FWHM), full width to half power (FWHP) and D86. All of those values, with accordance to the X and Y directions of the slits, are captured by the BeamAssure software and stored in a results file.

The simplest, and most widely quoted beam width definition, is full width at half maximum (FWHM). It is defined as the width measured at half of its peak value. As FWHM is very sensitive to peak intensity of the beam, FWHP was created and defined as the width of the beam containing half of the beam current.

If the beam intensity distribution follows a Gaussian distribution, then the $1/e^2$ definition of beam width can be used and it is defined as width at an intensity of 13.5% of the maximum current value. In fact, EB intensity distributions are rarely Gaussian due to misalignments of the electron beam and aberrations in the lenses, which prevents the formation of ideal Gaussian intensity distributions. This, in turn, causes the differences between actual and calculated beam width and restrain the $1/e^2$ value to be widely used for EB characterisation.

To reduce the noise effect on measured beam characteristics, it is possible to integrate the probe signal. From there, many width characteristics can be derived from the integral by measuring the distance interval between different limits. One of them, mentioned above – FWHP, contains 50% of the beam power and is derived from the distance interval between the 25% and 75% levels of the integral (also called interquartile range). Other possible range combinations include 20/80, 10/90 and D86 (between 7% and 93%), where the beam widths are measured for 60%, 80% and 86% intervals respectively.

The last width definition, commonly used in laser beam measurements, is called $D4\sigma$. It is mathematically defined in Equation 1, where r is the centroid of the beam profile and i is the beam profile function.

$$D4\sigma = 4 \sqrt{\frac{\int_{-\infty}^{+\infty} ir^2 dr}{\int_{-\infty}^{+\infty} idr}} \quad (1)$$

However, $D4\sigma$ is sensitive to the noise floor level and it is not considered as a robust measurement of the EB width [6, 29]. All of the described beam width definitions are presented on the Figure 13.

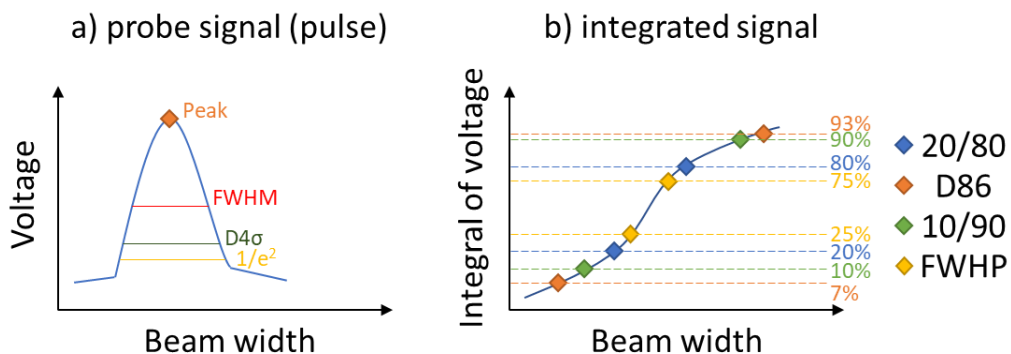


Figure 13: Beam width definitions. a) FWHM, $D4\sigma$, $1/e^2$, b) 20/80, D86, 10/90, FWHP. Adapted from [29].

Specified definitions for measuring beam widths can be found in the ISO 11146 [32, 33] series standards and are based on laser beam measurements.

2.8 Multi-slit probing

Multi-slit probing is based on the same principle as 4-slit beam probing described in chapter 2.6, but the number of slits is greater than four. Additionally, the beam shape is reconstructed using computed tomography (CT). The process starts with obtaining the current density distribution at all possible angles from a multi-slit probe. An example of such a device, shown in Figure 14 is the TWI-developed 17-slit prototype probe for research purposes, which was used in this thesis.



Figure 14: The multi-slit (17 slits) probe design. The small circle between slits is used as a signal reference.

Slits need to be equally spaced around the beam, in the case of the TWI 17-slit probe, they are apart by a 21.18° angle. The probe small round slit, placed between the 17 slits, provide an even more precise measurement as it marks the beginning and end of the beam deflection pattern. As the round slit is wider, it will allow more electrons to pass through, and location of the reference slit can be easily extracted from the signal as it is observed as two strong peaks with the same height as shown in Figure 15.

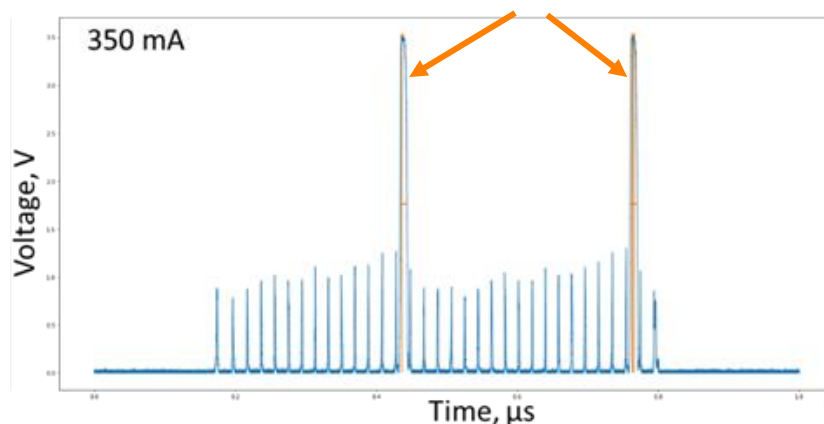


Figure 15: Typical multi-slit probe signal. Orange arrows (highest peaks) point to the centres of the signal references. As the beam is swept multiple times over the slits, the signal of interest is located between two signal references.

2.9 Radon transform

To reconstruct the beam from a multi-slit probe, several projections must be captured, each of them acquired at a different angle between the rays with respect to the object (Figure 16 (1)). Each projection of the object is called a slice (or section), which is one-dimensional. The multi-slit probe signal has seventeen slices (Figure 16 (2)). CT is the process of building an image out of those individual projections (Figure 16 (3)) rotated to each other by 21.18° . Compiled projections (Figure 16 (4)) at several angles may be displayed in an array, which is called a sinogram (Figure 16 (5)). This is the first step in reconstructing a 3D image (Figure 17).

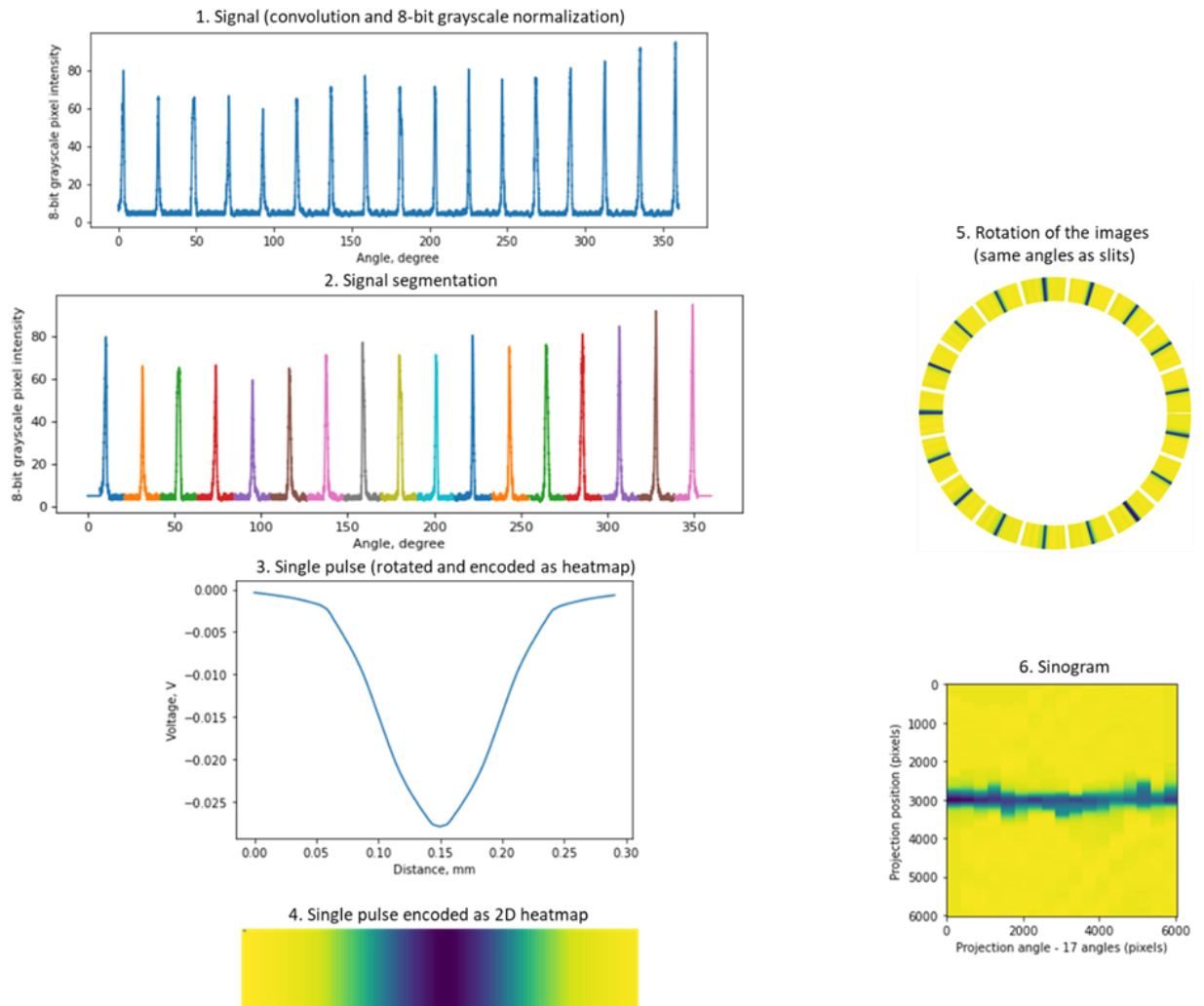


Figure 16: Signal processing applied to 17-slit probe measurements required to obtain sinogram. The process starts with extracting the signal between signal reference peaks (1), signal segmentation for each slit (2), extracting each signal (3), encoding each signal as a heatmap (4), rotating the heatmaps by a 21.18° angle (5), creating the sinogram from the rotated heatmaps (6).

The next step is utilising inverse Radon transform to reconstruct an image from the acquired sinogram. This process is called back-projection. The resulting image will always be affected by the blurring effect. However, this effect can be reduced by the usage of the filtered back projection (FBP) and the simultaneous algebraic reconstruction technique (SART) [15, 23]. Figure 17 presents image reconstructed using simultaneous algebraic reconstruction technique – the noise and profiles are smoothed out.

There are different filters used for FBP and the most basic filter is the Ram-Lak filter, which is also known as the Ramp filter. The frequency response of the Ram-Lak filter is $|f|$, which makes it sensitive to noise in the projections. The Shepp-Logan filter multiplies the Ram-Lak filter by the sinc function. Ram-Lak and Shepp-Logan filters are high-pass filters, which preserve the edge information. The cosine filter multiplies the Ram-Lak filter by the cosine function. Hamming and Hann filters are calculated by multiplying the Ram-Lak filter by Hamming and Hann windows respectively. Cosine, hamming and Hann filters are bandpass filters and they smooth out the reconstructed image by removing the edges from the image [34].

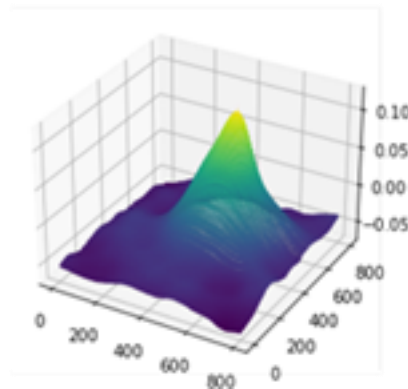


Figure 17: Reconstructed image using SART technique.

2.10 Melt pool dynamics

As the keyhole formation in electron beam welding is similar to laser welding, this may be determined by visual observations of those processes [35]. Only a few works were conducted in the EBW field by utilising high-speed cameras [36] and X-ray imaging [37, 38], but none of those works introduced any classification for different melt pool regimes. For that reason, and taking into consideration that EBW is a type of power beam welding, laser welding regimes proposed by Fabbro (2010) [39, 40] are described in this chapter. The recent advancements in imaging technology and usage of high-speed video cameras allow the analysis of the melt flow with high temporal and spatial resolution [41]. Laser beam welding experiments conducted by Fabbro were controlled by differentiating the welding speed. Additionally, the plasma plume behaviour was recorded and analysed by adjusting the angle of view of the camera and using wavelength filtering. As a result, five welding regimes were determined, which are summarised in the subchapters below.

2.10.1 “Rosenthal” regime

This regime is observed for low welding speeds below 5m/min. It can be described as a large melt pool area, which extends over the front of the keyhole. This is caused by low welding speed, which promotes a heat conduction regime. The behaviour of the melt pool surface is chaotic with large swellings of liquid fluctuating around the circular and distinct keyhole shape. These surface fluctuations create laminar flow around the keyhole and influence the creation of spatter, mainly splashed from the front side of the keyhole rim. Additionally, the vapour plume interferes with melt pool swelling fluctuations by changing spatter trajectories.

Considering only thermal aspects is characteristic of the Rosenthal heat flow regime, where the keyhole surface is uniformly heated at a temperature close to the evaporation and is surrounded by a large melt pool with a nonsignificant flow. The “Rosenthal” regime will be visible on macrographs cross sections of the weld seam as a wine cup shape and a typical cross-section is presented in Figure 18.

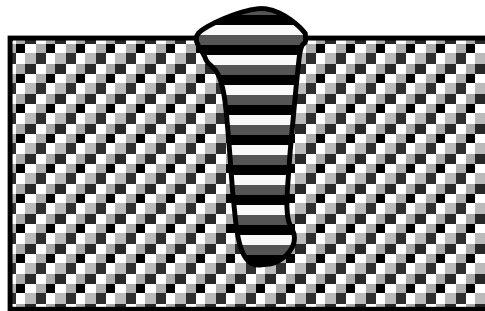


Figure 18: Typical cross-section of the “Rosenthal” regime weld. Adapted from [39].

2.10.2 “Single wave” regime

This regime is observed for medium welding speeds between 6 to 8 m/min. During welding, a large single swelling can be observed near the top of the rear keyhole wall, where melt droplets are ejected. They are periodically emitted towards the back of the melt pool, which causes visible oscillations. This also affects the keyhole behaviour, which is characterized by periodic closures. The vapour plume also influences the keyhole, as it is emitted deeply inside it and collides with the melt pool causing local heating of the liquid surface. In case of “single wave” regime, the cross section of the weld seam resemble elongated wine cup shape and is presented in Figure 19.

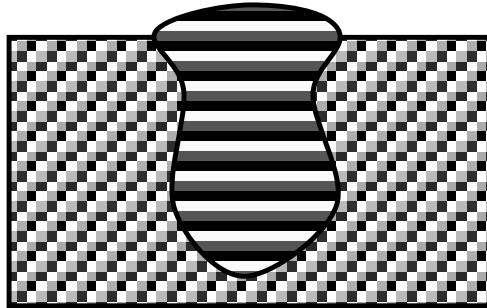


Figure 19: Typical cross-section of the “Single wave” regime weld. Adapted from [39].

2.10.3 “Elongated keyhole” regime

This regime is observed for higher welding speeds, between 9 to 11 m/min. The keyhole shape is elongated and can be as long as 2 mm achieved near the upper limit of the welding speed range. The oscillations have lower intensity than in a single wave regime. The elongated keyhole consists of two zones that are heated during weld pass. The former is located on the inclined wall, similar to all other regimes. The latter is situated at the rear end of the keyhole, inside the melt pool. The vapour plume is emitted from the second zone and as in the previous regime, it collides with the melt pool and causes local heating of the liquid surface. The second zone is surrounded by the melt pool and is efficiently heated, which produces a side melt flow. Both the side flow from the keyhole front and melt pool collide with each other ejecting small droplets directed upwards considered as defects after weld seam solidification. The cross section of “elongated keyhole” regime doesn’t look like wine cup anymore, instead the seam is wide and edges are straight as presented in Figure 20.

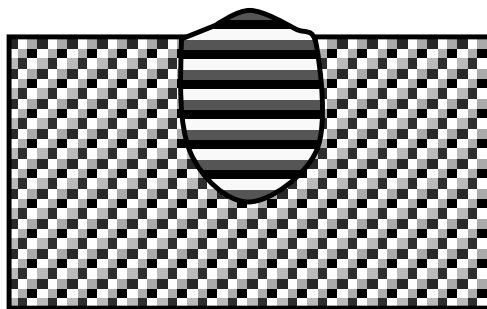


Figure 20: Typical cross-section of the “elongated” regime weld. Adapted from [39].

2.10.4 “Pre-humping” regime

This regime is observed for high welding speeds between 12 to 19 m/min. The keyhole is elongated, but with a shorter length than in the elongated keyhole regime. The oscillations have low frequency and the heated rear zone is smaller than when compared to the elongated keyhole regime. This results in no spatters and droplets emitted during welding. However, above a certain speed (around 15

m/min) it is common to observe the undercuts on the sides of the seam. The vapour plume does not fluctuate and is very stable. In “pre-humping” regime undercuts are becoming visible and the weld bead is pressed towards its centre. Typical cross-section is schematically presented in Figure 21.

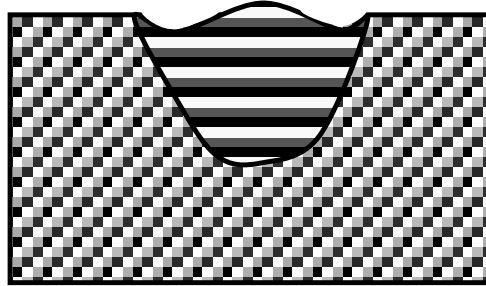


Figure 21: Typical cross-section of the “pre-humping” regime weld.
Adapted from [39].

2.10.5 “Humping” regime

This regime is observed for welding speeds above 20m/min. The humping regime exhibits very strong undercuts, where large swelling of ellipsoidal shape are separated by smaller valleys. This characteristic “valleys and humps” weld bead shape is shown in Figure 22.

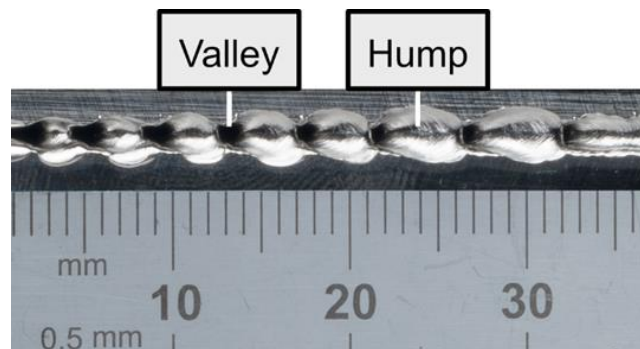


Figure 22: The hump weld bead in electron beam welding (focusing current 330 mA, beam current 18 mA, accelerating voltage 60 kV, welding speed 500mm/min, working distance 330 mm).

In “humping” regime undercuts are much deeper than in “pre-humping” regime. For that reason, the weld bead is pressed even more towards its centre and forms a hump. Typical cross-section is presented in Figure 23.

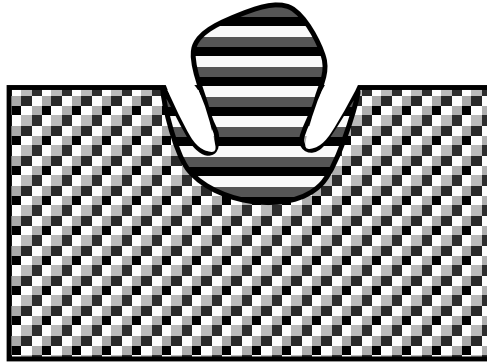


Figure 23: Typical cross-section of the “humping” regime weld. Adapted from [39].

The mechanism of the humping formation in electron beam welding was investigated by Tsukamoto (1983) [42], who introduced an indicator based on the ratio of working distance to focal distance. If the beam is just focused or under-focused, which falls into values between 0.83 to 1, it will promote humping formation. During under-focused beam welding, the molten pool ejects the metal from the rear side of the keyhole, which can be also proven by the particle trajectory. The slag-type particles' position also depends on the ratio of working distance to focal distance. With a lower ratio limit, the slag is moving backwards and it is present at the halfway point along the length of the weld pool. With the higher ratio limit, the slag is getting closer to the melt pool and the flow becomes stronger, which may lead to undercut formation. During over-focused beam welding, the rear flow is weaker, so the molten metal concentrates around the keyhole and creates nail head-type welds with a wide bead that expands near the surface. To ensure stable bead formation, the ratio value should be from 1 to 1.3, which corresponds to the focal point slightly above the surface. The effect of the ratio of working to focal distance is presented in Figure 24, where the top 2 weld pools are representing the humping formation and the difference in the slag position. The third weld pool showed in Figure 24 represents favourable conditions to prevent formation of the aforementioned defect. In all cases, the effect of the penetration depth is negligible, as no correlation can be found between depth and the formation of humping defects under constant accelerating voltage and beam current.

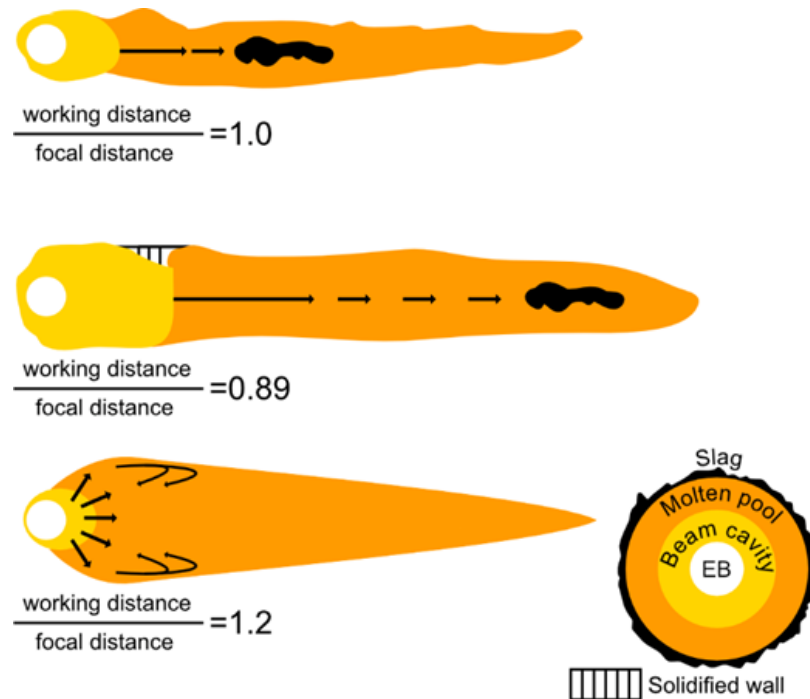


Figure 24: The ratio between the working distance to the focal distance and its impact on weld pool shape. Adapted from [41].

As the ratio parameter has been found to have the greatest impact on humping, it still can have an effect on welding imperfections. Generally, focusing the beam below the surface (Figure 25c), which increases the penetration, is used for thick materials and it improves weld root characteristics. Those improvements include the elimination of cracks, voids, porosity and cold shuts, which may occur with normally focused and overfocused beams [43]. The risk with normally focused beam is that metal vapours will be pushed into the middle part of the keyhole and this uneven pressure will create shrinkage cavities (Figure 25a). On the other hand, overfocused beams may push this metal vapours further to the bottom of the keyhole and during the solidification phase this stress concentration may results in formation of cracks. As proposed by Tong (1969) [37], the existence of the cavity oscillations in size and shape or humping formation can be registered by x-ray radiographs during a bead-on-plate weld pass. A more simplified method is monitoring the top view of the keyhole using imaging devices or by general observations.

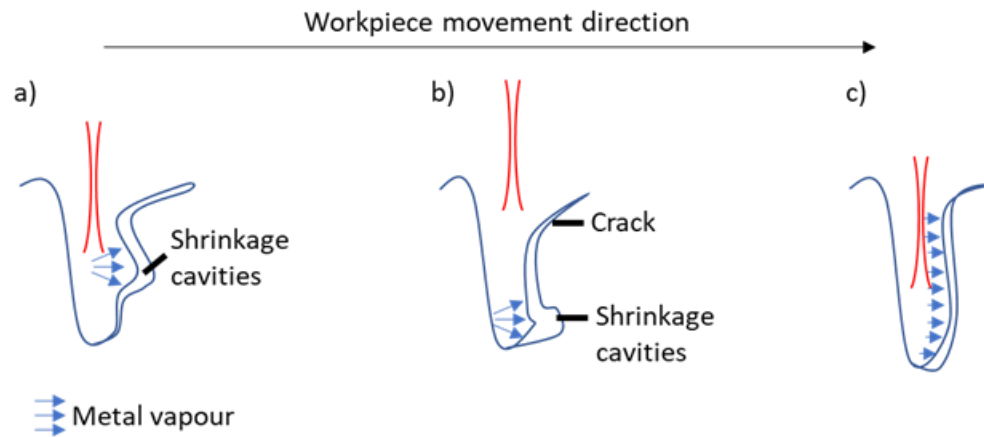


Figure 25: Relationship between focus position a) normal focus, b) overfocus, c) defocus, and weld imperfections. Adapted from [26].

2.11 Electron beam welding related standards

Establishing standard conventions for naming rules and weld defects classification is needed to ensure that they can be clearly identified and described. This can be achieved by reviewing standards in EBW field and best practices guidelines.

ISO 13919-1:2019, mentions spatters and spiking, whose acceptance depends on the application and the presence of other imperfections. While many research papers have been published about the humping, it is not precisely classified in standards as defects. As the humps and valleys are related to multiple types of imperfections at the same time, humping can be described as a mixture of incomplete root penetration and undercuts with excess weld metal and sagging. Humping can be also related to the spiking defect, as the average pitch of the spikes and humps and mechanism is the same [44], but those are not the same defects. AWS D17.1/D17.1M [45] and AMS2680C [46] do not allow any incomplete penetration in the joint, so the humping would not be accepted either. The closest imperfection similar to humping is presented in ISO 13919-2:2001 [47], which is related to aluminium, and is called shrinkage groove with the pulsating beam (Figure 26).

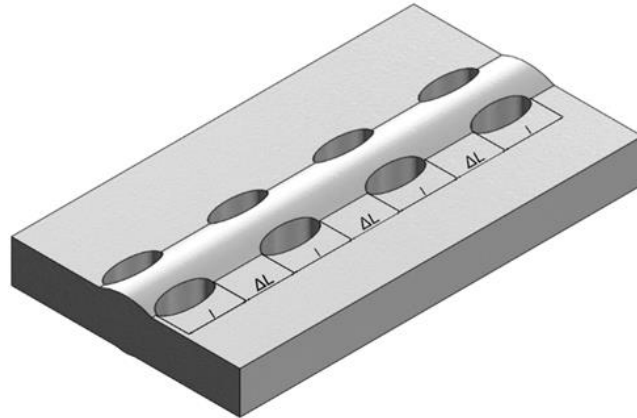


Figure 26: Visualisation of the shrinkage groove based on the ISO 13919-2:2001 standard. Adapted from [47].

In BS EN 1011-7:2004 [48], there is a simplified root cause analysis of defects and their prevention, but it mainly includes imperfections other than spiking and humping. According to the aforementioned standard, spatters can be reduced by using the backing plate and spatter protection shield/paint and incomplete penetration can be improved by properly setting focus, welding speed and beam power. AWS C7.1M/C7.1:2013 [10] can be used as a guideline when setting up the EB welding process, as the power curves provide reasonable starting parameters for different materials based on desired penetration depth, travel speed and power. All EBW related standards are summarized in Table 5.

Table 5: Selected standards and guidelines related to electron beam welding and quality.

Number	Title
BS EN 1011-7:2004 [48]	Welding. Recommendations for welding of metallic materials. Electron beam welding
C7.3:2016 [49]	Process specification for electron beam welding
C7.1M/C7.1:2013 [10]	Recommended practices for electron beam welding and allied processes
ISO/TR 17671-7 [50]	Welding — Recommendations for welding of metallic materials — Part 7: Electron beam welding
ISO 13919-1:2019 [51]	Welding — Electron and laser-beam welded joints — Guidance on quality levels for imperfections — Part 1: Steel

ISO 13919-2:2021 [52]	Electron and laser-beam welded joints — Requirements and recommendations on quality levels for imperfections — Part 2: Aluminium, magnesium and their alloys and pure copper
AMS2681B [53]	Welding, electron-beam
AMS2680C [46]	Electron-Beam Welding for Fatigue Critical Applications
AWS D17.1/D17.1M [45]	Specification for Fusion Welding for Aerospace Applications
DVS 3210:2007-07 [54]	Test procedures for the quality assurance of electron and laser beam welds
ISO 15614-11 [55]	Specification and qualification of welding procedures for metallic materials — Welding procedure test — Part 11: Electron and laser beam welding
ISO 15609-3 [56]	Specification and qualification of welding procedures for metallic materials — Welding procedure specification — Part 3: Electron beam welding

2.12 Vision systems used in EBW

General observations during the welding process are possible through viewing ports located on the vacuum chamber walls. The effectiveness of such a method is usually low, because of the remoteness of the part from the operator and the possibility of line-of-sight obstruction. Mono- and binoculars can be installed to provide greater magnification for precise observations during the welding. Those optical instruments were mostly used in the older designs of EBW machines [57]. In general, observation by operators to control the process has been shown to lead to variable weld performance (e.g. Elmer [7]).

Developments in the field of vision process monitoring for electron beam welding has led to the widespread use of cameras and, in more limited cases, backscattered electron (BSE) detector plates.

In particular, these methods are used for:

- monitoring the EBW process,
- positioning of the beam,
- tracking of the joint during welding,
- running the beam parallel to the joint or edge of the workpiece,
- visual quality assessment of welding inside the vacuum chamber [57].

2.13 Imaging devices including welding cameras

Modern electron beam welding machines are equipped with industrial video cameras. Cameras offer the option to document the welding operation, as images and video recordings can be stored with date and part number. These recordings can be used as a part of a quality management system.

Levels of eye strain are significantly reduced when operators use the video system to observe workpiece, compared to a stereoscopic binocular telescope [58]. The machine vision system can further relieve operator fatigue associated with continued viewing of the PC monitor and thus reduce the risk of developing computer vision syndrome [59]. The image quality of industrial camera mounted in the EB machine can be further improved with filters, like neutral density (ND) filters or welding bandpass filters [60]. High-speed digital video cameras can be coupled with a monochromator for dynamic observations of spectral images [61].

The interference of the high-intensity heated spotlight and sensor noise [62] prevents the acquisition of high-quality images. Images collected by traditional industrial cameras are sensitive to noise, which is caused by illumination from the metallic surface. The electron beam welding environment exceeds a dynamic range for common industrial camera sensors.

To solve this problem, there are two possible solutions:

- decrease the dynamic range inside the vacuum chamber,
- increase the dynamic range of the camera [60].

In the first case, an auxiliary light source, such as a laser or LED [63], with a narrow bandpass filter on the camera can be used. The main three limitations include deposition of the dust from the EB process on the light source and camera filters, selecting the wavelength of the filter can be difficult, and auxiliary lights in the industrial environment cause safety concerns [60, 64]. An example of the preventive measure is the sacrificial window for the camera system which can be found in Figure 27. A roll of clean polyester film is unwound, in the front of the lens, to prevent dust deposition. Although the presence of the film prevents dust build-up, it affects the image quality by introducing an additional optical element in the lens system and magnifies associated optical defects (glares, coma, astigmatism and field curvature).

The second option requires the use of an HDR camera, which is equipped with a high dynamic range sensor [56]. Cameras with low dynamic range will register welding process as a bright white blob, losing all of the fine details. However, cameras with high dynamic range can preserve the subtle differences in light intensities and register tiny details occurring in weld pool. An example of the splash from the weld pool registered by HDR sensor is presented in the Figure 28. Main welding cameras manufacturers include (in alphabetical order) Cavitator Ltd (Finland), MeltTools LLC (USA), and Xiris Automation GmbH (Germany). Usage of such cameras could lead to better image quality, the creation of better datasets for deep learning models and, as a result, improved surface focus evaluation.

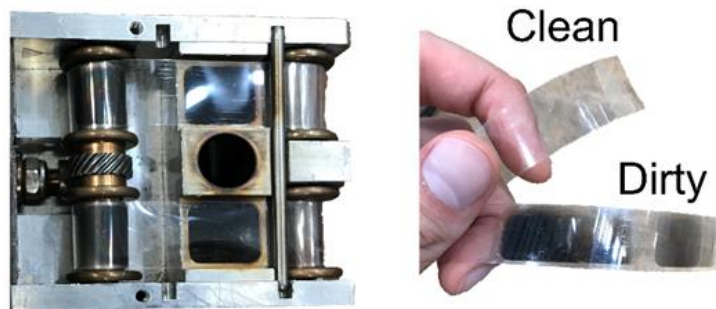


Figure 27: Left: sacrificial windows made from polyester on rollers to protect the visual optics. Right: Clean and dirty films.

Another challenge for imaging devices is related to the frame rate. Welding events are occurring faster than the finer details that the human eye can capture. The same problem is faced by the cameras. For example, according to Wei (2012) [44], spikes can occur between 2 to 4 per mm of weld, so considering typical welding speeds which are in the range of 125 to 250 cm per minute [65], it raises the minimum sampling rate to values as high as 333 frames per second (FPS), which can exceed the capabilities of industrial cameras. This forces the usage of high-speed cameras with high-intensity light systems, in which uniformity of illumination can be affected by the dust from metallic vapour and the whole system itself generates much more data for storing and processing.

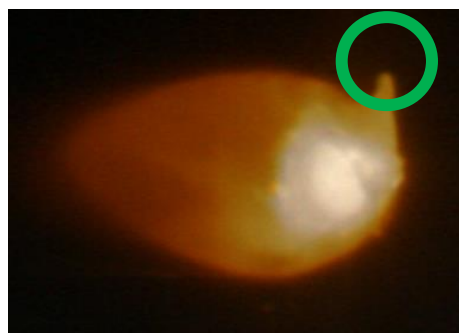


Figure 28: Splash registered (marked in green) by the HDR camera Xiris XVC-1100.

2.14 Electron beam imaging using backscattered electrons

Monitoring backscattered electrons can be as simple as registering the current collected by the plate, or in more advanced applications, they can be used to reconstruct images. Backscattered electron (BSE) detectors are commonly used in electron microscopy. The basic method of using backscattered electrons to obtain an image of the workpiece, starts with the electron beam scanning the surface of the workpiece, which is similar in principle to a scanning electron microscope. This means that the EB follows a vertical path through the EB gun in a vacuum. Once the beam hits the sample, various secondary emissions are generated, including BSEs. Then, the electrons reflected from the workpiece surface are collected in the collector of secondary electrons, which is fixed under an electron beam gun. These voltage readings from this sensor are used to grade a pixel greyscale. This greyscale image processing is based on the proportional number of electrons emitted from the surface at that pixel location. The last step involves arranging the pixels in the same order as the beam scan to form an image of the workpiece [66, 67].

Those systems are also widely used during the setup of the EB welding process. High contrast allows to easily distinguish different metals on the electron-optical image [18], due to their different electron reflectivities and this image brightness increases with increasing atom number in the workpiece. This is particularly useful to find the weld groove. However, this contrast highly depends on the amount of secondary emissions generated from the workpiece during the EB process. The highest number of BSEs is generated when the beam is not focused and the workpiece is not melted. Once the energy density of the beam is increased, the emission of thermoelectrons also increases and metallic ions are generated. As metallic ions have a positive electric charge, the number of BSEs will decrease. Once a beam is focused on to a workpiece, it will drill a keyhole. Re-radiation is intercepted by the walls and thus emissions have difficulty in reaching the collector surface. This leads to minimum quantity of BSEs and X-Rays observed, but also the number of thermoelectrons and metallic ions decreases too. Schematic illustrations of the change in the secondary emissions generated from the workpiece during EB irradiation are illustrated on Figure 29. Additional factors which reduce the amount of the collected BSEs are the distance between detector and the material irradiated by EB, and plasma torch formation once evaporation of material begins. Although the distance between the detector and the workpiece can be reduced, this poses a risk of sensor deformation due to the effect of thermal radiation from the melt pool.

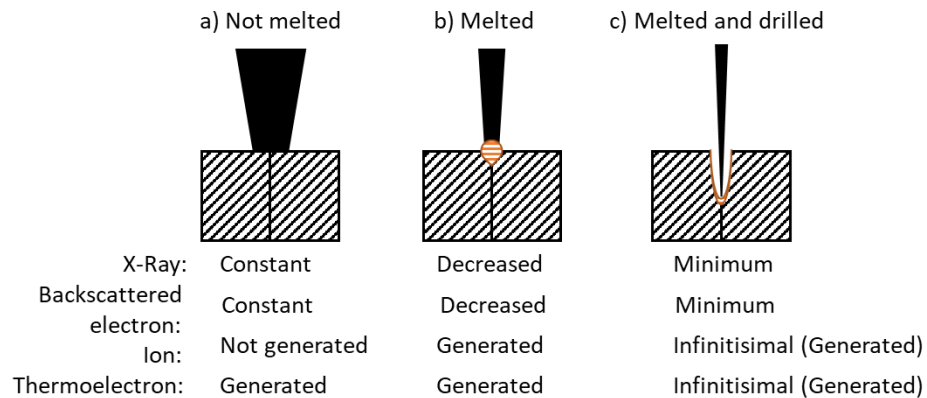


Figure 29: Process emissions from the electron beam welding zone.
Adapted from [19].

Due to that minimal number of BSEs generated once a keyhole is formed, Laptnek (2016) [67] stated that the picture quality is not enough to monitor the EBW process during welding. However, it is partially possible by regularly interrupting the welding process for a short time to make a scan at the current welding position [58, 26]. The fast beam deflection can be used to cause the beam to jump out of the weld pool during welding. During this process, the collected backscattered electrons are used to generate an electron-optical picture. There is a risk of the vapour capillary collapsing, but it will be maintained if the scan can be completed sufficiently quickly and the beam returned to the keyhole. It can be impossible to monitor thin and fast welds due to the early collapse of the capillary [58]. A further difficulty is related to the frame resolution. The triode electron guns can reduce power output during the time period allocated for scanning, but by using a diode gun, it is not possible to rapidly reduce the beam power. In the latter case, it is required to compress the frame scanning period into a few milliseconds. As a result, the amount of information collected during the scanning time window is limited [68].

This problem can be solved with electron optical video scanning, which is a simplified version of collecting electron-optical images – only three images are needed to show information about the whole process [54]. Each of the three pictures represents a sequence, which consists of a joint before welding, vapour capillary, and upper bead. Thus, the amount of collected data is drastically reduced and due to the shorter time, it is possible to monitor thin and fast welds [58].

2.15 Backscatter electron monitoring

As monitoring of electron beam manufacturing processes by the camera is limited due to thermal effects and dust deposition on sensitive parts of the sensors, backscattered electron monitoring offers the most appropriate method to use in the EBW machine chamber [67].

The main advantage of a backscattered electrons collector is insensitivity to vapour condensing on its surface during the welding. In contrast, light-optical systems, which are protected by sacrificial windows, suffer from image quality

degradation due to the aforementioned evaporated film and uneven illumination of the workpiece surface [57, 67]. The light source is reflected by a mirror to provide light in line with the camera (although it is non-collimated), which is the source of additional ghost reflections and shading problems.

As the electron beam has its own illumination, there is no need to use any concentrated light system for monitoring BSE as opposed to visual observations. This makes the operation and maintenance of BSE collectors much easier, even if they are covered by thick deposits of dust [26, 68]. BSE detector is mounted directly below focus and deflection coils so that the position of the beam is aligned with the BSE image. In contrast, light-optical systems require additional mirrors to align the axis of the lens with the axis of the beam, which is presented in Figure 30.

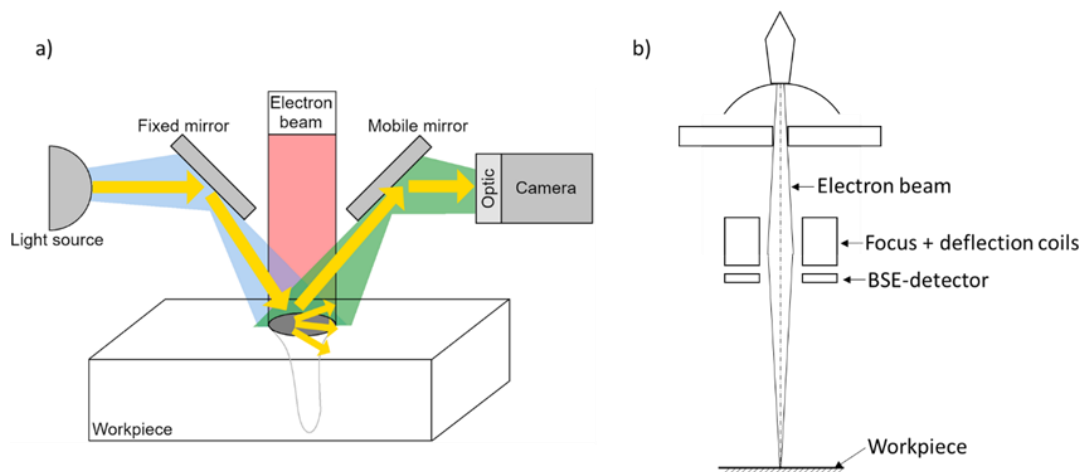


Figure 30: Electron beam imaging methods: a) light-optical systems and their non-collimated (rays are not parallel to the optical axis) illumination source b) BSE detector location

Usage of backscatter electron monitoring in EBW is not a new concept. The first examples of evaluating backscattered electrons during electron beam welding were carried out in the 1970s and 1980s: waveforms of the ion current were correlated by Mauer (1979) [69] to the weld geometry and electron backscattering usability in process control was evaluated by Ardenne (1976) [70]. A decade later, Sanderson (1988) [71] described a backscattered electron collector system with improvements in signal processing by using a reflecting electrode detector. Further, Anderl (1992) [72] described non-contact diagnosis using process emissions, but still without online process control.

In tandem, recent advances in EBAM are pushing BSE monitoring forward. There is the possibility to use backscattered electron monitoring for detecting surface defects such as pores during electron beam additive manufacturing. This method, presented by Arnold (2018) [73], was successfully applied to the development of processing windows in the selective electron beam melting process [74]. As Arnold's method uses electron-optical imaging (ELO) to capture images of the

sample surface, it requires the reconstruction of three-dimensional models of recorded layers. This method is aimed at process understanding and control, by possibly further increasing the spatial resolution and introducing additional off-axial detectors. The relationship and optimal trade-off between requirements of the EBM process and ELO-imaging are still not fully investigated. The alternative for in-process monitoring is the usage of thermography, but the field of view is smaller than ELO imaging. The most recent applications include monitoring the shape of the layer [66, 75] and layer-quality evaluation [76].

The more recent applications in EBW, related to the problem described in the experimental part of this thesis, were investigated by Olszewska (2004) [77], who introduced a split detector design for collecting ions, secondary and backscattered electrons. Later, those measurements were used to correlate the signals with weld root and active zone defects, but it was found that those examined signals contained weld channel shape data and less information about weld quality. Similar findings were presented by Trushnikow (2013) [78] to observe the behaviour of the keyhole. The most recent works are related to monitoring the electron signal distribution at different welding speeds by Gach (2021) [79] and monitoring gaps during welding by Kasitsyn (2020) [80].

2.16 Design considerations for the BSE collector

Two factors should be considered for designing the backscattered electron collector, material and size of the sensitive area, as the backscatter detector detection efficiency relies on them [81]. Additionally, workpiece material and weld shape contribute to the amount and strength of signal collected.

The influence of the material on the amount of BSE collected on the plate relies particularly on two parameters: backscatter coefficient and secondary electron emission coefficient. The former can be used to make corrections to the electron current collected on the plate, and the latter should be as low as possible to reduce the error in the current measurements to the minimum. Those values are important in the case of precisely controlled experiments using advanced high vacuum equipment, where it is possible to control scattering and generation of the BSE and secondary electrons [82]. However, in electron beam welding, the impact of such effects varies due to the type and geometry of the workpiece and the point of beam impingement.

During the welding, the shape of the workpiece largely contributes to the amount, energy spectrum and directional distribution of the BSE. On the one hand, this is caused by the unevenness of the surface such as eccentricity, thickness and geometric variations, surface finish and preparation. On the other, it is caused by the weld pool and keyhole dimensional changes [1]. This can be considered as the third design concern, but as workpiece geometry is an externally-controlled variable, it cannot be predicted unless working with a mass production process with repeatable products.

The other influencing parameters mentioned in the literature include transmission coefficient, fractional backscattering, absorption and transmission energies [83, 84]. However, these are beyond the scope of this thesis.

2.17 Time series imaging

As mentioned earlier in chapter 2.6, the beam probe signal is represented by a slit current and scan position. If the acquisition frequency is kept constant, then the measurements can be described as a 1D vector of numbers. Then, the BeamAssure signal can be treated as time-series data, which can be encoded in the form of images.

The rapid development of computer vision brought the idea of classifying time series data using 2D images [85]. Various transformation methods make it possible to encode time series as input images of convolutional neural networks, including, but not limited to Markov Transition Field (MTF), Gramian Angular Field (GAF), recurrence plot (RP) [86] and Continuous Wavelet Transform (CWT) [987]. Based on the fact that single-colour encoded images are of depth one, to utilise efficiently all three layers of colour (red, green and blue - RGB) of the image, the remaining layers can be filled with three differently encoded (GAF, MTF and RP) images of the same signal. This should also preserve more features from the signal itself and such images will be referred as mixed images (MIX) in this thesis.

The concept of encoding features of time-series data as visual elements is not a new concept and have been explored in the past. In 1990, Hermansky [88] presented a method of concatenating Mel-frequency cepstral coefficients (MFCCs) to encode speech data as images. In 2010, Donner [89] suggested Recurrence Networks as a method of interpreting time series data. In 2011, Campanharo [90] proposed a way of using first order Markov matrix to build adjacency matrices. Recent work carried by others includes the usage of time-series encoded images, like GAF, for pattern classification included data such as encoded candlestick charts [91], Electro-Cardiograph signals [92] and tool flank wear as a function of cutting time [93].

These complex visual models referenced above successfully illustrate various topological properties between various time-series data. They are able to maintain the spatial relationships of data by rendering spatial elements as underlying graph topological primitives. The problem is that these models fail to preserve a link to the original time-series data due to the lack of exact inverse operations. In 2015, Wang [94] attempted to address this issue by using novel representation for encoding time series data called Gramian Angular Field. It was developed on the top of the concept of a Gram Matrix, already used in machine learning application called Neural Style Transfer.

2.18 Encoding to GAF

For the given BeamAssure signal, considered as a time series, values are rescaled to fall within the interval $[-1,1]$. Then the rescaled time series is represented in

polar coordinates, where values are encoded as the angular cosine and the time stamp as the radius. The last step involves exploiting the angular perspective and calculating the trigonometric sum between each point.

The workflow to create GAF images is defined below [95, 96]:

- Normalisation

For a given time series $X = \{x_1, x_2, \dots, x_n\}$ of n real-valued observations, the time series is normalized to a segment $[-1,1]$ (Equation 2):

$$\hat{x}_i = \frac{(x_i - \max(X)) + (x_i - \min(X))}{\max(X) - \min(X)} \quad (2)$$

- Translation into the polar coordinate system (Equation 3):

$$\begin{cases} \varphi_i = \arccos(x_i) \\ r_i = \frac{t_i}{N} \end{cases} \quad (3)$$

Where t_i is the time stamp and N is a constant factor to regularise the span of the polar coordinate system.

- GAF calculation (Equation 4):

$$G = \begin{bmatrix} \cos(\varphi_1 + \varphi_1) & \cdots & \cos(\varphi_1 + \varphi_n) \\ \cos(\varphi_2 + \varphi_1) & \cdots & \cos(\varphi_2 + \varphi_n) \\ \vdots & \ddots & \vdots \\ \cos(\varphi_n + \varphi_1) & \cdots & \cos(\varphi_n + \varphi_n) \end{bmatrix} \quad (4)$$

The GAF image is created from top-left to bottom-right and it is symmetrical by the main diagonal. Therefore, the polar coordinates can be reverted to the raw time series using its transformation principle.

Based on the different trigonometric functions, which can be used to create a GAF image, two kinds of GAFs can be distinguished. The first one is Gramian Angular Summation Field which is based on cosine functions (presented above) and the second, Gramian Angular Difference Field, is based on sine functions. The process of encoding signal to GAF image is presented in Figure 31.

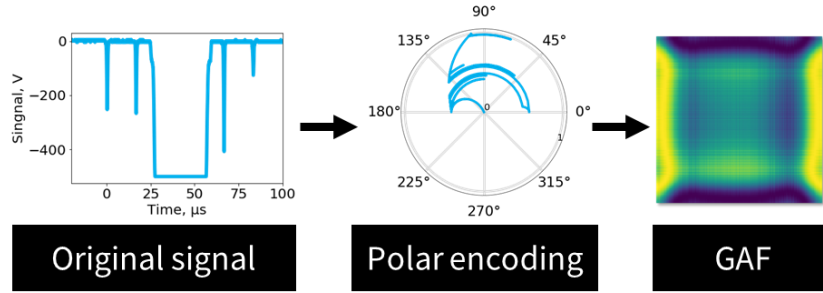


Figure 31: Transition process of the GAF conversion.

2.19 Encoding to MTF

Given the BeamAssure signal X , it is needed to identify its Q quantile bins, which contain the data at time steps i , and j are $q_j (q \in [1, Q])$. The $Q \times Q$ weighted adjacency matrix M is constructed by counting transitions among quantile bins in the manner of a first-order Markov chain along the time axis. Each element of the matrix, M_{ij} , denotes the probability of transition from q_i to q_j . The Markov transition matrix is created after normalisation by $\sum_j w_{ij} = 1$, discarding the conditional relationship between the distribution of X and the temporal dependency on the time steps t_i . The spread-out matrix M (Equation 5), which contains the transition probability of the magnitude axis, creates an MTF matrix by considering temporal positions [96, 97]. The process of encoding signal to MTF image is presented in Figure 32.

$$\begin{aligned}
 M &= \begin{bmatrix} M_{11} & M_{12} & \cdots & M_{1n} \\ M_{21} & M_{22} & \cdots & M_{2n} \\ \vdots & \ddots & \ddots & \vdots \\ M_{n1} & M_{n2} & \cdots & M_{nn} \end{bmatrix} \\
 &= \begin{bmatrix} w_{ij} | x_1 \in q_i, x_1 \in q_j & \cdots & w_{ij} | x_1 \in q_i, x_n \in q_j \\ w_{ij} | x_2 \in q_i, x_1 \in q_j & \cdots & w_{ij} | x_2 \in q_i, x_n \in q_j \\ \vdots & \ddots & \vdots \\ w_{ij} | x_n \in q_i, x_1 \in q_j & \cdots & w_{ij} | x_n \in q_i, x_n \in q_j \end{bmatrix} \quad (5)
 \end{aligned}$$



Figure 32: Transition process of the MTF conversion.

2.20 Encoding to RP

This is a simple method for visualising time series data introduced by Eckmann (1995) [98]. The recurrence plot is an array formed from dots in an $N \times N$ matrix, where N is the number of reconstructed points $x(i)$. The dot is placed at (i, j) whenever $x(j)$ is adequately close to $x(i)$. The matrix is usually symmetric by construction, with respect to the diagonal $i=j$. It is caused by closeness of $x(i)$ to $x(j)$ and then $x(j)$ is close to $x(i)$ (Equation 6) [86].

$$R_{i,j} = \theta(\varepsilon_i - \|\vec{x}_i - \vec{x}_j\|), \quad \vec{x}_i \in \mathbb{R}^m, \quad i, j = 1, \dots, N \quad (6)$$

The plot, describing time correlation information, is represented by black and white dots in the plane of indices. Based on visual inspection of the recurrence plots, it can give information about the noise component of the data and chaos [99]. The process of encoding signal to RP image is presented in Figure 33.

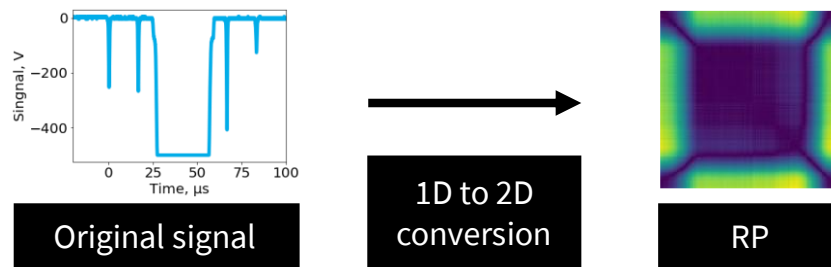


Figure 33: Transition process of the RP conversion.

2.21 Encoding to MIX

Input images for a neural network consist of three layers: red, green and blue (RGB). To keep the convolutional neural network structure simple, and maintain the same number of input channels, each layer of RGB channels can be filled with a different encoding method. Based on the fact that single-colour encoded images are of depth one, to utilise efficiently all layers of colour, the remaining layers can be filled with 3 differently encoded (GAF, MTF and RP) images of the same signal. Deep learning algorithms try to learn high-level features from data in an incremental manner from GAF, MTF and RP images. Although GAF, MTF and RP encoding contain machine recognizable differences, each of them may preserve them in different way due to the non-identical mathematical calculations. However, if those three encoding methods are mixed in one image, there is a higher chance of preserving more features from the signal itself. This may greatly improve the accuracy of deep learning model, as there is higher chance that relevant features are preserved. The process of encoding signal to MIX image is presented in Figure 34.

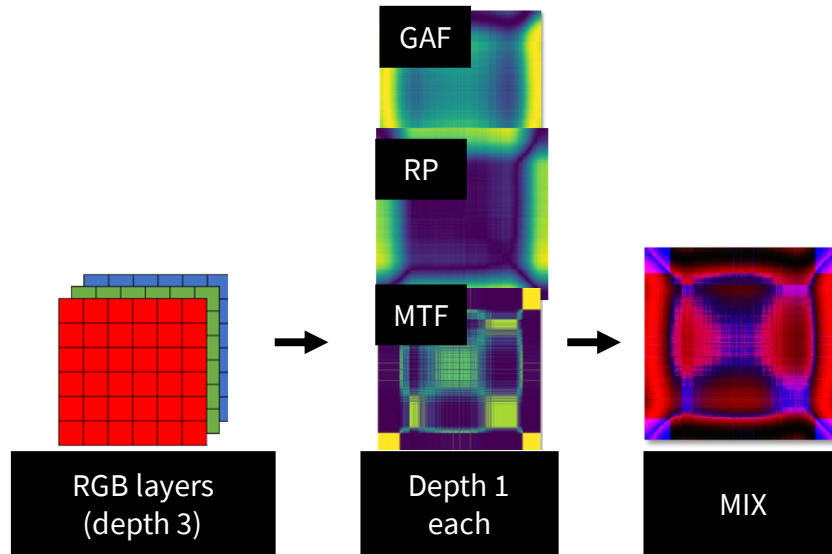


Figure 34: Transition process of the MIX conversion. Each encoding method (GAF, RP, MTF) occupies one layer of the RGB image.

2.22 Deep learning for time series images classification

Deep learning algorithms are based on artificial neural networks and have a large model complexity. The model size is controllable, which means that the number of model parameters can be adjusted by changes in number of network layers, connections and layer sizes. This enables easy model complexity changes and usage of massive datasets, on which the accuracy of deep learning can be further increased. Additionally, in contrast to machine learning, deep learning automatically learns effective feature representations via a nonlinear transformation on the primitive data features [100]. In case of images, those features are pixels.

As mentioned previously, recent work in time series imaging field [91, 92, 93] are based on image classification models. A deep learning (DL) approach, convolutional neural networks (CNN) in particular, helps with extracting relevant features automatically and is successful at handling large volumes of data [93], but it is still limited by the hardware used for deep learning, especially Graphics Processing Units (GPU). Deep learning models are usually large and the computational efficiency is a very important factor to accelerate the computation. Such an example of the usage of huge datasets, used in combination with CNNs, include CIFAR-10 (60000 images) [101], Tiny ImageNet (100000 images) [102] and ImageNet (1 million images) [103]. The main benefit of training machine learning models on any of the above datasets is applying knowledge gained while solving one task to a different, but related task. For computer vision, ImageNet is frequently used as it can classify images into 1000 classes, so pre-trained models on ImageNet have undergone extensive training to handle diverse tasks and scenarios. This reuse of a pre-trained model on a new problem is known as transfer learning and it offers numerous advantages, with the primary benefits

being reduced training time, improved performance of neural networks, and the ability to achieve satisfactory results with limited data. As the laborious task of optimising these parameters (i.e. model weights) has already been accomplished, the only outstanding task is fine-tuning the model by experimenting with the hyperparameters. In the manufacturing context, this can solve some of the challenges, including issues like insufficient training data or the rapid fluctuations of the industrial processes.

Recent developments in deep learning frameworks and strong communities supported by top companies have helped with the boom of deep learning. Examples of frameworks, capable of automatic optimisation and loaded with predefined models, are TensorFlow, PyTorch, Keras and Fast.ai. This makes deep learning development much quicker and simpler. The big support from the user community is another driver for popularisation of deep learning research. Developers quickly implement, validate and share the models using open-source code platforms and academic paper repositories.

2.23 Residual Networks

Residual Network (ResNet) architecture is one of many open source models, available in frameworks mentioned in Chapter 2.22. It quickly became one of the most popular architectures in computer vision applications, as it allows the model to skip layers without affecting performance and as a result significantly enhances the classification accuracy [104, 105]. Various ResNet models can be found as off-the-shelf CNN architectures and the number suffix in the name of the network (e.g., 34, 50, 101) means the number of layers with learnable parameters.

For example, Resnet34 model, available in the Fast.ai framework, is pre-trained on the ImageNet dataset. It contains 1,281,167 training images, 50,000 validation images and 100,000 test images across 1000 different classes [103]. This transfer learning approach allows taking the model that was trained to recognise existing features in one domain and apply its knowledge and feature extraction to another model which will learn in-depth features from another domain [106]. Pre-trained model selection depends on the size of the training set and complexity of image features to be detected. Models with more than 34 layers, known as deeper ResNet models, can achieve superior training outcomes. However, this comes at the expense of increased training duration and a potential risk of overfitting, where the model excessively conforms to its training dataset.

As ResNet models can have variable sizes, to describe the structure of these networks, ResNet 34 based on original paper [104] is analysed and presented in Figure 35. This model is readily available in deep learning frameworks mentioned above, i.e. TensorFlow, PyTorch, Keras and Fast.ai.

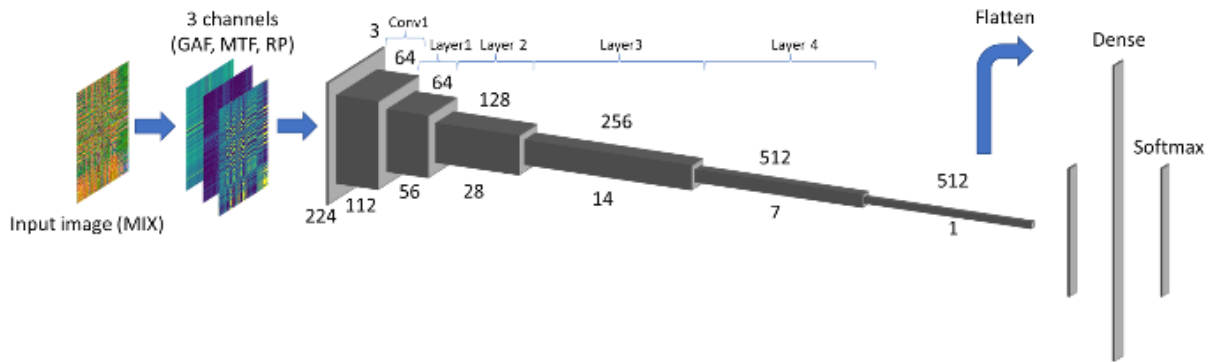


Figure 35: CNN architecture based on the PyTorch implementation of ResNet 34 for MIX encoded BeamAssure signal as an input image. Adapted from [105].

The structure of the 34 layers ResNet 34 is demonstrated in Figure 35, where the input is represented by an RGB image, in this case a BeamAssure encoded image. Initially, the architecture starts with the first convolution (Conv1, Figure 35), which is 64 filters with a kernel size of 7x7 and stride specified as 2 (compression). A kernel is a filter that is used to extract features from the images and stride is the number of pixel shifts over the input volume. Then it is followed by a max-pooling layer with stride of 2. These layers are grouped in pairs and connected by residual blocks, which consist of skip connections to link the output of a specific layer to the input of a preceding layer (orange arrow, Figure 36). Each next layer follows the same pattern, with following modifications: the size of the kernel is 3x3 and number of filters is 64 (3 layers), 128 (4 layers), 256 (6 layers), 512 (3 layers) respectively (Layer 1-4 in Image 35). Input is bypassed every 2 convolutions. The last layers are called flatten, dense and softmax. Those layers are applied after convolutional layers to transform the multi-dimensional matrix into the shape of the required output to obtain scores for each class. The highest score corresponds to the most likely class according to the weights. The differences between ResNet34, ResNet50 and ResNet101 architectures are presented in Table 6.

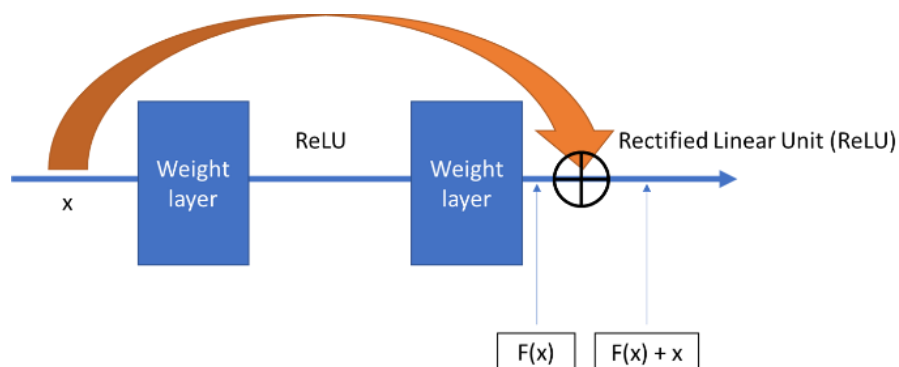


Figure 36: Residual block. Orange line represents shortcut (skipped connection). Adapted from [107].

Table 6: Architectures for ResNet34, ResNet50 and ResNet101. Adapted from [107].

Layer name	Output size	34-layer	50-layer	101-layer
conv1	112 x 112	7 x 7, 64, stride 2		
conv2_x	56 x 56	3 x 3 max pool, stride 2		
		$\begin{bmatrix} 3 \times 3, 64 \\ 3 \times 3, 64 \\ \times 3 \end{bmatrix}$	$\begin{bmatrix} 1 \times 1, 64 \\ 3 \times 3, 64 \\ 1 \times 1, 256 \end{bmatrix} \times 3$	$\begin{bmatrix} 1 \times 1, 64 \\ 3 \times 3, 64 \\ 1 \times 1, 256 \end{bmatrix} \times 3$
conv3_x	28 x 28	$\begin{bmatrix} 3 \times 3, 64 \\ 3 \times 3, 64 \\ \times 4 \end{bmatrix}$	$\begin{bmatrix} 1 \times 1, 128 \\ 3 \times 3, 128 \\ 1 \times 1, 512 \end{bmatrix} \times 4$	$\begin{bmatrix} 1 \times 1, 128 \\ 3 \times 3, 128 \\ 1 \times 1, 512 \end{bmatrix} \times 4$
conv4_x	14 x 14	$\begin{bmatrix} 3 \times 3, 64 \\ 3 \times 3, 64 \\ \times 6 \end{bmatrix}$	$\begin{bmatrix} 1 \times 1, 256 \\ 3 \times 3, 256 \\ 1 \times 1, 1024 \end{bmatrix} \times 6$	$\begin{bmatrix} 1 \times 1, 256 \\ 3 \times 3, 256 \\ 1 \times 1, 1024 \end{bmatrix} \times 23$
conv5_x	7 x 7	$\begin{bmatrix} 3 \times 3, 64 \\ 3 \times 3, 64 \\ \times 3 \end{bmatrix}$	$\begin{bmatrix} 1 \times 1, 512 \\ 3 \times 3, 512 \\ 1 \times 1, 2048 \end{bmatrix} \times 3$	$\begin{bmatrix} 1 \times 1, 512 \\ 3 \times 3, 512 \\ 1 \times 1, 2048 \end{bmatrix} \times 3$
	1 x 1	average pool, softmax		

2.24 Related works

The review of the literature has not found any papers studying the problem of evaluating the surface focus or backscattered electron monitoring using a neural network and machine vision approach. However, there are a few works related to visual and BSE monitoring, neural networks and computer vision used in electron beam manufacturing technologies.

2.24.1 Vision system process monitoring

Starting with camera systems, a video seam tracking idea was described in a technical report by Burkhardt et al. (1978) [108]. The system was also equipped with a parameter recording system and video recording capability. While the systems presented in this report are considered outdated by modern standards, it represents a great example of automation possibilities in the EBW field.

Usage of the camera and thresholding of the image of the weld pool, in the area of EBW, was first mentioned by Petrov (1998) [109, 110]. His work describes an

online weld pool monitoring and inspection system. Both a photodiode and a charge-coupled device (CCD) camera were used to follow the behaviour of the weld pool and keyhole during EBW. The CCD sensor used in the research had nearly two times lower dynamic range (74 dB) than modern HDR welding cameras (140 dB). Besides the basic image analysis, which consists of thresholding the weld pool image and obtaining its length, there is a lack of further detailed image analysis.

As modern cameras have greater capabilities (dynamic range, resolution, signal to noise ratio) and computer vision algorithms are more developed, the vision systems can be vastly improved in terms of image quality and anomaly detection. Higher level of captured details with modern HDR cameras offers possibility to detect small changes in weld pool and extract them in real time. Examples of utilisation of modern monitoring techniques can be found in laser beam welding [111], but those are not observed in EBW field.

2.24.2 Electron-optical process monitoring

Seam monitoring can be also performed using electron-optical imaging. An example of a computer vision model for control seam trajectory and intermediate steps such as an autofocus system for electron-optical images, image processing procedure and 3D trajectory decomposition was described by Oltean (2008 and 2018) [112, 113]. This work is based on low-resolution ELO imaging (256x256 pixels) and was focused on controlling the welding parameters based on the processed images. This approach, although suitable for seam monitoring, cannot be used for observing the real time weld pool monitoring due to the limited resolution and electron-optical imaging response time. The similar problems were found by Laptенок (2016) [67]. Despite the possibility of using fast beam deflection to monitor the process during the welding as described by Mücke (2014) [58], this solution still generated low resolution images and increased the risk of introducing additional defects to the welding process due to possible capillary collapse. In general, due to the slow and low-resolution response of electron-optical systems, it is not possible to register weld defects in real time.

2.24.3 Backscatter electron monitoring

Although less advanced than electron-optical process monitoring, due to the simplicity of data collection and processing, BSE monitoring is the oldest process monitoring concept in EBW. There are several works from the past, including Ardenne (1976) [70], Mauer (1979) [69], Sanderson (1988) [71] and Anderl (1992) [72]. Process of collecting BSE was well described in the past and it is well-understood. Due to the time when the research was carried out, there was no wide accessibility to solutions available nowadays such as USB digital oscilloscopes and advanced signal processing. Recently, in the world of EBAM, Arnold (2018) [73], Shcherbakov (2020) [66, 75] and Wong (2020) [76] successfully used the BSE monitoring to monitor the electron beam melting process for layer monitoring. However, EBAM processes are slower than EBW, which makes the monitoring task easier.

2.24.4 Neural network assisted EBW

In terms of simulation and parameter set up, there are several works which utilise neural networks to obtain high quality EB welds and maintain stable EBW process.

In the area of neural networks as tools for predicting materials properties, in electron beam-related processes, Hayes (2015) [114] created a single constitutive equation to predict the yield strength of Ti-6Al-4V. Their work concerns electron beam additive manufacturing and it was based on interrelationships between microstructure and mechanical properties determined using artificial neural networks [115, 116].

Regarding power supply units used in EBW, Malik (2010) [117] compared two MATLAB Simulink models: a proportional-integral (PI) controller based on Ziegler Nichols frequency response tuning method and a controller based on a neural network. The neural network controller gives a better performance in comparison to the PI controller, considering maximum overshoot and maximum undershoot, but it also worsened step-response characteristics such as rise, settling and delay time. Other parameters, like average integral absolute error, integral squared error and average integral squared error also revealed the better performance of the neural controller over the PI controller.

Furthermore, neural networks can be used to model electron beam welding. The work in this area is especially useful for weld quality assurance. Shen (2009) [118] uses a neural network to predict processing parameters and weld penetration in EBW to reduce trail times and lower production cost. The input parameters include accelerating voltage, beam current and welding speed and the output parameters consist of penetration depth and penetration width of the weld. The neural network architecture includes forward and backward prediction models.

Jha (2014) [119] in their research proposed a neural network model to predict weld-bead profile (weld width and depth of penetration), weld strength (yield strength and ultimate tensile strength) and micro-hardness of the fusion zone. Tsonevska (2018) [120] used a neural network to establish a relationship between the geometry of the weld bead and weld parameters, which can be later optimised to obtain the desired weld shape.

Das (2018) [121] suggested a model for predicting the depth of penetration of the weld pool, length of the pool, cooling time and half-width of the weld pool. Input parameters include power, welding speed, beam radius, and distribution factors. They are also used in the inverse model as output parameters. It is also capable of predicting bead geometries.

Koleva (2017) [122] used neural networks to predict the occurrence of defects. The neural network in this work is used to classify the welds with and without defects. Input parameters include power, welding velocity, working distance and focal distance.

Reddy (2011) [123] developed predictive tools for determining temperature profiles of EB welding, in which neural network models have been utilised for the predictions of pre- and post-maximum temperature profiles.

The most similar work, developed by Olszewska (2004) [77], is related to automatic EB focusing using neural networks combined with secondary emission measurements. However, this work did not use a camera to evaluate the focus position. Instead, the three models presented in this paper are based on selected welding parameters. The first model utilises as inputs the accelerating voltage, EB current, focusing current and DC components of three types of charged particles' currents. The second model was limited to chosen values of accelerating voltages and EB currents. The third one was an inverse model, which used input coded numbers to predict the inputs of the first model. These inputs' numbers, also implemented as output values for the first two models, described the focus position of the electron beam active zone to the workpiece surface.

Recent work, described by Yin (2022) [124] focused on predicting the penetration depth during EBW. Besides basic welding parameters, beam width measured by BeamAssure probe is taken into consideration, which greatly improved the accuracy of predictions for models based on an empirical equation, a second-order regression and an artificial neural network.

From the works described in this subchapter, there is a lot of effort to use deep learning tools to support parameter set up. Those researches mainly used as input parameters chemical composition of the materials, basic welding parameters and temperature readings. Some of the most advanced works used data from beam probing to further improve prediction models. However, the deep learning development shouldn't be limited only to easily accessible data, but it should utilise new sensors and multi sensor fusion to find new patterns in data. This may help to understand previously unexplainable and incomprehensible data collected, for example from EB process emissions, and accelerate the development of improved sensors and process monitoring techniques.

2.25 Knowledge gap

This chapter has presented a comprehensive review of the devices and methods employed in characterising electron beams for EBW in the field of QA/QC. Specifically, it identified and described three methods, which included vision and camera systems, BSE monitoring and beam probing. Furthermore, it highlights the possible applications of neural networks in EBW quality evaluation.

As indicated, each device has its advantages and disadvantages. Depending on the device, they are limited to different welding stages, i.e. pre-process (beam probing), in-process (cameras and BSE monitoring) and post-process (destructive and NDT testing). Additionally, some of the devices are susceptible to regular maintenance, like the cameras where post-welding dust deposition obscures the lens view. On the other hand, there are devices, such as beam probes and BSE collectors, capable of operating despite the dust deposition and need less maintenance. However, the available evidence regarding the effective utilisation

of extracted information from these devices is limited. Consequently, the usage of such devices in the industry is uncommon. Some of the barriers to the successful implementation of these devices are related to human decision-making tasks, where the operator may feel more comfortable setting the focus current manually, rather than correcting the values by the ones obtained from beam probing. Beam probing also requires training and preparation time to be reserved before carrying out the actual welding job. Current systems are unable to do quick and autonomous data analysis with real-time parameter correction, which is the core of the Industry 4.0 paradigm.

This thesis aims to explore the potential of three aforementioned EBW monitoring methods through innovative data processing techniques supported by the deployment of neural network frameworks to bring the autonomous and real-time capacities closer. By conducting research work in this direction, the subsequent chapter will present experimental endeavours undertaken to achieve the aforementioned objective.

3 Experimental methods

As the literature review shows, there are still gaps to deliver a reliable and accurate quality assurance system to prevent the occurrence of weld imperfections and maintain the sharp focus setting of the beam. There is no good method of analysing real-time camera footage, which is limited by camera modules, i.e. ELO imaging is too slow for typical EBW speeds and visual cameras are limited by the dust deposition on optics. On top of that, computing power, data bandwidth and storage capacity are further limiting factors. This chapter illustrates the equipment used and the signal analysis methods to provide more useful information about the beam focal conditions and register the occurrence of defects.

3.1 EBW machine

All of the welding experiments were carried out using an EB machine manufactured by Cambridge Vacuum Engineering (serial no. CVE 661). The high voltage power supply can deliver 60 kV maximum voltage and 4 kW maximum power. The vacuum level was kept at the level of $<10^{-3}$ mbar and the working distance, measured from the chamber roof to the workpiece surface, was 330 mm. For controlling and monitoring welding parameters, SINUMERIK 840D controller is used. The machine was equipped with SIMATIC S7-300 PLC with 317 CPU and was programmed using STEP 7 classic, with the data dictionary provided by CVE (Appendix A). The machine was also upgraded from a fully populated 5-way Ethernet switch with an 8-way switch to accommodate simultaneous connections from multiple data collection systems. The IP address of the PLC system was found using PLC Scanner software developed by PLCDataTools.com [125] and it was found to be 192.168.0.34. This allowed to communicate with the EBW machine and log the data with a custom Python script. For the purpose of this thesis, the EBW machine was equipped with welding camera and custom-designed BSE detector, both detailedly described in Chapters 3.3 and 3.4. The location of the camera and BSE detector in relation to the EB gun is presented in Figure 37.

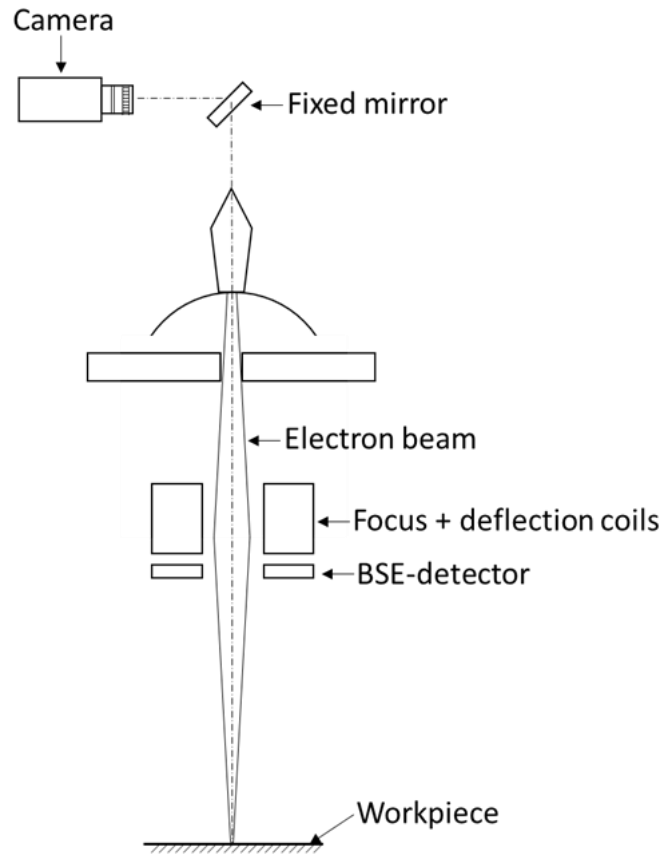


Figure 37: Location of the camera and BSE detector

3.2 PLC data

The beam was controlled by adjusting the principal parameters of beam voltage, beam current and lens current. As mentioned previously, numerical values for these parameters were recorded using a SINUMERIK 840D controller, which includes a SIMATIC S7-300 PLC. Communication between a personal computer (PC) and the PLC was implemented using the Snap7 library [126] and utilized Ethernet protocol. The camera was connected using the Xiris software development kit (SDK) and also used Ethernet to transfer the data. Digital oscilloscope was accessed through PicoSDK and USB3.0 protocol. The relationship between the SDKs and communication protocols are presented in Figure 38. Those libraries were accessed through a custom Python script, which allowed sharing of the same real-time clock inside the PC to provide a common timestamp. It also made the software triggering easier so that when the beam current was above 1 mA, the digital oscilloscope (Picoscope 3203D) started collecting the BSE signal and the camera (Xiris XVC-1100) was triggered at the same time (welding start stage in Figure 38). Similarly, with a drop in the beam current below 1 mA, the recording of any data from the sensors was stopped (welding end stage in Figure 38). This reduced data traffic, unnecessary sensor communications and the temperature of the camera sensor. The timestamp from the PC clock was attached to data received from connected devices.

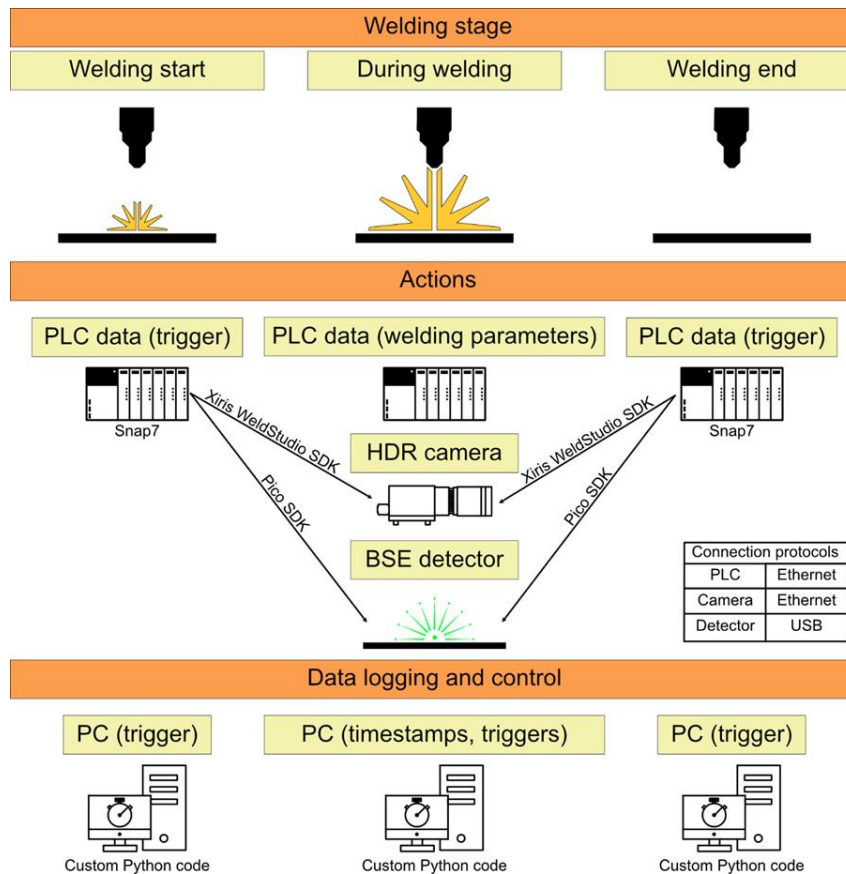


Figure 38: Schematic of the triggering and data collection process.

The 1 mA threshold value was set to avoid triggering the data collection system with the focusing and positioning stage performed by the operator. This allowed distinguishing between pre-welding and welding operations. Additionally, PLC control showed that the beam current value ramps up quicker than PLC is capable of recording, from value 0 to the target value, without registering or setting intermediate steps (slope in). The workpiece surface melted with a 1 mA beam is also re-radiating not enough infrared and visible light energy to capture the welding process with the camera without any external lighting system.

3.3 BSE collector plate

During EBW, similarly to scanning electron microscopy, various electron emissions can be observed, and as mentioned in literature review chapter, those include backscattered electrons, secondary electrons, charged plasma and, thermionic emission [4]. Those electron emissions and their directions are summarised in Figure 39. Among them, BSE are a predominant source of the emissions, with wide angular distribution and are more energetic (as opposed to secondary electrons). For this reasons BSE are easier to detect and are used in commercial EBW machines for positioning the beam on the workpiece.

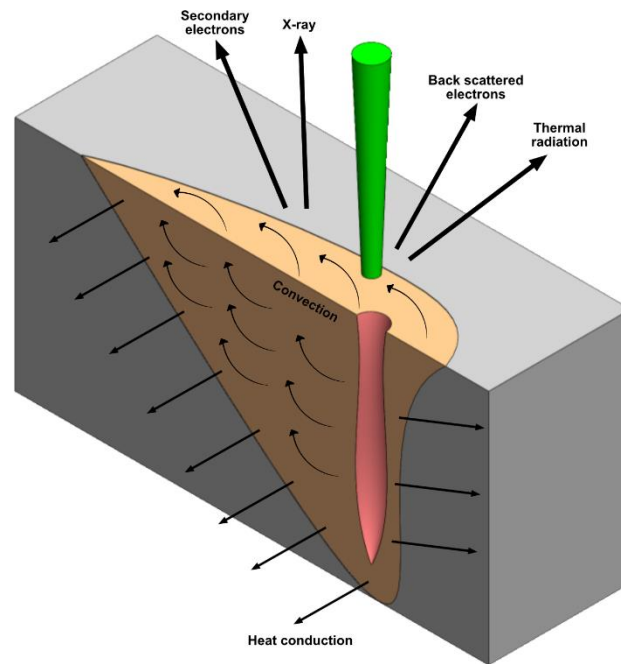


Figure 39: Emissions created during welding process. Adapted from [19].

BSE are created during an elastic collision between EB-generated electrons and workpiece atoms. A part of these electrons hits the surface of the detector and the detector current is conducted. As the CVE machine, used in the experiments, was not equipped with BSE detector, a single plate detector was designed as a part of this study and 3D visualisation is presented in Figure 40a. The BSE collector plate was an aluminium disk, 4 mm thick with a 40 mm inner and 136 mm outer diameter as shown in Figure 40b. It was a CNC machined plate that was isolated from the chamber wall and connected to the earth through a 100-ohm resistor, to allow monitoring of the BSE current picked up by the plate.

BSE detector was mounted to the protective shield of the vacuum chamber, below the electron beam gun exit hole, using bolts inserted through ceramic inserts (to prevent the flow of current between the plate and EB machine). Additionally, M6 penny washers were used on the top of the ceramics to prevent metallic dust deposition, which may become conductive once a certain thickness of the metal deposition is reached. The final BSE plate-EB chamber assembly is documented in Figure 40c. A digital oscilloscope (Picoscope 3203D) was used for recording voltage data from the backscattered electron flux during welding for further processing and this connection is illustrated in Figure 41.

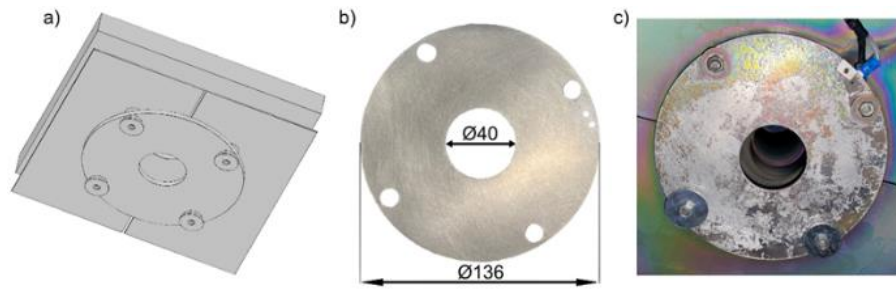


Figure 40: BSE plate design. a) 3D concept, b) machined plate and its main dimensions (4 mm thick), c) plate installed inside the EBW chamber with a deposited dust layer.

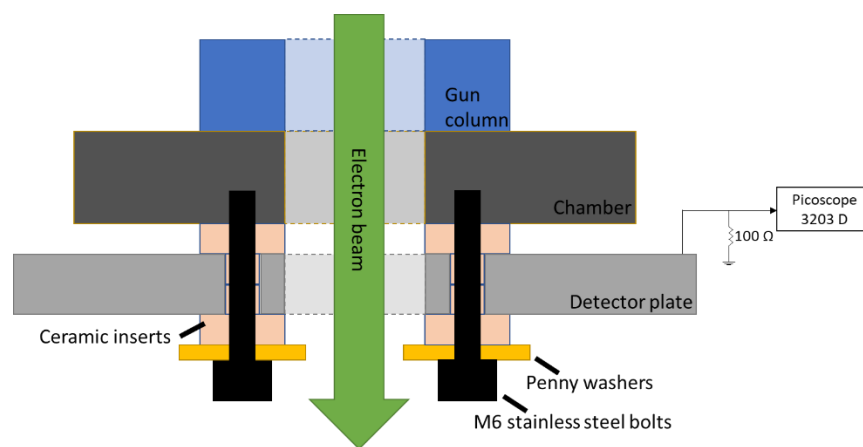


Figure 41: Schematic of the detector assembly inside vacuum chamber and connection circuit between detector and data acquisition device (Picoscope 3203D).

3.4 Welding cameras

As the experiments carried out in this thesis are based on a multi-sensor fusion approach, and based on the fact that BSE emissions can give uncertain results, a light optical system was also used. To support data derived from the collector plate, a Xiris XVC-1100 welding camera was used for monitoring the weld pool and mounted directly onto a movable electron beam gun. This ensured that the optical axis of observation and the axis of the electron beam was in a plane. The lens used was Kern YVAR 150mm f/3.3 Macro with C-Mount. It was attached with custom-designed mount, presented in Figure 42, to prevent any environmental light leaks and securely support the long assembly. In order to focus the lens in the workpiece, it was needed to use spacer rings, for the 330 mm working distance the total length of them was 30.4 mm. Additionally, a Cosmicar x2 extender was used to narrow the field of view and fit the molten pool in the frame.

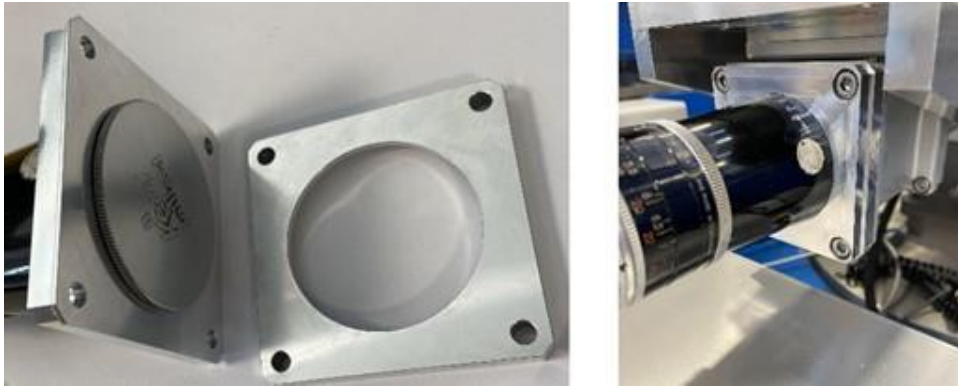


Figure 42: Custom-designed lens mounts prevents any environmental light leaks and provide stable support for the lens.

Regarding the camera capabilities, Xiris XVC-1100 offers a global shutter sensor, which is used for capturing moving objects. In the case of high-speed welding processes, such as electron beam welding, this allows for avoiding artefacts created by rolling shutter sensors and results in higher light sensitivity. The main difference between both types of shutters is that the global shutter sensor starts and stops exposure of all pixels at the same time, which ensures the timing of exposure is the same in every line of the image. In contrast, rolling shutter sensors read exposure line by line, one line at a time. By the time the rolling shutter read the next line, the exposure may have changed or the object moved. This is usually noticeable as artefacts, where a high-speed moving target is distorted and blurry.

Besides the global shutter, the camera itself was equipped with an HDR sensor, which gave detailed images of the weld pool and allowed avoidance of additional auxiliary light sources. Obtained images were of sufficient quality for weld pool segmentation and calculating its 'centre of mass', which is the brightness-weighted average of the x and y coordinates for all pixels in the image. Prior to segmentation, all images were converted to grayscale. As the HDR images preserve local contrast as well as surrounding darker background areas, it was possible to use Otsu's (OpenCV implementation [127]) method for extracting the weld pool image from the background and thus automate the segmentation process. From segmented images, the centre of mass was calculated using the scikit-image package [128]. A summarised pipeline of this process is illustrated in Figure 43.

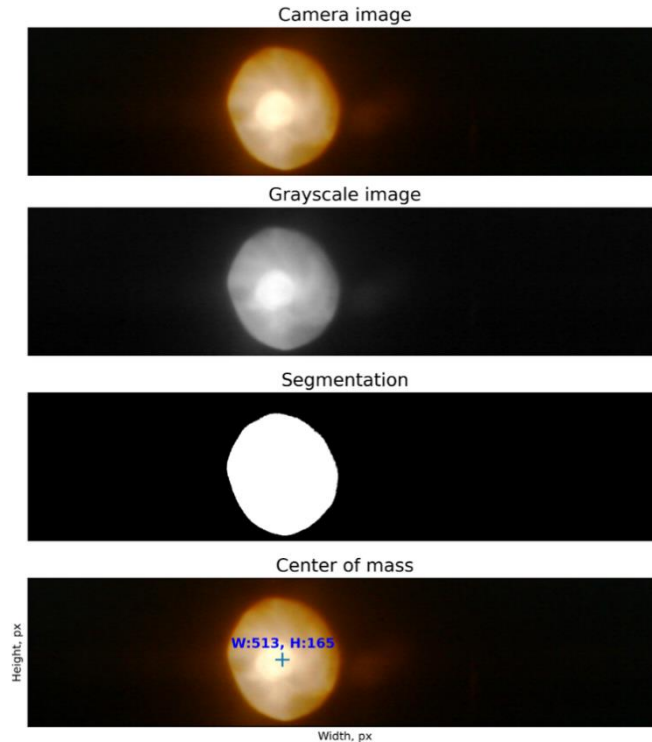


Figure 43: Image processing steps of the beam capillary registered by HDR camera, starting with camera raw images, converting them to grayscale, extracting background from weld pool image using Otsu's thresholding and calculating centre of mass of the segmented.

The scikit-image software can calculate several parameters at the same time. The eccentricity parameter was obtained, values can fall in the interval 0-1 and 0 means the ellipse becomes a circle. Another useful parameter, the total image intensity, consists of a sum of all pixels inside the segmented mask (obtained from centre of mass step - segmentation). Area parameter is the number of pixels of the region and the solidity, a ratio of pixels in the region, to pixels of the convex hull image with values in the range 0-1, a value of 1 indicates a solid object, and a value less than 1 means that the object has irregular boundaries. It took 0.65s for each image (1280x300 pixels) to obtain above mentioned metrics and write them into .csv file. These measurements were then used to evaluate if the anomalies discovered with BSE signal can be also captured by observing the weld pool and relate them to specific events. The code is attached in the Appendix B.

3.5 8-bit and 12-bit image encoding

The raw images from the Xiris camera can be encoded as colour images using one of the GenICam pixel format naming conventions: BayerRG12Packed or BayerRG8 [129]. Bayer RG8 is the simplest to decode as one byte is used per pixel, with the odd lines of the picture encoded with R,G, and the even lines as G,B. This mode, despite the reduced intensity distribution, is suitable for multi-camera systems as it reduce data transfer. The basic idea behind decoding images is presented in Figure 44.

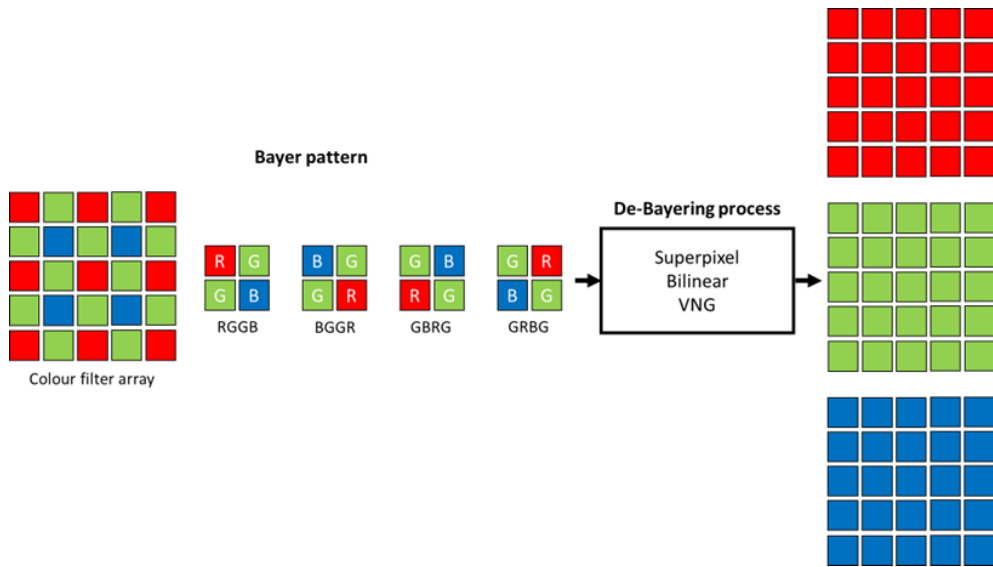


Figure 44: Interpolated output obtained through debayering process, by which image gets decoded from a colour matrix into a full resolution colour image. Adapted from [130].

The BayerRG12Packed is problematic because the raw pixel data is packed in 1.5 bytes per pixel, which means that three pixels are packed as per Mono12Packed, the odd lines of the picture are created in R,G order, and the even lines in G,B order. Such encoding ensures that the camera transmits the full HDR for each frame, but at the cost of bandwidth (33% more usage than 8-bit encoding) used to transfer the images to the PC and CPU load due to the tone-mapping. This causes difficulties in processing such images and it will require unpacking them to 2 bytes per pixel for ease of use. The difference between packed and unpacked formats I shown in Figure 45. The advantage of the full HDR is that the images are not overly saturated nor dark when the welding start and stops. To preserve this local contrast changes on the images, the BayerRG12Packed encoding format is used in this thesis.

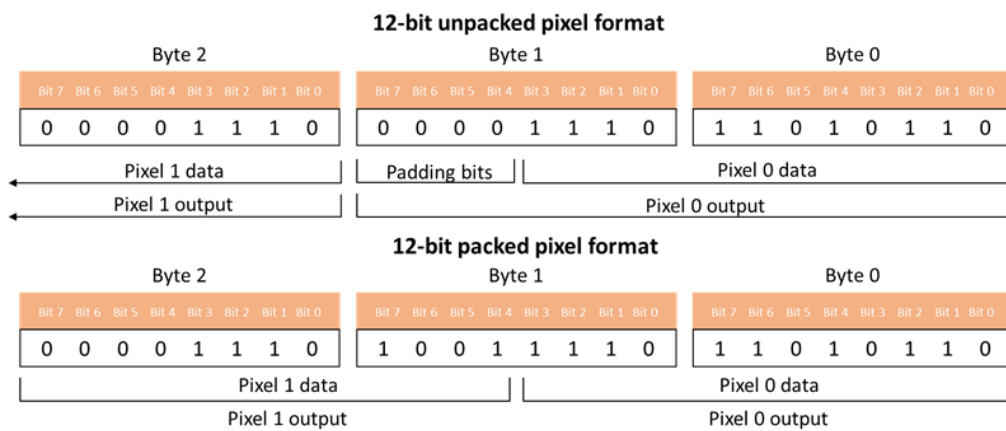


Figure 45: Differences in camera output between packed and unpacked pixel formats. Adapted from [131].

3.6 Welding data monitoring triggering control

The Xiris XVC-1100 camera is equipped with an input/output (I/O) connector and GigE (Gigabit Ethernet) interface. The Ethernet connector is used for data connection and to provide power via Power over Ethernet (PoE) using a suitable network card or PoE injector. Another way of powering the camera is through the Hirose connector (I/O interface), which can be used to trigger the camera, depending on the trigger mode. The main difference between the trigger controls is how the camera controls the exposure, so in trigger mode 1 the camera uses pre-set exposure and shutter settings, and in trigger mode 2 the camera will use the length of the trigger pulse as the length of the exposure. It is recommended by Xiris to use the external hardware trigger combined with specific events, such as peak laser power during a cycle or each pulse of pulsed GTAW welding.

In order to continuously trigger the camera, it is possible to use Picoscope 3203D. This digital oscilloscope is equipped with a 12-bit arbitrary function generator with the output voltage range ± 2 V, which is not enough to trigger the Xiris XVC-1100 camera, so it requires an additional device to boost voltage. Using RS PRO RSDG 2042X arbitrary function generator, in combination with a Picoscope function generator, the Picoscope waveform can be used as an input (RS PRO accepts 2 to 5.5V signal input), and using the pulse waveform with burst function it is possible to output the duplicated waveform with higher voltage (5V), which is enough to trigger the camera. The main advantage of the hardware trigger is that it bypasses the Ethernet network and connects directly to the welding camera which results in a shorter trigger delay. The disadvantage is that the images in the Xiris WeldStudio software are saved as raw .dat files, which represent the raw pixel data coming from the camera. Such images are 12-bit colour depth files with the RG2RGB (from BayerRG12Packed) colour pattern, so they are subject to at least debayering and, in case of saving them as .png files, normalising tonal values to 16-bit, as 12 bits have 4,096 tonal values per channel and this value needs to be in the range of 16 bits (65,536 tonal values per channel). This trigger mode can be considered in high precision applications, but its implementation in electron beam welding is limited due to the lack of triggering events from the power source (e.g. lack of alternating polarity) and requires a function generator to trigger frames continuously. With the equipment available in the lab and the voltage requirement to trigger the camera, this system required more devices coupled together. It was found that usage of RS PRO with Picoscope caused grounding and coupling issues, which were visible during backscatter signal collection as mixed-frequency voltages. The time delay recorded between digital oscilloscope and arbitrary function generator is illustrated in Figure 46.

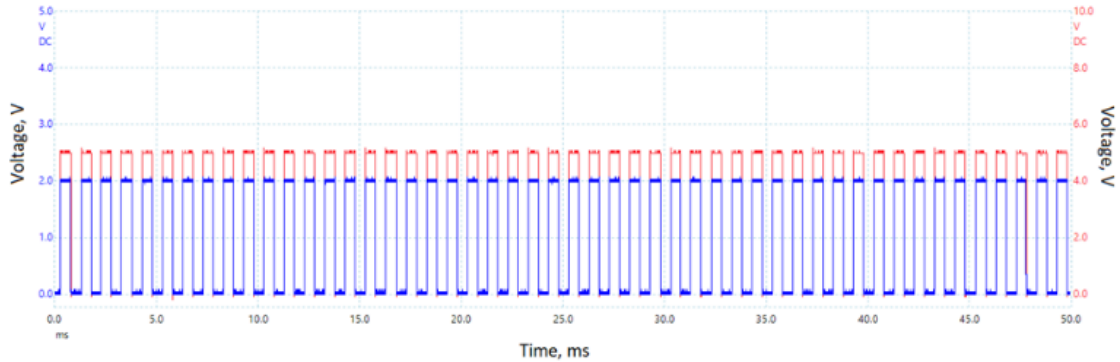


Figure 46: Time delay between Picoscope (blue) and RS PRO arbitrary function generator (red) introduced an additional 0.001 ms delay between triggering pulses (shifted signals).

Besides hardware triggering, there is also software triggering available through XirisSDK API. As it is layered transmission, the delays between camera and host are present, and they are larger than in hardware triggers. However, this type of trigger offers greater flexibility, and it is easier to implement as it is in the form of a computer command sent from the PC to the camera. Upon testing, the software trigger didn't cause any problems with the mixed-frequency signals, so this mode was selected for triggering the camera. As visualized in figure 38 in Chapter 3.2, the welding camera is connected with an Ethernet cable for data connection and to provide power via PoE, so the amount of the equipment and cables have been reduced to the minimum. This software trigger relies on the beam current value, and it is fired once it exceeds 1 mA and data acquisition stops once the value drops below 1 mA. The code is attached in the Appendix C.

3.7 Data post-processing pipeline

The system architecture consists of three data sources and their processing methods are illustrated in Figure 47. Computer vision methods and artificial intelligence tools have developed rapidly over recent years to become sophisticated tools for image classification. Signal encoding was a necessary stage for further processing of the BSE plate signal, as this allowed automatic classification using said computer vision methods. The methods used in this thesis included Recurrence Plots (RP), Gramian Angular Fields (GAF), and Markov Transition Fields (MTF). As each of them produced single-colour encoded images, all three layers (GAF, MTF and RP) were combined to create an RGB image (MIX).

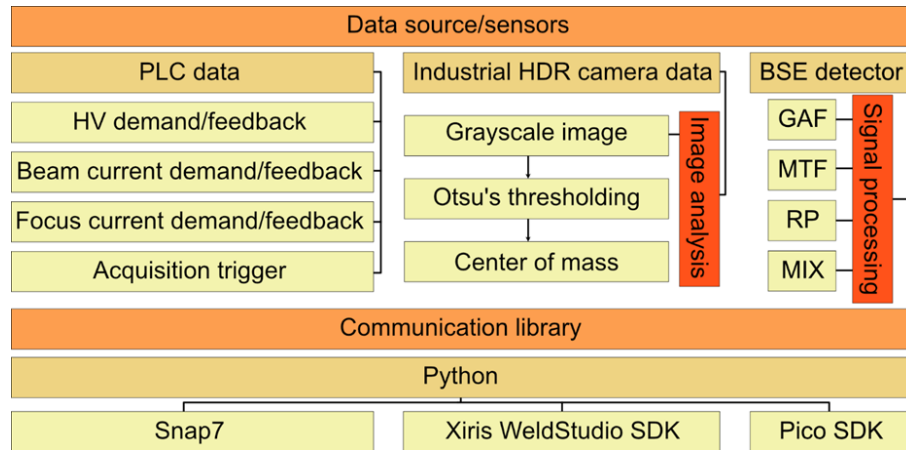


Figure 47: System architecture.

Data collected from the PLC was not only used as an acquisition trigger, but also to verify stability of the three main welding parameters. There is a limitation on the maximum amount of data which can be transferred by the snap7 library. The maximum number of variables is 20 in a single request, a limitation which doesn't exist in S7 protocol but is present in the snap7 library. To simplify data collection process, registered parameters included high voltage, beam current and lens current.

Regarding the data from the BSE plate, it was saved as .csv files with two columns: times in nanoseconds and channel A response in millivolts. Simple noise elimination has been applied to the collected signal using a Butterworth low pass filter.

The last step utilised images from the camera, which were used to track the centre of the weld pool. Registered pictures were in .bmp format, which is the default format for the Xiris WeldStudio SDK. Although the camera is also capable of outputting raw .dat image files, which later can be opened either in Xiris WeldStudio software or properly decoded, the .bmp format was chosen as it reduced computing power of the system. As mentioned above, there is also a risk associated with proper decoding of the raw images, which included steps such as debayering (from BayerRG12Packed), normalising colours in the 16-bit range and encoding in any desired image file format. This risk is related to the time consuming postprocessing of the images, which may affect the final image quality. The possible advantage of processing .dat files externally (e.g. in Python) leaves the image processing to the decision of the user but is less convenient as it requires custom-written software which may lower the image quality and it is an additional time-consuming step. Additionally, raw .dat Images opened in WeldStudio are characterized by higher contrast and colour saturation due to the built-in image processing step over which the user doesn't have great control. The same effect is visible in default outputted .avi movie files and .bmp images, with permanently processed frames. The visual difference between .dat file decoded in custom Python code and opened using Xiris WeldStudio is presented in Figure 48. The code is attached in Appendix D.

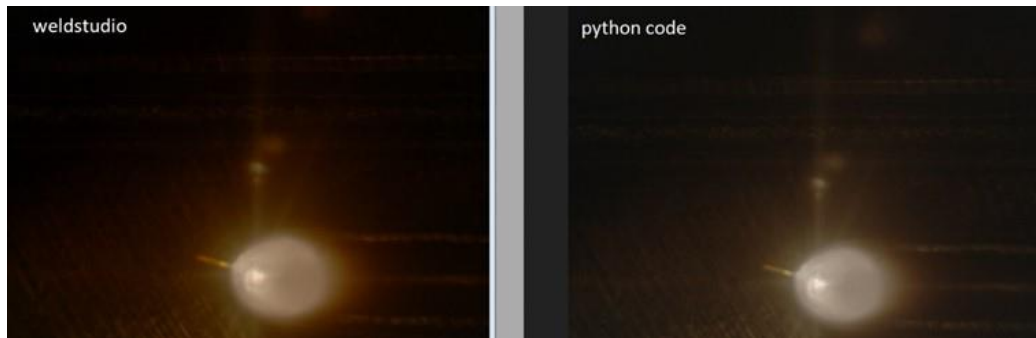


Figure 48: Image processing. The same raw image (.dat) was decoded in Xiris WeldStudio and custom Python code.

3.8 Design of the samples

Titanium Ti-6Al-4V, also called ASTM Grade5, is an alpha-beta titanium alloy, with excellent mechanical and chemical properties. Ti6Al4V alloy has almost 50% market share among other titanium alloys, and the aerospace sector uses over 60% of the titanium mill product, of which over 75% is used for airframes and engines [132, 133]. As filler metal is not added, which is the requirement to save weight and maintain tight tolerances, electron beam welding is used for manufacturing and repairing jet engines and gas turbines in the aerospace industry [1]. The popularity of Ti-6Al-4V alloy in these industries put a lot of pressure to follow exacting standards and maintain the highest weld quality. In such applications, defective welds could lead to safety and infrastructure concerns.

The two main difficulties, which are related mainly to the welding process and not the metallurgy itself, are porosity and solid-state cracking. Those can occur due to poor cleaning and shielding prior to welding. As electron beam welding is performed in a vacuum environment, there is no contamination from the atmosphere, but carelessly set welding parameters and joint preparation may lead to weld defects. The general industry practice to prepare surfaces for joining in EBW, depending on the material, is to use ultrasound cleaning, pickling, vapour or hot detergent, followed by abrading and acetone washing [133, 134, 135]. As titanium Ti-6Al-4V is prone to weld defects due to poor mishandling, it was anticipated in this study to detect these types of defects.

In regard to the backscatter emission characteristics, titanium alloy is a low atomic number material (22.15), which means (when compared to steel) it has a higher transmission coefficient and the maximum backscatter is lower [84, 136]. Despite this, according to the literature [137, 138, 139], the number of backscatter electrons is high enough for detection, which is also proven by applying electron beam surface imaging to titanium workpieces [68]. This made Ti-6Al-4V alloy an excellent choice for BSE monitoring as it assured that the collected signal contained enough information for signal processing.

For these three reasons, which are popularity, BSE characteristics and weldability, all samples used in experiments were manufactured from the titanium Grade5 and

the corresponding material certificate is attached in the appendices section (Appendix E) of this thesis.

To simulate gap defects, the samples were machined to form a single groove butt joint with a gap opened stepwise from zero to 0.5 mm followed by 1 mm, based on the design proposed by Gach (2021) [79] and shown in Figure 49. Those gap's width, when samples were mounted with clamping jigs, averaged 1.26 ± 0.064 and 0.7 ± 0.062 mm, as measured with a feeler gauge on 30 samples. The “zero gap” was below the range of the feeler gauge, which means less than 0.05 mm, an acceptable value for a well-prepared EBW joint.

As the samples were face milled, they required cleaning from cutting fluids. However, only acetone washing was used, which is not the industry standard as mentioned earlier, and it was expected to see the cleaning-induced defects which may be registered on the signal.

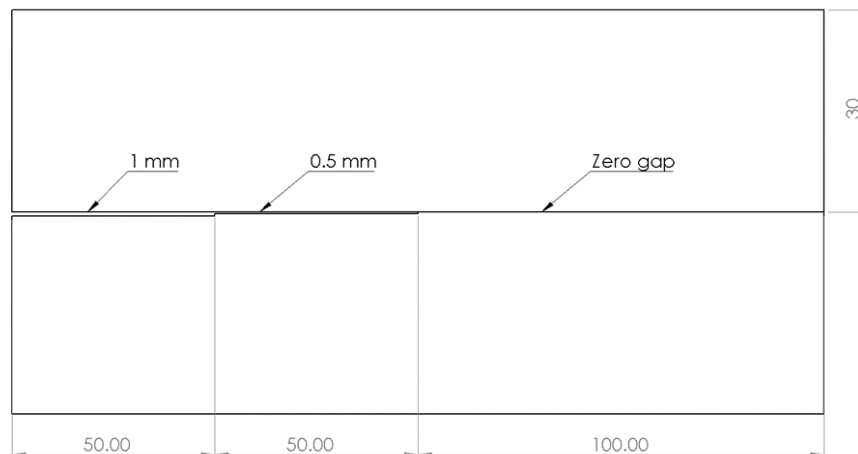


Figure 49: Stepwise opening gap sample design (t=10mm). The welding direction is from the beginning of the zero gap until the end of the 1 mm gap.

Samples were fixed to the welding table with clamps and the clamping points were located around the beginning and the end of the “zero gap” region. This setup ensured low variability of gap widths before welding as opposed to clamping points located at the beginning of the “zero gap” region and the end of the 1 mm gap. Tack welds were not used due to time constraints of the EBW machine, but a backing plate, made of the same material as samples (Ti-6Al-4V), was put below the joint. The welds were made as partial joint penetration to prevent fusion between the backing plate and the samples. In order to achieve partial penetration, welding mode varied between transition keyhole welding and conduction welding. The welding process started from “zero gap” towards 1 mm gap and samples were prone to gapping distortion around the 0.5 and 1mm gaps. A summarised setup and clamping method is presented in Figure 50.

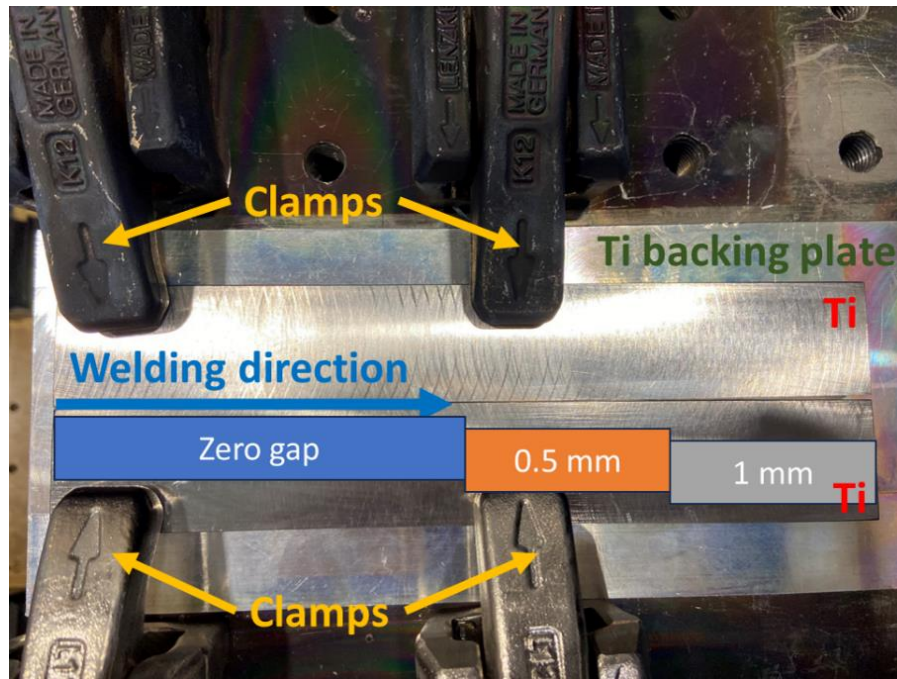


Figure 50: Setup and clamping of welded materials.

3.9 Sources of errors

This chapter describes potential and observed error sources during the backscatter electron collector plate signal acquisition.

3.9.1 The charge build-up on the surface of the plastic liner

The first trials were interrupted due to the static electricity in the plastic liner used on the cable connecting the collector plate with the digital oscilloscope. When the cable was close enough to the detector plate, the voltage of the BSE signal recorded was lower than the voltage of static charge, which was increasing after every weld (charge accumulation) and occasionally discharged. Those repeated discharges were limited in energy, as only a limited amount of the charge decayed from the surface because the static charge doesn't flow across an insulator surface. The cable sleeving was always negatively charged, which agrees with the type of material it was made from [140] – silicone-impregnated braided fibreglass – as silicone is negatively charged. The solution to this issue was to move away the cable from the BSE collector plate to avoid the disturbance of the BSE signal. The location of the cable after rewiring is presented in Figure 51.

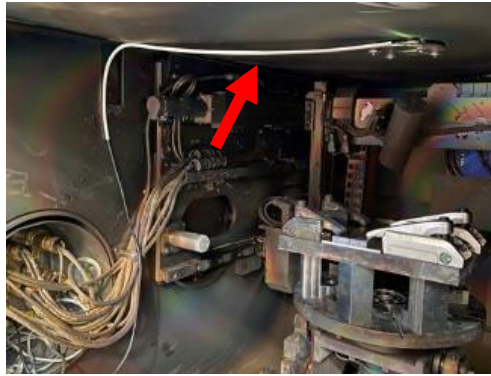


Figure 51: White cable sleeving (marked with the red arrow) made of silicone impregnated braided fibreglass – positioned closer to the roof of the chamber to avoid charge build-up.

3.9.2 Size of the samples

Weld length and thickness – the length of the welds was measured at 200.32 ± 0.08 mm and the thickness 10.04 ± 0.06 mm as measured on 30 samples. These dimension differences affect the precision of displaying the data, as it was assumed that samples are 200 mm long during the data processing.

3.9.3 Welding parameters (PLC)

The parameters used to adjust the beam, which included focusing current (330 mA), beam current (18 mA) and accelerating voltage (60 kV), were stable and this was verified by the PLC recordings. Their variation was less than the maximum acceptable variation according to DIN 32 505 Part 1 [141]. The welding speed was kept constant at 500 mm/min. Beam current had the highest standard deviation (0.94) which was caused by increasing the beam current during the first seconds of the welding to the target value. The measured differences between parameters set in the EB machine and read from the PLC are presented in Table 7.

Table 7: Difference between target and measured values for each welding parameter.

	Demand	Actual	σ , n=30
Focus current	330 mA	331.84	0.2
Beam current	18 mA	18.25	0.94
Accelerating voltage	60 kV	60.13	0.01
Welding speed	500 mm/min	508.91 mm/min	0.13

3.9.4 Digital oscilloscope error

Picoscope 3203D offers 8-bit resolution and 3% accuracy [142]. This is good enough to get a visual representation of the signal. At the same time, signal acquisition is limited by noise floor, which can mask the true characteristics of the input signal.

3.9.5 Trigger delay

The reading speed from SIMATIC S7-300 PLC is quite slow. The PLC updates each value every 32 ms, but the code is set to inquire PLC every 4 ms including the time for the Ethernet data transfer. This also affects the software trigger, as the value of beam current needs to be above 1 mA, to start data capture, and this value is obtained from PLC data with the observed initial delay. The trigger delay mainly affects the registration of the weld start position.

3.9.6 Sources of uncontrolled errors

There are two sources of uncontrolled errors, backscatter from the backing plate and motion-controlled table below it (in cases when the beam penetrated through the backing plate) and electrons scattered from the beam gun exit hole to the backscatter collector plate. These electrons, scattered due to the uncontrolled effects, lose part of their energy and the collected signal doesn't contain any distinguishable features anymore.

The first uncontrolled error was partly reduced by the usage of the backing plate from the same material as the workpiece. Twenty samples, where the backing plate was continuously penetrated through the backing plate were discarded during analysis. The second error is unavoidable and depends on the design of the beam gun exit hole (manufacturer related) and the location of the BSE plate (closeness to the weld pool). The BSE plate was located as close as possible to the EB gun exit hole to minimise the electron interference with the BSE collector.

3.10 Workstation

The workstation for data analysis was equipped with Intel i7 9800X CPU, 32GB RAM and Nvidia Titan V GPU. All of the time series images encoding have been done using custom python scripts. As BeamAssure files are saved in tdsM file format, which are produced by National Instruments LabVIEW software, they were converted to CSV for ease of processing. Python packages installed on the workstation are summarised in Table 8.

Table 8: Python packages installed on workstation and their usage.

Package	Description
SciPy [143]	Least-square method to fit the curve data, peak finding algorithm
Pyts [144]	Encode BeamAssure singals as images, reduce image size (PAA)
npTDSM [145]	Convert BeamAssure tdms files to csv
Pandas [146]	Operations on arrays
PyTorch [105]	Machine learning framework
Scikit [128]	Image processing algorithms (3D reconstruction), stratified sampling of dataset
XIRIS SDK [129]	Data acquisition and trigger control for XIRIS camera
PICOSCOPE SDK [147]	Data acquisition and trigger control for Picoscope USB digital oscilloscope
SNAP7 [126]	PLC communication
OpenCV [127]	Otsu's thresholding, rotation of images

4 Beam probing experimental results and discussion

This chapter describes the results from BeamAssure probing and encoding its signal as time-series images. The automatic segmentation and classification developed in this work comprises three parts: signal segmentation, encoding the electron beam pulses as images and usage of a convolutional neural network for image classification. In this work the accuracy of classification of time-series images obtained from different encoding methods such as Recurrence Plots (RP), Gramian Angular Fields (GAF), and Markov Transition Fields (MTF) were compared and the concatenation of images (MIX) from these different methods was explored.

Diagrams presented in the Figure 52, 53 and 54 represents code in a graphical format, to show the relationship between packages used in the software developed for this thesis. Green boxes are the parts of the code written from scratch using existing libraries (marked with circular markers on top of the boxes), blue boxes were developed based on existing libraries and TWI's expertise (papers, technical reports, pieces of code, conversations with Colin Ribton) and purple boxes are related to the modified code written based on the examples provided in the code documentation of each package.

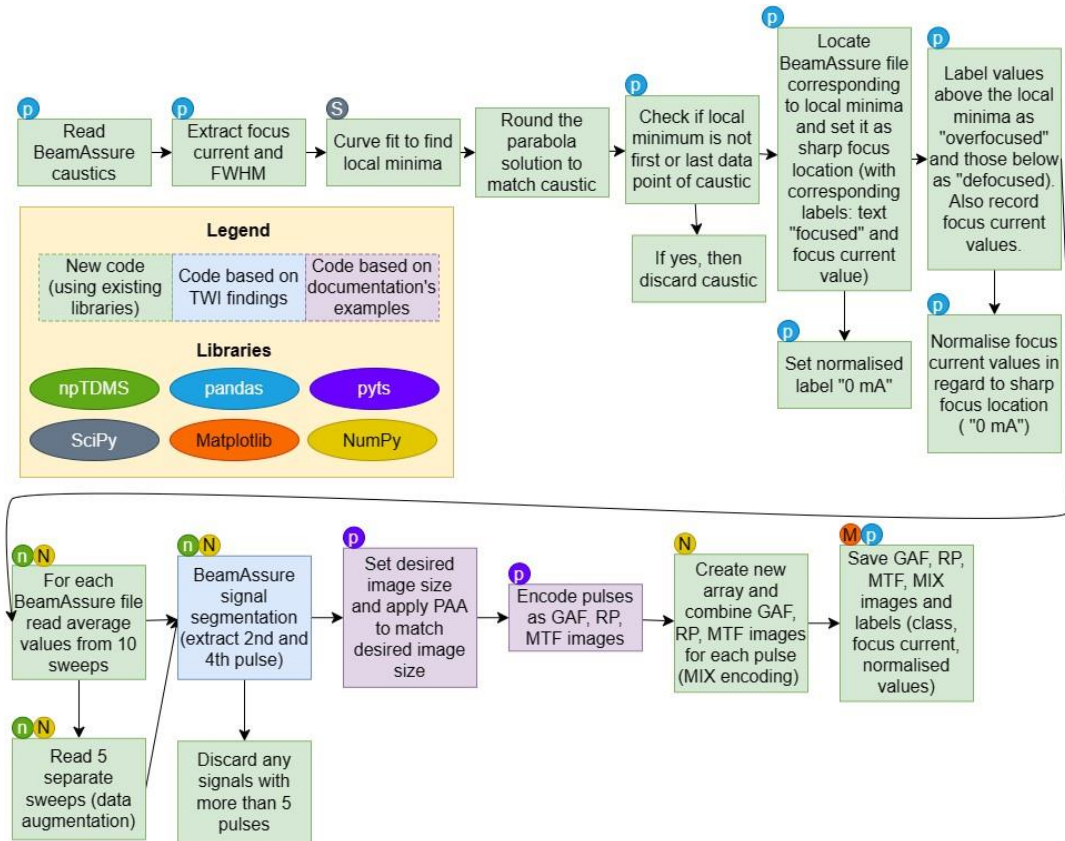


Figure 52: Code schematics of BeamAssure signal processing and encoding it as time-series images. Each step is colour coded according to the level of contribution and marked with circular markers to highlight the Python packages used, as per the legend.

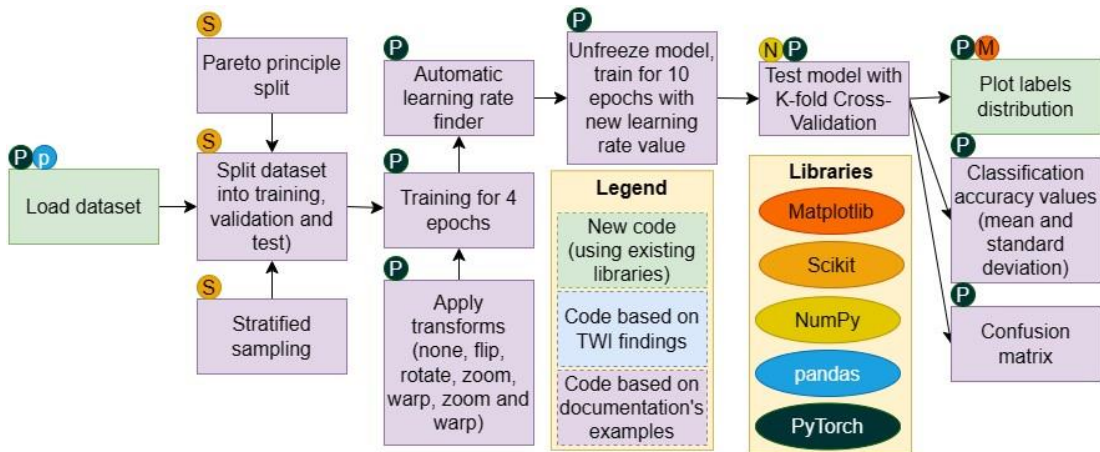


Figure 53: Code schematics of neural network training pipeline. Each step is colour coded according to the level of contribution and marked with circular markers to highlight the Python packages used, as per the legend.

Additionally, as the tomographic reconstruction methods for electron beam probing are not widely described in the literature, this chapter compared the method and algorithms used to generate beam shapes from multi-slit probes,

which are based on computed tomography. The code schematics of CT reconstruction are presented in Figure 54.

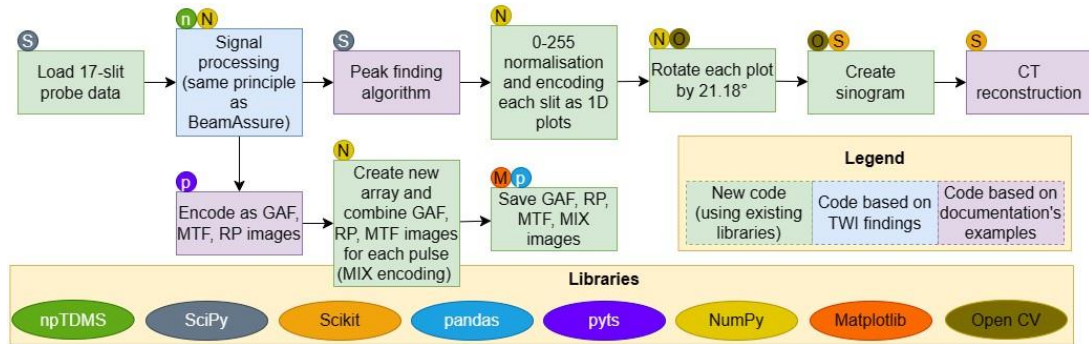


Figure 54: Code visualisation of CT reconstruction of 17-slit probe signal. Each step is colour coded according to the level of contribution and marked with circular markers to highlight the Python packages used, as per the legend.

4.1 BeamAssure signal processing

The data output from the BeamAssure software include values of the beam width as described in Chapter 2.7 and raw data from the probe. To encode this raw data to time series images, signal segmentation is a necessary stage for further processing of the probe signals and to enable automatic classification using a deep learning pipeline. The BeamAssure probing signals always contain 5 pulses, but only the 2nd and 4th pulses describe the width of the beam. Signal processing started with calculation of the offset, because the signal may be offset from zero. Based on the known value of the period of the deflection, the duration of a radian is calculated as follows (Equation 7):

$$\text{duration of the radian} = \frac{\text{period of the deflection frequency}}{2 \times \pi} \quad (7)$$

The average of the first $\pi/4$ radians of the continuous average signal established the signal baseline, which was subtracted from the signal. The signal was then filtered, which simplified determination of the intersection with the threshold voltage by eliminating signal jitter which would have otherwise caused multiple crossing points for each intersection. The filter time constant was derived as 0.01 radians. The signal was filtered using a convolution function. The voltage threshold was the minimum value in the filtered waveform (i.e., the maximum excursion of the signal as all the pulses were negative) multiplied by a threshold value (e.g. 3%). Ten crossing points were found between the voltage threshold and the filtered signal. Those values create the start and end values of 5 pulses, which are extracted from the original probe signal.

The beam probe signal is represented by a slit current and scan position. If the acquisition frequency is kept constant, then the measurements can be described as a 1D vector of number. Then, the BeamAssure signal can be encoded in the form of images. Encoding time series as Recurrence Plots (RP), Gramian Angular Fields

(GAF), and Markov Transition Fields (MTF) resulted in matrices of the size $N \times N$ when the time series was of length N . The combined effect of this augmentation and a large amount of time-series data acquired from beam probe (in an order higher than thousands of measurements) created images of unreasonable size. Due to hardware limitations, it is essential to keep the images at an optimum resolution without losing time coherence [93, 148]. In this work, concatenated images were also used, where each layer of RGB channels consists of a different encoding method. Since single-colour encoded images are of depth one, to utilise efficiently all layers of colour, the remaining layers were filled with 3 differently encoded (GAF, MTF and RP) images of the same signal. This also preserved more features from the signal itself.

The size of the time series image can be reduced by applying a Piecewise Aggregation Approximation (PAA) and example of its application is shown in Figure 55. PAA allowed reducing time series size without losing its trend. Since neural networks receive inputs of the same size, all signals need to be resized to a fixed length before inputting them into the CNN. This size depends on the neural network architecture, so the data reduction was matched to the resolution of images required by the ResNet model – 224 pixels. PAA is a recommended pre-processing method for time series before encoding them to images [148,149].

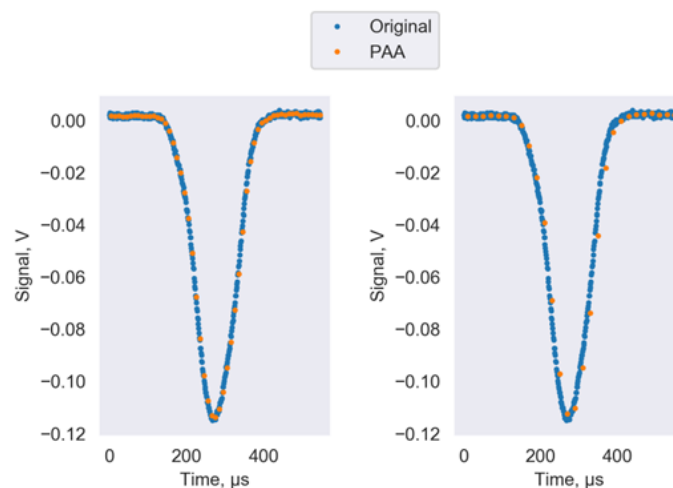


Figure 55: Enlarged part of the probe signal. PAA 10x (left) and PAA 20x (right) were applied to beam probe signals to reduce data and at the same time to preserve features.

Once the pulses have equal dimensions, they are encoded as single colour time-series images, which include GAF, MTF and RP. In this work, a software library called Pyts [144] was used to encode time series data as images. The last encoding method, mixed (MIX), involved the concatenation of different encoding methods to create colour RGB time-series images. All those encoded images have been used for a deep learning classification neural network, which is the last step of the framework. The code is attached in Appendix F.

4.2 BeamAssure dataset

The dataset used was a set of 3015 measurements (excluding 5 unreadable files) through the beam focus at a range of beam powers between 80 W to 6.4 kW, collected from one EBW machine and one BeamAssure probe. The dataset was collected around anticipated sharp focus location. It also contained 302 beam caustic profiles, which helped to find beam waist positions and automatic labelling of images with one of the three possible classes. Each beam caustic contained ten BeamAssure measurements with steps of 10 mA focus current. Graphical representation of the dataset is presented in Figure 52.

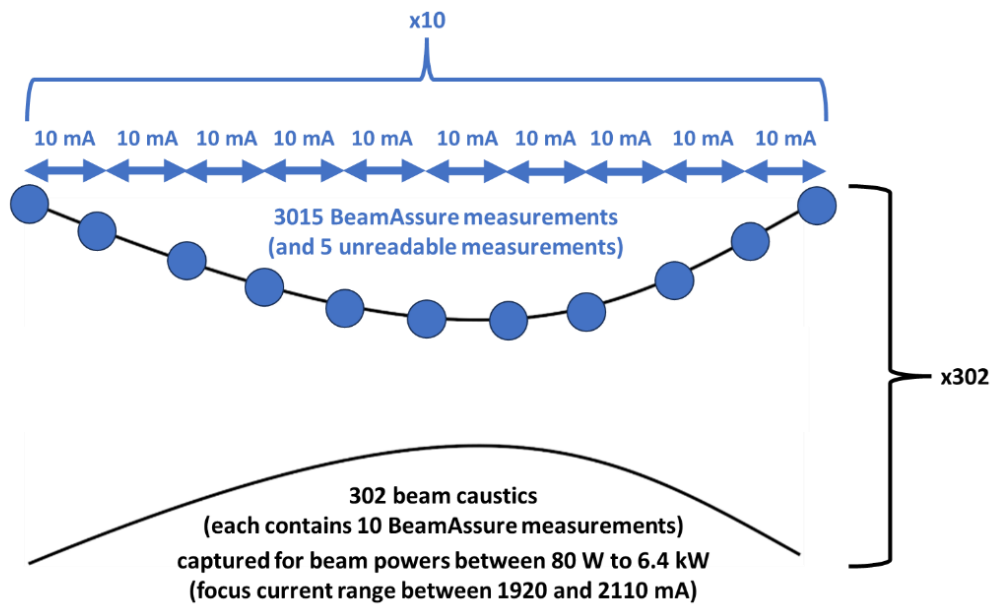


Figure 56: Graphical representation of the BeamAssure dataset.

By fitting a quadratic parabolic function to the beam caustic data, a local minimum (beam waist) was found and labelled as focused. Focus current values which were above the focus point were labelled as overfocused, and those below as defocused. For the defocused beams, features have been scattered all over the image for MTF and RP. In the case of overfocused beams, they appeared to be similar to focused beam images. However, the features were noisier and blurrier. Another visible difference is the sharpness of the image: beams which are in focus produced extremely sharp images. Additionally, each image has been labelled with a focus current value (increments by 10 mA).

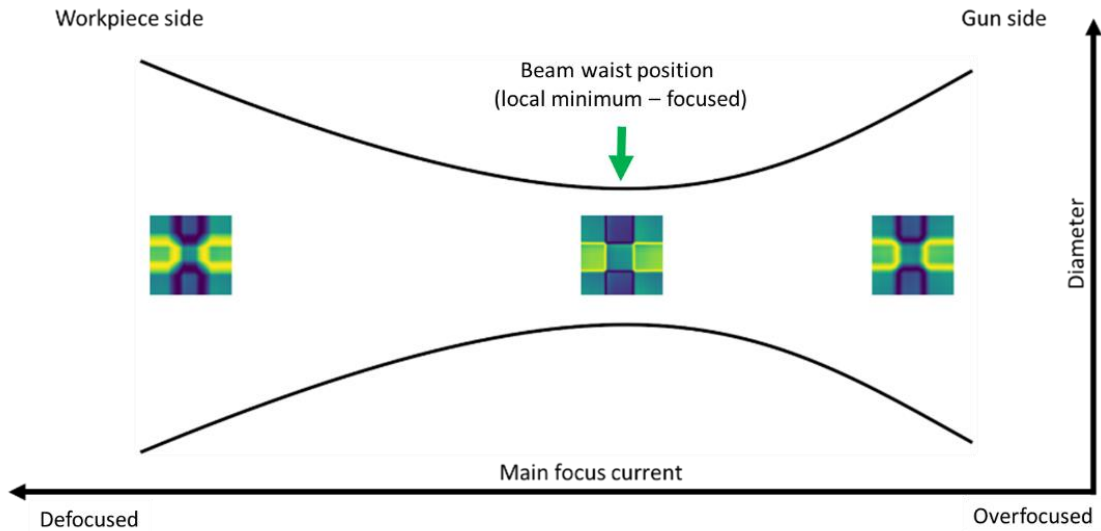


Figure 57: GAFs generated for defocused, focused and overfocused beam conditions. These images were used to train a neural network, but a human can also easily spot focus-based patterns in the beam caustic. Labels based on [150].

For the classification task, the 2nd and 4th pulses were encoded and resized using PAA into the 224x224 images required by the ResNet architecture. This resulted in 7806 images with one of three labels based on beam caustic position: defocused, focused and overfocused beam.

Each electron beam, measured at ten different focus positions, has only one sharp focus location. The relation of encoded GAF images and beam caustic position is presented in Figure 57. This led to an imbalanced data problem. To overcome this issue, focused beam probe data was augmented using data from multiple beam sweeps to match the distribution of overfocus and defocus images. Figure 58 presents dataset distribution before and after augmentation. This dataset was used in combination with ResNet (34, 50, 101) models and trained with encoded images generated from the BeamAssure signal. This allowed to identify relevant features and relate them to the beam focus condition.

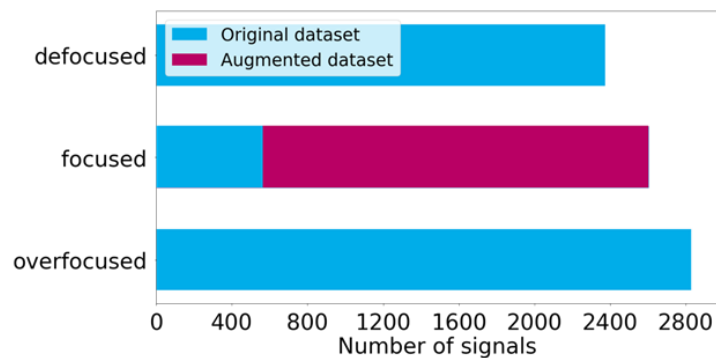


Figure 58: Class distributions for original (unbalanced) and augmented data.

Standard statistical measures including accuracy (Equation 8), precision (Equation 9), recall (Equation 10) and F1 score (Equation 11) were used to evaluate the proposed neural network model through confusion matrix elements.

$$Accuracy(A) = \frac{tp + tn}{tp + fp + tn + fn} \quad (8)$$

$$Precision(P) = \frac{tp}{tp + fp} \quad (9)$$

$$Recall(R) = \frac{tp}{tp + fn} \quad (10)$$

$$F1 = \frac{2 \times precision \times recall}{precision + recall} \quad (11)$$

Where, tp is the number of true positives classified by the model, fp is the number of false positives classified by the model, tn is the number of true negatives classified by the model, fn is the number of false negatives classified by the model. A perfect model has an scores of 1 in all of the metrics above.

4.3 Multi-slit probe data processing

The current density distribution has been obtained at all possible angles from a multi-slit probe. The beam current was set as 40mA and 14 measurements were made with 20 mA increments varied between 210-470 mA. This range allowed for the collection of beams with defocused and sharp focus conditions. In this work, scikit-image, a package for Python programming language was used. It is a collection of image processing algorithms, including the ones used in computed tomography.

Firstly, the raw signal was filtered using a convolution function and normalised between 0-255 values to fit the 8-bit grayscale image format. Such pre-processed signals have been segmented, making sure that the peaks of segments are at the same location. This was performed by the peak finding algorithm available in SciPy [143], which is a Python package that is used for scientific computing. This step also included signal shifting using zero padding to align the centres of the peaks.

Segmented signals with corrected peak locations were then encoded as 2D heatmaps, which were rotated with the same angles (21.18°) as the location of the slits. The last step was stacking heatmaps together to create a sinogram.

Obtained sinograms have been used to reconstruct the radial current density in 2D, and based on the intensity of the grayscale image – a 3D surface plot. The images were characterised by distinct types of noise, which is the combination of the reconstruction kernel used (sharper kernels produce noisier images) and noise from the probe itself. The simultaneous algebraic reconstruction technique and other filters (ramp, Shepp-logan, cosine, Hamming, Hann) have been used to

reduce the noise. To estimate the noise variance, Immerkær's (1996) [151] fast noise variance estimation have been used.

4.4 Encoding BeamAssure signals to images

Encoding BeamAssure signals to 2D images started with the automatic segmentation of the beam probe signal, based on the approach described in Chapter 4.1. First, the BeamAssure signal is loaded from *.tdsm files into Python code, which is presented in Figure 59 a). Next, the signal baseline is established, based on the duration of the radian. This shifted channel data is shown in Figure 59 b). To avoid multiple crossing points for each pulse, the signal was filtered using the convolution function and it is presented in Figure 59 c). Finally, ten crossing points at the base of the were found, which formed 5 pulses highlighted in Figure 59 d).

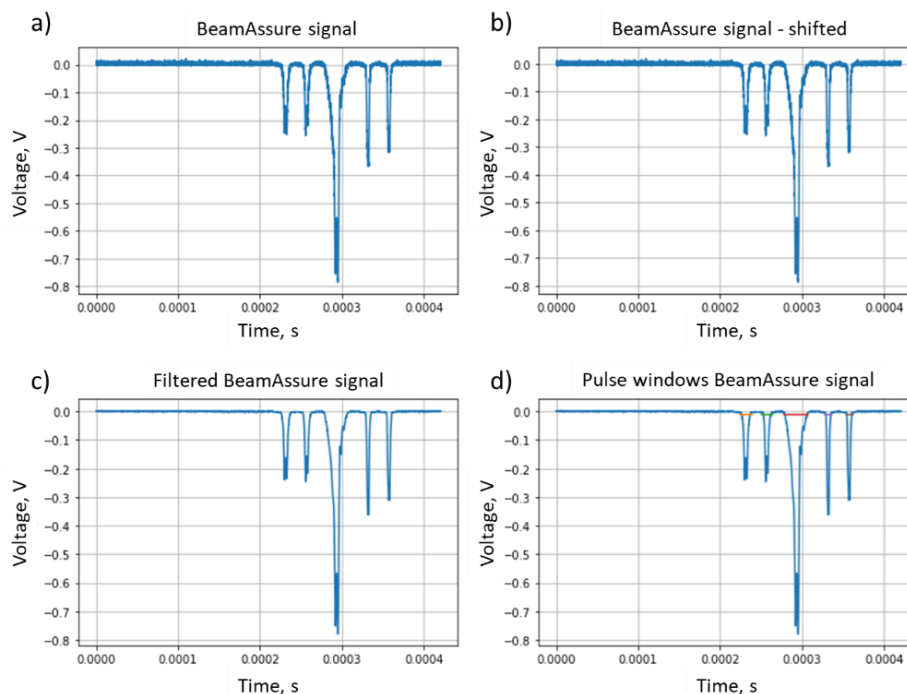


Figure 59: BeamAssure signal segmentation steps.

The 2nd and 4th pulses were selected for further signal encoding, using the Pyts library. As the input image size required for the neural network model is constant, the data reduction was matched to the resolution of images – 224 pixels. Once the pulses have equal dimensions, they were encoded as single colour time-series images, which included GAF, MTF and RP. The last encoding method, mixed (MIX), involved the concatenation of different encoding methods to create colour time-series images. ResNet models used in this work required 3-channel input images. To keep the convolutional neural network structure simple and maintain the same number of input channels, the other colour layers were filled with Viridis colourmap to expand the grayscale image to a colour one. Processed images were used for training the ResNet neural network, which is the last step of the framework.

Examples of the BeamAssure pulses and their corresponding encoded images can be found in Figure 60. For the defocused beams, features are scattered all over the image for MTF and RP. In the case of overfocused beams, they look similar to focused beams images, however, the features look more noisy and blurry. Another difference is visible in the sharpness of the image. Beams which are in focus produce extremely sharp images. In addition, GAF images preserve the graphical shape of the signal. The images were labelled using the method described in Chapter 4.2 and the labels were stored in a .csv file. The labels were created based on the beam waist, which is the location where the beam radius has a minimum. This method is also used by the BeamAssure operator, who will analyse the beam caustic to find the minimum beam radius location. To ensure that the code correctly labelled images, data was verified manually on a statistically selected sample. In the case of the three classes, 326 labels of each class (33% data proportion, with 5% precision and 95% confidence level) were verified against the BeamAssure measurements.

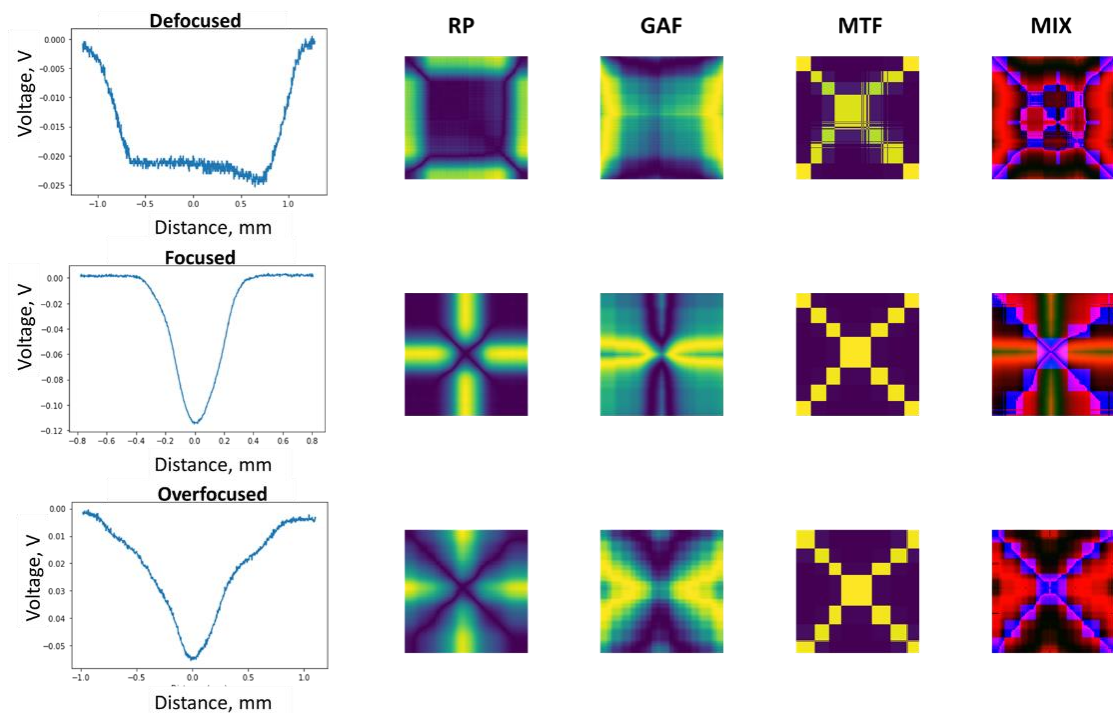


Figure 60: Different encoding methods revealed distinguishable patterns of the BeamAssure signal.

4.5 Three-classes neural network model

In this work, residual CNNs (called ResNet) for image classification tasks were explored. Three variants of ResNet models, i.e. ResNet-34, 50 and 101, were pre-trained on ImageNet and then retrained on BeamAssure data. The training was done on the workstation described in Chapter 3.10 using a three-classes dataset (overfocused, focused, defocused). The signals were divided for training and test dataset using the Pareto principle (80/20). Additionally, using the same split value (80/20), the validation dataset was obtained from training images. As a sampling

strategy, stratified sampling was chosen to ensure the same distribution of the classes in each dataset. The final distribution of the classes is presented in Table 9. After distributing the data, all images were normalised at input with ImageNet statistics according to the dataset mean and standard deviation. This ensured compliance with the weights of the pre-trained ResNet models.

Table 9: Dataset distribution for training, validation and test sets.

	Training + Validation	Test (unseen data)
Overfocused	2262	566
Focused	2083	521
Defocused	1899	475

In total, 4995 images were used for training and 1249 for validation. The test dataset, with unseen data, consisted of 1562 images. There were three label types. The training was done for each encoding method separately. Training included finding learning rate value and transfer learning (model pretrained on ImageNet and classification layer retrained on BeamAssure dataset) for 4 epochs. Then, after unfreezing all the model layers, a new learning rate value was obtained and training continued for 10 epochs. The train time need for one epoch was measured and the results are presented in Table 10.

Table 10: The training time in seconds for one epoch.

	GAF	RP	MTF	MIX
ResNet-34	26	25	18	25
ResNet-50	36	35	29	35
ResNet-101	51	50	44	50

To obtain a less biased estimate of the model skill, the k-fold Cross-Validation method was used with 10 folds for ResNet-34, 50, 101 model. The whole process was automated using an automatic learning rate finder since the focus of this work was more on comparing different encoding methods rather than optimisation of one specific network. The results, as shown in Table 11, were analysed to select the most suitable architecture, which was found to be the ResNet-34.

Table 11: The K-fold cross-validation classification accuracy on unseen data for ResNet-34, ResNet-50, ResNet-101 architectures and four encoding methods.

		GAF	MTF	RP	MIX
ResNet-34	Mean, %	94.56	80.3	94.64	97.6
	Standard deviation	0.83	0.9	0.77	0.55
ResNet-50	Mean, %	94.76	81.3	94.73	97.6
	Standard deviation	0.94	0.96	0.81	0.63
ResNet-101	Mean, %	94.94	81.33	95.07	97.8
	Standard deviation	0.87	0.91	0.77	0.53

To fully understand where the neural network failed to predict correct classes, the false classifications plots based on a confusion matrix was obtained for the ResNet-34 model and it is shown on Figure 61. To make the analysis easier, the dataset also contained labels which weren't used during the training. Their purpose was to check how the false labels are distributed over normalised focus current values. For focused labels, the wrong predictions are located +/-10 mA around a focus point and this conforms with the expected behaviour. Similarities in images close to focus value can be not always sufficient for a neural network to make proper prediction between three classes. However, this means that the maximum deviation from the sharp focus location is only 0.5%. From the literature review [8], it was found that a 1% deviation of focus current from optimal focus current decreases the depth-to-width ratio between ± 2 to $\pm 10\%$. This means that the neural network approach deviation is much smaller, particularly when compared to the machine operators, in which case a $\pm 20\%$ to $\pm 40\%$ dimensional variation due to manual focus adjustment is expected [8].

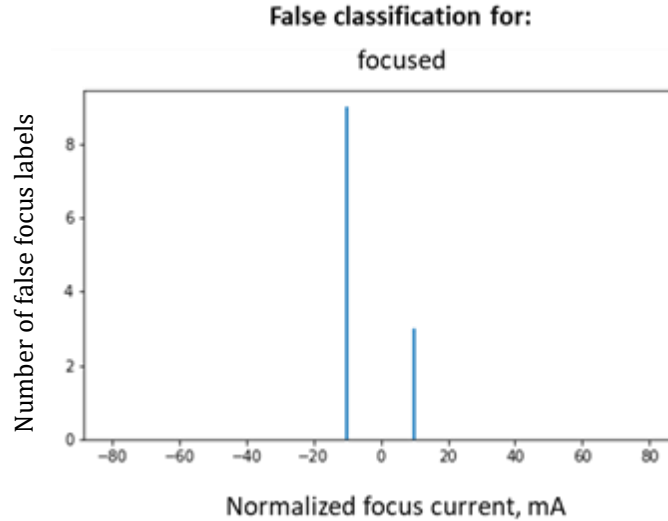


Figure 61: False focus labels for different normalized focus current values obtained from Resnet-34 model trained with concatenated images.

4.5.1 Three-classes neural network model with data augmentation

Data augmentation in deep learning models has three main advantages, which are improving the generalisation ability of these models, adding variability to the data and minimise data overfitting. It also reduces the cost of collecting and labelling additional data and can improve the accuracy of the deep learning model. The data augmentation methods such as flip, rotate, zoom and warp were introduced to the training pipeline to verify if the base model accuracy can be increased further. The results, as shown in Table 12, were analysed to find the appropriate data augmentation technique for the BeamAssure dataset. Flipping and rotating transforms decreased the accuracy values, which may be caused by a drastic change in the meaning of the images. Warping increased the accuracy of the model by 0.1% as compared with the base model, and zooming increased further by 0.14%. The combination of both, zoom and warp, was found as the most suitable data augmentation technique for the BeamAssure dataset as it resulted in the highest accuracy gain (1.22%),

Table 12: The K-fold cross-validation classification accuracy on unseen data for the ResNet-34 architecture. Training done with MIX-based dataset and various data augmentation techniques.

	None	Flip	Rotate	Zoom	Warp	Zoom and Warp
Mean, %	97.6	90.12	92.46	97.84	97.7	98.22
Standard deviation	0.55	1.24	0.81	0.87	0.63	0.87

The experimental results indicate that the CNN is capable of identifying the existing correlation between the beam focus state and beam probing signal. To classify the beam signal based on focus state (defocused, focuser or overfocused), there is no need to generate a beam caustic. Instead, the neural network model can predict, based on one measurement, in which focus state the beam is set. This can greatly save time and manual labour needed for setting up and collecting data with the traditional process of measuring the beam caustic or observing a bright spot on the workpiece. The information from the neural network model can be used by the operator to increase or decrease the focus current and as a result find a sharp focus location. However, as the information from the neural network model contains only the direction of the change and not the precise focus current value, the operator will need to repeat the inference step for every focus current change.

Markov Transition Field images give the worst results (80.3% accuracy) among the four described encoding methods. The poor results obtained with MTF are also visible in the time required to train one epoch, which is the lowest, which means that the neural network couldn't find relevant features. The Gramian Angular Field encoding increases the accuracy to 94.56% and Recurrence Plots can slightly increase the score up to 94.64%. The highest accuracy was obtained using concatenated images. The combined effect of all RGB layers connected allows neural network to correctly classify beam focus condition with an accuracy as high as 97.6%. The accuracy of the MIX model can be increased further by utilising zoom and warp transforms for data augmentation to achieve an accuracy value of 98.22%. This accuracy increase, due to the data augmentation, is caused by artificially increasing the amount of data by the warped and zoomed images. Warp and zoom transforms can be used separately, achieving slightly lower scores of 97.7% and 97.84% respectively. This slight drop in accuracy, if the zoom and warp transforms are used independently, is caused by reducing the amount of data to half of the combined zoom and warp dataset. Flipping and rotating augmentations reduced the accuracy to 90.12% and 92.46% respectively, and this was caused by drastic changes in the meaning of the images. Therefore, it can be concluded that time-series encoded images are heavily reliant on consistent features and their orientation.

Deep and complex neural networks are not needed to classify BeamAssure signals encoded as images. It was proven, for a BeamAssure signal dataset, that smaller ResNet architectures like ResNet-34 achieved the same accuracy as deeper ones such as ResNet-50 and ResNet-101. Such models require less storage for their model parameters, so they can be used in embedded industrial systems. The time needed for inference, measured using CPU, was on average 120 ms (based on 3 measurements, 1 dry run before the measurement was performed). Regarding the GPU, the Python timing function isn't accurate enough as it considers the time consumed to launch the kernels, but not the actual GPU execution time of the kernel. However, using PyTorch commands it was possible to accurately measure the time taken to execute, which was 65 ms. Ignoring visualisation operations and displaying them to the user, 65 ms seems like a fast-enough response time for the operator to use it as a part of a semi-automated focusing procedure.

4.6 Seventeen-classes neural network model

As the feasibility of time-series encoding for BeamAssure probe data was proven with the three classes model, the model was further improved by including additional classes. These classes, which are based on labels with 10 mA increments from sharp focus location, allowed to indicate how many mA is the beam out of focus (or 0 in case of sharp focus location).

As the same dataset as the one used in the three-classes model contained labels with 10 mA increments from the focus point (labelled as 0 mA), the dataset was split into seventeen classes between -80 mA to 80 mA. Following the three-classes neural network model, it was decided to retrain it with seventeen, more precisely describing the focus point, classes and using the same images as in the previous experiment. As found previously, ResNet-34 had been chosen to speed up the model training step. The training had been done on the same workstation as the three-classes model, and the training/test dataset split was using same principles, which is 80/20 split combined with stratified sampling. The final dataset distribution is presented in Table 13.

Table 13: Dataset distribution for training, validation and test sets.

	Training + Validation	Test (unseen data)
-80	1	1
-70	6	2
-60	24	12
-50	159	39
-40	369	91
-30	453	93
-20	424	130
-10	463	107
0	2083	521
10	461	123
20	455	125
30	466	112
40	431	111
50	312	72

60	97	19
70	31	3
80	9	1

In total 4995 images were used for training and 1249 for validation. The test dataset consisted of 1562 images. There were seventeen label types and the training was done for each encoding method separately. Training included automatic finding learning rate value and transfer learning for 4 epochs. Then, after unfreezing all the model layers, a new learning rate value was obtained and training continued for 10 epochs. Times needed for training one epoch are presented in Table 14. As previously, the k-fold Cross-Validation method was used with 10 folds for the ResNet-34 model, and the results for the seventeen-class model can be found in Table 15.

Table 14: The train time in seconds for one epoch.

	GAF	RP	MTF	MIX
ResNet-34	25	25	22	33

Table 15: The K-fold cross-validation classification accuracy on unseen data for ResNet-34 architecture and four encoding methods.

	GAF	MTF	RP	MIX
Mean, %	79.12	65.26	75.28	87.51
Standard deviation	0.93	0.73	0.91	0.53

To understand weak points of the neural network, the confusion matrix, presented in Figure 62, was analysed to find the distribution of true positives and true negatives. In the case of the seventeen-classes model, most of the incorrect recognitions were distributed closer to the boundaries of the confusion matrix, which are -80 and 80 mA. This was caused by insufficient amount of the data in those categories to properly train the neural network. In the range between -60 mA and 60 mA, the predictions were more accurate. Prediction accuracy rises towards 0 mA labels as there was more data to train model on. However, at the 0 mA, point there is a sudden drop in accuracy as the data is mis-predicted with the closest neighbours in -10 to 10 mA range.

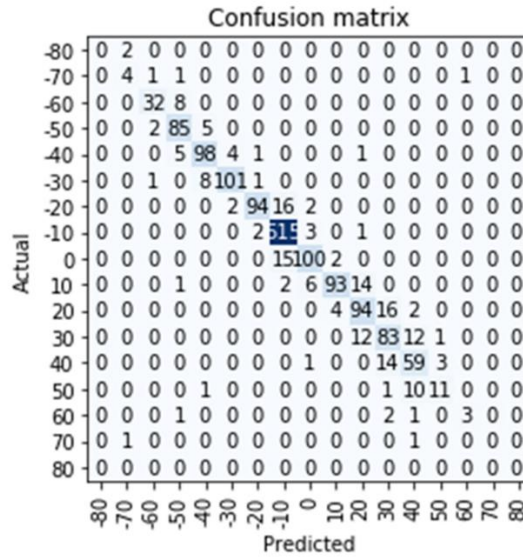


Figure 62: Confusion matrix obtained from seventeen-classes Resnet-34 model trained with concatenated images.

4.6.1 Seventeen-classes neural network model with data augmentation

Similarly to the three-classes model, the data augmentation tested with the seventeen-classes model included methods such as flip, rotate, zoom and warp to verify if the base model accuracy can be increased further. The results, as shown in Table 16, were analysed to find the appropriate data augmentation technique for the BeamAssure dataset with seventeen classes. As with the three-classes model, flipping and rotating transforms decreased the accuracy values. Warping increased the accuracy by 0.61% and zoom transformation increased accuracy further by 0.31%. Again, using a combination of both, accuracy was found to be the highest – 88.32%.

Table 16: The K-fold cross-validation classification accuracy on unseen data for the ResNet-34 architecture. Training done with MIX-based dataset and various data augmentation techniques.

	None	Flip	Rotate	Zoom	Warp	Zoom and Warp
Mean, %	87.51	84.61	84.32	87.81	88.12	88.32
Standard deviation	0.53	0.41	0.55	0.32	0.95	0.44

The seventeen-classes model is able to distinguish 10 mA increments, with 87.51% accuracy for concatenated images, which is a helpful indication of where

exactly the sharp focus location is located. Once again, MTF images gave the worst results (65.26%), followed by RP (75.28%) and GAF (79.12%). To further increase the accuracy of the MIX model, data augmentation using zoom and warp transforms is recommended for the same reasons as the three-classes model. Combining zoom and warp transformations together, it was possible to achieve an accuracy of 88.32%. The training times followed the same trend as the three-class model, where MTF train time per epoch was the quickest. As computational complexity between three-classes and seventeen-classed models is almost equal, only the 11.15% drop in accuracy using seventeen-classes model (for MIX-based models without data augmentation) needs to be taken in consideration. Despite the drop in accuracy, the seventeen-classes model offers precise focus location value, which is highly desirable to save the manual focusing time and reduce it further from three-classes model. This can lower the requirements for training skilled operators and reduce their inconsistency in the beam focus set-up. The seventeen-classes model has the greatest potential to be deployed as a completely autonomous system, which is the core of the Industry 4.0 paradigm. However, the model was proven to work with a dataset collected from a single machine. To maintain the highest possible accuracy, in case of the machine or filament change, it is expected to collect a new dataset and retrain the model using transfer learning. As the filament life is counted in hours (20 to 300), the model retraining step, which requires 7 minutes and 42 seconds, is, in the worst-case scenario, equal to 0.0064% of the minimum expected filament life.

The model is trained on the BeamAssure signal, the labelling process is highly dependent on the accuracy and post-processing of the data from the beam probe. The correctness of the encoded image labels was verified during the creation of a three-classes dataset, and the generated labels were consistent with the BeamAssure generated beam caustics. The wrong predictions near 0 mA are really similar to those observed with three classes model and are located between the -10 to 10 mA range. This proves that no matter how the data is labelled, the neural network used the same features as the three-class model to predict the possible more precise labels. This also can help with justifying the drop in accuracy, as most of the error predictions will be distributed close to the focus position, which still can be fine-tuned by operator if needed. The accuracy of the model can be potentially further increased if the measured focus current increments are reduced, for example to 1 mA or less.

The inference time using a GPU is 65ms, similar to the three classes model. This means that the seventeen-classes model is also a good candidate for real-time monitoring and could be potentially used in fully autonomous systems to find and set sharp focus location.

4.7 Multi-slit beam probing results

Generalisation is the ability of the trained model to make accurate predictions in new and unseen data. The model proved to be useful in combination with the BeamAssure dataset and its capabilities were further explored using 17-slit probe

data to prove generalisation limits on the three-classes model and compare them against traditional CT reconstruction methods.

Due to the limited dataset, this work focused on efficient CT reconstruction methods for the 17-slit probe. During the analysis of the multi-slit beam probe signal, it was found that a reference peak, which is collected two times (a small hole between two of the slits in Figure 14 in Chapter 2.8) is not always clearly recognised by the peak finding algorithm. The instability of the signal with the defocused beam indicates that the beam is not stable in acquired cross sections. As a result, this made fine-tuning the peak-finding algorithm difficult. This phenomenon is presented in Figure 63. With highly defocused or overfocused signals, acquired with 210 and 470 mA focusing current respectively, the peaks are either not recognised (210 mA) or overfitted (470 mA). The usable range of focusing current was between 270 and 390 mA, when the beam produced the most stable output signal for the peak finding algorithm.

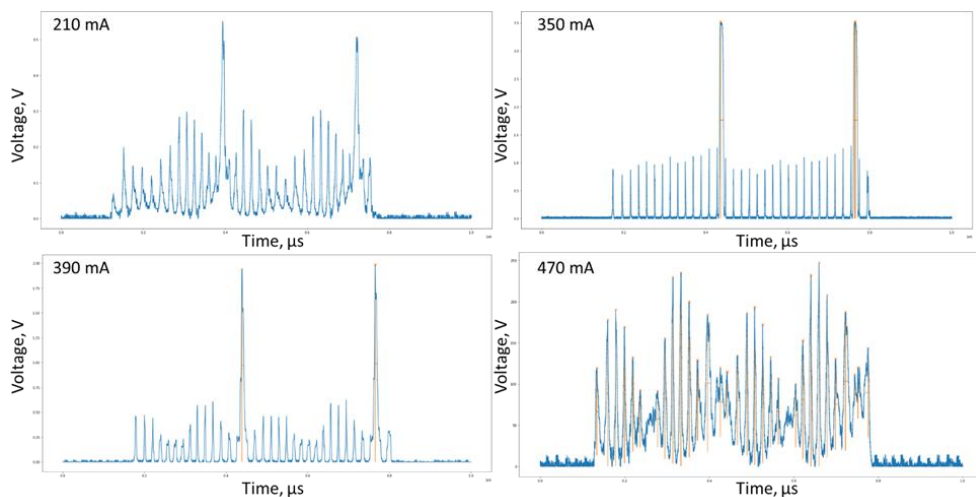


Figure 63: Selected raw signals for various focusing currents – 210, 350, 390 and 470 mA. Orange lines are drawn by the peak finding algorithm.

For the aforementioned focus current range, 270 and 390 mA, the beam shapes have been reconstructed using various reconstruction techniques and kernels. As for techniques, Simultaneous Algebraic Reconstruction Technique (SART) and Filtered Back Projection (FBP) were used. The choice of the filters for FBP were as follows: ramp, Sheep-logan, cosine, Hamming and Hann. The computing time required for each filter type and noise variance estimation, based on Immerkaer's (1996) fast noise variance estimation [151], is summarised in Table 17. The examples of the obtained visualisations using various filters for 350 mA beam are presented in Figure 64.

Table 17: Reconstruction time in seconds for different reconstruction kernels.

	SART	Ramp	Shepp logan	Cosine	Hamming	Hann
Time, s	11.09	3.46	3.5	3.43	3.41	3.49
Noise variance estimation, σ	0.0009	0.0190	0.0146	0.0079	0.0053	0.0045

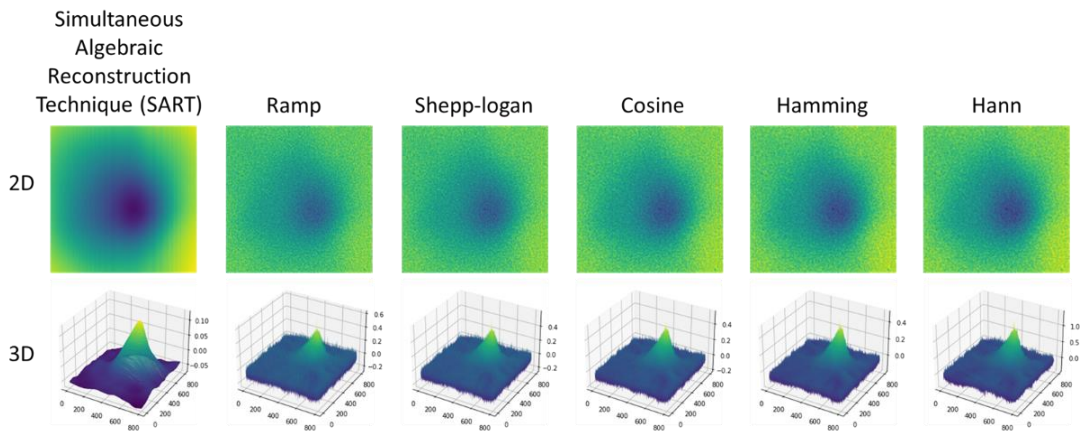


Figure 64: Reconstructed radial current density distributions in 2D and 3D with different reconstruction kernels (350 mA focusing current – sharp focus location).

The simultaneous algebraic reconstruction technique was found to smooth the noise and greatly improve the reconstructed image quality, but at the same time, it needed nearly three times the computing power than other filters (ramp, Shepp-logan, cosine, Hamming, Hann). Cosine, Hamming and Hann are more aggressive than Shepp-logan and ramp kernels, by visibly sharpening the images, while at the same time producing less noisy output. In terms of the best noise to compute the time ratio, the Hann filter performed best for reconstructing multi-slit probe signal.

4.7.1 Three-classes neural network model with 17-slit probe

As the tomographic reconstruction required at least 3.41 seconds processing time per collected signal, an alternative approach for reconstructing the data was examined. All three transformations (RP, GAF, MTF) require 0.001 seconds to generate the image and MIX encoding requires 0.003 seconds. The three-classes model from Chapter 4.5 was reused to detect the focus state of the 17-slits probe measurements. Due to the limited dataset size, consisting of 7 measurements, it was not feasible to use K-fold cross-validation. Instead, the 7 images have been fed

directly to the model for the inference and the resulted accuracy was 71.42% for GAF, 57.14% for MTF, 57.14% for RP and 71.42% for MIX. Examples of the 17-slit probe signals encoded images can be found in Figure 65.

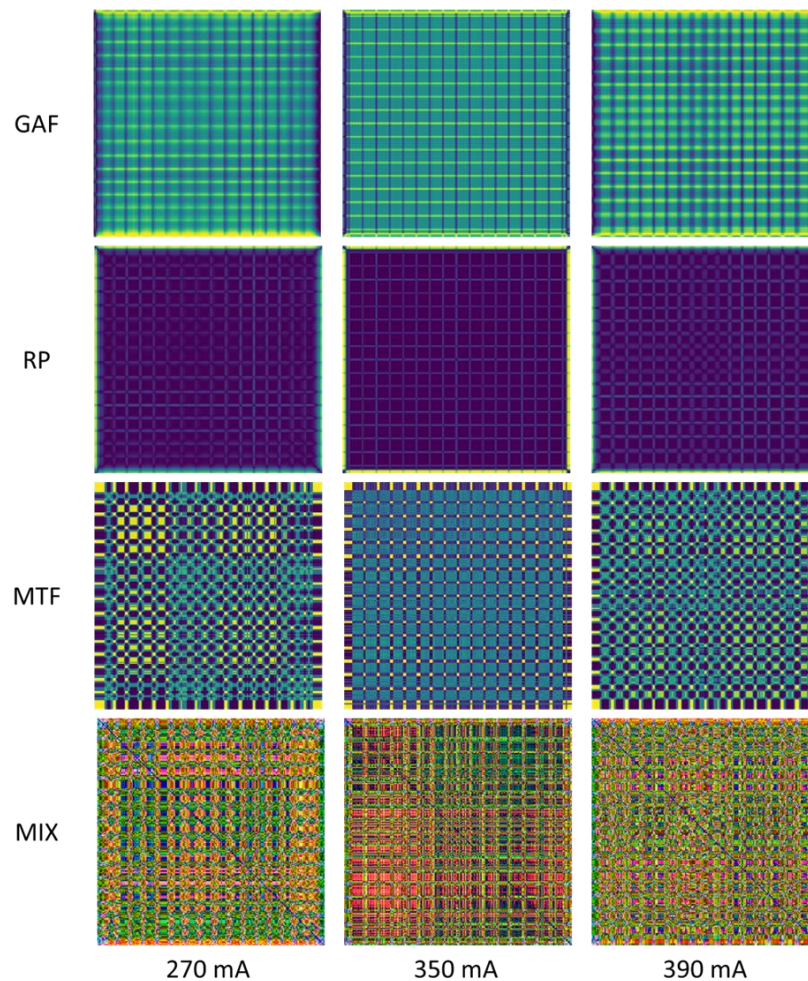


Figure 65: Time series encoded data from a 17-slit probe for 270, 350 and 390 mA focus currents.

Traditionally, multi-slit beam probing data needs CT reconstruction in order to reveal the 3D shape of the beam. This has several advantages, such as revealing parts of the beam which may cause problems during the welding (such as hot and cold spots). However, CT reconstruction times, measured in seconds, range between 3.41 to 11.09 s for 800x800 px images and therefore uses a significant amount of computing power. As an alternative approach, time-series imaging offers a quicker (0.001-0.003s) way of visualising multi-slit beam probing data. This allows to feed encoded images directly to the neural network model and classifies the focus state of the beam. By using the three-classes model, a good accuracy score was achieved and shows that the model generalises well, even if provided with the signal from the different types of probes. The main reason that contributed to generalisation capabilities is the fact that the only difference between a 17-slit probe and a 4-slit probe is the length of the signal collected. The shape of the signal peaks remains the same between the different types of probes (after the PAA step), which allowed the model to use the same image features to

predict the state of the beam. Due to the limited dataset, there is no difference between GAF and MIX encoding, which is caused by the lack of variability between the images. However, RP and MTF performed slightly worse, which means that those images carried less distinguishable features.

4.8 Summary

This chapter presented a deep learning model that was successfully deployed to find the sharp EB focus location based on one BeamAssure measurement. This was achieved using a large BeamAssure dataset, which was automatically labelled, in combination with an off the shelf ResNet 34 neural network model. As the ResNet 34 model was trained using transfer learning with BeamAssure signals encoded as images, the training time was quick and can be quickly repeated and reproduced in the industrial set-up when the accuracy of the NN drops due to the filament or after machine servicing, upgrades or changes. The three classes model generalised well and was also able to classify data from the 17-slit probe to find the focus state of the beam. This makes the three classes model more resistant to changes in the machine or filament, but cannot work in a fully automated mode. Furthermore, it can be only used as a guide for operator in which direction the focus current needs to be changed in order to achieve sharp focus. Although the seventeen classes model cannot generalise well and may be affected by the machine maintenance, it was able to predict the sharp focus location within 10 mA range. Both of the models, three and seventeen classes, benefited from data augmentation and concatenation. Zoom and warp augmentation have been found to work best with BeamAssure data. Concatenation always improved classification accuracy due to the combined effect of each encoding methods.

5 BSE collector plate experimental results and discussion

In electron beam welding, the weld pool behaviour analysis is needed to determine welding quality. To better observe and control the EBW process, reliable signal processing algorithms and computer vision tools are required. This chapter presents the results from weld pool monitoring system based on a high dynamic range camera and backscattered electron collector plate. The stability of the weld pool was investigated by examining images and signals generated during the welding of samples with artificial flaws. Similarly to the graphical representation of the code described in Chapter 4, diagrams presented in Figures 66 and 67 are the schematics of the code structure to show the level of contribution and packages used.

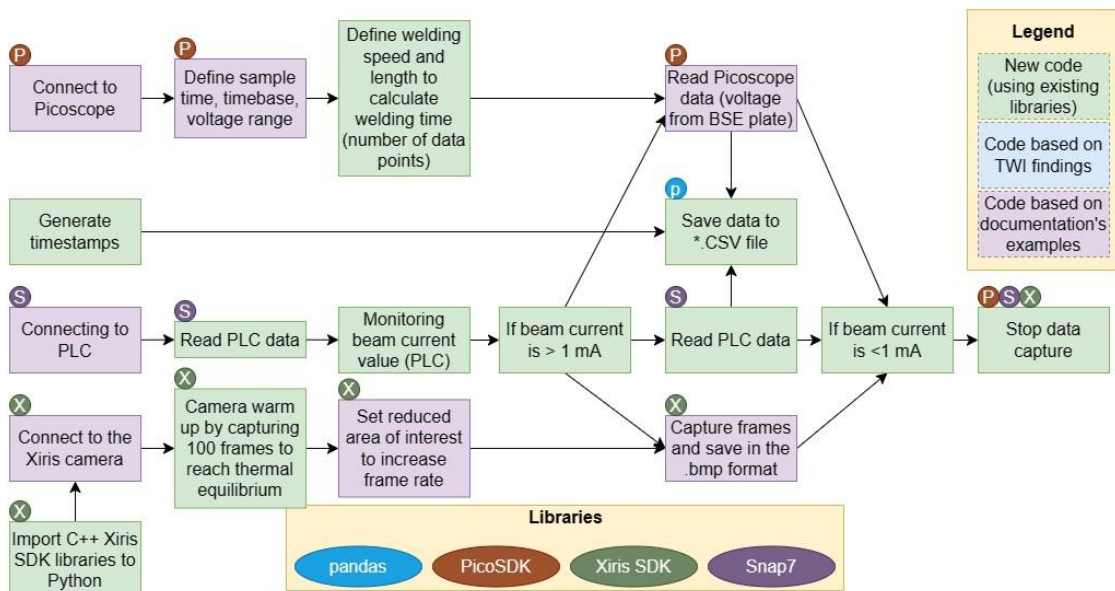


Figure 66: Code visualisation of data acquisition steps. Each step is colour coded according to the level of contribution and marked with circular markers to highlight the Python packages used, as per legend.

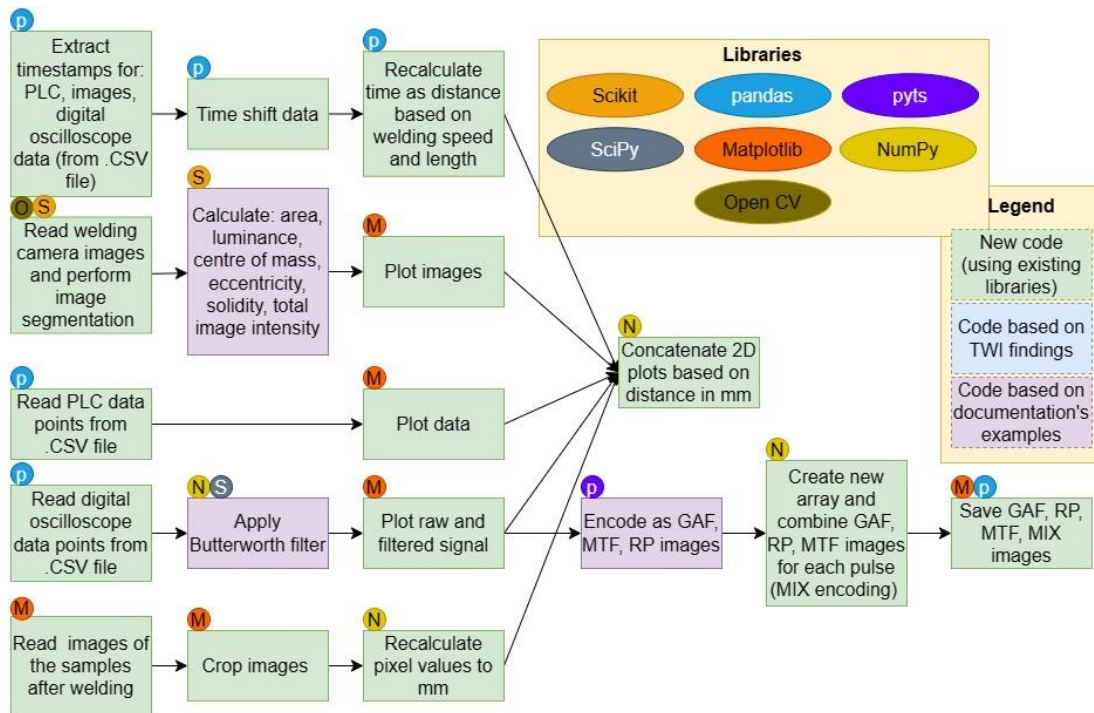


Figure 67: Code visualisation of data visualisation steps. Each step is colour coded according to the level of contribution and marked with circular markers to highlight the Python packages used, as per legend.

Despite the monitoring methods described in the literature review (Chapter 2), there is a lack of reliable tools to assign BSE signal perturbations to welding defects. The main requirement for online process monitoring systems in EBW is to build them on indicators which can describe the current stability of the electron beam active zone (EBAZ) and the adjacent areas. The usefulness of such an indicator can be evaluated by verifying the correlation between a significant change in its value and the resulting weld quality. Additionally, collecting the data shouldn't disturb the EBAZ to avoid process interruption. This requirement can be easily fulfilled by cameras and BSE collator plates as those sensors can observe the process from a distance.

5.1 BSE collector plate signal

During welding, the parameters used to adjust the beam, which include focusing current (330 mA), beam current (18 mA), accelerating voltage (60 kV) and welding speed (500 mm/min), were stable. This was verified by the PLC recordings. Although the parameters were overshoot, they didn't exceed the target values by more than 1.6%. Rise time, as measured from PLC, was 192 ms and settling time (within the 2% tolerance band) was less than 32 ms. This stability of PLC data collected during a welding experiment is visualized in Figure 68, which clearly shows the stable distribution of data related to welding parameters. However, samples were designed to simulate gap defects as described in Chapter 3.8, and it was expected that these misalignments will disturb the welding process.

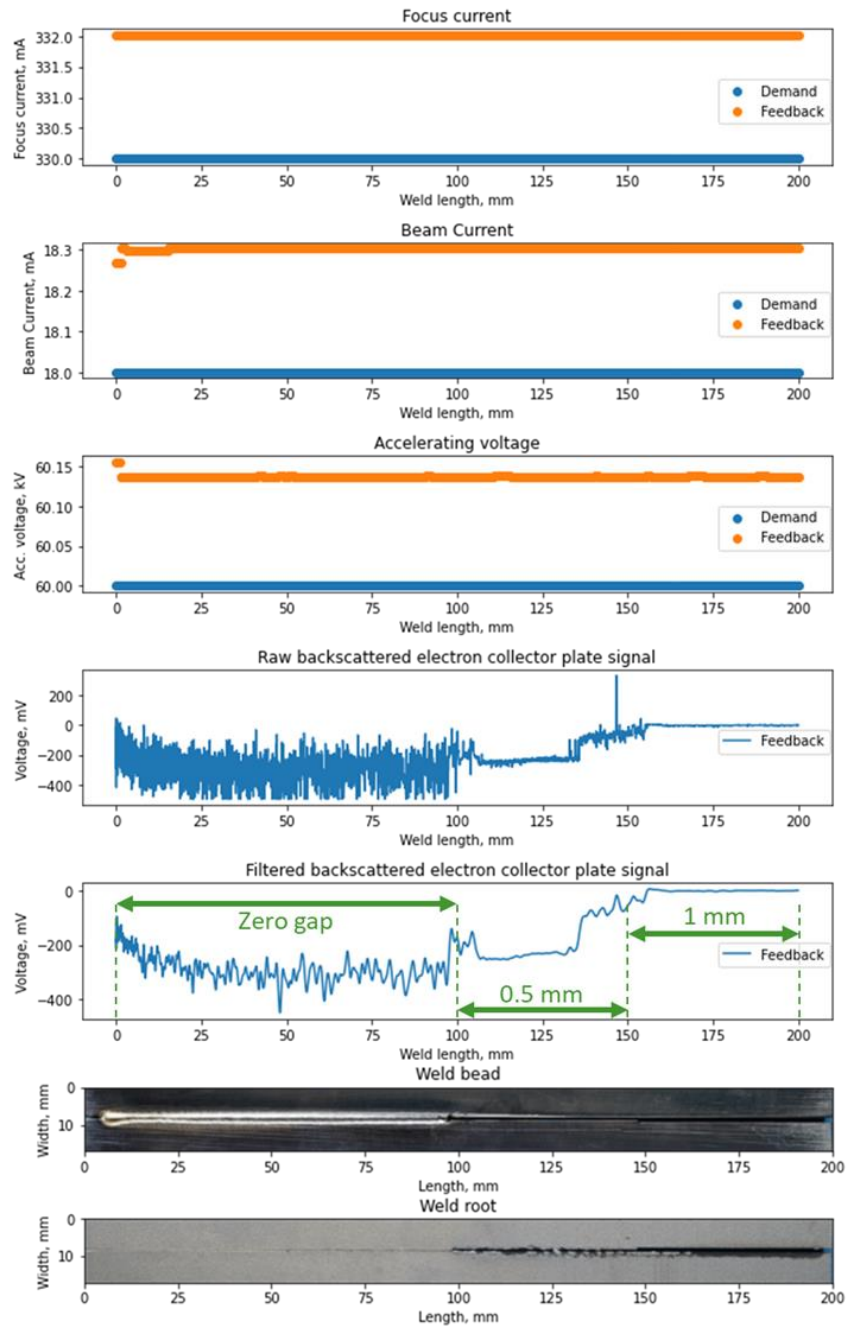


Figure 68: Example of BSE signal (raw and filtered) plotted against PLC signal (Appendix O). No changes were observed in the welding parameters such as focus current, beam current and accelerating voltage. Green double arrows marking three regions of interest.

These gap defects were picked up by the BSE collector plate signal. As the signal from the BSE collector plate was collected during the time axis (converted to weld length), it was possible to observe the regions of interest at 0-100, 100-150 and 150-200 mm from the weld start location (marked with green double arrows in Figure 68). Those stepwise openings allowed the observation of the effect of joint misalignment during welding on the BSE signal. Readily apparent was the intensity of the BSE signal change with the width of the steps. As the BSE collector plate is connected through a 100-ohm resistor to the ground, voltage values are

negative and increase with the width of the steps. Only one sample, number three (Appendix I), oscillated between positive and negative voltage values, which may be caused by a charged plastic liner (as described in Chapter 3.9.1). Seven of the tested samples showed the same trend, the exceptions were samples number five (Appendix K) and ten (Appendix P). Those samples didn't preserve any trend and showed little reaction to gap changes. In the case of sample number five, it had a low signal level, possibly caused by the combination of the signal source (weld pool geometry), trajectory of the BSE and low resolution of the digital oscilloscope (only 8-bit). In the case of sample number ten, as it was the last sample welded, the noise was added into the signal from other sources, possibly from metal vapour deposited on the surface of the BSE collector. As the raw signals were found to be noisy, a simple Butterworth low pass filter has been used to smooth out the trends.

Following the initial evaluation, samples were cut to obtain longitudinal cross-sections. Then, microscopic images of those sections were plotted against longitudinal cross-section and top-section. This revealed additional defects imprinted on the signal shape. The first defect observed was incomplete fusion, preceding the humping, where the bead height decreased too. This case is visualized in Figure 69. Interesting features, visible on the BSE signal, were related to humping. This periodic occurrence of bead-like protuberances caused by the artificially introduced weld gaps was projected on the signal. As Butterworth low pass filter was used, the pattern of those periodic defects was amplified and easier to notice.

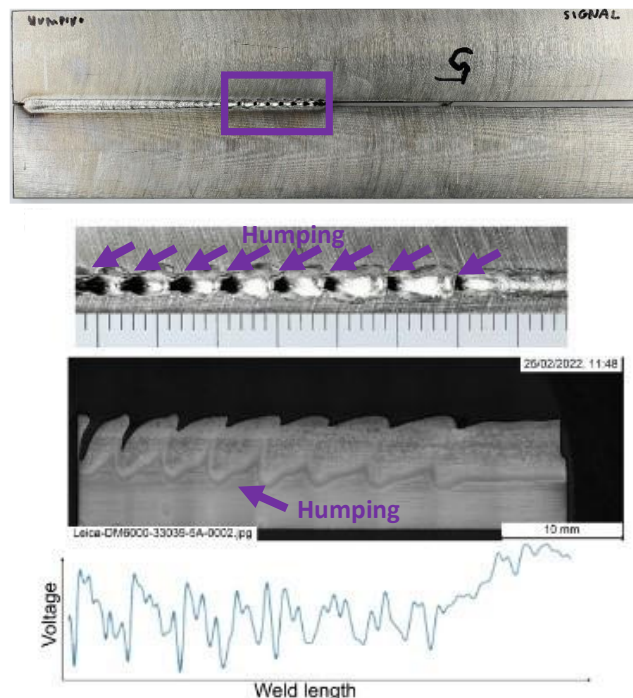


Figure 69: Sample (number eight - Appendix N), weld bead, longitudinal cross-sections and corresponding BSE signal shape (time-shift corrected). Metal leak on the root side. Handwritten markings on the samples are unrelated to the numeration in the thesis.

The second defect observed was related to a metal through the root being solidified in the root area and it is presented in Figure 70. Metal leak may be observed if there is too much molten material trapped in the lower weld zone, either from the sample material or backing material (or both). In this case, the signal drops significantly at the initial location of the metal leak and recovers where it ends. The length of the low signal is corresponding to the length of the metal leak.

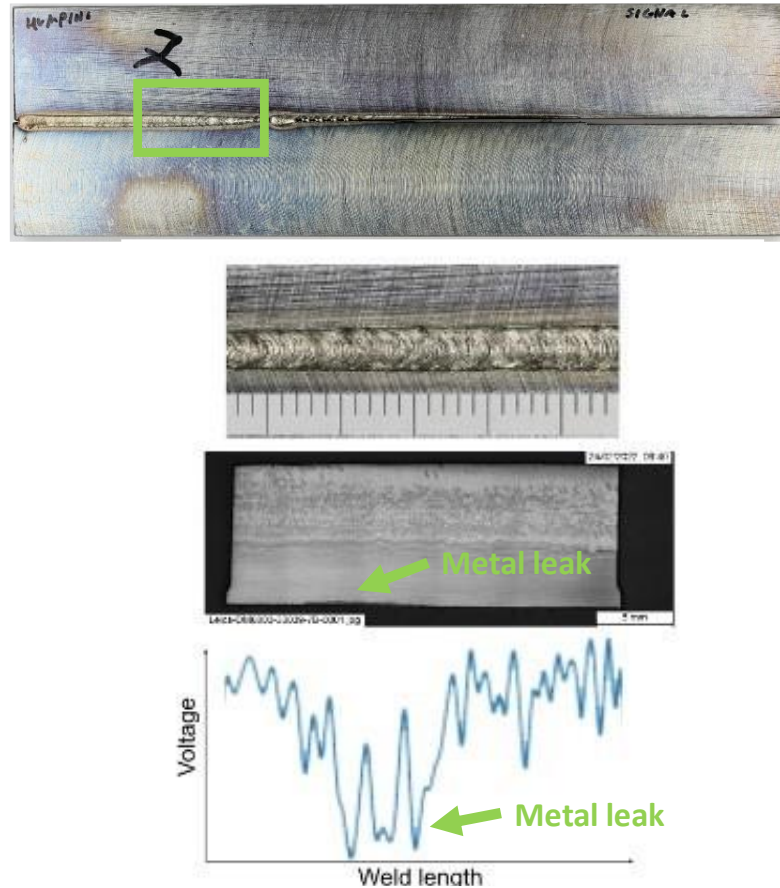


Figure 70: Sample (number ten – Appendix P), weld bead, longitudinal cross-sections and corresponding BSE signal shape (time-shift corrected). Metal leak can be seen on the root side.

The third type of defect, shown in Figure 71, was related to the porosity and was observed as a pore (cavity) with the ejected metal drop trapped afterwards. This ejected metal drop is registered as a sharp negative spike on the signal. The humping defect is also observed and registered as smaller positive spikes in the signal.

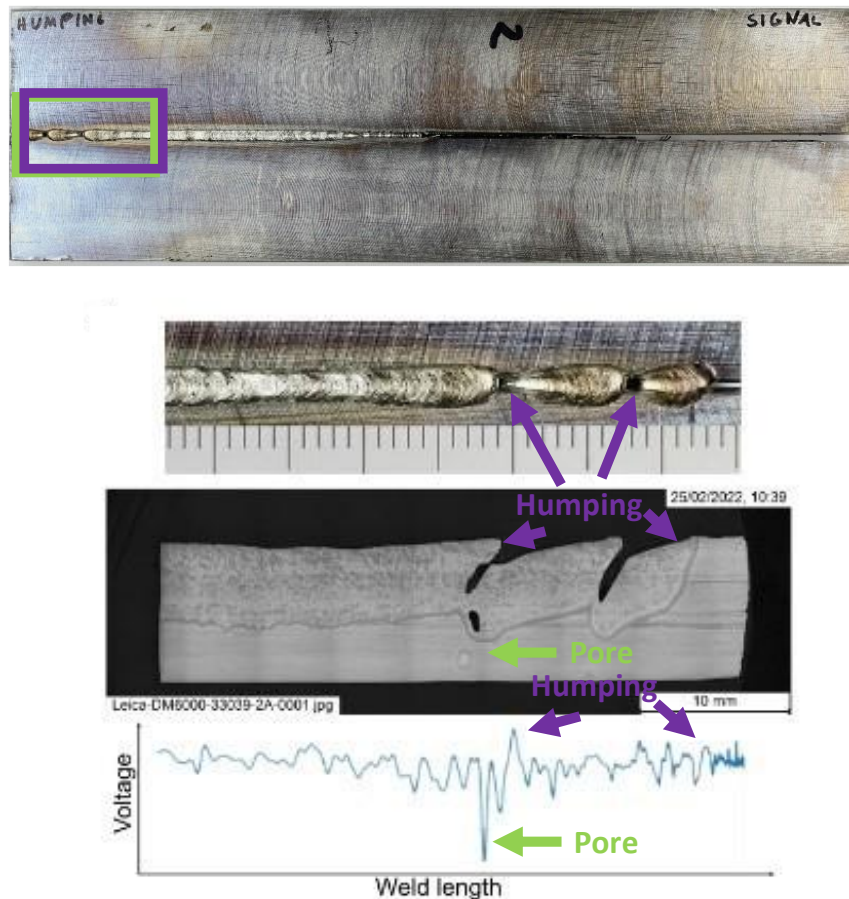


Figure 71: Sample (number five - Appendix K), weld bead, longitudinal cross-sections and corresponding BSE signal shape (time-shift corrected). Humping and visible pore which ejected metal droplet.

The biggest difficulty in analysing BSE signals, for defect detection, was the shape variability of the signal. Similar defects may be registered with different voltage values and polarity, which made signal processing difficult. Although the shape of the waveforms is different between the welds, the trends in the signal were maintained. Humping was registered as a periodic pattern, pores as a sudden spike in the signal and metal leak as a signal drop for the duration of the defect. Those differences between the same defects observed on different welds may be related to the difficulties in reliable measurements due to a metal vapour deposited on the collector plate. Although, as mentioned previously, this dust layer doesn't affect the ability to monitor the welding process (as opposed to the light-optical systems), but still has an impact on the data collected as it changes the degree of absorption of the detector material. If the dust layer is homogeneous, the measurement error will be easier to control, but those deposited layers tend to peel off (Figure 40c) and are prone to oxidation when the vacuum chamber is opened [16].

5.2 HDR camera

Those weld irregularities can be also detected by the camera, which observed a weld pool, aided by image processing tasks. To detect possible deviations of actual process parameters based on the vision system, several machine-vision based algorithms were used to observe the optical emissions. Those image-processing algorithms included: area, luminance, centre of mass, eccentricity, solidity, total image intensity and were also used to verify their usefulness.

Starting with a simple area analysis, it was found that, in the zero-gap region, the weld pool had a symmetrical elongated shape and sharp round partially formed keyhole with the smallest area in pixels. The next region, 100-150 mm, was characterised by the triangular shape of the weld pool with the less intense beam. The third region, 150-200 mm, is where the weld pool is split in two. Additionally, when the humping behaviour was observed, the partially formed keyhole oscillated between all three modes back and forth. These three types of the welding behaviour are summarised in Figure 72.

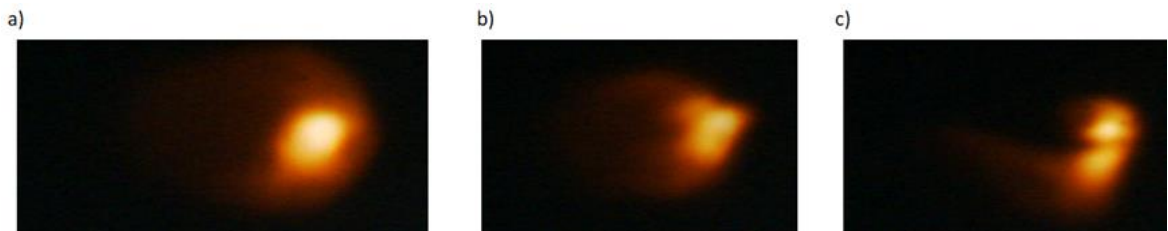


Figure 72: Three different welding behaviours. a) partially formed keyhole behaviour in the range 0-100 mm (area in pixels 3753), b) weld pool behaviour in 100-150 mm range (area in pixels 4197), c) weld pool behaviour in 150-200 mm range (area in pixels 4361).

In terms of the intensity of the images, the highest luminance value was observed for the 0-100 mm welding region. In the 100-150 mm section, the intensity dropped significantly, and rose again in the 150-200 mm region with two weld pools. This phenomenon is presented in Figure 73. However, if there is no beam split in the 150-200 mm region, the intensity may stay on the same level as the 100-150 mm region or drop further down. And similarly, if the split occurs in the 100-150 mm zone, the intensity may be higher than in 0 – 100mm.

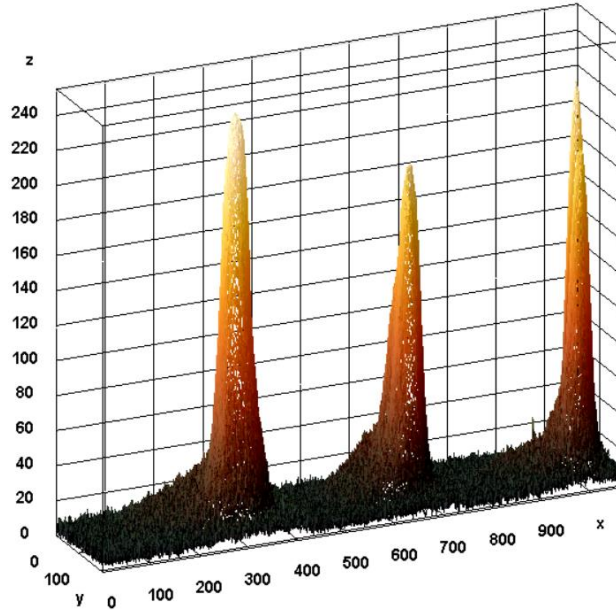


Figure 73: Three different weld pools behaviours plotted as 3D surface plots. X and Y axis correspond to the resolution of the image in pixels, and Z is interpreted as height for the plot based on the luminance as 0-255 pixel value (grid size is 1024 pixels). From left to right are visualised the welding sections: 0-100 mm, 100-150 and 150-200 mm.

This two weld pools region was highly dependent on where the split happened. In general, the weld pools with the split closer to the one of the edges of the workpiece had higher intensity than the ones which were split by the gap. Selected cases of split locations are shown in Figure 74.

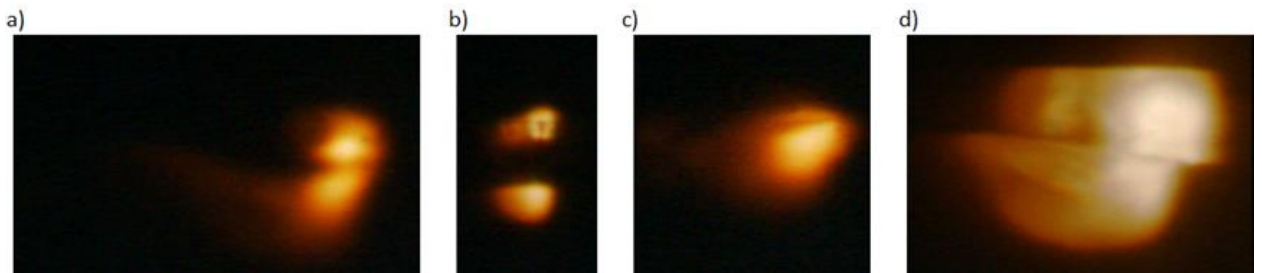


Figure 74: Different weld pool split locations. a) half-half split close to the edge, b) split by the gap, c) split close to the edge, most of the weld pool visible on the top surface of the workpiece, d) split between the gap, weld pool located between two edges and on the workpiece top surface.

The next method to analyse the HDR image data was the use of the centre of mass as the indicator of the weld pool instability. Both, longitudinal and transverse directions, contained enough information to distinguish between three different welding sections: 0-100 mm, 100-150 and 150-200 mm.

The last methods are related to shape descriptors, which are eccentricity and solidity. Shape descriptors are generally sensitive to noise and variations. This results in different results when the shape of the weld pool changes slightly.

To make comparison easier between machine-vision-based parameters, all of the analysed parameters were plotted against each other and an example is presented in Figure 75. Analysis of the camera data, presented in Figure 75, indicated that the process was disturbed, and the position of the weld pool changed due to unstable welding behaviour, as the process was interrupted due to the gap openings (steps). Those stepwise openings are marked with orange arrows in Figure 75.

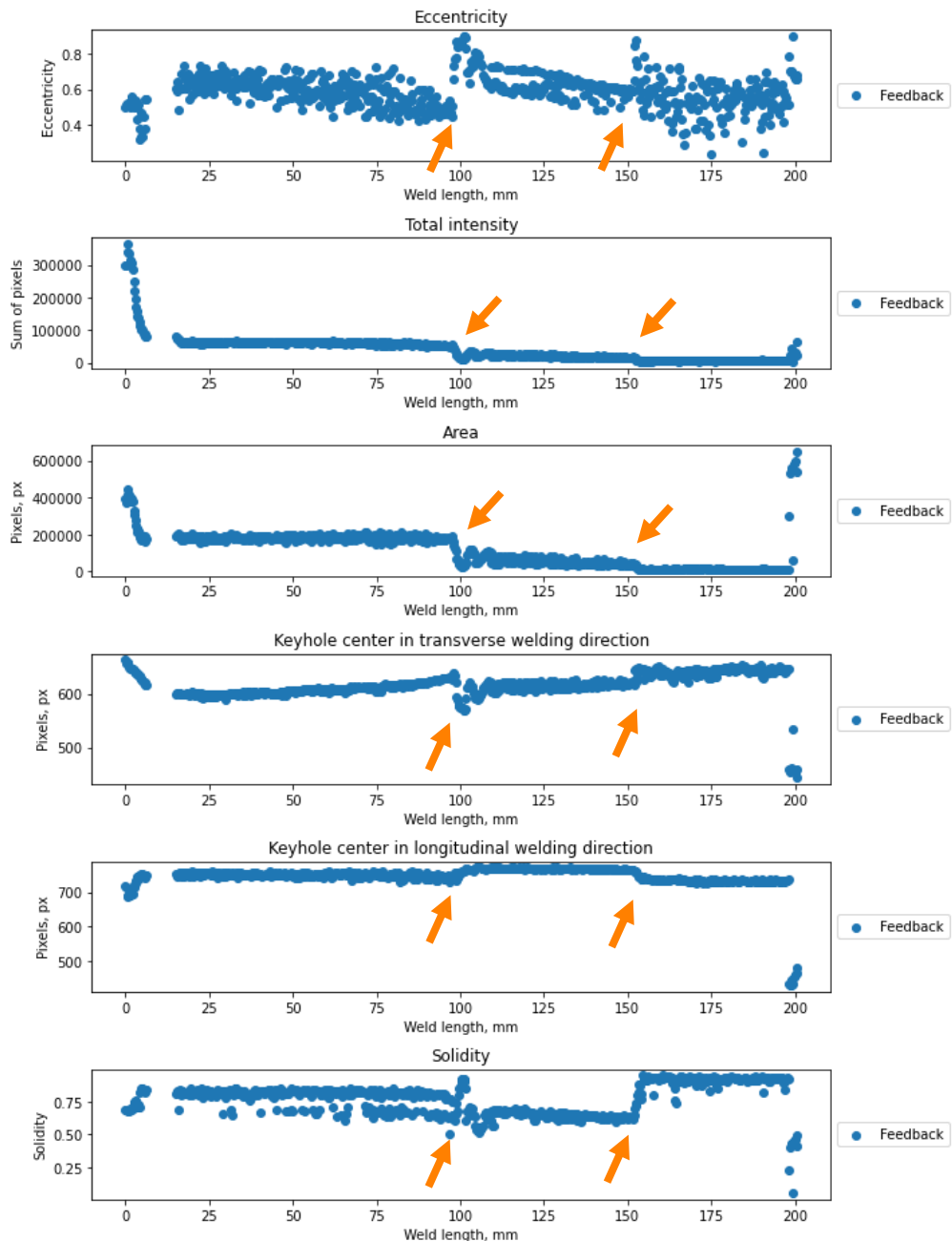


Figure 75: Example comparison of the eccentricity, change of the total intensity, pixel area, centre of mass in transverse and longitudinal welding direction, and solidity. Locations of observed changes are marked with orange arrows. All welds can be found in Appendices G-P.

In terms of the comparison between BSE and camera data, it was found that the camera can detect only defects on the weld surface. Any imperfections below the surface are not registered unless the formation of the defect is accompanied by changes in the weld pool shape. As presented in Figure 76, porosity inside the weld wasn't registered on the camera data as it is created below the top weld surface. However, this defect appears in the BSE collector plate signal as a clear spike.

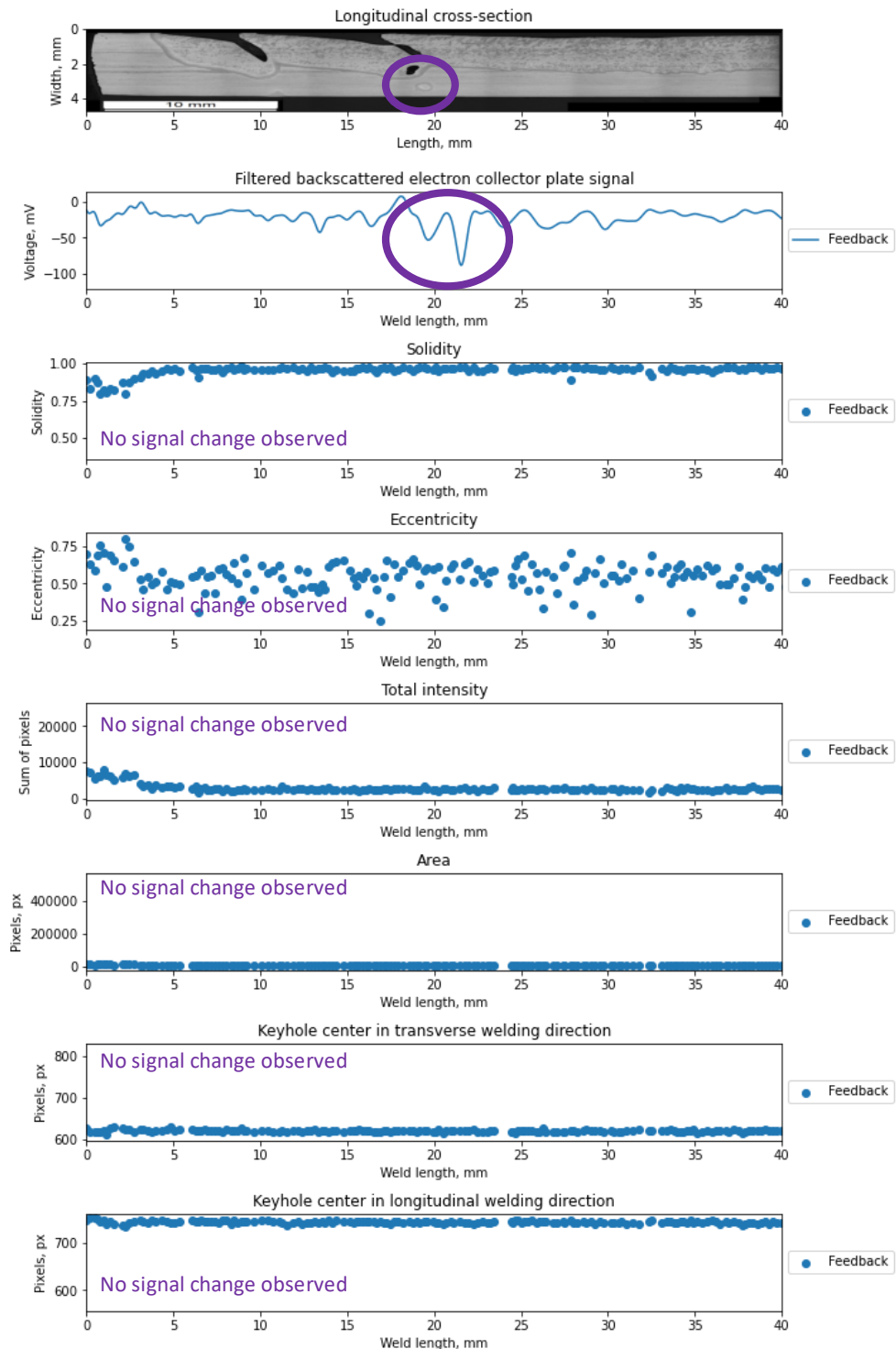


Figure 76: Comparison between BSE signal and camera data for visible pore which ejected metal droplet. Purple circle mark the location of the defect.

5.3 Time series imaging

As the purpose of the experiment was also to verify the feasibility of encoding BSE signals to time series imaging methods, GAFs were initially selected to verify the features between the three steps. An example of different encoding methods plotted against different weld sections is presented in Figure 77. During the stable welding region (no gap) the GAFs pattern was scattered evenly across the image. When the beam was melting the edge of the joint (0.5 mm gap), the pattern was focused more in the centre. And finally, when the beam reached a 1 mm gap, it was not able to penetrate or melt the joint anymore due to the width of the gap, the GAFs lines in this case were further focused into the centre in the form of “bars”. In the case of the MIX encoding, it combines three encoding methods at the same time, where the red layer is GAF, the blue is MTF and the green is RP.

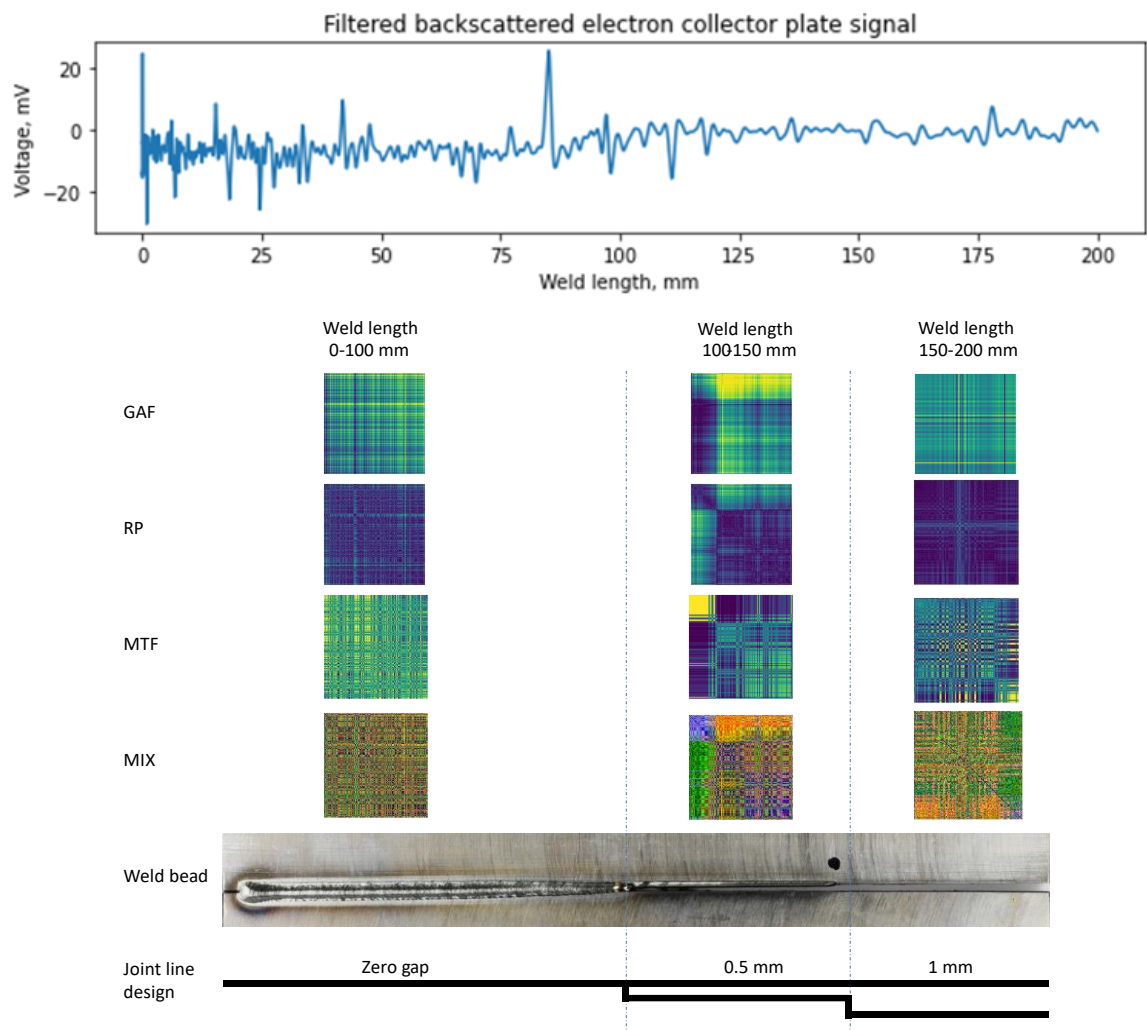


Figure 77: 4x3 matrix representing different encoding methods for different weld sections and their location corresponding to weld bead. The top of the image presents a filtered BSE collector plate signal.

The experimental results indicate that the GAF encoding method is capable of preserving the existing correlation between joint misalignment and BSE signal. All

three weld regions carried enough features to distinguish three different welding regions, i.e. no gap, 0.5 mm and 1 mm gap. In particular, regions shown in Figure 78, are indicating if the signal rise or falls. For step change, which is a misalignment defect, the time-series image is divided into four regions. In the case of the rising signal and GAF images, the yellowish (pseudo-colour) part of the image was located in the top right corner. Similarly, in the case of the falling signal, the yellowish part of the signal was located in the bottom left corner.

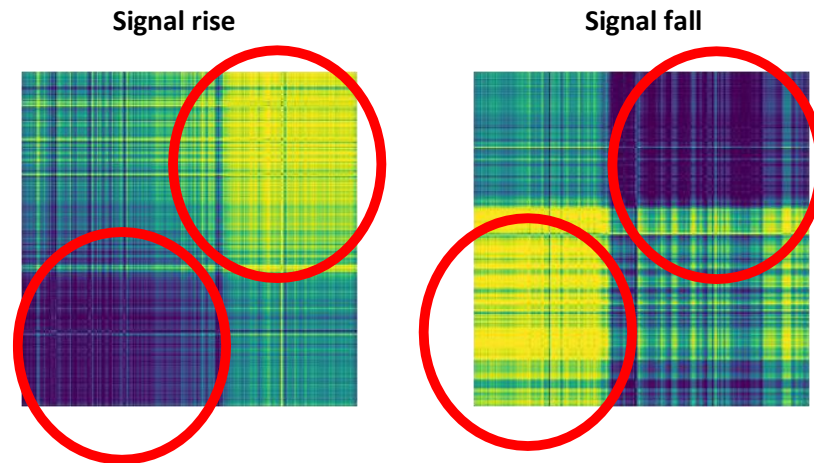


Figure 78: Region of interest, marked in red circles, in GAF encoded signal for rising and falling signal.

In a situation, if there is a pore or metal leak registered on the BSE signal, this sudden spike is registered as two thick crossing lines and it is presented in Figure 79. The location of those lines is the same as the location of this sudden spikes and line thickness depends on the size of the spike. The thickness of the lines corresponds to a bigger spike.

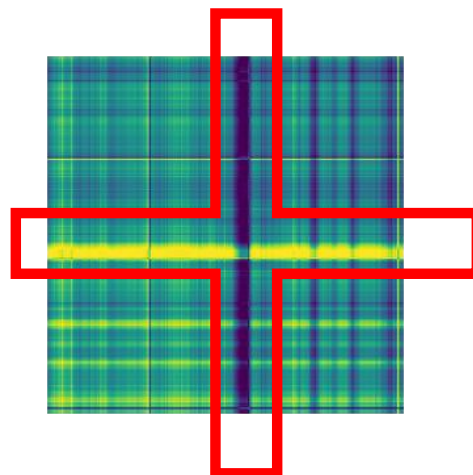


Figure 79: Features of interest, marked in the red cross, in GAF encoded signal for the spike in the signal.

Lastly, the expected images for stable welding conditions are presented in Figure 80. These images mainly consist of noise and no apparent features can be

highlighted. The amount of thin lines depends on the amount of noise – less noisy images have fewer lines.

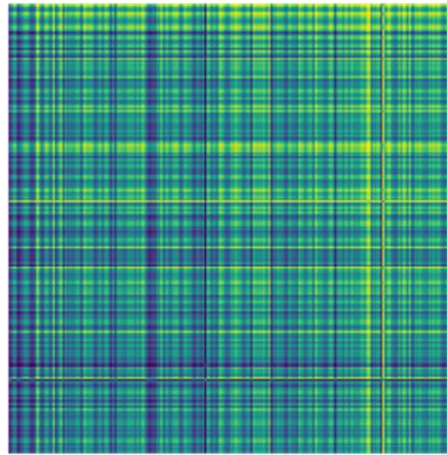


Figure 80: Stable welding conditions. No apparent features in the image.

The main difference between image acquisition and BSE signal data was the size of the files. The uncompressed frame was around 2 MB of data and in the case of the BSE signal, it was 150 KB for the whole welding process. So, for 700 images captured over the entire weld length (captured with 29 FPS), the amount of data collected was around 1.4 GB, which required ~9333 times more space when compared to the BSE signal file. The smaller size of the BSE data can help overcome the challenges of big data storage, as we can get the same amount of information as from the camera, but in the optimised form. This means four orders of magnitude lower data storage requirement. The BSE signal is also capable of registering the welding defects such as humping, where the shapes and location of humps are projected onto the BSE signal amplitude.

However, data analysis of the signal collected from BSE collector plate is limited by a number of issues. The first noticeable issue is the signal noise. The recorded signal is negative, as BSE electron are negatively-charged, but the signals oscillates heavily (differences as much as 200 mV). These fluctuations may be due to the positively charged ions from plasma, which contains an equal number of positively and negatively charged particles. Once plasma-generated positively charged particles hit the BSE detector, at the same time as negative electrons, it will lead to phase cancellation. This uncontrolled noise made data analysis more difficult, especially finding the differences and location of the gaps. Implementation of the Butterworth band-pass filter helped with flattening out the signal response in the gap areas, but the signal in the stable welding region (no gap) was still heavily influenced by the oscillations. Some of these oscillations, in the no gap zone, were caused by defects such as humping and porosity. However, the longitudinal cross-sections revealed that only the biggest oscillations are related to welding imperfections and the smaller oscillations are the residues from the noise. This may be explained by the amount of the vapour-plasma plume, which is the biggest at the no gap region (transition keyhole welding mode), and the keyhole became progressively smaller with the gap openings (conduction welding mode). The bigger EB-induced plasma plumes have more ions, whose amount increases the

probability of hitting the BSE collector. As plume size depends highly on the mode of the welding, BSE collector can distinguish transitions between the different welding modes. This may not be always accurate as the backing material below the workpiece, if it differs from parent material and is unexpectedly hit by the EB, may suddenly increase or reduce the number of backscattered electrons and distort the signal. This may hide the information about the gap or keyhole mode change, but still will retain information about the stability of the process.

The last issue is related to the deposition of the metal vapours on the BSE collector surface and the risk that it may become conductive. During the experiments, between the weld passes, the BSE collector has been assessed visually and by observing the data collected to ensure the stability of the data collection process. It was noticed that the collector surface exhibited some level of self-cleaning as deposited metallic layers peeled off from the detector surface on a regular basis.

An evaluation of the BSE signals relative to the welding defects revealed that effects such as porosity and humping can be detected. Single occurrence of the imperfection, either porosity or material leak, is accompanied by weld pool instability. These instabilities, including keyhole fluctuation, collapse, bubble grow and shrinkage, lead to the change of the emitted ions from plasma plume and thus it is observed as a sharp spike in the signal. Detected pore diameters are in range 1.5 to 4 mm, and material leak height is in range from 1 to 3 mm. Periodic imperfections, such as humping, are represented by evenly spaced spikes in the signal. Due to the noise, this pattern starts to slowly fade towards the decreasing defects size and there is a risk that noise may obscure the information. Detected humping depths are in the range between 1 to 5 mm.

Regarding the HDR camera recordings, which consumes more computing power and computer data storage than BSE signal, observed parameters contained enough information to distinguish between three different gap sizes. Those measured parameters included area, weld pool centre in longitudinal and transverse direction, eccentricity, total intensity and solidity. All had periodically gaps in the displayed signal due to the large magnitude of change exceeding capabilities of the data analysis code. This was found to be helpful, as those changes were mostly observed on the boundary regions of the welding zones and easily pointed to where instability occurred. The eccentricity parameter has been found as the one with highest variance: over 50% from the mean. The next signal with high variance is solidity, with appx. 10% variance. Both of them are shape descriptors. As the instable weld pool changed the shape rapidly and the beam split on the edge of the workpiece, those parameters were most susceptible to register big changes. Area and total intensity measurements have been found to give similar outputs to each other, but the changes are much more visible on total intensity plots. Regarding the weld pool centre measurements, most of the time longitudinal and transversal directions look inverse to each other. However, transversal measurements look exaggerated. The reason of the similarity between them, and transversal direction measurements becoming more sensitive to changes, is the beam “jumping” between the workpiece edges. This phenomenon is illustrated in Figure 81.

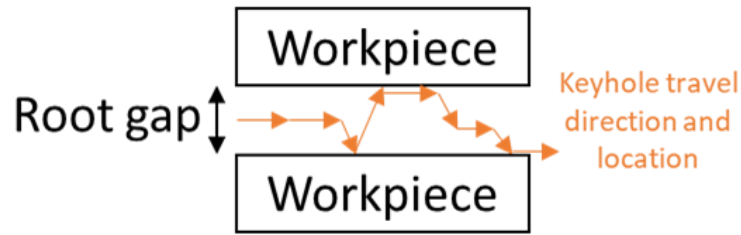


Figure 81: Weld pool travelling between two workpiece edges.

This effect is easily noticeable when the weld pool split in two and is registered on the plots as two datapoints at the same time. An example of such behaviour is shown in Figure 82. Defects detection, other than welding process instability, due to the amount of noise in the data, is not possible. Furthermore, it is not possible, as opposed to the BSE signal, to detect any defects below the weld bead surface.

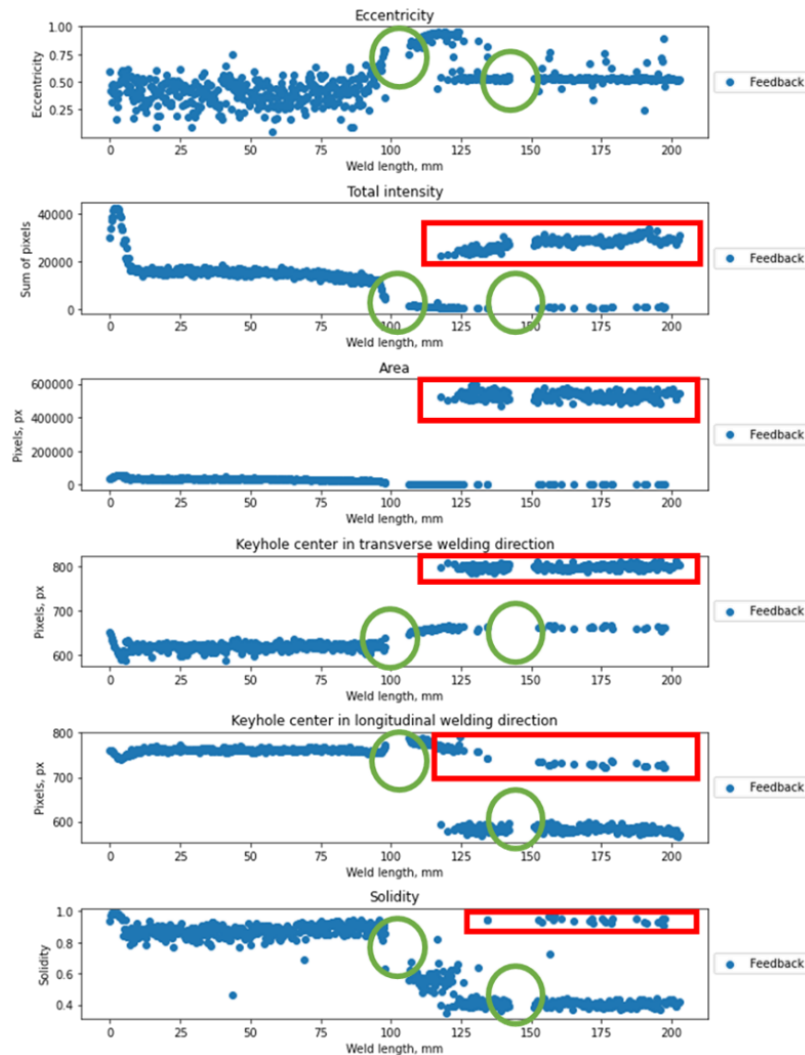


Figure 82: Weld pool split (marked green) visible on the signal and gaps (marked red) in the signal due to the code limitations.

Encoding BSE signals as time-series images, by simply splitting signal in 0-100, 100-150 and 150-200 mm regions based on welding speed and signal recording time, allows to observe easily the changes in the signal. By just visual observation it is easy to distinguish different welding modes in three different regions, but it is not possible to distinguish specific defects.

5.4 Summary

Both BSE and HDR camera monitoring can detect surface imperfections. The camera can monitor well any weld pool instabilities, and therefore process stability, but this doesn't always mean the occurrence of defects. On the other hand, the BSE collector can also register process stability and defects occurring below the weld bead plane. Both of the signals were found to be noisy and in the case of a BSE signal, a Butterworth low pass filter smoothens out the noise clearly enough to see the patterns in the signal. Due to the high acquisition rate of the USB oscilloscope used to collect the BSE signal, it was possible to detect quick changes in weld pool condition and therefore humping defects. In comparison, the HDR camera data acquisition rate was much lower and overall registered images used more storage space. On top of that, HDR images require more processing, as each image needs to be analysed separately to obtain the centre of mass and shape descriptors, further increasing processing time.

Despite a lot of benefits of BSE signal collection, there are two risks. First of them is related to the variability of the signal shape, which makes data analysis difficult. This can be partly mitigated if the algorithm or operator looks for sharp peaks and sudden changes in the signal, but if the registered change is smaller than the noise floor, it may be easily overlooked. The second risk is related to the time interval and there is a danger that the welding process is not sampled for enough time and therefore potential defects can be missed. The signal was able to register porosity defect as small as 1 mm, but due to the slight time shift caused by the triggering system and the slightly delayed signal response, the actual interval window should sample a minimum of 5mm of the signal. This included delayed response time, acquisition trigger delay and the defect itself. The main benefit of the usage of BSE monitoring may be a quality check before NDT quality control. If there is any suspicion of weld defects based on the BSE signal, then the weld may be discarded before time and cost-consuming 100% (percentage of inspection of weld) ultrasonic or radiographic testing. Additionally, BSE signal analysis can indicate the possible location of the defect and there may be possible to attempt repair in this region or help with the decision to discard the part.

6 Conclusions

This thesis developed novel QC tools for monitoring the stability of electron beam welding with the assistance of a 4-slits beam probing technology, HDR camera and BSE collector. This research provides a promising approach for quality assurance in EBW, which could lead to higher weld integrity and reduce the amount of manual work. The research contents include beam characterisation using AI tools, BSE collector design and deployment, BSE signal analysis to find defects and welding process instabilities, image analysis of the weld pool behaviour and data visualisation.

In this research, it was found that cameras, BSE collectors, beam probing and ANN can be applied in QA/QC of the EBW process, but those had several difficulties during the implementation step. Therefore, in this thesis, the focus was on proposing updated methods in terms of equipment and data analysis, to overcome those challenges.

The camera system introduced in this study was equipped with an HDR sensor. By using a modern HDR welding camera, it was possible to detect small changes in the weld pool and extract the shape parameters, which can be used later for monitoring the stability of the welding process. Although the real-time monitoring capability was not met in this thesis, it is believed that such capability can be delivered in the future. It will require utilising multiprocessing and a more efficient programming language than Python (e.g. C++).

As BSE monitoring is the oldest process monitoring concept in the EBW, it also benefited from the utilisation of a modern USB digital oscilloscope. The problem found in the literature review was related to the analysis of BSE signal perturbations to welding defects. This thesis made a successful attempt to find relationships between signal and imperfections such as pores, metal leaks and humping with millimetre accuracy. By comparing the camera system and BSE collector, it was found that the BSE signal contains more information and it is easier to store and process. An added benefit of the BSE signal is that it can register defects occurring below the weld bead plane, as BSE can be reflected back from the weld root to the sensor, whereas camera data may not have enough resolution or visibility to register them. An interesting feature of the BSE signal is that it can register the frequency and size of humping, so the signal follows the observed pattern in welds' longitudinal cross-sections. It was also proven that 2D time-series encoded BSE signal carried enough information to be distinguished visually, and potentially with a larger dataset, can be used as an input image for deep learning models. Due to the low processing requirements, BSE monitoring is believed to be easier to implement in real-time than camera systems, as it required ~9333 times less storage space as opposed to the images.

The biggest area of EBW quality improvements is the usage of neural networks. The previous studies mostly focus on the simulation part of the AI tools to predict welding parameters, shape, penetration depth, defects, weld pool dimensions and temperature profiles. One of the scholarly works presented a method of automatic EB focusing, using EBW parameters combined with secondary emission measurements, to describe the focus position of the EBAZ to the workpiece surface. In this thesis, a simpler approach has been chosen to reduce manual work traditionally needed by the operator, which is either observation of the bright spot on the workpiece surface or utilisation of the beam probing and taking a few measurements of the beam to find the beam caustic. To simplify this process, the 2D time-series encoding of a 4-slit probe signal was introduced and, using AI tools, it was verified that it can distinguish between different focus states of the beam. The tool was created to take only a single BeamAssure measurement and predict how much the beam is out of focus. The simulated results showed a good agreement with beam caustic. Additionally, the model can generalise well, as it was tested with the newly developed 17-slit probe in TWI and the model still retained high accuracy. The biggest advantage of using the AI tool for a 4-slit beam probe is that the information about the beam focus state can be extracted from just one image. In the case of the 17-slit probe, it reduced the required signal processing time from 3.41 to 0.003 seconds, by replacing the time-consuming CT reconstruction of the beam with time-series image encoding.

By now, a clear set of methods for QA/QC of EBW has been drawn:

- Ensuring that the beam is properly focused, using the tool developed in this thesis, to save time over the traditional beam measurement pipeline.
- Using an HDR camera system to collect data about the process stability. On top of that, a BSE collector can be used to detect possible defects.
- Using longitudinal cross-sections to verify the BSE collector signal with the expected outcomes.

In the case of the BeamAssure probe supported by AI tools, based on the size of the dataset and degree of achieved generalisation, it can be concluded that the focus state prediction model is robust and can be used in real industrial productions to save time and allow a less-experienced operator to quickly achieve sharp EB focus conditions. Therefore, 2D time-series encoding is recommended for BeamAssure probe data as the achieved accuracy of the models was high, with the focus on mixing different encoding methods on the same image to achieve the highest possible accuracy (98.22% with data augmentation). In the case when the focus label needs to be classified within the 10 mA range, the model achieved 87.51% accuracy. The model has also great potential for real-time implementation as the inference time using GPU is 65ms.

In the case of the BSE collector and camera, the methods described in the thesis have been tested only for a limited dataset and had not been verified by another material. However, the collected data and analysis methods, including BSE signal processing, would be a good reference for future monitoring sensors. Based on the

limited dataset, experiments showed that it is possible to observe process stability with an HDR camera and additionally track possible defects with a BSE collector.

In conclusion, the QA/QC methods introduced in this thesis are promising to be applied in industry to achieve high weld quality and reduce the time needed for welding set-up and quality control.

7 Future work

Considering the results obtained in previous sections and the subsequent discussions, a collection of recommendations has been formulated that could further enhance knowledge. In case of the beam focus identification, only ResNet neural networks were explored. There is a chance that there are other CNN architectures which may perform better than ResNet for time-series images classification, and those may include diffusion models and variational autoencoders.

Regarding BSE monitoring, to automate the recognition of the actual condition of the process, the signal from the BSE collector plate needs to be continuously optimised for each new welding condition. Usage of neural networks with open-loop training or expert systems looks like a promising solution. However, their main disadvantage is that they require updating the dataset each time welding conditions change, which may be time-consuming and they are vulnerable if the material type or welding parameters are changed. This also contradicts the whole idea of using a neural network to create a model which generalises well and further training has no effect. On the other hand, usage of unsupervised learning method may lead to unpredictable results, which are difficult to understand and measure.

As the general process stability can be monitored using a BSE collector, the main problem of the BSE detector is that in many cases there is no clear correlation between the captured BE signal and the existing defects. This can partly be mitigated by the usage of a high dynamic range camera, which provides a higher spatial resolution capable of registering EBAZ and adjacent areas but at the cost of higher computing power usage. When considering cameras, it is also important to maintain high temporal resolution, as the events during electron beam welding are quick.

Worth mentioning that the workstation used in this work was configured to be used over the Internet network (data collection and analysis) and this approach is called cloud computing. In case of insufficient Internet connection speed and concerns about cloud systems data security, data can be stored and analysed locally. This approach is called edge computing and it is driven by development of hardware accelerators specialised in deep learning tasks (Intel Compute Stick, NVIDIA Jetson and Google Coral). However, the local systems can be still vulnerable to cyber-physical attacks, but if the system is properly implemented the hacking risk can be greatly minimised. As electron beam welding is used for confidential projects in aerospace and defence industries, any insecure data transfer poses a possible risk of leaking the manufacturing data to competitors or

enemies. For this reason, any further work in this area should focus on exploring edge computing and secure communication protocols to protect confidential data. BSE signal, as verified in the Chapter 5, already provide the benefit of reduced amount of data in contrast to the camera images. This means that BSE signals are less susceptible to data leaks as they can be transferred quicker. Additionally, once signals are encoded to time-series imaging, it is not possible to decode the images without data loss, which adds additional layer of protection.

The tools developed in this thesis didn't focused too much real time feedback loop and feeding the data to the welding personnel. The future opportunity is to improve real time capability of the developed tools. This can be achieved by implementing faster data communication protocols (including higher buffer size) between the EBW machine and PC. Besides the hardware improvements, the code itself can be further optimized to use multithreading and multiprocessing. Additionally, in combination with the real-time data processing, user interface is a key area for development. Increased usage of augmented and virtual reality, driven by development of products such as Google Glass and Microsoft HoloLens, is believed to further improve virtual experience. Machine maintenance using augmented reality will lead to faster problems diagnosis with less time spend identifying relevant components of the welding machine – for example in case of the filament break or vacuum pump failure.

8 Bibliography

- [1] Schultz, H. (1993). *Electron beam welding* (Vol. 93). Woodhead Publishing.
- [2] Böhm, S. (2014). *The electron beam as a welding tool: German study on the state of the art and future requirements*. International Institute of Welding, Commission IV-Power Beam Processes Annual Assembly.
- [3] Krüssel, T., & Orlick, H. (2013). *Person for Electron Beam Welding - A Basic Course for Operators, Work Planners and Engineers according to DVS Guideline 1199*, Proceedings of the 9th International Conference Beam Technology.
- [4] Ledford, C., Tung, M., Rock, C., & Horn, T. (2020). Real time monitoring of electron emissions during electron beam powder bed fusion for arbitrary geometries and toolpaths. *Additive Manufacturing*, 34, 101365.
- [5] Bocharov, A. N., Murygin, A. V., & Laptinok, V. D. (2018, November). Calculating the geometric parameters of the distribution of electron beam energy density on its section in EBW. In *IOP Conference Series: Materials Science and Engineering* (Vol. 450, No. 3, p. 032010). IOP Publishing.
- [6] Kaur, A. P. (2016). *Electron beam diagnosis for weld quality assurance* (Doctoral dissertation, Brunel University London). <http://bura.brunel.ac.uk/handle/2438/13436>
- [7] Elmer, J. W. (2009). *Characterization of defocused electron beams and welds in stainless steel and refractory metals using the enhanced modified faraday cup diagnostic* (No. LLNL-TR-410110). Lawrence Livermore National Lab.(LLNL), Livermore, CA (United States).
- [8] Giedt, W. H., & Tallerico, L. N. (1988). Prediction of electron beam depth of penetration. *Welding journal*, 67(12), 299-305.
- [9] Nunn, M. *Electron Beam Probing to Ensure Product and Process Integrity*, TWI Ltd presentation. Retrieved from https://www.researchgate.net/publication/267901360_Electron_Beam_Probing_to_Assure_Process_and_Product_Integrity
- [10] American Welding Society (AWS). (2013). *Recommended Practices for Electron Beam Welding and Allied Processes: AWS C7.1M/C7.1:2013* (4th Edition). American Welding Society (AWS). Retrieved from <https://app.knovel.com/hotlink/toc/id:kpRPEBWAP4/recommended-practices/recommended-practices>

- [11] Abdul Jawwad, A. K., Strangwood, M., & Davis, C. L. (2003). The role of the slope out region on fatigue crack initiation in electron beam welded waspaloy. *Metallurgical and Materials Transactions A*, 34(8), 1637-1645.
- [12] A.J. Dack (2011), Introduction to the Measurement of the Quality of Electron Beams. TWI Industrial Member Report Summary 1009/2011.
- [13] Elmer, J. W., Giedt, W. H., & Eagar, T. W. (1990). The transition from shallow to deep penetration during electron beam welding. *Welding journal*, 69(5), 167s-175s.
- [14] Burgardt, P., Pierce, S. W., & Dvornak, M. J. (2016). Definition of beam diameter for electron beam welding (No. LA-UR-16-21655). Los Alamos National Lab.(LANL), Los Alamos, NM (United States).
- [15] Elmer, J. W., Teruya, A. T., & O'Brien, D. W. (1993). Tomographic imaging of noncircular and irregular electron beam current density distributions. *Welding Journal(USA)*, 72(11), 493.
- [16] T B Layzell (1995), An Improved Backscattered Electron Vision System for High Power Electron Beam Welding Operation. TWI Industrial Member Report Summary 529/1995
- [17] Trushnikov, D. (2013). Electron Beam Welding In-Process Control and Monitoring. In *Proceedings of International Conference on Applied Innovation in IT* (Vol. 1, No. 1, pp. 1-6). Anhalt University of Applied Sciences.
- [18] Elmer, J. (2008). Standardizing the art of electron-beam welding. Lawrence Livermore National Laboratory. Consultado el, 16.
- [19] Hiramoto, S., Ohmine, M., & Sakamoto, M. (1991). Development of an automatic beam focus system for electron beam welding. *Welding international*, 5(10), 763-768.
- [20] Warren H. Giedt, Richard Campiotti. Method of automatic measurement and focus of an electron beam and apparatus therefor. Patent Application No. US5483036A. October, 1993.
- [21] John Elmer, Todd Palmer, Alan Teruya. Automatic focusing of electron beams using a modified Faraday cup diagnostic. Patent Application No. US20070210041A1. March, 2006.
- [22] John W. Elmer, Alan T. Teruya, Dennis W. O'Brien. System for tomographic determination of the power distribution in electron beams. Patent Application No. US5382895A. December, 1992.

- [23] Koleva, E., Mladenov, G., Todorov, D., Koleva, L., & Kardjiev, M. (2016, March). Electron beam characterization by a tomographic approach. In *Journal of Physics: Conference Series* (Vol. 700, No. 1, p. 012013). IOP Publishing.
- [24] Kaur, A., Ribton, C., & Balachandaran, W. (2015). Electron beam characterisation methods and devices for welding equipment. *Journal of materials processing technology*, 221, 225-232.
- [25] Palmer, T. A., Elmer, J. W., Nicklas, K. D., & Mustaleski, T. (2007). Transferring electron beam welding parameters using the enhanced modified faraday cup. *WELDING JOURNAL-NEW YORK-*, 86(12), 388.
- [26] Volker A., Clauss U. et al. (2011). *The fundamentals of a fascinating technology., Probeam.*
- [27] Dack, A. J., and M. Nunn. (2013), *Laboratory and industrial validation of electron beam probing equipment. TWI industrial member report summary 1045/2013.*
- [28] A.J. Dack (2011), *Introduction to the Measurement of the Quality of Electron Beams. TWI Industrial Member Report Summary 1009/2011.*
- [29] Ribton, C., Ferhati, A., Longfield, N., & Juffs, P. (2018). Production weld quality assurance through monitoring of beam characteristics. *Електротехника и електроника*, 53(9-10), 231-235.
- [30] Rempe, N., Kornilov, S., Beniyash, A., Murray, N., Hassel, T., & Ribton, C. (2014). Characterisation of electron beams generated by a plasma-cathode gun. In *Eleventh international conference on electron beam technologies*, Varna, Bulgaria.
- [31] Elmer, J. W., & Teruya, A. T. (2001). An enhanced Faraday cup for rapid determination of power density distribution in electron beams. *WELDING JOURNAL-NEW YORK-*, 80(12), 288-s.
- [32] ISO 11146-1/2 (2021) International Organization for Standardization: Geneva, Switzerland.
- [33] ISO 11146-3 (2004) International Organization for Standardization: Geneva, Switzerland.
- [34] Haider, Y., Arif, M., Rahman, N., & Haseeb, M. (2009, December). A prototype system for infrared computed tomography for image reconstruction. In *2009 IEEE 13th International Multitopic Conference* (pp. 1-5). IEEE.
- [35] Elmer, J. W., Vaja, J., & Gibbs, G. (2022). Reduced pressure laser weld comparison to electron beam welds in Ti-6Al-4 V. *Welding in the World*, 66(10), 2053-2071.

- [36] Schwarz, H. (1964). Mechanism of High-Power-Density Electron Beam Penetration in Metal. *Journal of Applied Physics*, 35(7), 2020-2029.
- [37] Tong, H., & Giedt, W. H. (1969). Radiographs of the electron beam welding cavity. *Review of Scientific Instruments*, 40(10), 1283-1285.
- [38] Arata, Y., Abe, N., & Yamamoto, S. (1980). Tandem Electron Beam Welding (Report III): Analysis of Front Wall of Beam Hole by Beam Hole X-ray Observation Method (*Welding Physics, Processes & Instruments*). *Transactions of JWRI*, 9(1), 1-10.
- [39] Fabbro, R. (2010). Melt pool and keyhole behaviour analysis for deep penetration laser welding. *Journal of Physics D: Applied Physics*, 43(44), 445501.
- [40] Fabbro, R. (2010). Physical mechanisms controlling keyhole and melt pool dynamics during laser welding. In *Advances in Laser Materials Processing* (pp. 211-241). Woodhead Publishing.
- [41] Lawrence, J. R. (Ed.). (2017). *Advances in laser materials processing: technology, research and applications*. Woodhead Publishing.
- [42] TsukaMOTO, S., Irie, H., Inagaki, M., & HASHIMOTO, T. (1983). Effect of focal position on humping bead formation in electron beam welding. *Transactions of National Research Institute for Metals*, 25(2), 62-67.
- [43] Sarafan, S., Wanjara, P., Champlaud, H., Mathieu, L., & Lanteigne, J. (2013). Characteristics of electron beam welded CA6NM. *Proceeding of Material Science and Technology*, 720-732.
- [44] Wei, P. S., Chuang, K. C., Ku, J. S., & DebRoy, T. (2012). Mechanisms of spiking and humping in keyhole welding. *IEEE Transactions on Components, Packaging and Manufacturing Technology*, 2(3), 383-394.
- [45] American Welding Society (AWS). (2017). D17.1/D17.1M:2017-AMD2 SPECIFICATION FOR FUSION WELDING FOR AEROSPACE APPLICATIONS
- [46] Society of Automotive Engineers (SAE). (2019) Electron-Beam Welding For Fatigue Critical Applications AMS2680C
- [47] ISO, E. (2001). 13919-2: 2001. Welding-Electron and laser beam welded joints Guidance on quality levels for imperfections Part, 2.
- [48] EN 1011-7:2004-10. Recommendations for welding of metallic materials – Part 7: Electron beam welding.
- [49] American Welding Society (AWS). (2016). C7.3:2016 PROCESS SPECIFICATION FOR ELECTRON BEAM WELDING
- [50] ISO/TR 17671-7:2004 Welding — Recommendations for welding of metallic materials — Part 7: Electron beam welding

- [51] ISO 13919-1:2019 Electron and laser-beam welded joints — Requirements and recommendations on quality levels for imperfections — Part 1: Steel, nickel, titanium and their alloys
- [52] ISO 13919-2:2021 Electron and laser-beam welded joints — Requirements and recommendations on quality levels for imperfections — Part 2: Aluminium, magnesium and their alloys and pure copper
- [53] Society of Automotive Engineers (SAE). (2022) Welding, Electron-Beam AMS2681B
- [54] DVS 3210:2007-07 Prüfverfahren zur Qualitätssicherung von Elektronen- und Laserstrahlschweißnähten (Test procedures for the quality assurance of electron and laser beam welds)
- [55] ISO 15614-11:2002 Specification and qualification of welding procedures for metallic materials — Welding procedure test — Part 11: Electron and laser beam welding
- [56] ISO 15609-3:2004 Specification and qualification of welding procedures for metallic materials — Welding procedure specification — Part 3: Electron beam welding
- [57] Tallman, C. S. (1987). Stereoscopic vision for electron beam welding (No. UCRL-94099; CONF-870372-2). Lawrence Livermore National Lab., CA (USA).
- [58] Mücke, M., et al. "Fast beam deflection - a contribution to quality enhancement in electron beam welding." Proceedings-67th IIW International Conference, Seoul. 2014.
- [59] Sheppard, A. L., & Wolffsohn, J. S. (2018). Digital eye strain: prevalence, measurement and amelioration. *BMJ open ophthalmology*, 3(1), e000146.
- [60] Luo, X., Wang, Z. Y., & Jia, C. B. (2014, October). A Low-Cost Vision System for Open Arc Welding Based on Multi-exposure. In *International Conference on Robotic Welding, Intelligence and Automation* (pp. 273-281). Springer, Cham.
- [61] Huang, Y., & Chen, S. (2019). Key Technologies of Intelligentized Welding Manufacturing: The Spectral Diagnosis Technology for Pulsed Gas Tungsten Arc Welding of Aluminum Alloys. Springer.
- [62] Chen, S. B., & Wu, J. (2009). *Intelligentized methodology for arc welding dynamical processes*. Springer Berlin Heidelberg.
- [63] Xue, B., Chang, B., Peng, G., Gao, Y., Tian, Z., Du, D., & Wang, G. (2019). A vision based detection method for narrow butt joints and a robotic seam tracking system. *Sensors*, 19(5), 1144.

- [64] Zhao, C. X., Van Steijn, V., Richardson, I. M., Saldi, Z., & Kleijn, C. R. (2009). Experimental characterization of GTA weld pool surface flow using PIV. In *Trends in Welding Research 2008: Proc. 8th Int. Conf.* (pp. 201-210).
- [65] Britannica, T. Editors of Encyclopaedia (2023, June 15). welding. Encyclopedia Britannica. <https://www.britannica.com/technology/welding>
- [66] Shcherbakov, A. V., Gaponova, D. A., & Rodyakina, R. V. (2020). Control of Weld Bead Position in Additive Manufacturing Process with Using Backscattered Electrons Collector Signal. *Russian Internet Journal of Industrial Engineering*, 7(2), 3-8.
- [67] Laptенок, V. D., Seregin, Y. N., Bocharov, A. N., Murygin, A. V., & Tynchenko, V. S. (2016, April). System of video observation for electron beam welding process. In *IOP Conference Series: Materials Science and Engineering* (Vol. 122, No. 1, p. 012022). IOP Publishing.
- [68] T.B. Layzell (1994), *Surface Imaging of the Electron Beam Welding Process by Backscattered Electrons*, TWI, Ltd. Industrial Members Report No. 500/1994.
- [69] Mauer, K. O. (1979). Stulego dos of ion current and electron backscattering current in electron beam welding. *ZIS-Mitteilungen*, 21(11), 1299-1312.
- [70] Schiller, S., & VON ARDENNE, T. (1977). PROZESSKONTROLLE DURCH RUECKSTREUELEKTRONEN.
- [71] Sanderson, A., and C. N. Ribton (1988). "NEW DETECTOR DESIGN FOR SEAM TRACKING IN ELECTRON BEAM WELDING." *Power Beam Processing: Electron, Laser, Plasma-arc: Proceedings of the International Power Beam Conference, 2-4 May 1988, San Diego, California, USA*. ASM International.
- [72] Anderl, P., & Scheffels, W. (1992). Process control for electron beam welding. *Rivista Italiana della Saldatura*(Italy), 6(44), 551-557.
- [73] Arnold, C., Pobel, C., Osmanlic, F., & Körner, C. (2018). Layerwise monitoring of electron beam melting via backscatter electron detection. *Rapid Prototyping Journal*.
- [74] Pobel, C. R., Arnold, C., Osmanlic, F., Fu, Z., & Körner, C. (2019). Immediate development of processing windows for selective electron beam melting using layerwise monitoring via backscattered electron detection. *Materials Letters*, 249, 70-72.
- [75] Rodyakina, R. V., A. V. Shcherbakov, and D. A. Gaponova. "Computer simulation of metals ionization process during electron-beam welding." *IOP Conference Series: Materials Science and Engineering*. Vol. 759. No. 1. IOP Publishing, 2020.

- [76] Wong, H. (2020). Bitmap generation from computer-aided design for potential layer-quality evaluation in electron beam additive manufacturing. *Rapid Prototyping Journal*.
- [77] Olszewska, K., & Friedel, K. (2004). Control of the electron beam active zone position in electron beam welding processes. *Vacuum*, 74(1), 29-43.
- [78] Trushnikov, D. N., Mladenov, G. M., & Belenkiy, V. Y. (2013). Controlling the electron beam focus regime and monitoring the keyhole in electron beam welding. *Quarterly journal of the japan welding society*, 31(4), 91s-95s.
- [79] S. Gach, Aachen, S. Olschok, U. Reisgen (2021), Process monitoring in electron beam welding by optimizing the in-process sensor technology by means of backscattered electrons and optical emission, 6th International Electron Beam Welding Conference in Aachen
- [80] Kasitsyn, A. N., Agafonov, R. Y., Leonov, A. V., & Grigoriev, G. V. (2020, February). Control of electron beam welding parameters based on the gap scanning system data during the welding process. In *IOP Conference Series: Materials Science and Engineering* (Vol. 759, No. 1, p. 012013). IOP Publishing.
- [81] Zhang, Q., (2021). Backscatter detection module (U.S. Patent No. US20210141103A1). U.S. Patent and Trademark Office
- [82] Nicholson, W. A. P. (1981). Electron beam current measurement in the electron microscope. *Journal of Microscopy*, 121(2), 141-147.
- [83] Williamson Jr, W., & Antolak, A. J. (1987). Monte Carlo electron backscattering and transmission coefficients for thin aluminum and gold films. *Journal of applied physics*, 61(10), 4880-4884.
- [84] Miller, W. E. (1970). Transmission and backscatter coefficients of 1.0-to 3.0-mev electrons incident on some metals and alloys. National Aeronautics and Space Administration.
- [85] Chen, W., & Shi, K. (2019). A deep learning framework for time series classification using Relative Position Matrix and Convolutional Neural Network. *Neurocomputing*, 359, 384-394.
- [86] Hernández Sánchez, S., Fernández Pozo, R., & Hernández Gómez, L. A. (2019, June). Deep neural networks for driver identification using accelerometer signals from smartphones. In *International Conference on Business Information Systems* (pp. 206-220). Springer, Cham.
- [87] Ahmet Taspinar, A guide for using the Wavelet Transform in Machine Learning, <http://ataspinar.com/2018/12/21/a-guide-for-using-the-wavelet-transform-in-machine-learning/>
- [88] Hermansky, H. (1990). Perceptual linear predictive (PLP) analysis of speech. *the Journal of the Acoustical Society of America*, 87(4), 1738-1752.

- [89] Donner, R. V., Zou, Y., Donges, J. F., Marwan, N., & Kurths, J. (2010). Recurrence networks—a novel paradigm for nonlinear time series analysis. *New Journal of Physics*, 12(3), 033025.
- [90] Campanharo, A. S., Simer, M. I., Malmgren, R. D., Ramos, F. M., & Amaral, L. A. N. (2011). Duality between time series and networks. *PloS one*, 6(8), e23378.
- [91] Chen, J. H., & Tsai, Y. C. (2020). Encoding candlesticks as images for pattern classification using convolutional neural networks. *Financial Innovation*, 6(1), 1-19.
- [92] Damaševičius, R., Maskeliūnas, R., Woźniak, M., & Połap, D. (2018, February). Visualization of physiologic signals based on Hjorth parameters and Gramian Angular Fields. In *2018 IEEE 16th World Symposium on Applied Machine Intelligence and Informatics (SAMI)* (pp. 000091-000096). IEEE.
- [93] Martínez-Arellano, G., Terrazas, G., & Ratchev, S. (2019). Tool wear classification using time series imaging and deep learning. *The International Journal of Advanced Manufacturing Technology*, 104(9), 3647-3662.
- [94] Wang, Z., & Oates, T. (2015, June). Imaging time-series to improve classification and imputation. In *Twenty-Fourth International Joint Conference on Artificial Intelligence*.
- [95] Bragin, A. D., & Spitsyn, V. G. (2019). Electroencephalogram analysis based on gramian angular field transformation. In *CEUR Workshop Proceedings (Vol. 24852019, pp. 273-275)*. Томский политехнический университет.
- [96] Wang, Z., & Oates, T. (2015, April). Encoding time series as images for visual inspection and classification using tiled convolutional neural networks. In *Workshops at the twenty-ninth AAAI conference on artificial intelligence*.
- [97] Liu, L., & Wang, Z. (2018, June). Encoding temporal markov dynamics in graph for visualizing and mining time series. In *Workshops at the Thirty-Second AAAI Conference on Artificial Intelligence*.
- [98] Eckmann, J. P., Kamphorst, S. O., & Ruelle, D. (1995). Recurrence plots of dynamical systems. *World Scientific Series on Nonlinear Science Series A*, 16, 441-446.
- [99] Kantz, H., & Schreiber, T. (2004). *Nonlinear time series analysis (Vol. 7)*. Cambridge university press.
- [100] Liu, S., Zhang, X., Zhang, S., Wang, H., & Zhang, W. (2019). Neural machine reading comprehension: Methods and trends. *Applied Sciences*, 9(18), 3698.

- [101] Krizhevsky, A., & Hinton, G. (2009). Learning multiple layers of features from tiny images.
- [102] Le, Y., & Yang, X. (2015). Tiny imagenet visual recognition challenge. *CS 231N*, 7(7), 3.
- [103] Deng, J., Dong, W., Socher, R., Li, L.-J., Li, K., & Fei-Fei, L. (2009). Imagenet: A large-scale hierarchical image database. In 2009 IEEE conference on computer vision and pattern recognition (pp. 248–255).
- [104] He, K., Zhang, X., Ren, S., & Sun, J. (2016). Deep residual learning for image recognition. In Proceedings of the IEEE conference on computer vision and pattern recognition (pp. 770-778).
- [105] Paszke, A., Gross, S., Massa, F., Lerer, A., Bradbury, J., Chanan, G., ... Chintala, S. (2019). PyTorch: An Imperative Style, High-Performance Deep Learning Library. In *Advances in Neural Information Processing Systems* 32 (pp. 8024–8035). Curran Associates, Inc. Retrieved from <http://papers.neurips.cc/paper/9015-pytorch-an-imperative-style-high-performance-deep-learning-library.pdf>
- [106] Luttrell, J., Zhou, Z., Zhang, C., Gong, P., & Zhang, Y. (2017, December). Facial recognition via transfer learning: fine-tuning Keras_vggface. In 2017 International Conference on Computational Science and Computational Intelligence (CSCI) (pp. 576-579). IEEE.
- [107] Hu, J., Shen, L., & Sun, G. (2018). Squeeze-and-excitation networks. In Proceedings of the IEEE conference on computer vision and pattern recognition (pp. 7132-7141).
- [108] Burkhardt Jr, J. H., Bowers, G. L., Davenport, C. M., Turner, P. C., & Greene, L. M. (1978). Computer automation on an electron-beam welder with automatic, stored seam tracking (No. Y-2114). Oak Ridge Y-12 Plant, Tenn.(USA).
- [109] Petrov, P. (2012). Techniques for on-line monitoring and inspection of electron beam welding process. In Proceedings of the 2nd International Electron Beam Welding Conference, Aachen, Germany, 26–30 March 2012 [German Welding Society (DVS), Aachen, 2012], pp. 114-116.
- [110] Petrov, P., Georgiev, C., & Petrov, G. (1998). Experimental investigation of weld pool formation in electron beam welding. *Vacuum*, 51(3), 339-343.
- [111] Haubold, M. W., & Zäh, M. F. (2019). Real-time spatter detection in laser welding with beam oscillation. *Procedia CIRP*, 79, 159-164.
- [112] Oltean, S. E., & Abrudean, M. (2008). Advanced control of the electron beam welding. *Journal of Control Engineering and Applied Informatics*, 10(1), 40-48.

- [113] Oltean, S. E. (2018). Strategies for monitoring and control with seam tracking in electron beam welding. *Procedia Manufacturing*, 22, 605-612.
- [114] Hayes, B. J., Martin, B. W., Welk, B., Kuhr, S. J., Ales, T. K., Brice, D. A., ... & Collins, P. C. (2017). Predicting tensile properties of Ti-6Al-4V produced via directed energy deposition. *Acta Materialia*, 133, 120-133.
- [115] Kar, S., Searles, T., Lee, E., Viswanathan, G. B., Fraser, H. L., Tiley, J., & Banerjee, R. (2006). Modeling the tensile properties in β -processed α/β Ti alloys. *Metallurgical and materials transactions A*, 37(3), 559-566.
- [116] Sun, Y., Zeng, W., Han, Y., Zhao, Y., Wang, G., Dargusch, M. S., & Guo, P. (2011). Modeling the correlation between microstructure and the properties of the Ti-6Al-4V alloy based on an artificial neural network. *Materials Science and Engineering: A*, 528(29-30), 8757-8764.
- [117] Malik, P., & Agrawal, P. (2010, December). A neural networks based controller for Electron Beam welding power supply. In *2010 Joint International Conference on Power Electronics, Drives and Energy Systems & 2010 Power India* (pp. 1-5). IEEE.
- [118] Shen, X., Huang, W., Xu, C., & Wang, X. (2009, May). Bi-directional Prediction between Weld Penetration and Processing Parameters in Electron Beam Welding Using Artificial Neural Networks. In *International Symposium on Neural Networks* (pp. 1097-1105). Springer, Berlin, Heidelberg.
- [119] Jha, M. N., Pratihar, D. K., Bapat, A. V., Dey, V., Ali, M., & Bagchi, A. C. (2014). Knowledge-based systems using neural networks for electron beam welding process of reactive material (Zircaloy-4). *Journal of Intelligent Manufacturing*, 25(6), 1315-1333.
- [120] Tsonevska, T. S., Koleva, E. G., Koleva, L. S., & Mladenov, G. M. (2018, September). Modelling the shape of electron beam welding joints by neural networks. In *Journal of Physics: Conference Series* (Vol. 1089, No. 1, p. 012008). IOP Publishing.
- [121] Das, Debasish, et al. "Phenomenological model-based study on electron beam welding process, and input-output modeling using neural networks trained by back-propagation algorithm, genetic algorithms, particle swarm optimization algorithm and bat algorithm." *Applied Intelligence* 48.9 (2018): 2698-2718.
- [122] Koleva, L., & Koleva, E. (2017). Neural networks for defectiveness modeling at electron beam welding. *Industry 4.0*, 2(1), 5-8.
- [123] Reddy, D. Y., & Pratihar, D. K. (2011). Neural network-based expert systems for predictions of temperature distributions in electron beam welding process. *The International Journal of Advanced Manufacturing Technology*, 55(5), 535-548.

- [124] Yin, Y., Kennedy, A., Mitchell, T., Sieczkiewicz, N., Jefimovs, V., & Tian, Y. (2022). Electron beam weld penetration depth prediction improved by beam characterisation. *The International Journal of Advanced Manufacturing Technology*, 1-17.
- [125] PLCScanner. <https://plcdataatools.com>. Accessed 29 Nov 2021.
- [126] SNAP7. <https://snap7.sourceforge.net>. Accessed 29 Nov 2021.
- [127] Bradski, G. (2000). The OpenCV Library. *Dr. Dobb's Journal of Software Tools*.
- [128] API design for machine learning software: experiences from the scikit-learn project, Buitinck et al., 2013.
- [129] Xiris WeldSDK. <https://info.xiris.com/weldstudio-sdk-datasheet>. Accessed 29 Nov 2021.
- [130] <https://pixinsight.com/doc/tools/Debayer/Debayer.html>. Accessed 29 Nov 2021.
- [131] <https://docs.baslerweb.com/pixel-format>. Accessed 29 Nov 2021.
- [132] Donachie, M. J. (2000). *Titanium: a technical guide*. ASM international.
- [133] Boshoman, Bonolo S., et al. "Laser Metal Deposition of Titanium Alloy: A Review." *Advances in Manufacturing Engineering: Selected articles from ICMMPPE 2019 (2020)*: 87-95.
- [134] *Electron beam welding best practice guide (2016)*, Electron Beam Processes Ltd, Retrieved from <https://www.ebpglobal.com/wp-content/uploads/2018/09/Best-Practice-Guide-2018.pdf>
- [87] Pinke, P., Caplovic, L., & Kovacs, T. (2011). The influence of heat treatment on the microstructure of the casted Ti6Al4V titanium alloy. *Slovak University of Technology Bratislava. Web*, 11.
- [136] Rajamanickam, T., Muthu, S., Murugan, P., Pathikonda, M., Senthilnathan, K., Raj, N. A. N., & Babu, P. R. (2019). Studies on Fundamental Interaction Parameters for Stainless Steel and Titanium Biomaterials Using Flattened and Un-Flattened Megavoltage X-Ray Beams. *Asian Pacific Journal of Cancer Prevention: APJCP*, 20(8), 2485.
- [137] Verhaegen, F., & Seuntjens, J. (1995). Monte Carlo study of electron spectra and dose from backscattered radiation in the vicinity of media interfaces for monoenergetic photons of 50-1250 keV. *Radiation research*, 143(3), 334-342.
- [138] Kanaya, K. A., & Okayama, S. (1972). Penetration and energy-loss theory of electrons in solid targets. *Journal of Physics D: Applied Physics*, 5(1), 43.

- [139] Rosengren, B., Wulff, L., Carlsson, E., Carlsson, J., Montelius, A., Russell, K., & Grusell, E. (1991). Backscatter Radiation at Tissue-Titanium Interfaces Analyses of Biological Effects from ^{60}Co and Protons. *Acta Oncologica*, 30(7), 859-866.
- [140] Burgo, T. A., Batista, B. C., & Galembeck, F. (2017). Electricity on rubber surfaces: a new energy conversion effect. *ACS omega*, 2(12), 8940-8947.
- [141] DIN 32 505 Part 1 Abnahmeprüfungen für Elektronenstrahl-Schweißmaschinen; Grundlagen, Abnahmebedingungen Acceptance inspection of electron beam welding machines
- [142] <https://www.picotech.com/oscilloscope/3000/picoscope-3000-oscilloscope-specifications>. Accessed 29 Nov 2021.
- [143] Pauli Virtanen, Ralf Gommers, Travis E. Oliphant, Matt Haberland, Tyler Reddy, David Cournapeau, Evgeni Burovski, Pearu Peterson, Warren Weckesser, Jonathan Bright, Stéfan J. van der Walt, Matthew Brett, Joshua Wilson, K. Jarrod Millman, Nikolay Mayorov, Andrew R. J. Nelson, Eric Jones, Robert Kern, Eric Larson, CJ Carey, İlhan Polat, Yu Feng, Eric W. Moore, Jake VanderPlas, Denis Laxalde, Josef Perktold, Robert Cimrman, Ian Henriksen, E.A. Quintero, Charles R Harris, Anne M. Archibald, Antônio H. Ribeiro, Fabian Pedregosa, Paul van Mulbregt, and SciPy 1.0 Contributors. (2020) SciPy 1.0: Fundamental Algorithms for Scientific Computing in Python. *Nature Methods*, 17(3), 261-272.
- [144] Johann Faouzi and Hicham Janati. pyts: A python package for time series classification. *Journal of Machine Learning Research*, 21(46):1–6, 2020.
- [145] <https://nptdms.readthedocs.io/en/stable/apireference.html>. Accessed 29 Nov 2021.
- [146] McKinney, W., & others. (2010). Data structures for statistical computing in python. In *Proceedings of the 9th Python in Science Conference (Vol. 445, pp. 51–56)*.
- [147] Oscilloscope Software Development Kit (SDK). <https://www.picotech.com/library/oscilloscopes/picoscope-software-development-kit-sdk>. Accessed 29 Nov 2021.
- [148] Ben Said, A., Erradi, A., Neiat, A. G., & Bouguettaya, A. (2019). A deep learning spatiotemporal prediction framework for mobile crowdsourced services. *Mobile Networks and Applications*, 24, 1120-1133.
- [149] Keogh, E. J., & Pazzani, M. J. (2000, August). Scaling up dynamic time warping for datamining applications. In *Proceedings of the sixth ACM SIGKDD international conference on Knowledge discovery and data mining (pp. 285-289)*.

- [150] Dutilleul, T., Priest, J., & Baufeld, B. (2016). Electron beam characterization. *Electrotechnica & electronica: The union of Electronics*, 175.
- [149] Immerkaer, J. (1996). Fast noise variance estimation. *Computer vision and image understanding*, 64(2), 300-302.

Appendix A. PLC data dictionary

Orangech anged v8		Description	Address	Type	Scaling	Eng Units
	Beam	HV Demand	DB100.0	REAL		kV
	Beam	Main Beam Current Demand	DB100.4	REAL		mA
	Beam	Main Focus Current Demand	DB100.24	REAL		mA
	Beam	Filament Demand	DB100.20	REAL		V
	Beam	BI ramp-in Demand	DB100.12	REAL		mA/s
	Beam	BI ramp-out Demand	DB100.16	REAL		mA/s
	Beam	HV Feedback	DB109.0	REAL		kV
	Beam	Beam Current Feedback	DB109.4	REAL		mA
	Beam	Focus Feedback	DB109.20	REAL		mA
	Beam	Filament Voltage Feedback	DB109.8	REAL		V
	Beam	Filament Current Feedback	DB109.12	REAL		A
	Beam	Anode Feedback	DB109.16	REAL		1 uA
	Beam	Bias Feedback	DB109.72	REAL		1 V
	Beam	X Deflection Demand	NI only (DB400.0)	REAL		mA
	Beam	Y Deflection Demand	NI only (DB400.4)	REAL		mA
	Beam	X Deflection Feedback	NI only			
	Beam	Y Deflection Feedback	NI only			
	Beam	FG Frequency X/Y	NI only (DB400.16)	REAL		Hz
	Beam	Offset X	NI only (DB400.8)	REAL		mA
	Beam	Offset Y	NI only (DB400.12)	REAL		mA
	Beam	Beam On	M12.2	BOO L		
	Tooling	X Axis Feedback Actual Feedrate	MD305	REAL		mm/min
	Tooling	Y Axis Feedback Actual Feedrate	MD309	REAL		mm/min
	Tooling	C Axis Feedback Actual Feedrate	DB303.0	REAL		deg/min
	Tooling	X Axis Feedback Actual Position	DB303.4	REAL		mm
	Tooling	Y Axis Feedback Actual Position	DB303.8	REAL		mm
	Tooling	C Axis Feedback Actual Position	DB303.12	REAL		deg
	Tooling	Wirefeed X2 Axis Feedback Actual Position	DB400.20	REAL		mm
	Tooling	Wirefeed Y2 Axis Feedback Actual Position	DB400.24	REAL		mm
	Tooling	Wirefeed Z Axis Feedback Actual Position	DB400.28	REAL		mm
	Tooling	Wirefeed Speed Demand	DB400.48	REAL		mm/min
	Tooling	Wirefeed Speed Feedback- Encoder Internal	DB400.32	REAL		mm/min
	Tooling	Wirefeed Speed Feedback- Encoder External	DB400.36	REAL		mm/min
	Tooling	Wirefeed Positon Feedback- Encoder Internal	DB400.40	REAL		mm
	Tooling	Wirefeed Positon Feedback- Encoder External	DB400.44	REAL		mm
	Tooling	Wirefeed Speed Feedback- Check Tacho	DB400.60	REAL		mm/min
	Tooling	Wirefeed Wire Present	I 45.4	BOO L		
	Tooling	Wirefeed Speed Tolerance	DB400.80	REAL		
	Temperature	Pyrometer 1 Part Temperature	DB400.100	REAL		Deg C
	Temperature	Pyrometer 1 Part Emissivity	DB400.104	REAL		v
	Temperature	Pyrometer 2 Baseplate Temperature	DB400.108	REAL		Deg C
	Temperature	Pyrometer 2 Baseplate E missivity	DB400.112	REAL		v
	Temperature	Pyrometer 1 Part Warning Setpoint	DB400.76	REAL		Deg C
	Temperature	Pyrometer 1 Part Alarm Setpoint	DB400.72	REAL		Deg C
	Temperature	Pyrometer 2 Baseplate Warning Setpoint	DB400.68	REAL		Deg C
	Temperature	Pyrometer 2 Baseplate Alarm Setpoint	DB400.64	REAL		Deg C

Orangech anged v8		Description	Address	Type	Scaling	Eng Units
	Process	Batch ID/Serial				
	Process	Works Request				
	Process	CVE_Process	DB404.0	STR1 NG[3] (32by tes)		
	Process	CVE_Recipe	DB404.34	STR1 NG[3] (32by tes)		
	Process	Machine Number				
	Process	Gun Type				
	Process	Surface focus	User manually enters text in WW			
	Process	Pause interval	User manually enters text in WW			
	Process	CNC Program number/name?	DB303.148	STR1 NG[1 60] (160b ytes)		
	Quality	Vacuum	Chamber Vacuum	DB90.44	REAL	1 mB
	Quality	Vacuum	Gun Vacuum	DB90.36	REAL	1 mB
	Alarms	Alarm 1 - CB24 Tripped	M 110.0			
	Alarms	Alarm 2 - E-Stop_Door Control	M 110.1			
	Alarms	Alarm 3 - E-Stop_Chamber	M 110.2			
	Alarms	Alarm 4 - E-Stop_Control Console	M 110.3			
	Alarms	Alarm 5 - Panel Switch Open	M 110.4			
	Alarms	Alarm 9 - Gun Gauge Fail	M 109.0			
	Alarms	Alarm 10 - Chamber Gauge Fail	M 109.1			
	Alarms	Alarm 11 - Conactor Fail	M 109.2			
	Alarms	Alarm 17 - Water Fail	M 112.0			
	Alarms	Alarm 18- Air Fail	M 112.1			
	Alarms	Alarm 19 - V1 Fail	M 112.2			
	Alarms	Alarm 20 - V2 Fail	M 112.3			
	Alarms	Alarm 21- V3 Fail	M 112.4			
	Alarms	Alarm 22- V4 Fail	M 112.5			
	Alarms	Alarm 23 - V5 Fail	M 112.6			
	Alarms	Alarm 24 - V14 Fail	M 112.7			
	Alarms	Alarm 25 - V10 Fail	M 111.0			
	Alarms	Alarm 26 - Gun Turbo Fault	M 111.1			
	Alarms	Alarm 30 - Chamber Diff O/T	M 111.5			
	Alarms	Alarm 32 - Chamber pump down too long	M 111.7			
	Alarms	Alarm 50 - HV Trip in Auto	M 116.1			
	Alarms	Alarm 51 - HV Current Limit	M 116.2			
	Alarms	Alarm 52 - Filament Failed	M 116.3			
	Alarms	Alarm 53 - HV CB or COM Fail	M 116.4			
	Alarms	Alarm 54 - Z2 Drive not ready	M 116.5			
	Alarms	Alarm 56 - HV Fault	M 116.7			
	Alarms	Alarm 57 - Work or Base OverTemp Beam Off	M 115.0			
	Alarms	Alarm 58 - Anode Current	M 115.1			
	Alarms	Alarm 59 - Door Drive Fail	M 115.2			
	Alarms	Alarm 63 - NC Battery low	M 115.7			
	Warnings	Warning 1 - Filament Change Due	M 118.0			
	Warnings	Warning 2 - Diffs Ready	M 118.1			
	Warnings	Warning 3 - Castell Key Off	M 118.2			
	Warnings	Warning 7 - CNC Beam Inhibited	M 118.6			
	Warnings	Warning 8 - System On button not pressed	M 118.7			
	Warnings	Warning 10 - Gun Anode current limit	M 117.1			
	Warnings	Warning 13 - Door switch override switch on	M 117.4			
	Warnings	Warning 15 - Partial Vac	M 117.6			
	Warnings	Warning 25 - Wire Running out Feed stopped	M 119.0			
	Warnings	Warning 26 - Wire Running Slow	M 119.1			
	Warnings	Warning 27 - Workpiece Hot	M 119.2			
	Warnings	Warning 28 - Baseplate Hot	M 119.3			
	Warnings	Warning 30 - H code out of range	M 119.5			
	Warnings	Warning 32 -Pump service is due	M 119.7			
	Inventory	Tooling/Fixture		STR1 NG		
	Material	Wire Material ID		STR1 NG?		
	Material	Baseplate Material ID		STR1 NG?		
	Material	Wire Mass (was Length Remaining)	DB400.92	REAL		kg
	Material	Wire Thickness		REAL		
		Filament current lifetime	DB123.8	INT		0.1 Hours
		Pump Hrs Since Service	DB123.96	INT		Hours
		Power consumption pulses from power meter.	DB400.96	DINT		1 pulse=0.1 kW

Appendix B. Image processing

```
import os
import pandas as pd
import skimage.color
import skimage.filters
import skimage.io
import sys
import matplotlib.pyplot as plt
from skimage.color import label2rgb
import datetime
import imageio as iio
from skimage import filters
from skimage.color import rgb2gray # only needed for incorrectly saved images
from skimage.measure import regionprops
from datetime import datetime, timedelta
mainpath = r"C:\alldata\paper5"
directory = os.listdir(mainpath)
print(directory)
plc=[]
img=[]
for f in range(0, len(directory)):
    pl=[s for s in os.listdir(os.path.join(mainpath, directory[f])) if s.endswith('.csv')]
    im=[s for s in os.listdir(os.path.join(mainpath, directory[f])) if s.endswith('.bmp')]
    img.append(im)
    if len(pl)==2:
        pass
    else:
        pl.append('None')
    plc.append(pl)
def totimestamp(dt, epoch=datetime(1970,1,1)):
    td = dt - epoch
    return (td.microseconds + (td.seconds + td.days * 86400) * 10**6) / 10**6
all_data=[]
for i in range (0,len(plc)):
    try:
        raw=pd.read_csv(os.path.join(mainpath, directory[i], plc[i][1]))
        processed=raw['Channel A (mV)'][1:].astype(float)
        all_data.append(processed)
    except:
        print('error')
centery=[]
centerx=[]
intensity_image=[]
solidity=[]
area=[]
eccentricity=[]
for i in range (0,len(img)):
    centery_part=[]
    centerx_part=[]
    area_part=[]
    intensity_part=[]
    solidity_part=[]
    eccentricity_part=[]
    for j in range (0, len(img[i])):
        image=skimage.io.imread(os.path.join(mainpath, directory[i], img[i][j]))
        image2=skimage.color.rgb2gray(image)
        threshold_value = filters.threshold_otsu(image2)
        labeled_foreground = (image2 > threshold_value).astype(int)
        properties = regionprops(labeled_foreground, image2)
        center_of_mass = properties[0].centroid
        weighted_center_of_mass = properties[0].weighted_centroid
        #print(center_of_mass)
        centery_part.append([center_of_mass[1]])
        centerx_part.append([center_of_mass[0]])
        intensity_imagea=properties[0].intensity_image.sum()
        solidity=properties[0].solidity
        areaa=properties[0].area
        eccentricitya=properties[0].eccentricity
        area_part.append([areaa])
        eccentricity_part.append([eccentricitya])
        solidity_part.append([solidity])
        intensity_part.append([intensity_imagea])
        print(center_of_mass)
    centery.append(centery_part)
    centerx.append(centerx_part)
    eccentricity.append(eccentricity_part)
    area.append(area_part)
    solidity.append(solidity_part)
    intensity_image.append(intensity_part)
```


Appendix C. Trigger control and data acquisition

```

import ctypes
from picosdk.ps3000a import ps3000a as ps
import numpy as np
import matplotlib.pyplot as plt
from picosdk.functions import adc2mV, assert_pico_ok
import pandas as pd
import numpy as np
import re
import snap7
import struct
from ctypes import c_int, byref, c_uint16, c_int32
from snap7.types import *
from snap7.common import check_error
import pandas as pd
import time
import datetime
import os
from threading import Thread
import os
#import re
import datetime

import clr
clr.AddReference(r'C:\Program Files\Xiris Automation Inc\Xiris Weld SDK\bin\XirisWeldSDK.dll')
import XirisWeldSDK
import clr
clr.AddReference(r'C:\Program Files\Xiris Automation Inc\Xiris Weld SDK\bin\XImage.dll')
import XImage
import clr
clr.AddReference(r'C:\Program Files\Xiris Automation Inc\Xiris Weld SDK\bin\XirisAutomation.XWeld.VideoProcess.dll')
import XirisAutomation.XWeld.VideoProcessing
from XirisAutomation.XWeld.VideoProcessing import VideoProcess

clr.AddReference('System.Drawing')
from System.Drawing import Rectangle

class picoscope():
    status = {}
    chandle = ctypes.c_int16()
    welding_speed=500 #mm/min
    welding_length=200 #put in mm
    welding_time=60*welding_length/welding_speed #seconds

    postTriggerSamples=int(welding_time*200)

    preTriggerSamples = 0
    sample_time = 0.01 # 0.01
    timebase = int(sample_time*62500000+2)
    maxsamples = preTriggerSamples + postTriggerSamples
    chARange = 5
    timeIntervals = ctypes.c_float()
    cmaxSamples = ctypes.c_int32(maxsamples)
    overFlow = (ctypes.c_int16 * 10)()
    returnedMaxSamples = ctypes.c_int16()

    def start():
        # Create chandle and status ready for use

        status=picoscope().status
        chandle=picoscope().chandle
        timeIntervals=picoscope().timeIntervals
        chARange=picoscope().chARange
        preTriggerSamples=picoscope().preTriggerSamples
        postTriggerSamples=picoscope().postTriggerSamples
        sample_time=picoscope().sample_time = 0.01 # 0.01
        timebase=picoscope().timebase
        returnedMaxSamples=picoscope().returnedMaxSamples
        preTriggerSamples=picoscope().preTriggerSamples
        postTriggerSamples=picoscope().postTriggerSamples

        # Opens the device
        status["openunit"] = ps.ps3000aOpenUnit(ctypes.byref(chandle), None)

        try:
            assert_pico_ok(status["openunit"])
        except:

            # powerstate becomes the status number of openunit
            powerstate = status["openunit"]

```

```

# If powerstate is the same as 282 then it will run this if statement
if powerstate == 282:
    # Changes the power input to "PICO_POWER_SUPPLY_NOT_CONNECTED"
    status["ChangePowerSource"] = ps.ps3000aChangePowerSource(chandle, 282)
    # If the powerstate is the same as 286 then it will run this if statement
elif powerstate == 286:
    # Changes the power input to "PICO_USB3_0_DEVICE_NON_USB3_0_PORT"
    status["ChangePowerSource"] = ps.ps3000aChangePowerSource(chandle, 286)
else:
    raise

assert_pico_ok(status["ChangePowerSource"])

# Set up channel A

chARange = 5
status["setChA"] = ps.ps3000aSetChannel(chandle, 0, 1, 1, chARange, 0)
assert_pico_ok(status["setChA"])

# Sets up single trigger

status["trigger"] = ps.ps3000aSetSimpleTrigger(chandle, 1, 0, 1024, 3, 0, 1000)
assert_pico_ok(status["trigger"])

# Setting the number of sample to be collected
#preTriggerSamples = 100
#postTriggerSamples = 400
welding_speed=500 #mm/min
welding_length=200 #put in mm
welding_time=60*welding_length/welding_speed #seconds

postTriggerSamples=int(welding_time*200)
#postTriggerSamples=1500

preTriggerSamples = 0 #100
#postTriggerSamples = 1500 #400
maxsamples = preTriggerSamples + postTriggerSamples

# Gets timebase information
sample_time = 0.01
timebase = int(sample_time*62500000+2)
print (timebase)

status["GetTimebase"] = ps.ps3000aGetTimebase2(chandle, timebase, maxsamples, ctypes.byref(timeIntervals), 1, ctypes.b
assert_pico_ok(status["GetTimebase"])
picoScope().status=status

def trigger_on():
    #https://www.picotech.com/download/manuals/TriggeringAPicoScopeSignalGeneratorUsingThePicoScopeAPIFunctions.pdf
    status=picoScope().status
    chandle=picoScope().chandle
    wavetype = ctypes.c_int16(3)
    sweepType = ctypes.c_int32(1)
    triggerType = ctypes.c_int32(0) #or 0 2
    triggerSource = ctypes.c_int32(0)
    status["SetSigGenBuiltIn"] = ps.ps3000aSetSigGenBuiltIn(chandle, 2000000, 1000000, wavetype, 32767, 32767, 0, 1, sweep
    assert_pico_ok(status["SetSigGenBuiltIn"])
    picoScope().status=status
    #https://www.picotech.com/download/manuals/TriggeringAPicoScopeSignalGeneratorUsingThePicoScopeAPIFunctions.pdf
def trigger_off():
    status=picoScope().status
    chandle=picoScope().chandle
    wavetype = ctypes.c_int16(3)
    sweepType = ctypes.c_int32(0)
    triggerType = ctypes.c_int32(0) #or 0 2
    triggerSource = ctypes.c_int32(0)
    shots= 0xFFFFFFFF
    #10 32767
    status["SetSigGenBuiltIn"] = ps.ps3000aSetSigGenBuiltIn(chandle, 0, 0, wavetype, 32767, 32767, 0, shots, sweepType, 0,
    assert_pico_ok(status["SetSigGenBuiltIn"])

    picoScope().status=status

```

Chapter 8: Bibliography

```
def capture(date_mp):
    status=picoscope().status
    chandle=picoscope().chandle
    maxsamples=picoscope().maxsamples
    preTriggerSamples=picoscope().preTriggerSamples
    postTriggerSamples=picoscope().postTriggerSamples
    timebase=picoscope().timebase
    chARange=picoscope().chARange
    cmaxSamples=picoscope().cmaxSamples
    overflow=picoscope().overflow
    timeIntervals=picoscope().timeIntervals
    # Starts the block capture

    status["runblock"] = ps.ps3000aRunBlock(chandle, preTriggerSamples, postTriggerSamples, timebase, 1, None, 0, None, No
    assert_pico_ok(status["runblock"])

    # Create buffers ready for assigning pointers for data collection
    bufferAMax = (ctypes.c_int16 * maxsamples)()
    bufferAMin = (ctypes.c_int16 * maxsamples)() # used for downsampling which isn't in the scope of this example

    # Setting the data buffer location for data collection from channel A
    status["SetDataBuffers"] = ps.ps3000aSetDataBuffers(chandle, 0, ctypes.byref(bufferAMax), ctypes.byref(bufferAMin), ma
    assert_pico_ok(status["SetDataBuffers"])

    # Creates a overLow location for data
    ready = ctypes.c_int16(0)
    check = ctypes.c_int16(0)
    while ready.value == check.value:
        status["isReady"] = ps.ps3000aIsReady(chandle, ctypes.byref(ready))

    # Handle = chandle
    status["GetValues"] = ps.ps3000aGetValues(chandle, 0, ctypes.byref(cmaxSamples), 0, 0, 0, ctypes.byref(overflow))
    assert_pico_ok(status["GetValues"])

    # Finds the max ADC count
    maxADC = ctypes.c_int16(0)
    status["maximumValue"] = ps.ps3000aMaximumValue(chandle, ctypes.byref(maxADC))
    assert_pico_ok(status["maximumValue"])

    # Converts ADC from channel A to mV
    adc2mVChAMax = adc2mV(bufferAMax, chARange, maxADC)

    # Creates the time data
    time = np.linspace(0, (cmaxSamples.value) * timeIntervals.value, cmaxSamples.value)

    # Plots the data from channel A onto a graph
    plt.plot(time, adc2mVChAMax[:])
    plt.xlabel('Time (ns)')
    plt.ylabel('Voltage (mV)')
    plt.show()
    # Stops the scope
    status["stop"] = ps.ps3000aStop(chandle)
    assert_pico_ok(status["stop"])

    picoscope().status=status
    # Closes the unit
    # Displays the status returns
    print(status)
    data={'Time (ns)':time, 'Channel A (mV)':adc2mVChAMax[:]}

    #folder=r'C:\Waveforms'

    filename_mp=os.path.join(folder_mp, str(str(date_mp)+'pico'+str(datetime.datetime.now())).replace(r':','r_')+r'.csv')
    print(filename_mp)

    pd.DataFrame.from_dict(data).to_csv(filename_mp, index = False)

def error_close():
    status=picoscope().status
    chandle=picoscope().chandle
    status["close"] = ps.ps3000aCloseUnit(ctypes.c_int16(16384)) #dont close
    assert_pico_ok(status["close"])
    picoscope().status=status
```

```

def plc_read():
    global isrunning
    global date_mp
    global folder_mp

    #start pico
    df=pd.read_excel(r'C:\WireAM EB661 MES V8.xlsx', index_col=1, header=1).reset_index(drop=True)
    df2=(df[df['Address '].str.contains("DB", na=False)])
    columns=df2['Description ']
    columnsstr=columns.to_csv(header=None, index=False).strip().split('\n')
    columnsdate=['date', 'time']+ [i.strip() for i in columnsstr]
    newdf = pd.DataFrame(columns=columnsdate)
    folder=r'C:\alldata'

    addresslist=[]
    for i in df2.index:
        value=df2.at[i,'Address '].replace("DB", "")
        value=re.sub(r"^\d.",'', value)
        address=str(value).split(".")
        addresslist.append(address)

    data_items=(S7DataItem * 19)()
    for i in range(19):
        data_items[i].Area = ctypes.c_int32(S7AreaDB)
        data_items[i].WordLen = ctypes.c_int32(S7WLByte)
        data_items[i].Result = ctypes.c_int32(0)
        data_items[i].DBNumber = ctypes.c_int32(int(addresslist[i][0]))
        data_items[i].Start = ctypes.c_int32(int(addresslist[i][1]))
        data_items[i].Amount = ctypes.c_int32(4) # reading a REAL, 4 bytes

    byte_to_value = [snap7.util.get_real, snap7.util.get_real, snap7.util.get_real, snap7.util.get_real, snap7.util.get_real,
                    snap7.util.get_real, snap7.util.get_real, snap7.util.get_real, snap7.util.get_real, snap7.util.get_real,
                    snap7.util.get_real, snap7.util.get_real, snap7.util.get_real, snap7.util.get_real, snap7.util.get_real,
                    snap7.util.get_real, snap7.util.get_real, snap7.util.get_real, snap7.util.get_real, snap7.util.get_real]

    IP = "192.168.214.1"
    RACK = 0
    SLOT = 2

    while True:
        try:
            plc = snap7.client.Client()
            plc.connect(IP, RACK, SLOT)
        except:
            plc = snap7.client.Client()
            plc.get_connected()

        if plc.get_connected() == True:
            while True:
                #picoscope.trigger_off()

                isrunning=False

                #print(connect_plc().isrunning)

                # create buffers to receive the data
                # use the Amount attribute on each item to size the buffer
                for di in data_items:
                    # create the buffer
                    buffer = ctypes.create_string_buffer(di.Amount)

                    # cast the pointer to the buffer to the required type
                    pBuffer = ctypes.cast(ctypes.pointer(buffer),
                                         ctypes.POINTER(ctypes.c_uint8))
                    di.pData = pBuffer
                try:
                    result, data_items = plc.read_multi_vars(data_items)
                except:
                    #print('disconnected')
                    try:
                        plc = snap7.client.Client()
                        plc.connect(IP, RACK, SLOT)
                    except:
                        pass
                        #print('connection failed')

                for di in data_items:
                    check_error(di.Result)

```

```

result_values = []
    # unpack and test the result of each read
    for i in range(0, len(data_items)):
        btw = byte_to_value[i]
        di = data_items[i]
        value = btw(di.pData, 0)
        result_values.append(value)

    if result_values[7]>1:
        isrunning=True
        #picoscope.trigger_on()
        #for picoscope trigger
        #if result_values[6]<60.12:
        date_mp=datetime.datetime.now()
        #print(connect_plc().date_mp)
        folder=r'C:\alldata'
        #####
        folder2 = os.path.join(folder, str(date_mp).replace(r':',r'_'))
        os.mkdir(folder2)
        folder_mp=folder2
        #####
        filename=os.path.join(folder_mp, str(date_mp).replace(r':',r'_')+r'.csv')
        #return(date_mp, result_values[1])
        newdf.to_csv(filename)

    while result_values[7]>1: ###normally 7 test 1
        #picoscope.trigger_on()

        #while result_values[6]<60.12:
        plctime=datetime.datetime.now()
        timedate = str(plctime).split()
        row=pd.DataFrame([[timedate[0],timedate[1],*result_values]])
        row.to_csv(filename, mode='a',header=False)

        for di in data_items:
            # create the buffer
            buffer = ctypes.create_string_buffer(di.Amount)

            # cast the pointer to the buffer to the required type
            pBuffer = ctypes.cast(ctypes.pointer(buffer),
                ctypes.POINTER(ctypes.c_uint8))
            di.pData = pBuffer
        try:
            result, data_items = plc.read_multi_vars(data_items)

        except:
            #print('disconnected')
            try:
                plc = snap7.client.Client()
                plc.connect(IP, RACK, SLOT)
            except:
                pass

        for di in data_items:
            check_error(di.Result)

        result_values = []

        # unpack and test the result of each read
        for i in range(0, len(data_items)):
            btw = byte_to_value[i]
            di = data_items[i]
            value = btw(di.pData, 0)
            result_values.append(value)
        isrunning=True
else:
    pass

```

```

def pico_read():
    try:
        picoscope.start()
    except:
        try:
            picoscope.error_close()
            picoscope.start()
        except:
            print('fatal error')
    while True:
        if isrunning == True:
            try:
                picoscope.trigger_on()
                picoscope.capture(date_mp)
            except:
                try:
                    picoscope.error_close()
                except:
                    try:
                        picoscope.start()
                        print('picoscope reconnected')
                        print(date_mp)
                    except:
                        print('fatal error 2')
        if isrunning == False:
            picoscope.trigger_off()

def camera_read():
    CameraInstance=XirisWeldSDK.CameraDetector.Instance
    e=CameraInstance.CameraEventArgs()
    e2=XirisWeldSDK.CameraReadyEventArgs()
    e3=XirisWeldSDK.CameraBufferReadyEventArgs()
    #folder=r'C:\camera'

    def camera_BufferReady(sender, e3):
        print('wow3')
        print(e3.Image)
        e3.Image.Save( os.path.join(folder_mp, str(str(date_mp)+'cam'+str(datetime.datetime.now()).replace(r':','r_')+r'.bmp'))

    def camera_CameraReady(sender, e2):
        print('done')
        if e2.IsReady:
            print('camera ready')
            camera.BufferReady += camera_BufferReady
            print('buffer ready ')

    def CameraDetector_CameraDetected(sender, e):
        if e.CanConnect:
            global camera
            camera=XirisWeldSDK.Camera()
            camera.CameraReady+=camera_CameraReady
            camera.Connect(e.CameraIPAddress)

    CameraInstance.CameraDetected+=CameraDetector_CameraDetected
    time.sleep(10)

    camera.set_ExposureTimeGlobal(300) #1
    camera.set_AOI(Rectangle(0, 0, 1280, 1024))
    camera.set_TriggerMode(1)
    camera.set_TriggerPolarity(0)
    camera.Start()
    #warmup
    for i in range(100):
        camera.SoftTriggerNow()
    while True:
        if isrunning==True:
            camera.SoftTriggerNow()
        else:
            pass

if __name__ == "__main__":
    thread1=Thread(target = pic_read).start()
    thread2=Thread(target = pico_read).start()
    thread3=Thread(target = camera_read).start()

```

Appendix D. Image debayering

```

import cv2
import numpy as np
from matplotlib import pyplot as plt
def bpp12(raw_image):
    data = np.frombuffer(raw_image, dtype=np.uint8)
    fst_uint8, mid_uint8, lst_uint8 = np.reshape(data, (data.shape[0] // 3, 3)).astype(np.uint16).T
    fst_uint12 = (fst_uint8 << 4) + (mid_uint8 >> 4)
    snd_uint12 = (lst_uint8 << 4) + (np.bitwise_and(15, mid_uint8))
    return np.reshape(np.concatenate((fst_uint12[:, None], snd_uint12[:, None]), axis=1), 2 * fst_uint12.shape[0])
#Adapted from https://stackoverflow.com/a/51967333/9173710
#BayerRG12Packed
#the first byte contains the top 8 bits of the first pixel
#the second byte contains the bottom 4 bits of the first pixel in the low nibble
#and the bottom 4 bits of the second pixel in the high nibble
#the third byte contains the top 8 bits of the second pixel
#the odd lines of the image contains R, G, R, G etc.
#the even lines of the image contain G, B, G, B etc.
datfile = r"C:\Xiris Data\XirisweldStudio\Images\Images-210218-131728\Image000823.dat"
outputimage = r"C:\Xiris Data\test\resokay2.png"
#define input and output path
with open(datfile, 'rb') as f:
    data = np.fromfile(f, dtype=np.uint16)
#Load image
pixels=bpp12(data)
#read raw pixel data
image= np.reshape(pixels[24:],(1024,1280))
#create image array
colour = cv2.cvtColor(image, cv2.COLOR_BAYER_RG2RGB)
#debayering using cv2
colournorm=cv2.normalize(colour, dst=None, alpha=0, beta=65535, norm_type=cv2.NORM_MINMAX)
#12 bits have 4,096 tonal values per channel and this value needs to be in range of 16 bits (65,536 tonal values per channel)
cv2.imwrite(outputimage, colournorm)
#save image using cv2

```

Appendix E. Material test report

Traceability ref 0459315774

315774

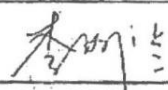
BAOJI TONGRUN METAL MATERIAL LIMITED COMPANY

MILL TEST CERTIFICATE

No: 20200512

EN10204 3.1

DATE:18.May.2020

Commodity: GRS TITANIUM PLATE						Finish: ANNEALED					
Specification: ASTM B265/NACE MR0175						Order No.: TT04351					
						TI-TEK(UK)Limited					
Size [mm]			Heat NO.		Quantity [pc]	Net Weight [kg]					
10×1000×2000mm			2019-1923		4	376		/			
Chemical Composition(WT%)											
Requirement		Ti	Al	V	Fe	C	N	O	H	Residual element	
		Remainder	≤	≤	≤	≤	≤	≤	≤	Each	Total
			5.5-6.75	3.5-4.5	0.30	0.08	0.05	0.20	0.0125	≤	≤
Result	Top	Remainder	6.00	3.90	0.214	0.020	0.010	0.186	0.001	≤	≤
	Bottom	Remainder	5.80	3.75	0.248	0.018	0.009	0.176	0.001	0.10	0.40
Tensile Test											
Requirement Min		Tensile Strength		Yield Strength		Elongation					
		[Mpa]		0.2%		[%]					
		895Min		828Min		10Min					
Result		1046		1008		15					
Other Test											
Visual Inspection			Dimensional Inspection			Hardness					
Acceptable			Acceptable			33(HRC)					
/			/								
								Ultrasonic Test			
/			/					Acceptable AMS2631 classA1 and AMS2154 classAA			
I hereby certify product conforms to all specifically listed technical requirements, and other requirements for these specifications. Furthermore, I certify the above quantitative were derived from testing and analysis and are in accordance with the reference specification(s) requirements.											
 VICE-MANAGER OF QUALITY DEPARTMENT BAOJI TONGRUN METAL MATERIAL LIMITED COMPANY											

ADD : Fanjiasi Industrial Park, Bayu Town, Baoji, Shaanxi, China. 721000 TEL: 86-917-6739157 FAX: 86-917-6739160

Appendix F. Time-series encoding

```

IMG_SIZE=224
ENCODING_METHOD='GAF' #GAF, MTF, RP, MIX(ED)
folder=r"E:\256\0"
from nptdms import TdmsFile, tdmsinfo
from scipy.optimize import leastsq
import pandas
import pandas as pd
#read all files
import os
df3=dict()
#error2 = []
alllines = []
mainpath = r"E:\Norbert\low disk\Results\Caustics"
filelist = [each for each in os.listdir(mainpath) if each.endswith('.csv')]
for f in range(0, len(filelist)):
    #read CSV
    beamonly=pandas.read_csv(os.path.join(mainpath,filelist[f]))
    beam_current=beamonly.iloc[4][1]
    columns=["Focus Current (mA)","FWHM x (mm)/2","Trace Filename","'- FWHM x (mm)/2"]
    #r=pandas.read_csv(r"D:\Results\Caustics\2019_11_26 - 10_08_39.csv",skiprows=15, usecols=columns)
    r=pandas.read_csv(os.path.join(mainpath,filelist[f]),skiprows=15, usecols=columns)
    r.head()

    new_value = dict()

    #make square values of Focus Current
    for x in range(0, len(r['Trace Filename'])):
        new_value[x] = int(r.loc[x,'Focus Current (mA)']**2)
    values=list(new_value.values())
    #add values to dataframe
    new_column = pandas.DataFrame({'LensI^2': [*values]})
    df = r.merge(new_column, left_index = True, right_index = True)
    #fit parabola
    #finished
    def func(params, x):
        a, b, c = params
        return a * x * x + b * x + c
    # Error function, that is, the difference between the value obtained by fitting curve and the actual value
    def error(params, x, y):
        return func(params, x) - y
    # Solving parameters
    def solvePara():
        p0 = [10, 10, 10]
        Para = leastsq(error, p0, args=(x_val, y_val))
        return Para
    # Output the final result
    def solution():
        Para = solvePara()
        a, b, c = Para[0]
        focus=(-b/(a*2))
        return focus
    def solution2(): #for charts
        Para = solvePara()
        a, b, c = Para[0]
        focus=(-b/(a*2))
        return a, b, c
    #extract columns
    import numpy as np

```

```

x=df.xs('Focus Current (mA)', axis=1)
x_val=x.values
y=df.xs('FWHM x (mm)/2', axis=1)
y_val=y.values
#calculate parabola
focus_current=solution()
#round the parabola solution to match csv file
focus_current=round(focus_current, -1)
#check max min A
min_a=df.iloc[0]['Focus Current (mA)']
max_a=df.iloc[-1]['Focus Current (mA)']
if min_a < focus_current < max_a:
    #Locate file for focus
    pos = df['Focus Current (mA)'].sub(focus_current).abs().values.argmin()
    #new current value
    focus_current_new=df.loc[pos,'Focus Current (mA)']
    #zero value -beam waist
    zero=0
    #Locate=df.loc[df['Focus Current (mA)'] == focus_current].index
    #Locate=np.squeeze(Locate.values)
    values_focused=df.values[pos][0]
    #Locate file for underfocus
    locate_underfocus=df.loc[df['Focus Current (mA)'] < focus_current_new].index
    locate_underfocus=locate_underfocus.values
    values_underfocus = dict()
    values_underfocus2 = dict()
    values_underfocusn = dict()
    for i in range(len(locate_underfocus)):
        values_underfocus[i]=df.values[locate_underfocus][i][0]
        values_underfocus2[i]=df.values[locate_underfocus][i][1]
        values_underfocusn[i]=df.values[locate_underfocus][i][1] - focus_current_new

    values_under=list(values_underfocus.values())
    values_under2=list(values_underfocus2.values())
    values_undern=list(values_underfocusn.values())
    #Locate file for overfocus
    values_overfocus= dict()
    values_overfocus2= dict()
    values_overfocusn= dict()
    locate_overfocus=df.loc[df['Focus Current (mA)'] > focus_current_new].index
    locate_overfocus=locate_overfocus.values
    for i in range(len(locate_overfocus)):
        values_overfocus[i]=df.values[locate_overfocus][i][0]
        values_overfocus2[i]=df.values[locate_overfocus][i][1] #####beamcurrent
        values_overfocusn[i]=df.values[locate_overfocus][i][1] - focus_current_new
    values_over=list(values_overfocus.values())
    values_over2=list(values_overfocus2.values())
    values_overn=list(values_overfocusn.values())
    #create empty array
    item_focus = values_focused[:-5]+' .png'
    augment=5 #define how many times augment
    item_focus_augmented=dict()
    for i in range(augment):
        item_focus_augmented[i]=values_focused[:-5]+'augmented'+str(i)+' .png'
    item_focus_augment=list(item_focus_augmented)

```

Chapter 8: Bibliography

```
values_focused_augmented=dict()
for i in range(augment):
    values_focused_augmented[i]=values_focused
val_focused_augmented=list(values_focused_augmented.values())
classified='focused'
data = [[item_focus, classified, beam_current, focus_current_new, zero]]
df2 = pd.DataFrame(data, columns=['image', 'class', 'beamcurrent', 'focuscurrent', 'normalized'])
for i in range(augment):
    df2.at[i+1, 'image'] = values_focused[:-5] + 'augmented' + str(i) + '.png'
    df2.at[i+1, 'class'] = 'focused'
    df2.at[i+1, 'beamcurrent'] = beam_current
    df2.at[i+1, 'focuscurrent'] = focus_current_new
    df2.at[i+1, 'normalized'] = zero
for i in range(len(values_under)):
    df2.at[i+augment, 'image'] = values_under[i][:-5] + '.png' #i+1 because we know that there is only one focus point
    df2.at[i+augment, 'class'] = 'defocused'
    df2.at[i+augment, 'beamcurrent'] = beam_current
    df2.at[i+augment, 'focuscurrent'] = values_under2[i]
    df2.at[i+augment, 'normalized'] = values_undern[i]
for i in range(len(values_over)):
    df2.at[i+augment+len(values_under), 'image'] = values_over[i][:-5] + '.png' #just add the rest
    df2.at[i+augment+len(values_under), 'class'] = 'overfocused'
    df2.at[i+augment+len(values_under), 'beamcurrent'] = beam_current
    df2.at[i+augment+len(values_under), 'focuscurrent'] = values_over2[i]
    df2.at[i+augment+len(values_under), 'normalized'] = values_overn[i]
#result_df=df3.append(df2, ignore_index=True)
df3[f]=df2
result_df=pd.concat(df3, ignore_index=True)
file_name = np.concatenate([[values_focused], values_under, values_over], axis=None) #val_focused_augmented
#Import TI file/beamassure file
from nptdms import TdmsFile, tdmsinfo
import os
folderin="E:\Norbert\low disk\Results"
#contectate all file names
#file_name = np.concatenate([[values_focused], values_under, values_over], axis=None) #val_focused_augmented
file_name = np.concatenate((val_focused_augmented, values_under, values_over), axis=None)
ch = 'Average'
augment_array= np.arange(augment)
channel_aug=dict()
for i in range(1, augment):
    a=augment_array[i]
    channel_aug[i]='Waveform'+ " "+'%02d' % a #(*a,)
channel_augm=list(channel_aug.values())

signals = dict()
windows = dict()
#seach folders for all beamassure singals for specific beam caustic
for i in range(len(file_name)):
    #search by date
    date=file_name[i][13:23]
    tdsms_file_name=(os.path.join(folderin, date, file_name[i]))
    tdms_data = TdmsFile(os.path.join(folderin, date, file_name[i]))
    if i == 0:
        ch = 'Average'
    elif i > 0 and i < augment-1: #because we use already 0
        ch=channel_augm[i-1]
```

```

else:
    ch = 'Average'
    file_type = "tdms"
    channel = tdms_data.object('Waveforms', ch)
    sig = channel.data
    time = channel.time_track()
    root_object = tdms_data.object()
    period=1/eval(root_object.property('WvFmFreq (Hz)'))
    timestep = time[1]
    pi=3.14159265
    duration_of_radian = period/(pi*2)
    filter_period_in_steps = 0.1*duration_of_radian/timestep
    filt = int(2*round(filter_period_in_steps//2))
    if filt<10:
        filt=10
    t=0
    v=0.
    ii=0
    sample = duration_of_radian*pi/4
    while time[ii] < sample:
        v += sig[ii]
        t = time[ii]
        ii += 1
    baseline = v/float(ii)
    sig = [s-baseline for s in sig]
    filtered = np.convolve(sig, np.ones((filt,))/filt, mode='same')
    low = min(filtered)
    if file_type == "tdms":
        threshold = eval( root_object.property("Threshold (%)") )
        resistor = eval( root_object.property("ProbeResistor (Ohms)") )
    else:
        threshold = 3.0
        resistor = 100.
    threshold = 3.0 # force to 3 so same as LV analysis s/w
    vthresh = low*threshold/100.0

    start = []
    fin = []
    for iii in range(len(filtered)):
        if (iii > 0) and (iii < len(filtered)-1):
            if (filtered[iii-1] >= vthresh) and (filtered[iii] < vthresh):
                start.append(iii)
            if (filtered[iii-1] <= vthresh) and (filtered[iii] > vthresh):
                fin.append(iii)

    if len(start) != 5:
        print ("/n ***too many pulses detected**")
        print (tdsm_file_name)
    elif len(start) == 5:
        listofsigs = [[],[],[],[],[]]
        listoftimes = [[],[],[],[],[]]
        listoffilts = [[],[],[],[],[]]

        for l in range(5):
            for iii in range ( start[l],fin[l] ):
                listofsigs[l].append( sig[iii] )

```

```

        listoffilts[l].append( filtered[iii] )
        listoftimes[l].append( time[iii] )
time_step = [ time[1],time[1],time[1],time[1],time[1] ]

wid = []
for l in range(5):
    wid.append( fin[l]-start[l] )
window_st = []
window_fin = []
extend = 0

for iii in range(len(start)):
    if iii!=2: # f-cup window doesn't need extending
        window_st.append( int(start[iii] - extend) )
        window_fin.append( int(fin[iii] + extend) )
    else:
        window_st.append( int(start[iii]) )
        window_fin.append( int(fin[iii]) )
    signals[i]=sig ##signal after correction
    windows[i]=np.append(window_st, window_fin)

key_val=[]
for key in windows:
    key_val.append(key)
res = not bool(signals)
if res is False:
    for i in [*key_val]:
        import numpy as np
        import os
        from pyts.approximation import PiecewiseAggregateApproximation
        #1 peak
        r=signals[i][windows[i][0]:windows[i][5]]
        g=signals[i][windows[i][0]:windows[i][5]]
        b=signals[i][windows[i][0]:windows[i][5]]
        r=np.array(r)
        g=np.array(g)
        b=np.array(b)
        #2peak
        r2=signals[i][windows[i][1]:windows[i][6]]
        g2=signals[i][windows[i][1]:windows[i][6]]
        b2=signals[i][windows[i][1]:windows[i][6]]
        r2=np.array(r2)
        g2=np.array(g2)
        b2=np.array(b2)
        #3peak
        r3=signals[i][windows[i][2]:windows[i][7]]
        g3=signals[i][windows[i][2]:windows[i][7]]
        b3=signals[i][windows[i][2]:windows[i][7]]
        #4peak
        r4=signals[i][windows[i][3]:windows[i][8]]
        g4=signals[i][windows[i][3]:windows[i][8]]
        b4=signals[i][windows[i][3]:windows[i][8]]
        r4=np.array(r4)
        g4=np.array(g4)
        b4=np.array(b4)
        #5peak
        r5=signals[i][windows[i][4]:windows[i][9]]
        g5=signals[i][windows[i][4]:windows[i][9]]
        b5=signals[i][windows[i][4]:windows[i][9]]

```

```

r2 = r2.reshape(1, *r2.shape)
g2 = g2.reshape(1, *g2.shape)
b2 = b2.reshape(1, *b2.shape)

r4 = r4.reshape(1, *r4.shape)
g4 = g4.reshape(1, *g4.shape)
b4 = b4.reshape(1, *b4.shape)

transformer = PiecewiseAggregateApproximation(window_size = None, output_size=IMG_SIZE)
r2=transformer.transform(r2)
g2=transformer.transform(g2)
b2=transformer.transform(b2)

r4=transformer.transform(r4)
g4=transformer.transform(g4)
b4=transformer.transform(b4)

r=np.concatenate((r2, r4), axis=None)
g=np.concatenate((g2, g4), axis=None)
b=np.hstack((b2,b4))
import matplotlib.pyplot as plt
from mpl_toolkits.axes_grid1 import ImageGrid
from pyts.image import GramianAngularField
from pyts.image import MarkovTransitionField
from pyts.image import RecurrencePlot
if ENCODING_METHOD == 'GAF':
    gadf = GramianAngularField(image_size=IMG_SIZE, method='difference', sample_range=(-1,1))
    b_gadf = gadf.fit_transform(b2)
    filename =df2['image'][i]
    plt.imsave(os.path.join(folder, filename),b_gadf.squeeze(), cmap='viridis')
elif ENCODING_METHOD == 'RP':
    rp=RecurrencePlot(dimension=1, time_delay=1, threshold=None, percentage=10)
    b_gadf = rp.fit_transform(b2)
    rgbArray = np.zeros((IMG_SIZE, IMG_SIZE, 3), 'uint8')
    rgbArray[..., 0] = r_gadf * 256
    rgbArray[..., 1] = g_gadf * 256
    rgbArray[..., 2] = b_gadf * 256
    filename =df2['image'][i]
    plt.imsave(os.path.join(folder, filename),b_gadf.squeeze(), cmap='viridis')
elif ENCODING_METHOD == 'MTF':
    mtf=MarkovTransitionField(image_size=IMG_SIZE, n_bins=4, strategy='quantile', overlapping=False)
    b_gadf = mtf.fit_transform(b2)
    filename =df2['image'][i]
    plt.imsave(os.path.join(folder, filename),b_gadf.squeeze(), cmap='viridis')

elif ENCODING_METHOD == 'MIX':
    gadf = GramianAngularField(image_size=IMG_SIZE, method='difference', sample_range=(-1,1))
    mtf=MarkovTransitionField(image_size=IMG_SIZE, n_bins=4, strategy='quantile', overlapping=False)
    rp=RecurrencePlot(dimension=1, time_delay=1, threshold=None, percentage=10)
    r_gadf = gadf.fit_transform(r2)
    g_gadf = rp.fit_transform(g2)
    b_gadf = mtf.fit_transform(b2)
    rgbArray = np.zeros((IMG_SIZE, IMG_SIZE, 3), 'uint8')
    rgbArray[..., 0] = r_gadf * 256
    rgbArray[..., 1] = g_gadf * 256
    rgbArray[..., 2] = b_gadf * 256
    filename =df2['image'][i]
    plt.imsave(os.path.join(folder, filename),rgbArray.squeeze(), cmap='viridis')

else:
    print(r['Trace Filename'][0])

print(result_df.shape)
pngfiles=[]
import os
for file2 in os.listdir(folder):
    if file2.endswith(".png"):
        pngfiles.append(os.path.join(folder, file2).split('\\')[-1])
df2=pd.DataFrame(pngfiles, columns=['image'])
df_result2=result_df.copy()

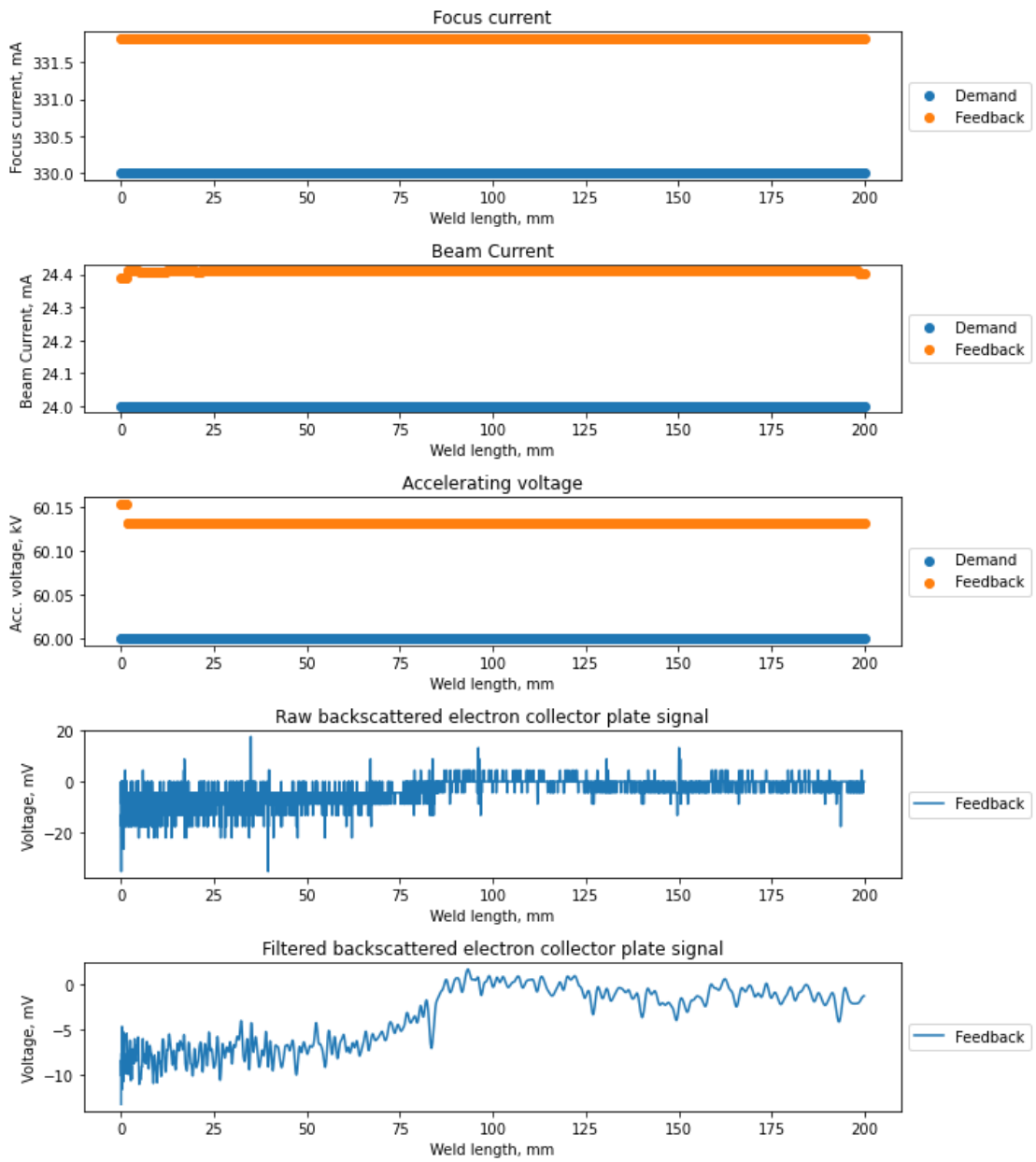
df2=pd.DataFrame(pngfiles, columns=['image'])
cond = result_df['image'].isin(df2['image'])
result_df.drop(result_df[cond].index, inplace = True)
df3=result_df.copy()
result_df=df_result2.copy()
cond2 = result_df['image'].isin(df3['image'])
result_df.drop(result_df[cond2].index, inplace = True)

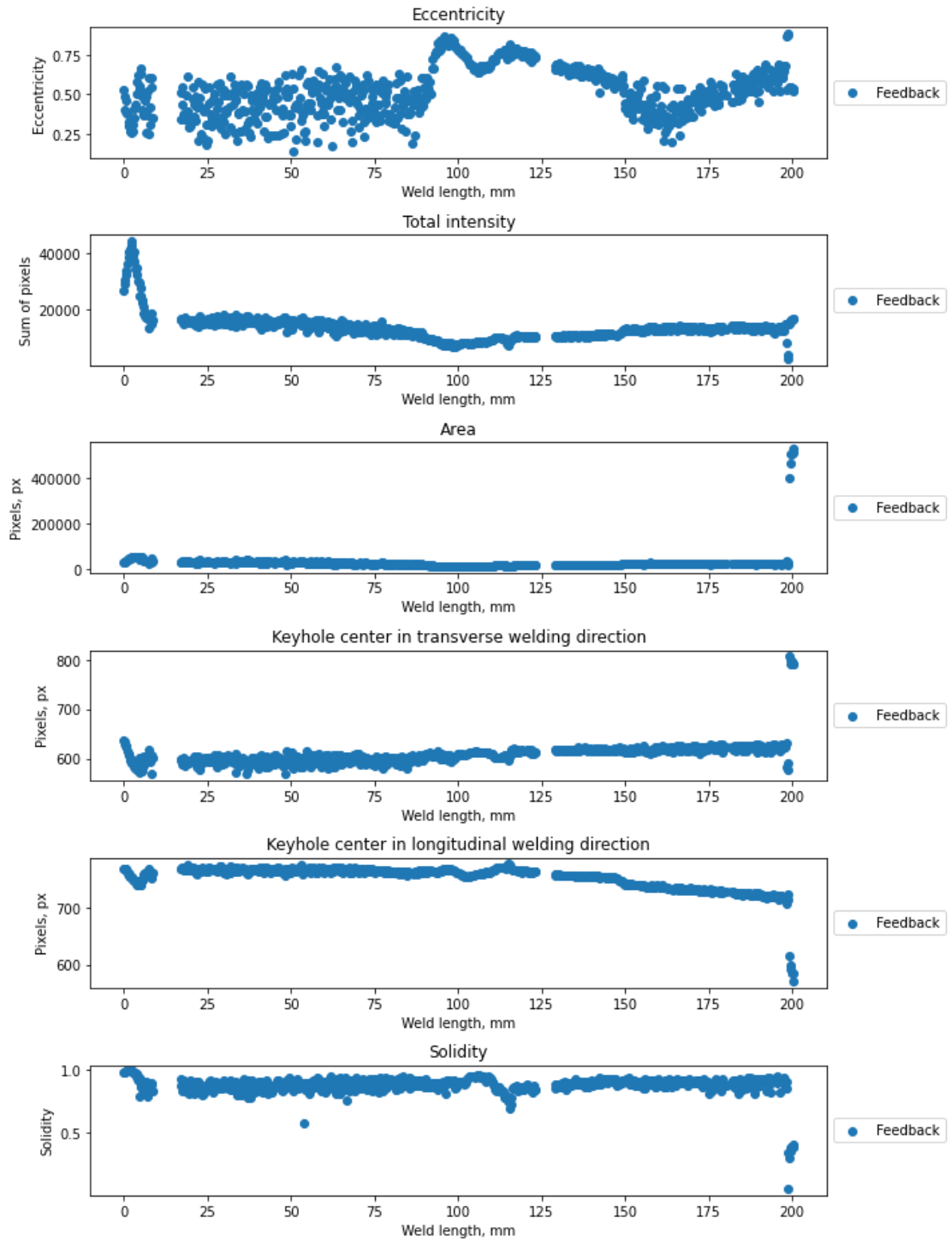
print(result_df.shape)

filenamelabel='labels3.csv'
result_df.to_csv(os.path.join(folder, filenamelabel), index=False)

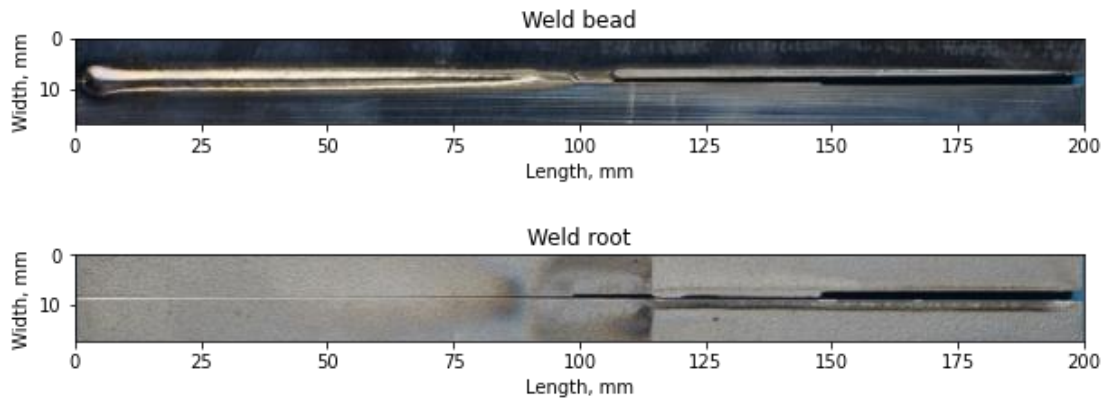
```

Appendix G. Weld 1

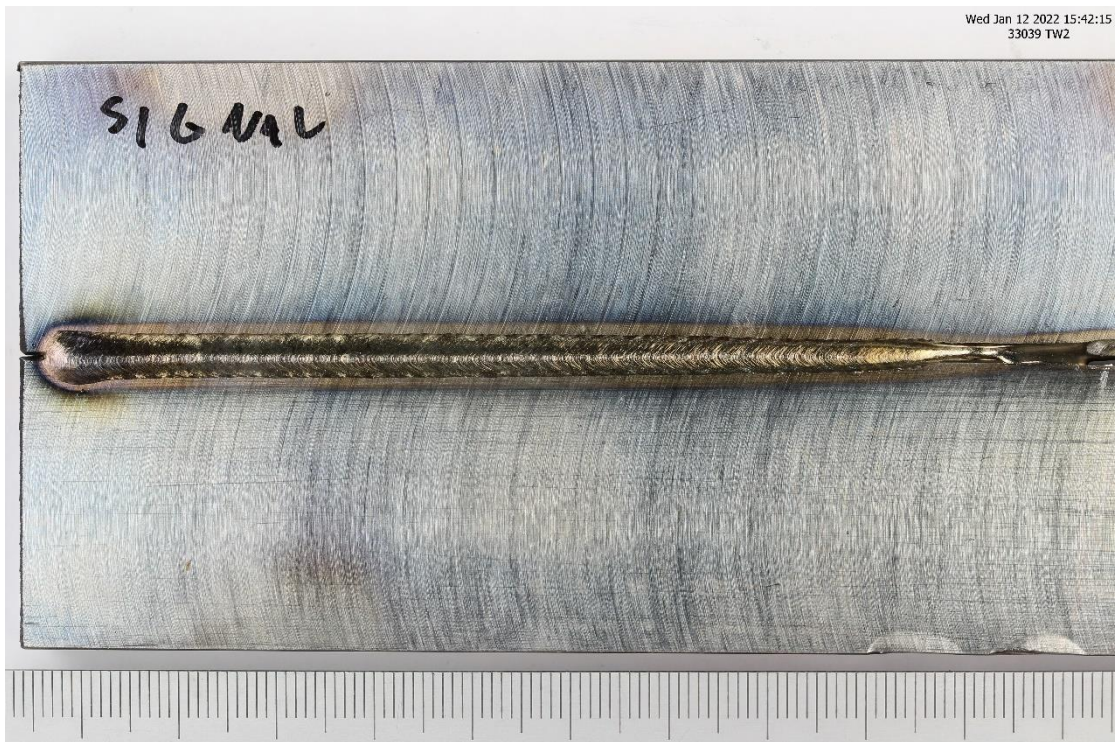


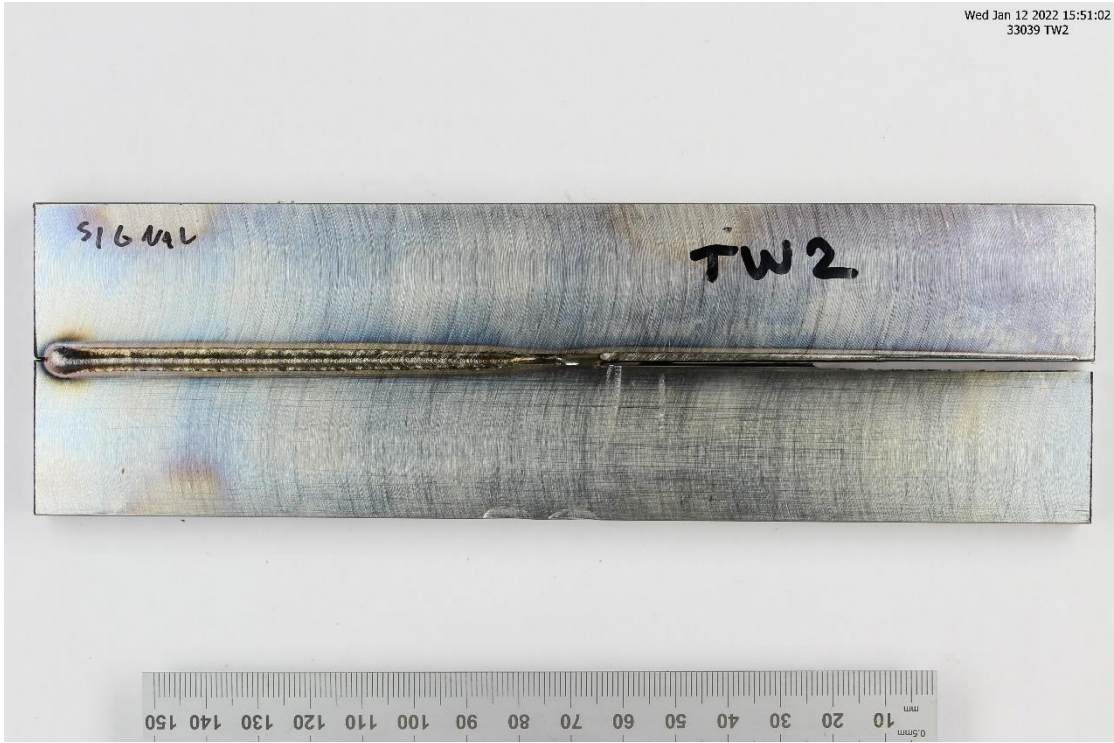


Chapter 8: Bibliography

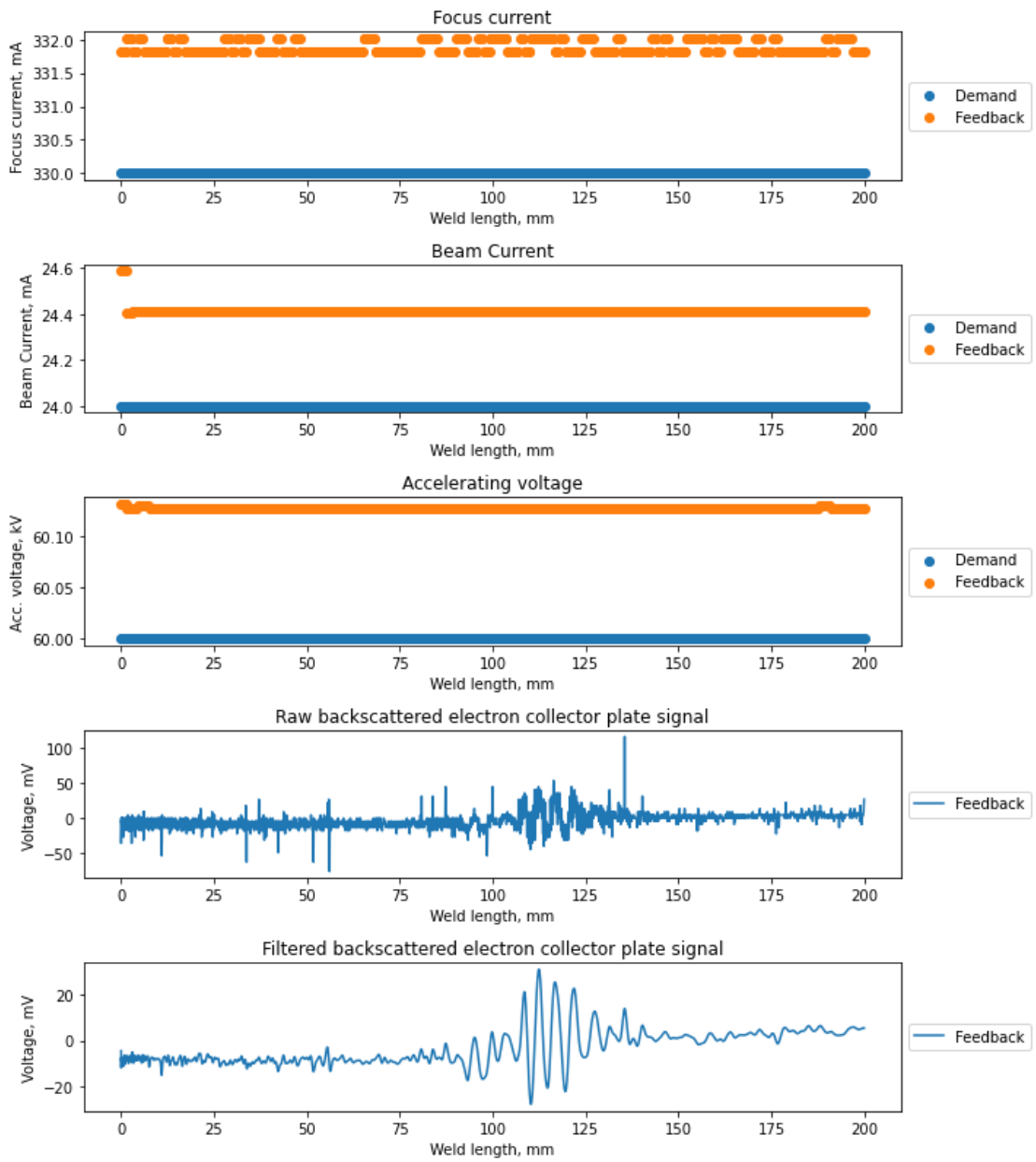


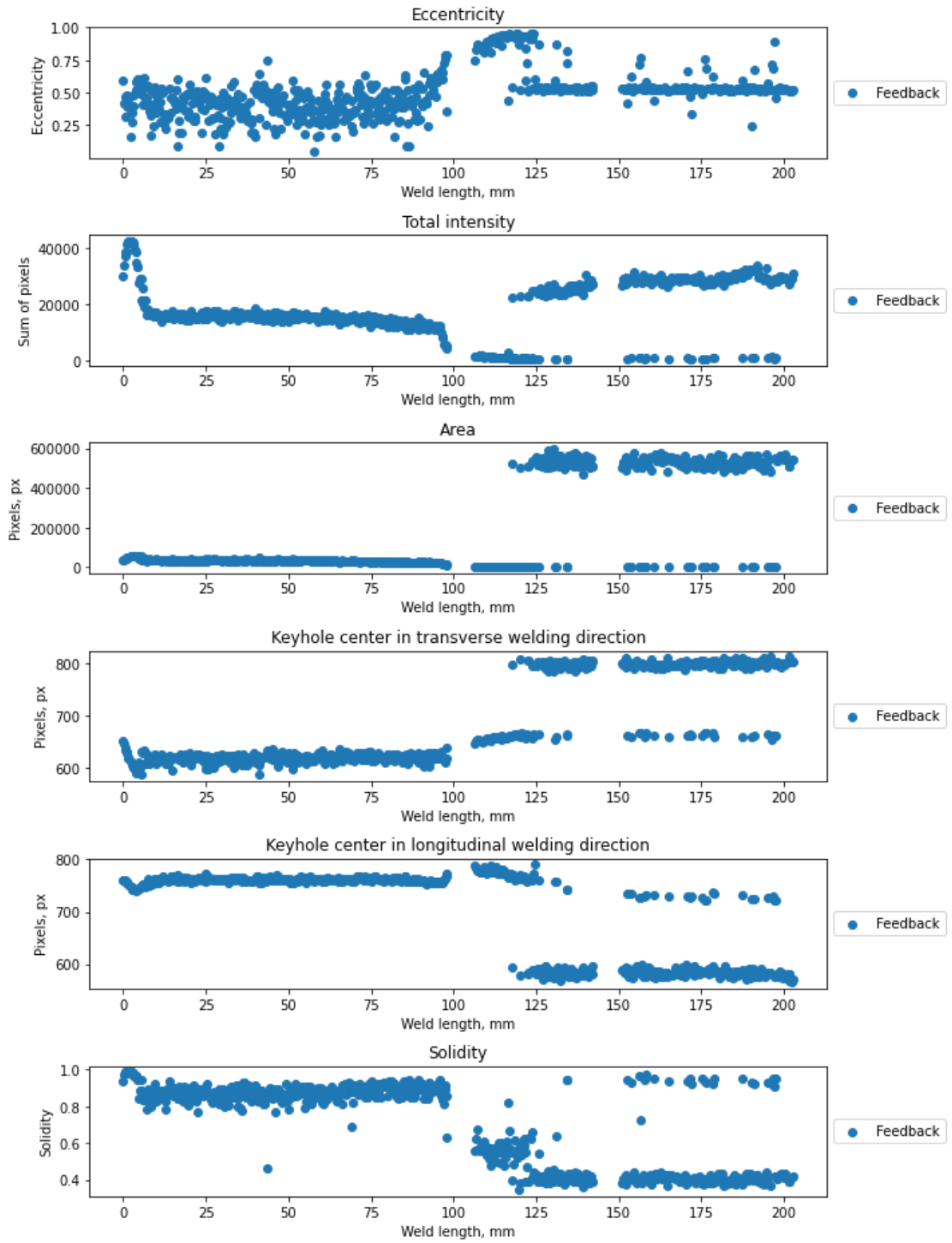
Handwritten markings on the samples are unrelated to the numeration in the thesis.



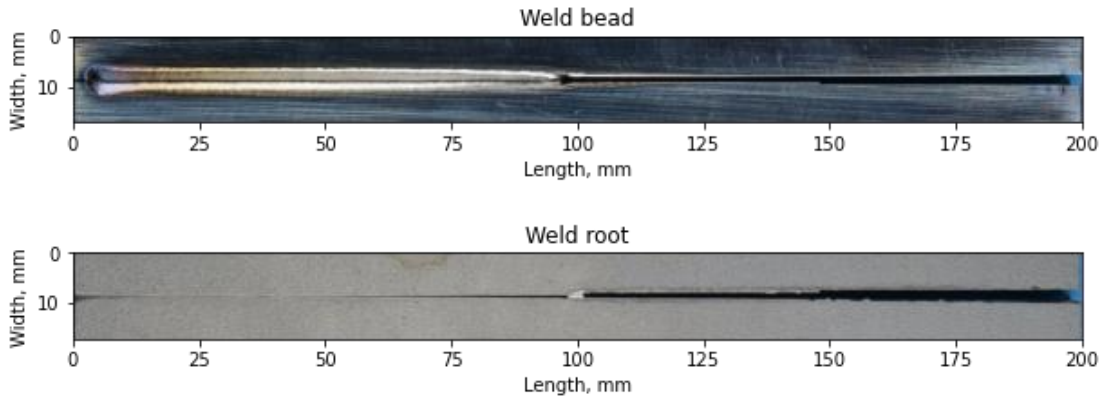


Appendix H. Weld 2



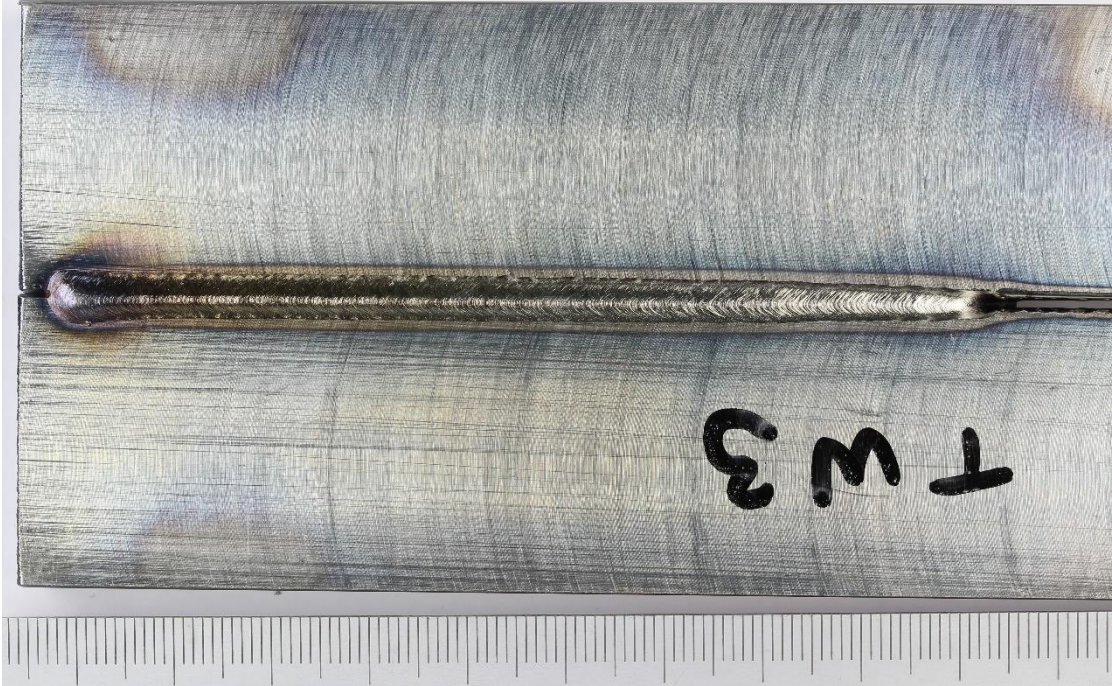


Chapter 8: Bibliography

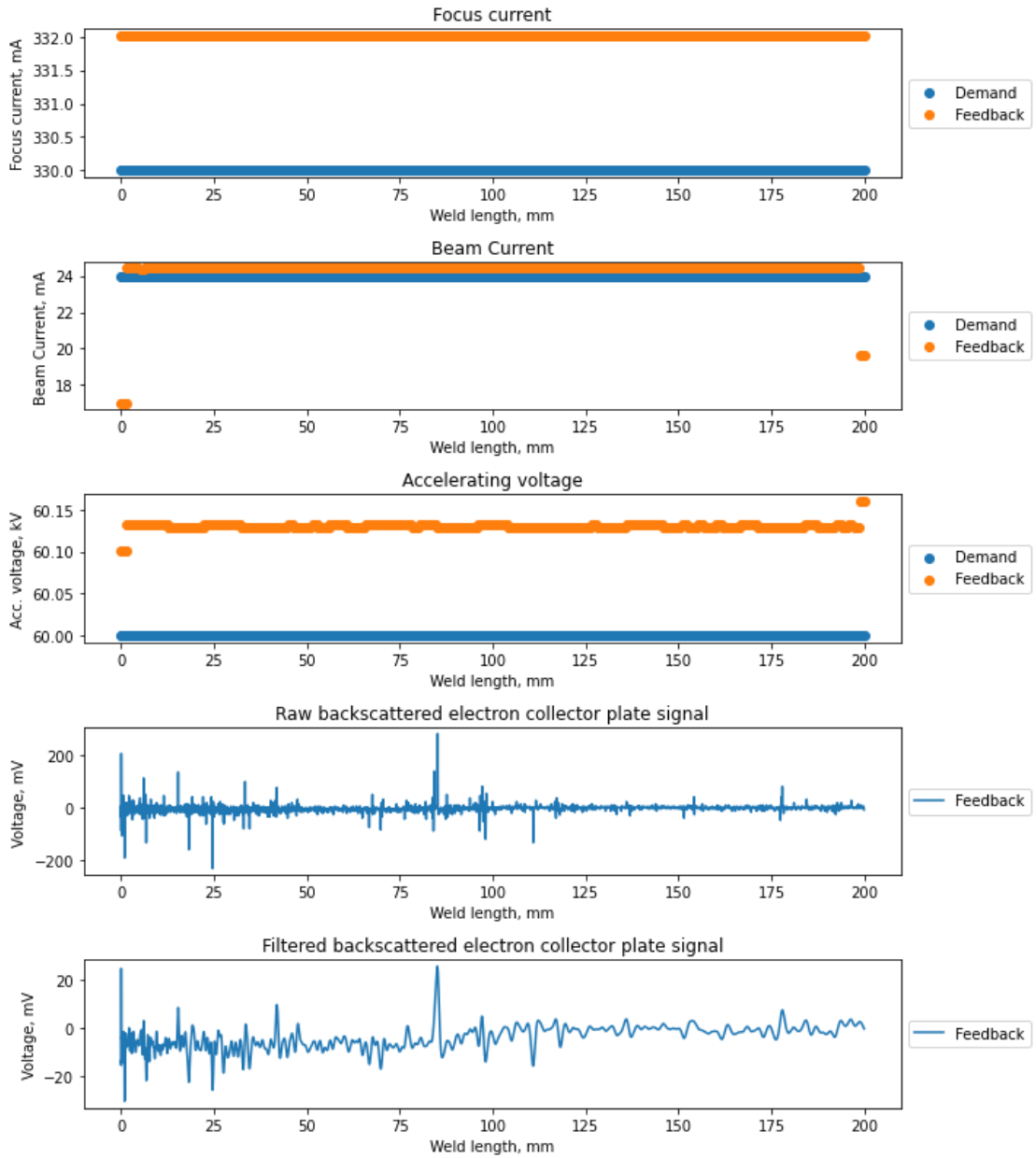


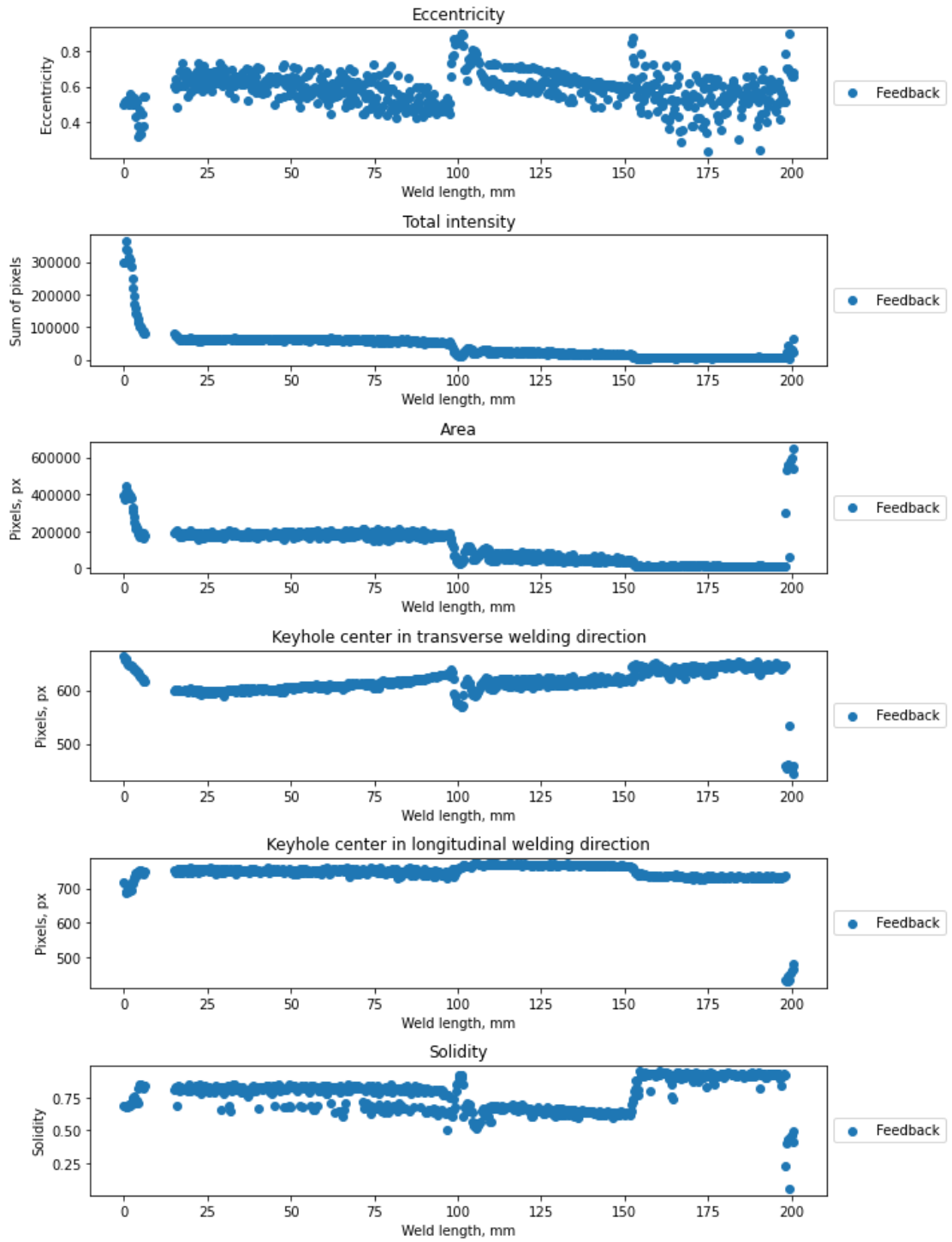
Handwritten markings on the samples are unrelated to the numeration in the thesis.



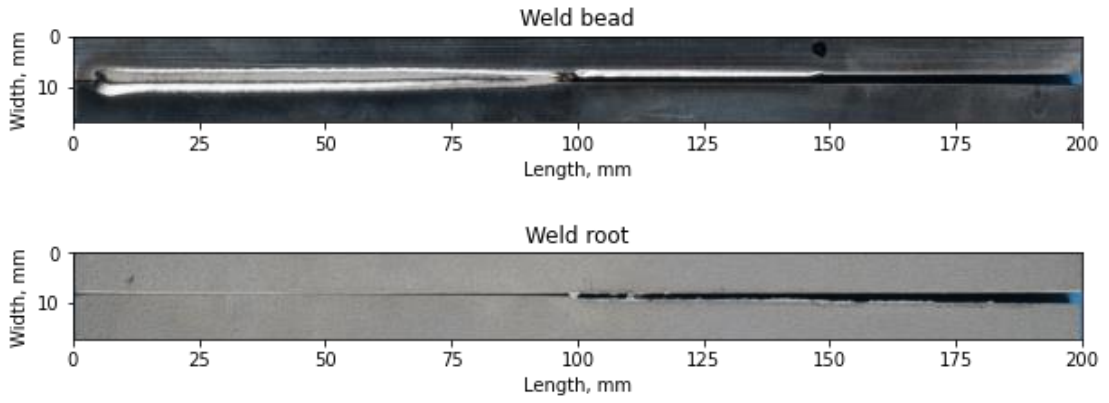


Appendix I. Weld 3

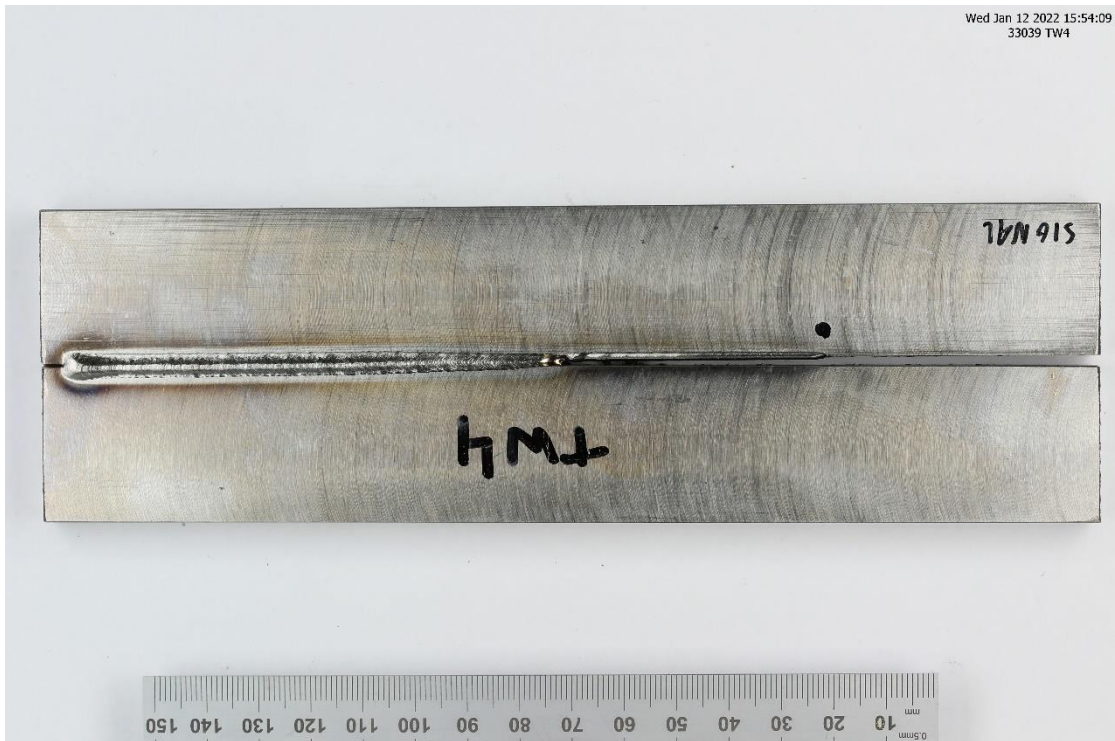




Chapter 8: Bibliography

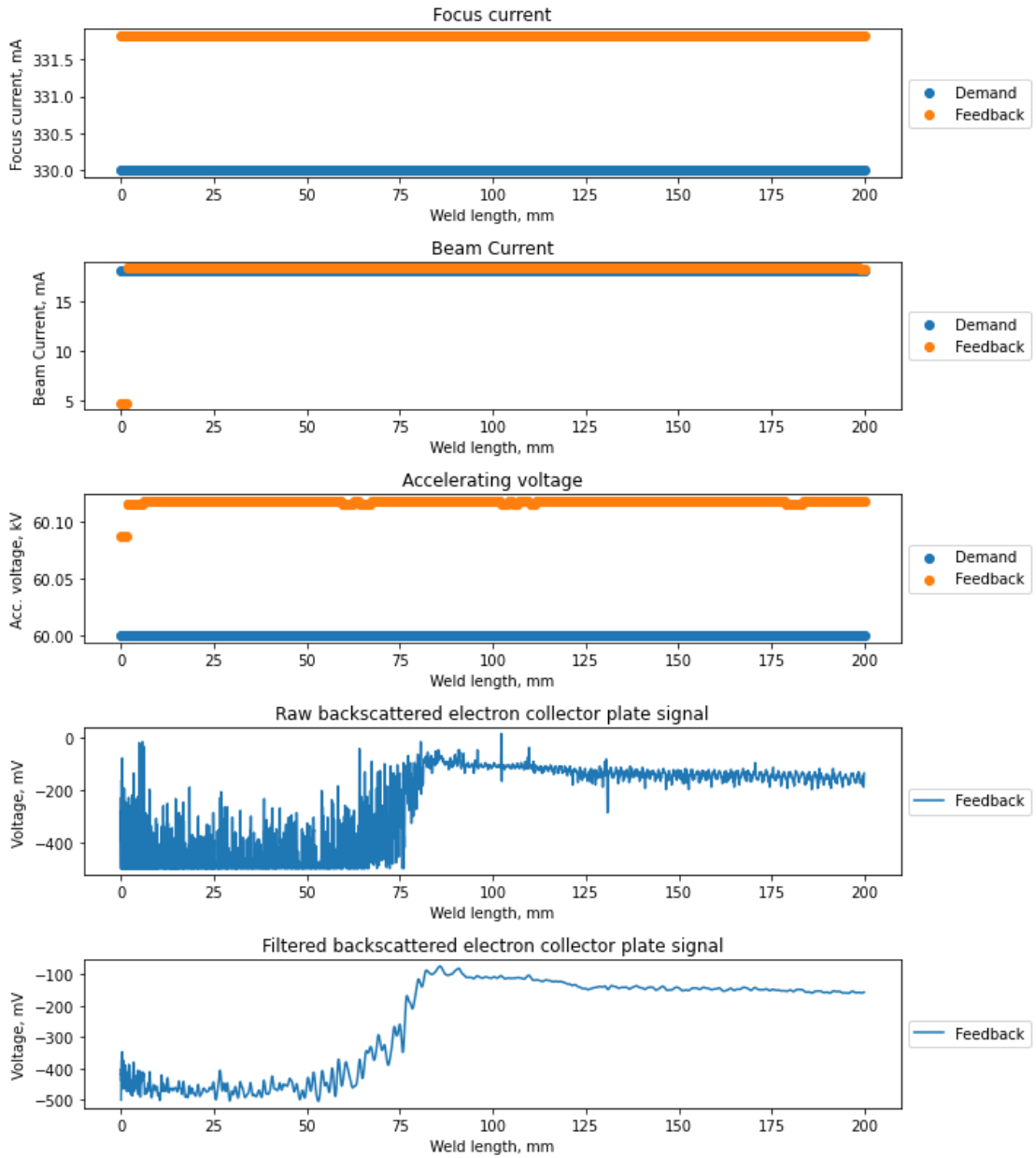


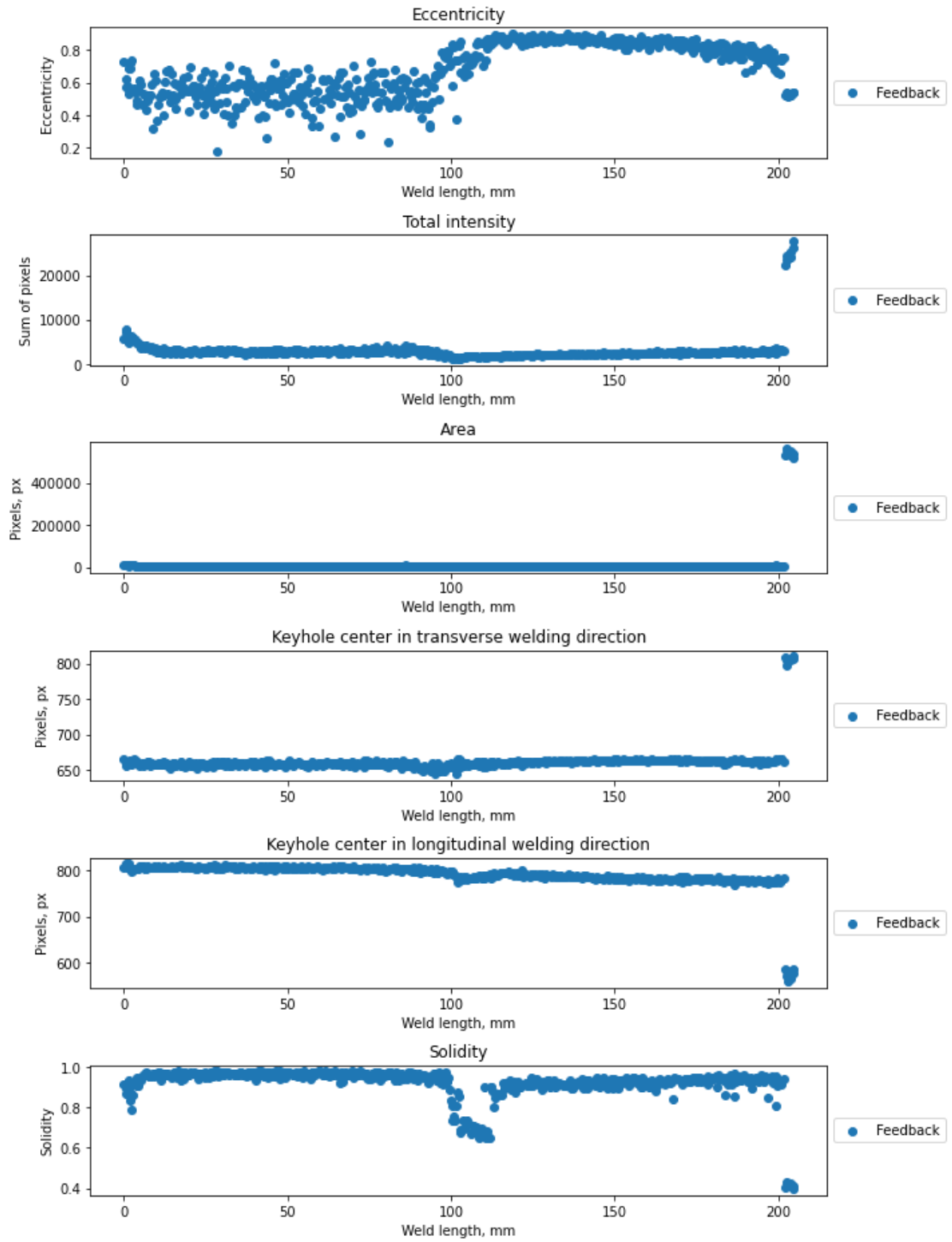
Handwritten markings on the samples are unrelated to the numeration in the thesis.



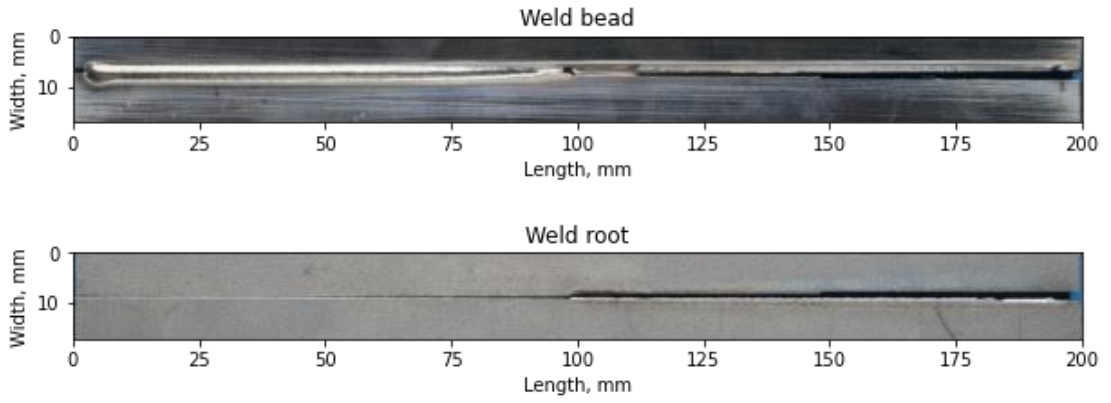


Appendix J. Weld 4



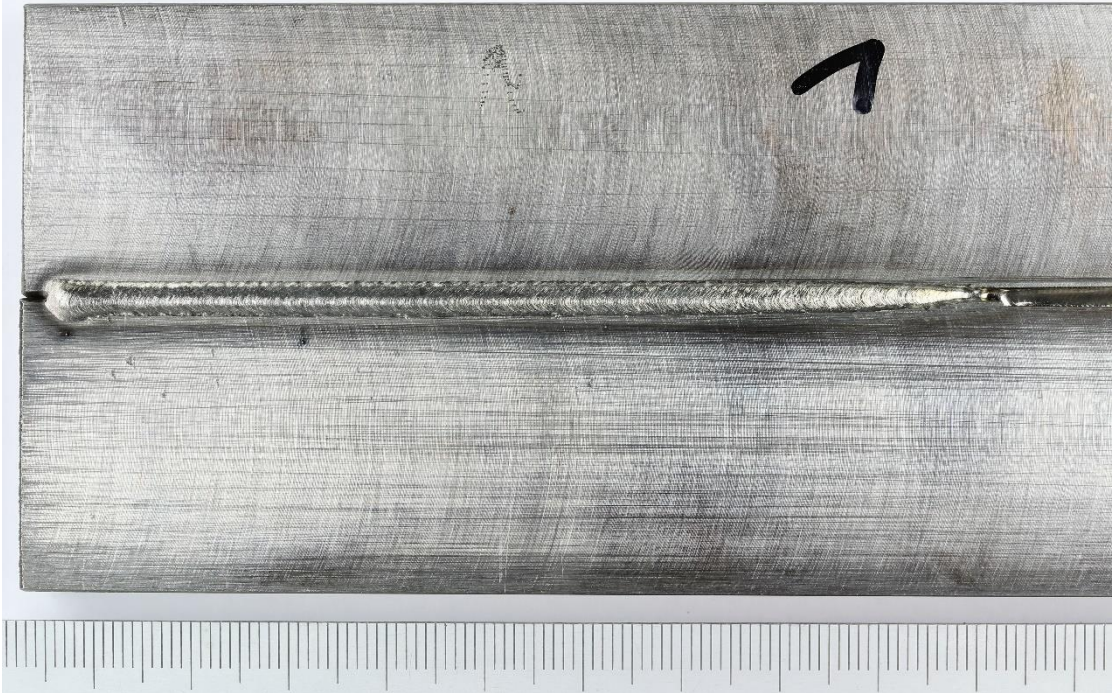


Chapter 8: Bibliography

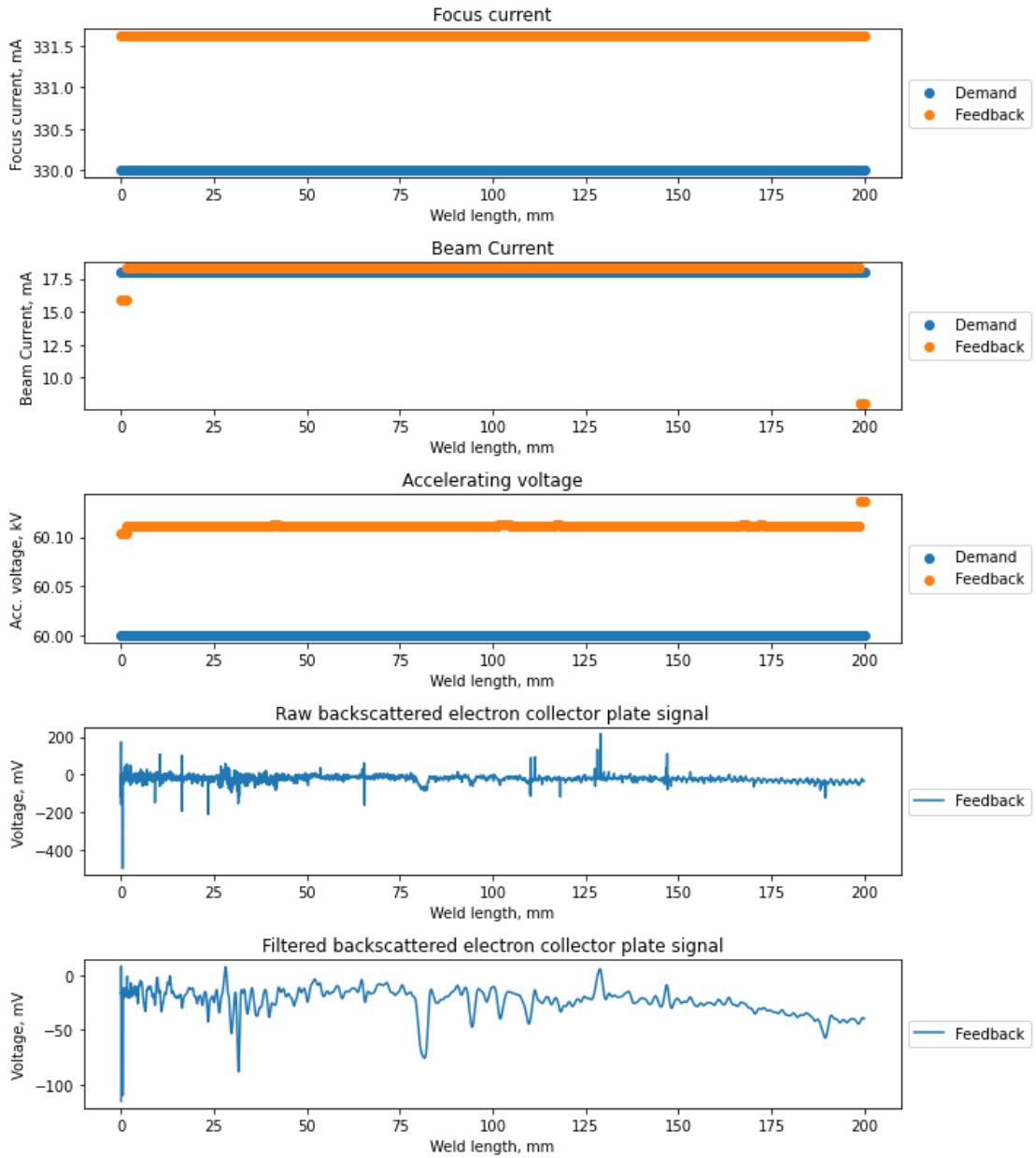


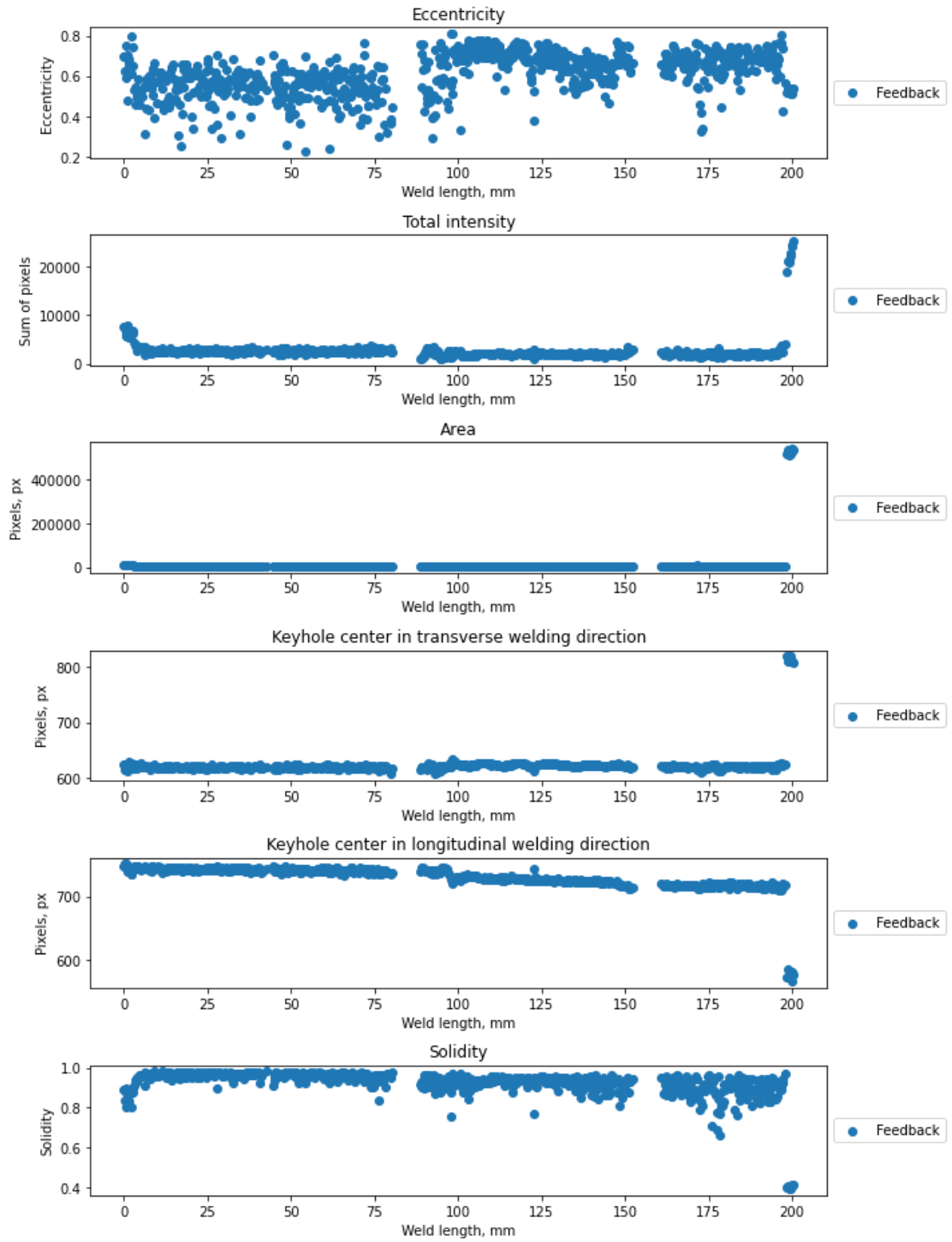
Handwritten markings on the samples are unrelated to the numeration in the thesis.



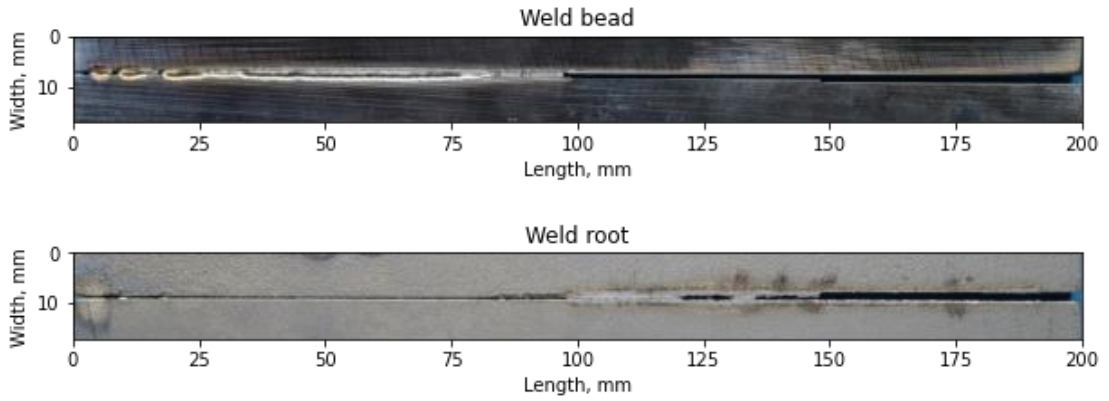


Appendix K. Weld 5

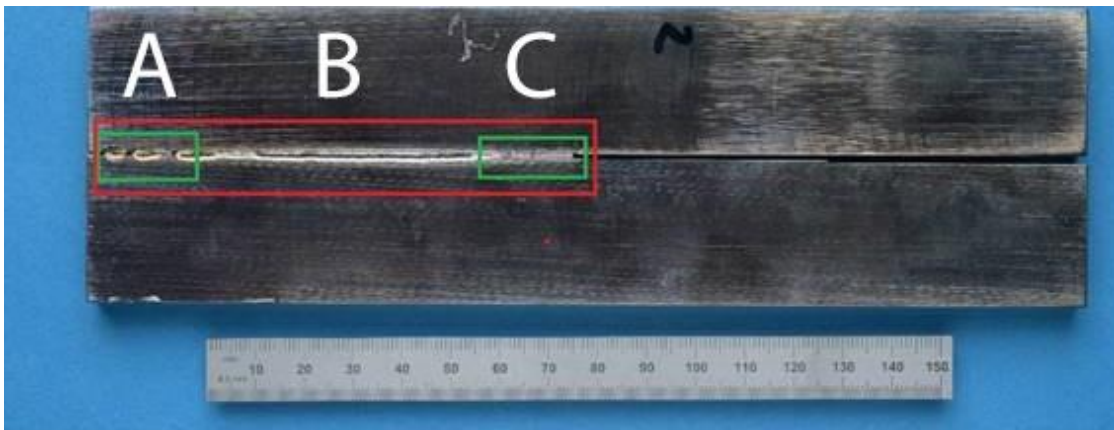




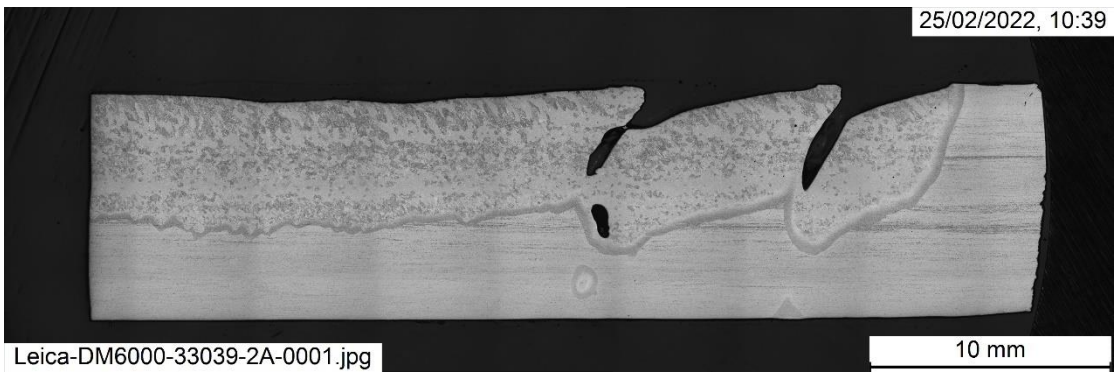
Chapter 8: Bibliography



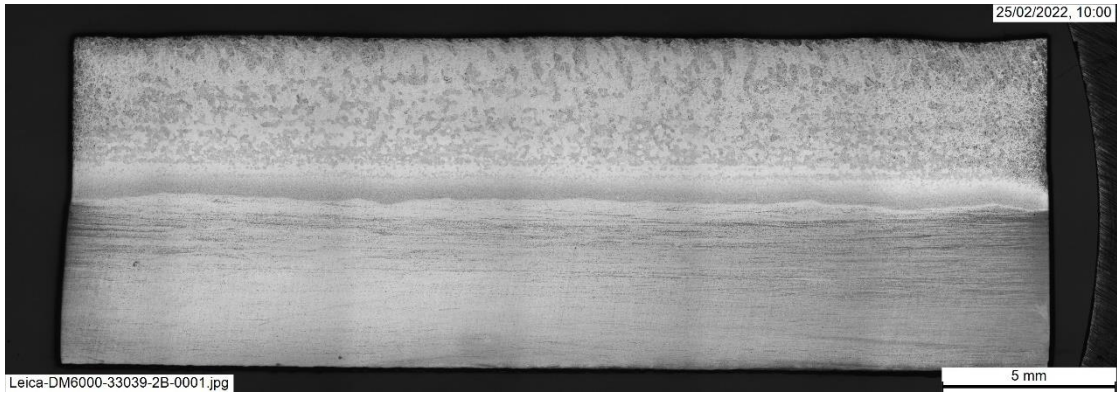
Longitudinal sections of weld 5. Due to the length of samples, only certain region of interest were selected for cutting (red square) and split in three parts (A, B, C). Some regions, due to the possible defects, were of particular interest and to ensure their continuity there were cut with greater care (green square).



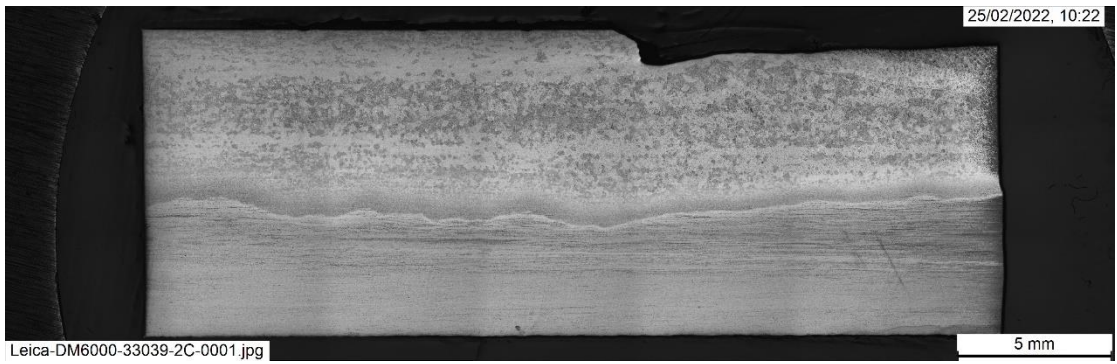
A)



B)

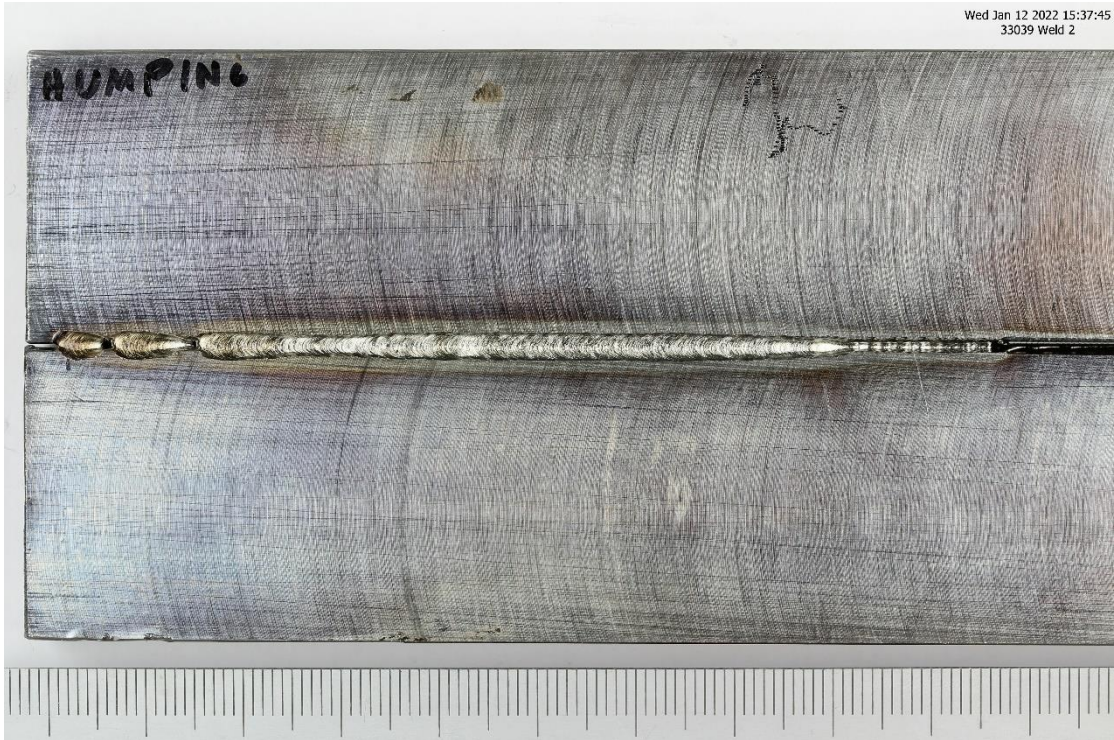


c)

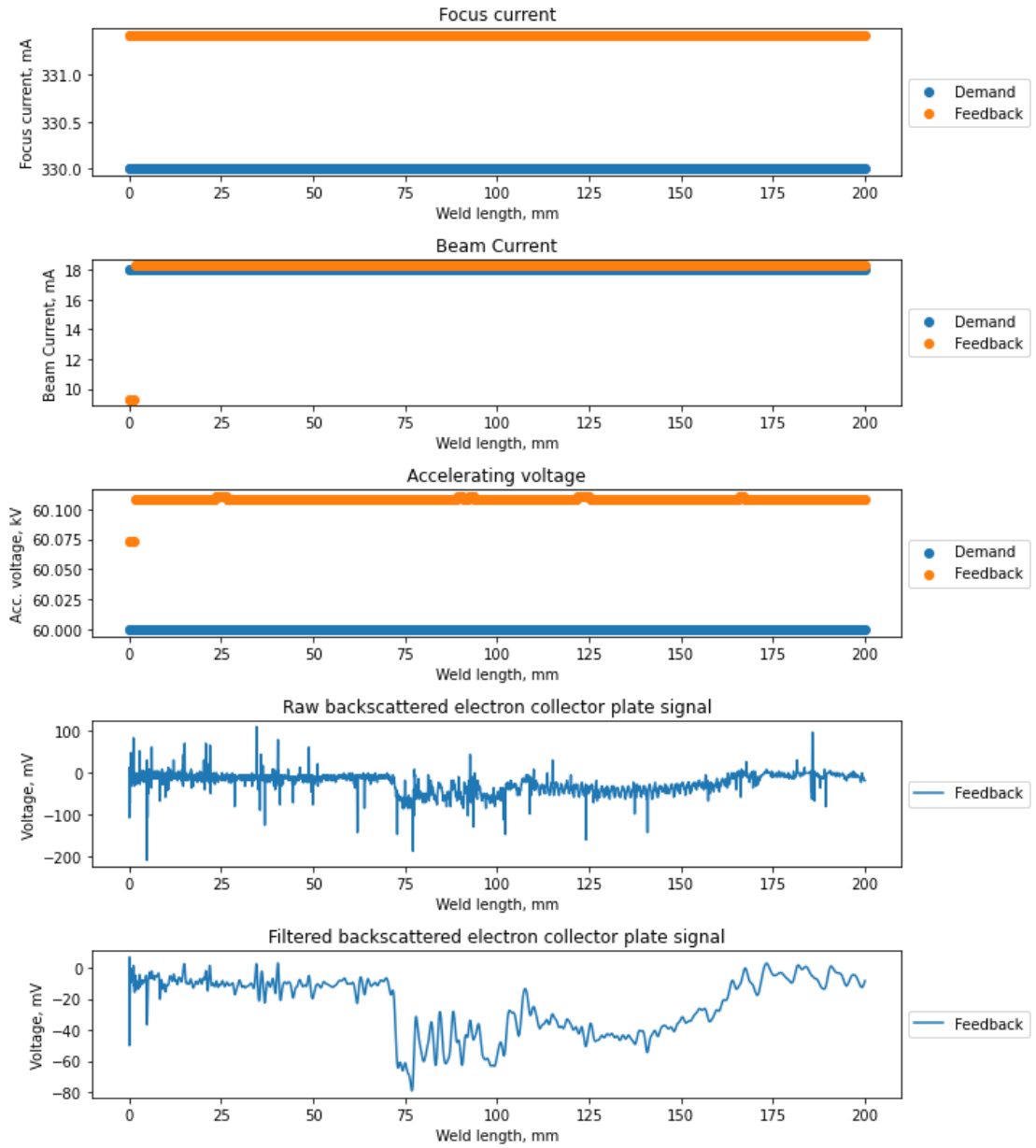


Handwritten markings on the samples are unrelated to the numeration in the thesis.

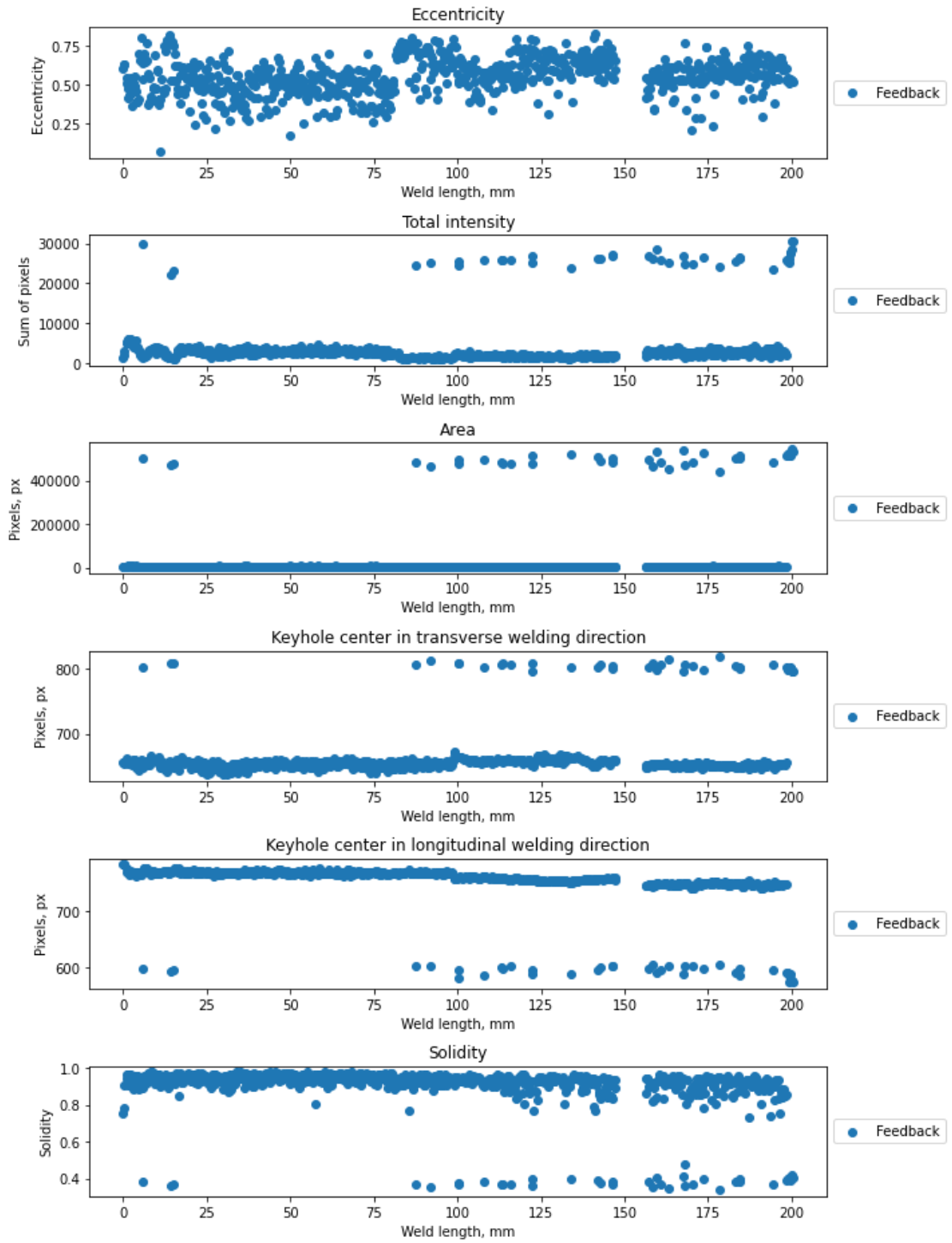


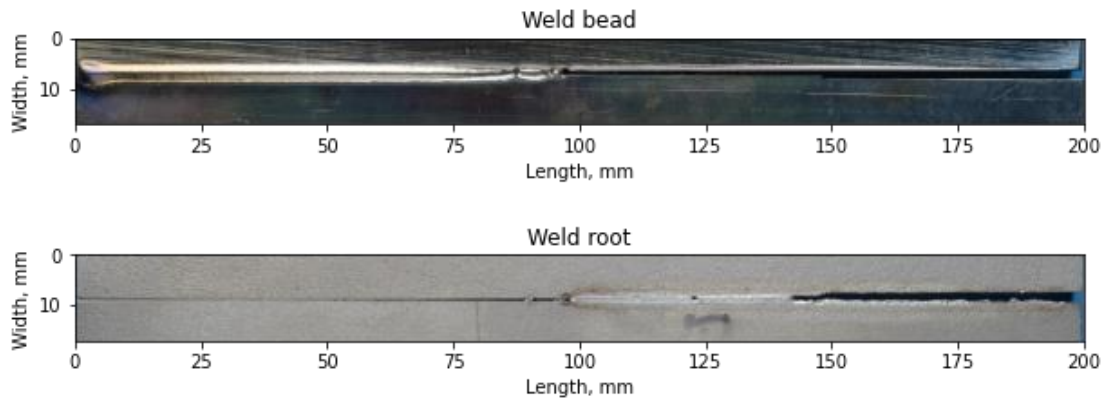


Appendix L. Weld 6

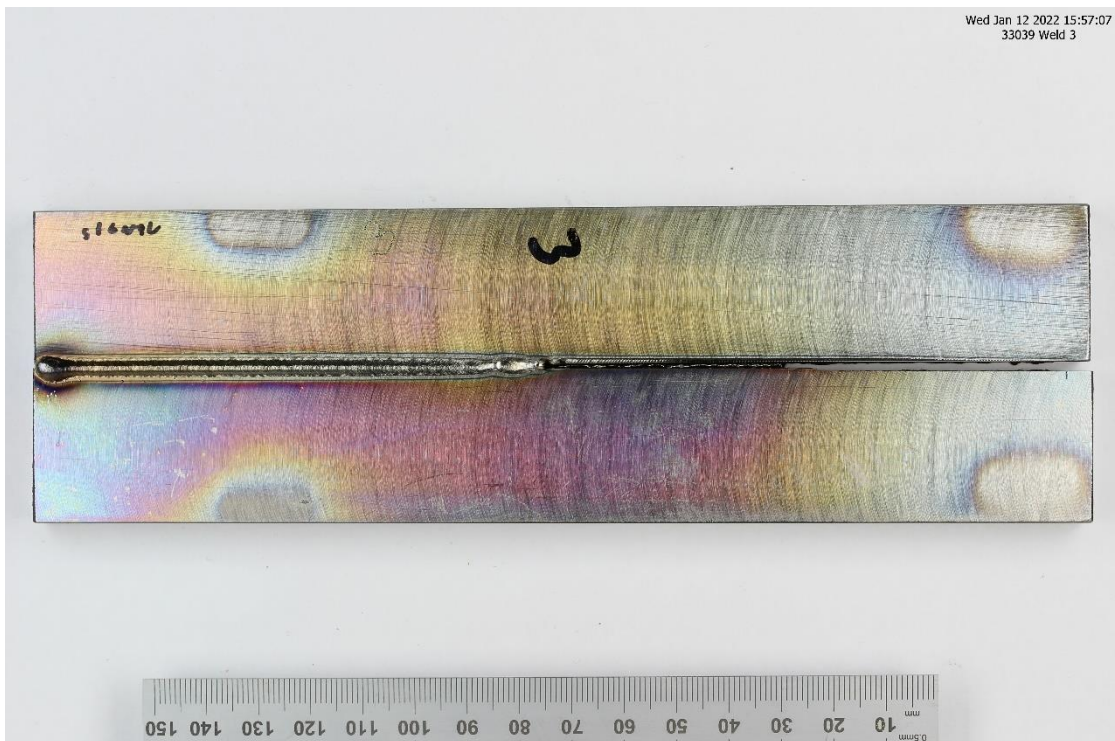


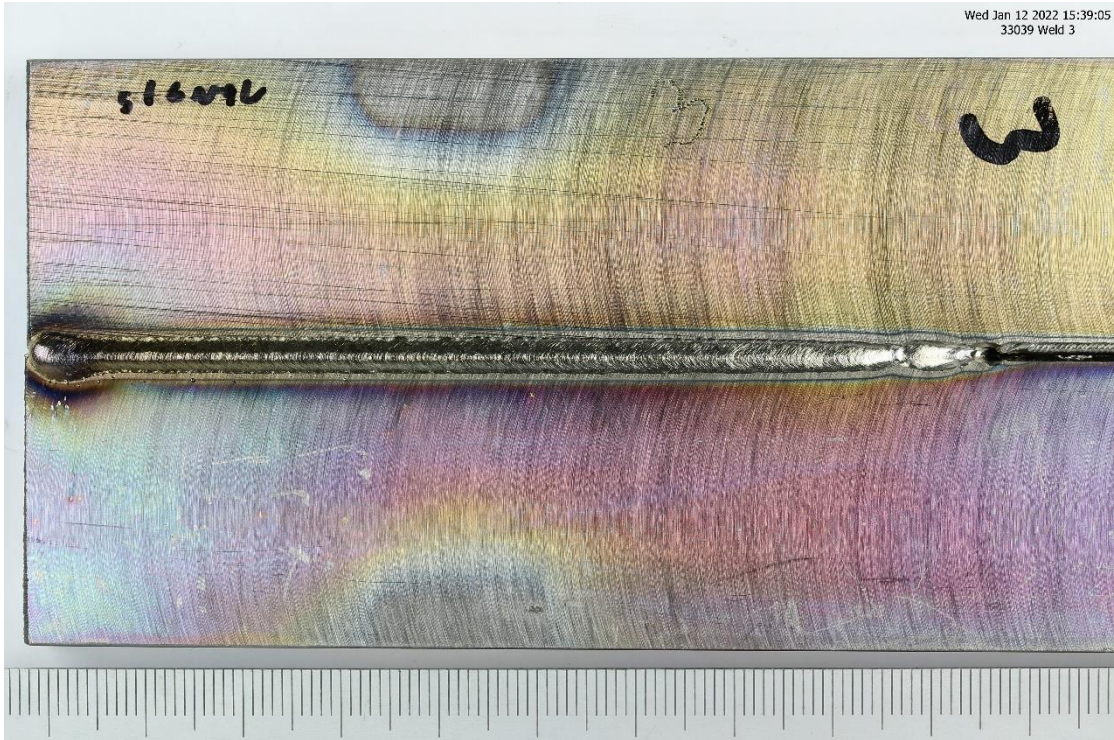
Chapter 8: Bibliography



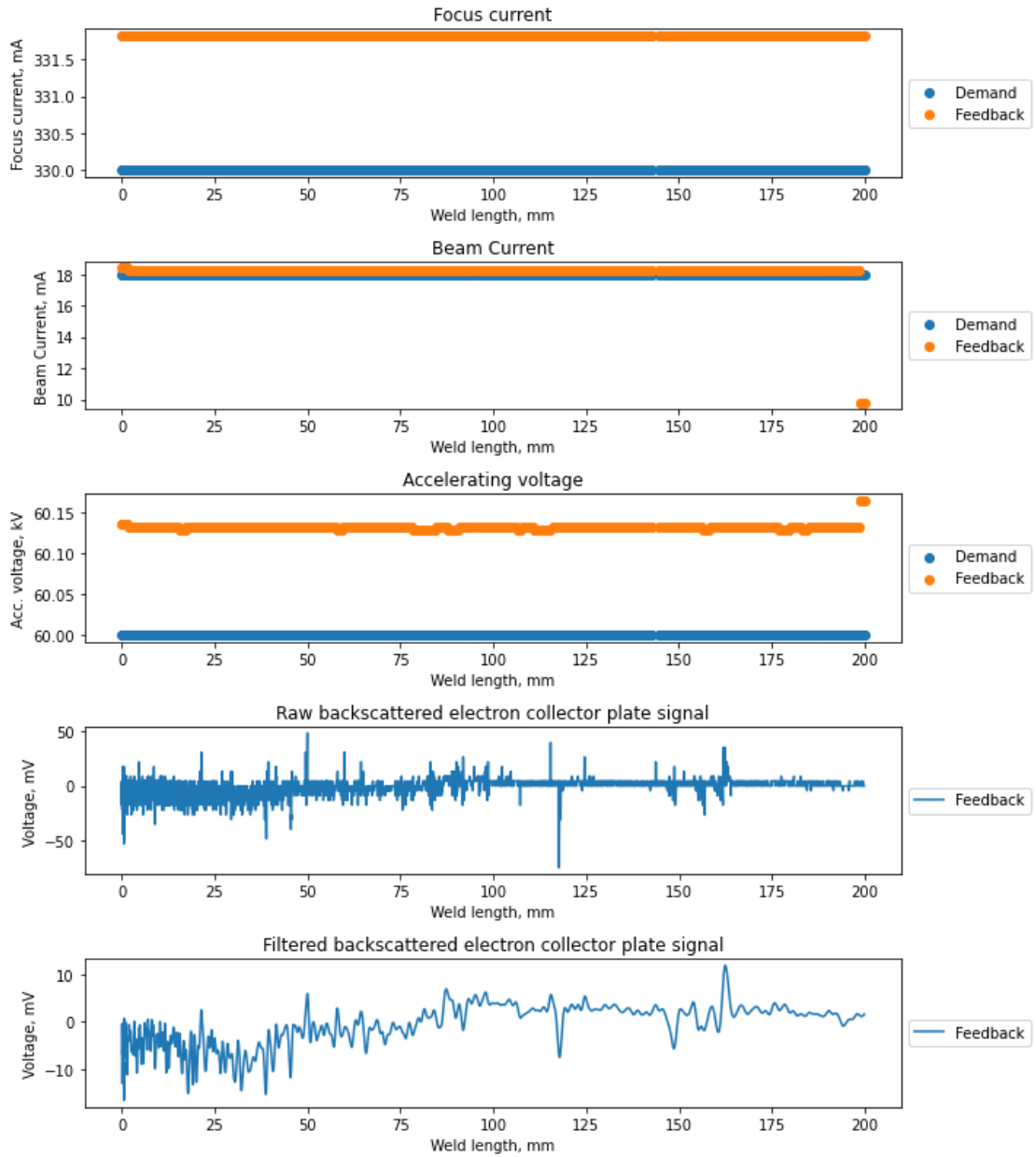


Handwritten markings on the samples are unrelated to the numeration in the thesis.

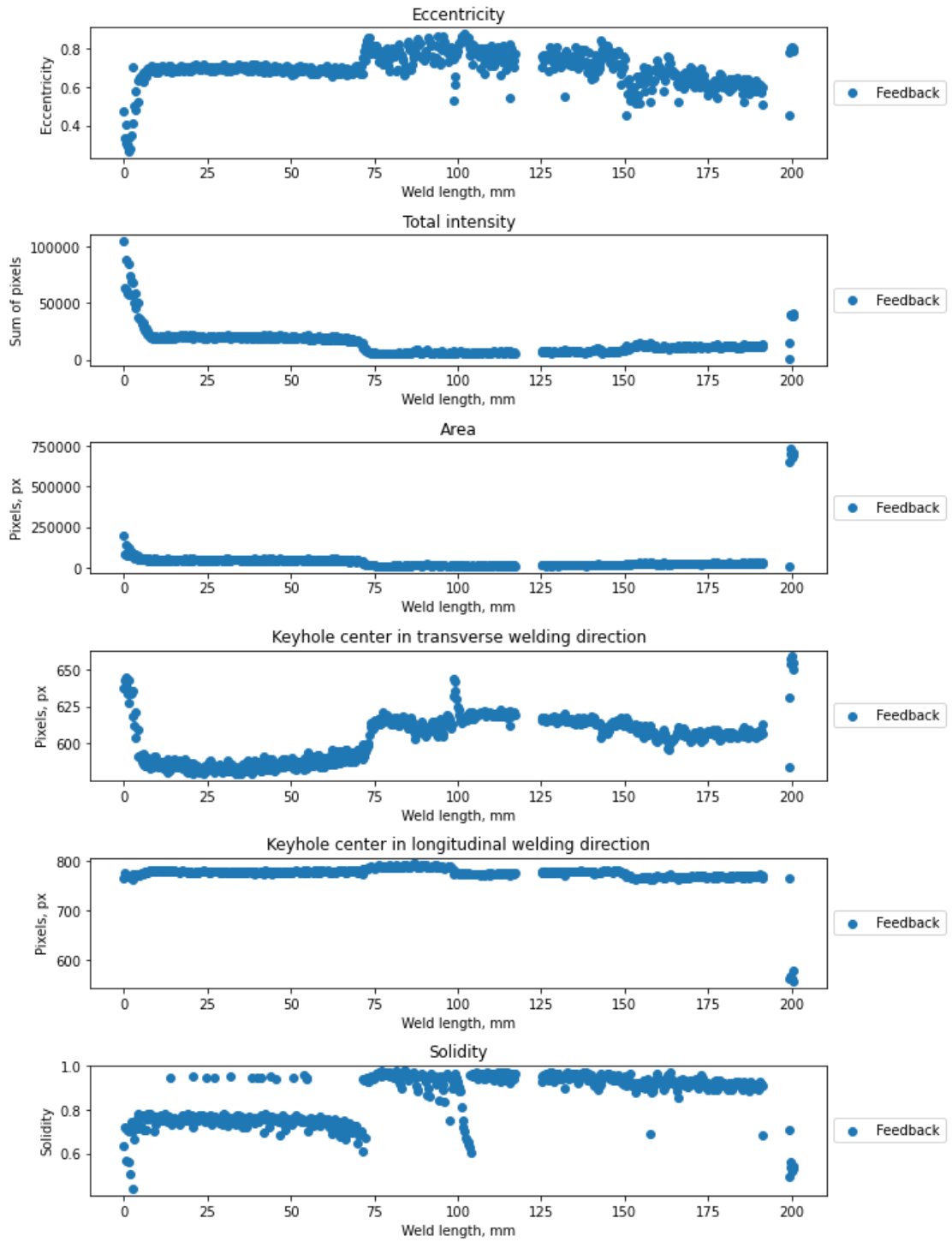


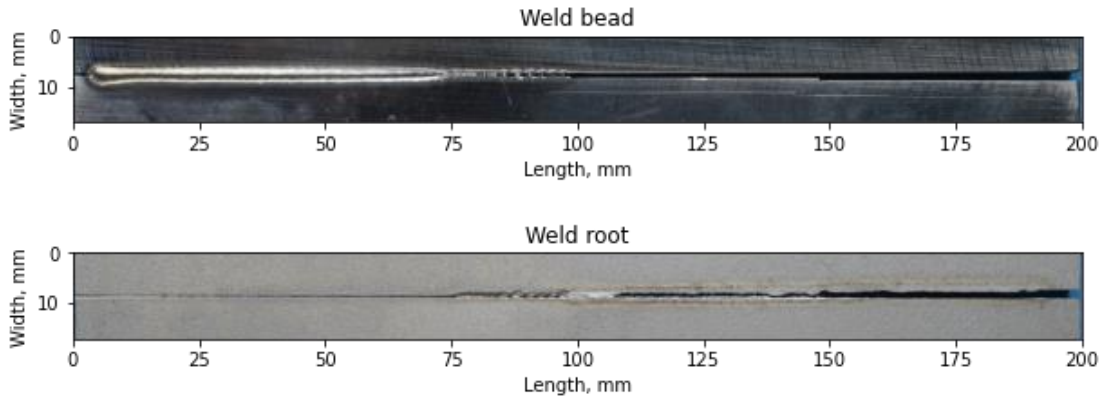


Appendix M. Weld 7

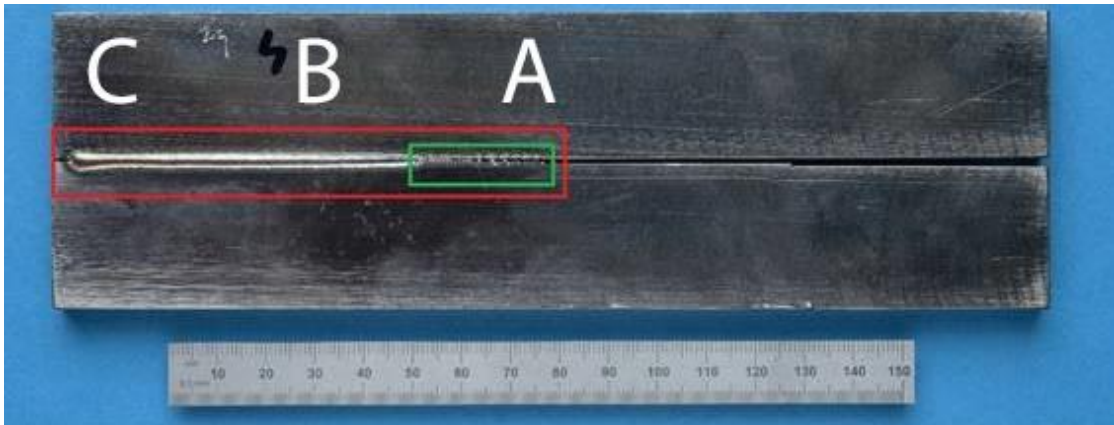


Chapter 8: Bibliography

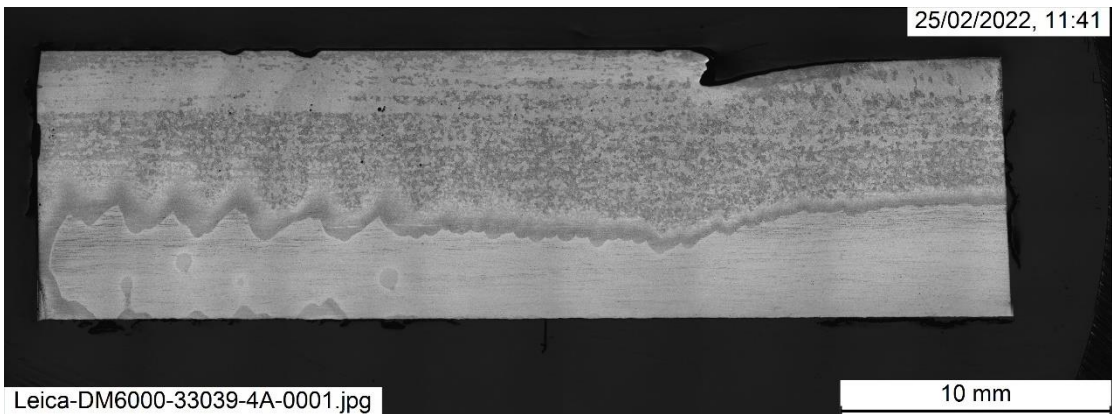




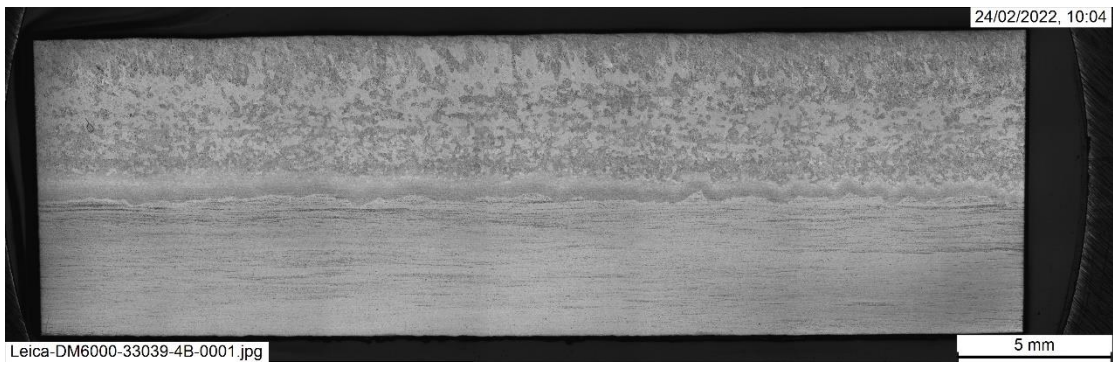
Longitudinal sections of weld 7. Due to the length of samples, only certain region of interest were selected for cutting (red square) and split in three parts (A, B, C). Some regions, due to the possible defects, were of particular interest and to ensure their continuity there were cut with greater care (green square).



A)



B)

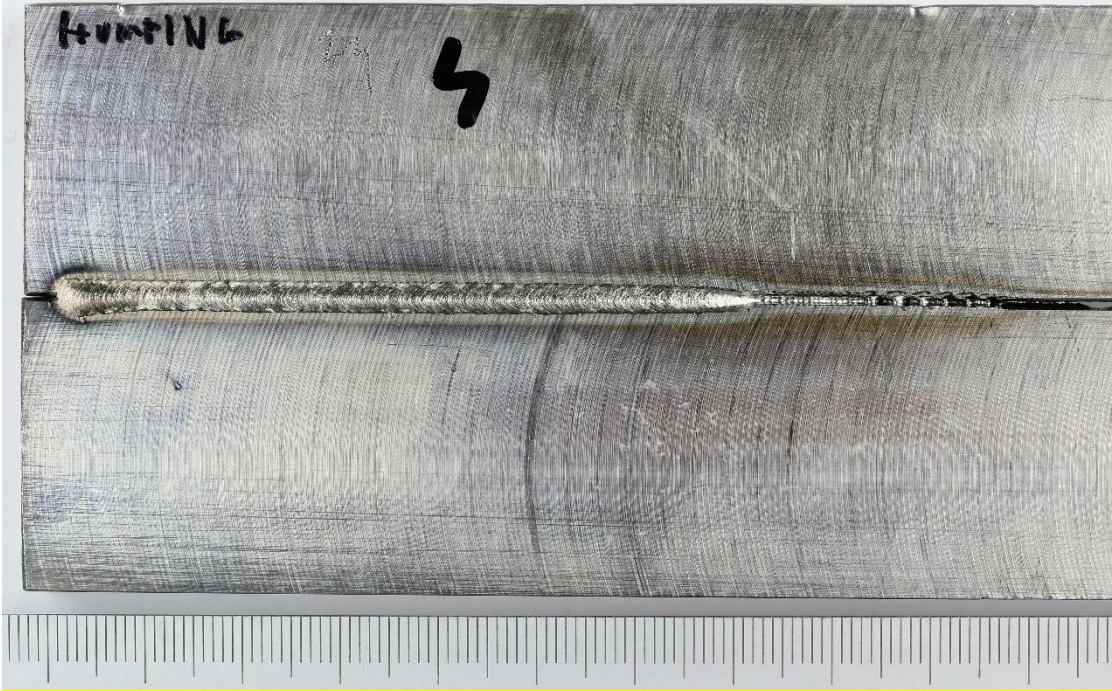


C)

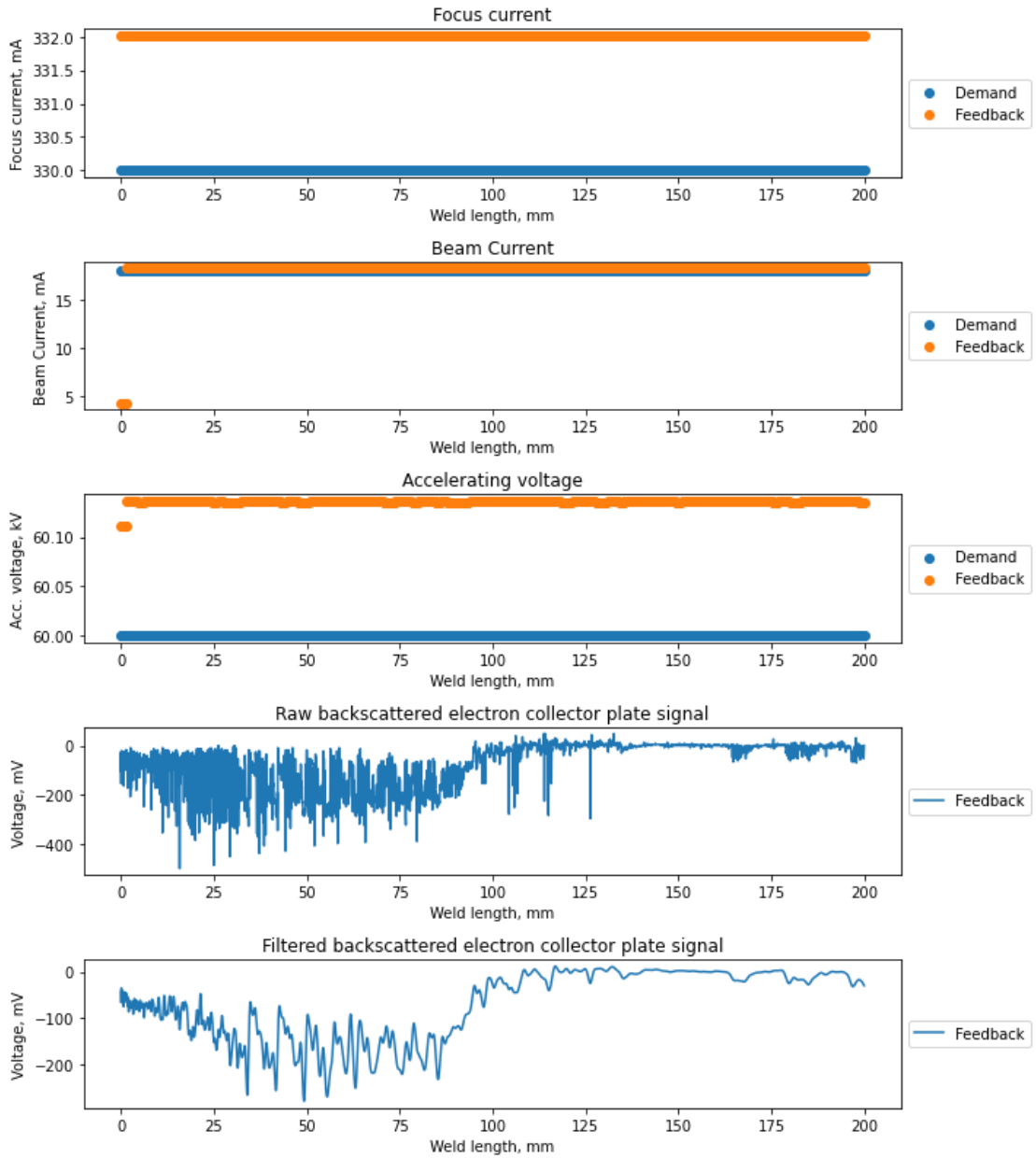


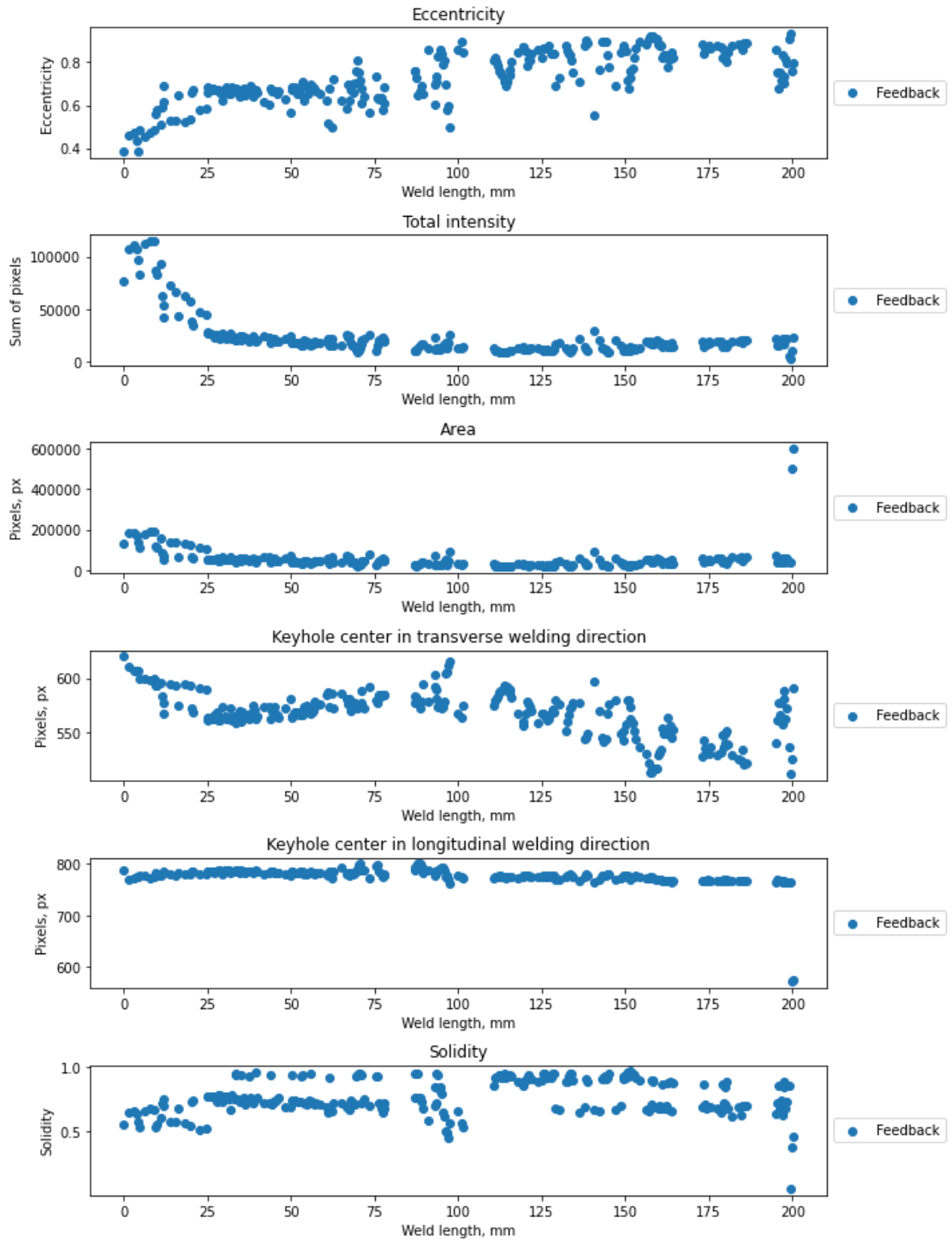
Handwritten markings on the samples are unrelated to the numeration in the thesis.



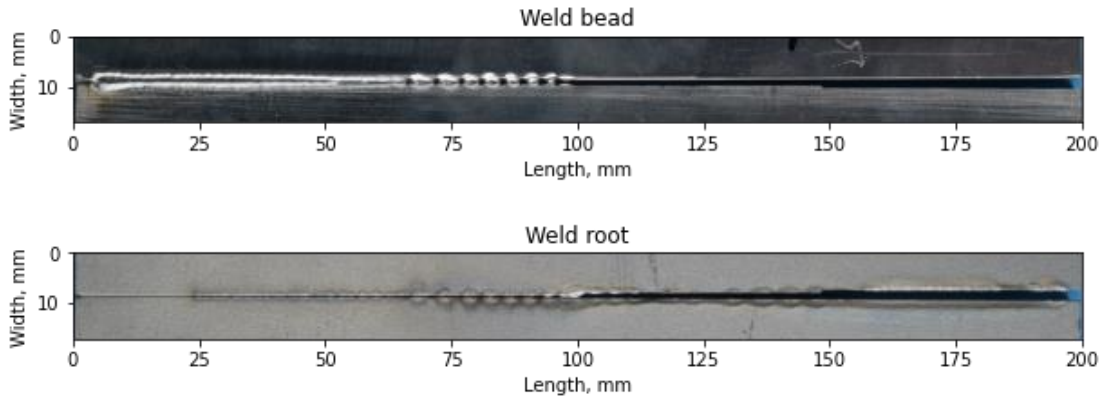


Appendix N. Weld 8

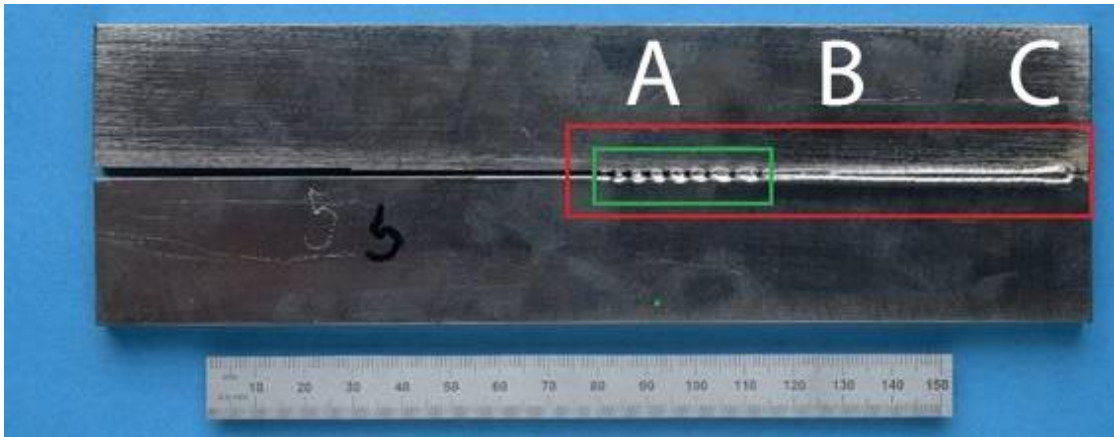




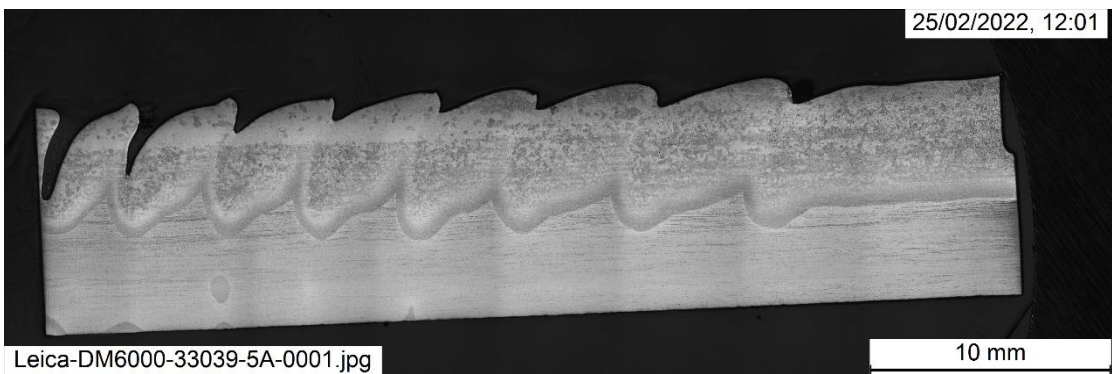
Chapter 8: Bibliography



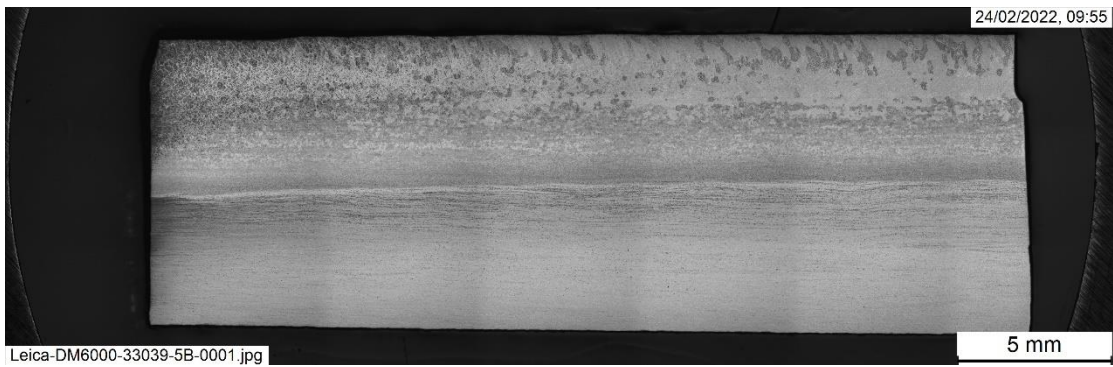
Longitudinal sections of weld 8. Due to the length of samples, only certain region of interest were selected for cutting (red square) and split in three parts (A, B, C). Some regions, due to the possible defects, were of particular interest and to ensure their continuity there were cut with greater care (green square).



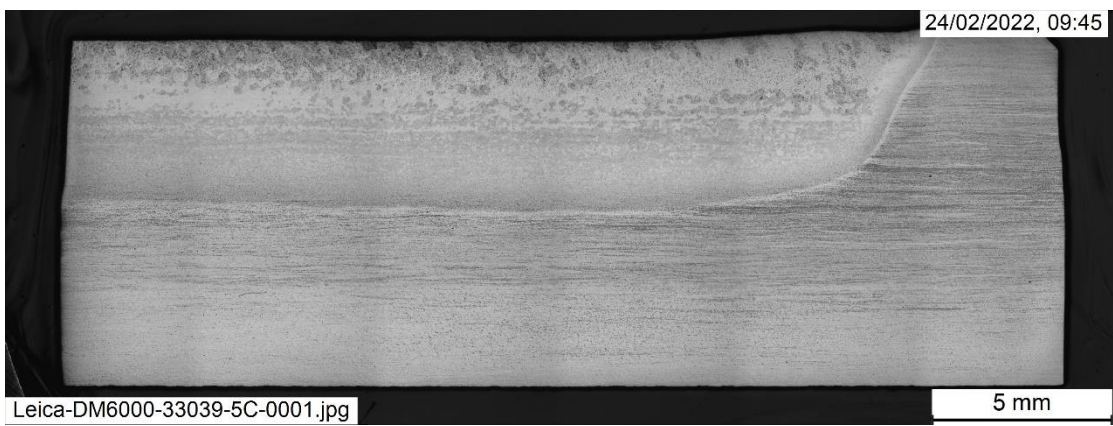
A)



B)



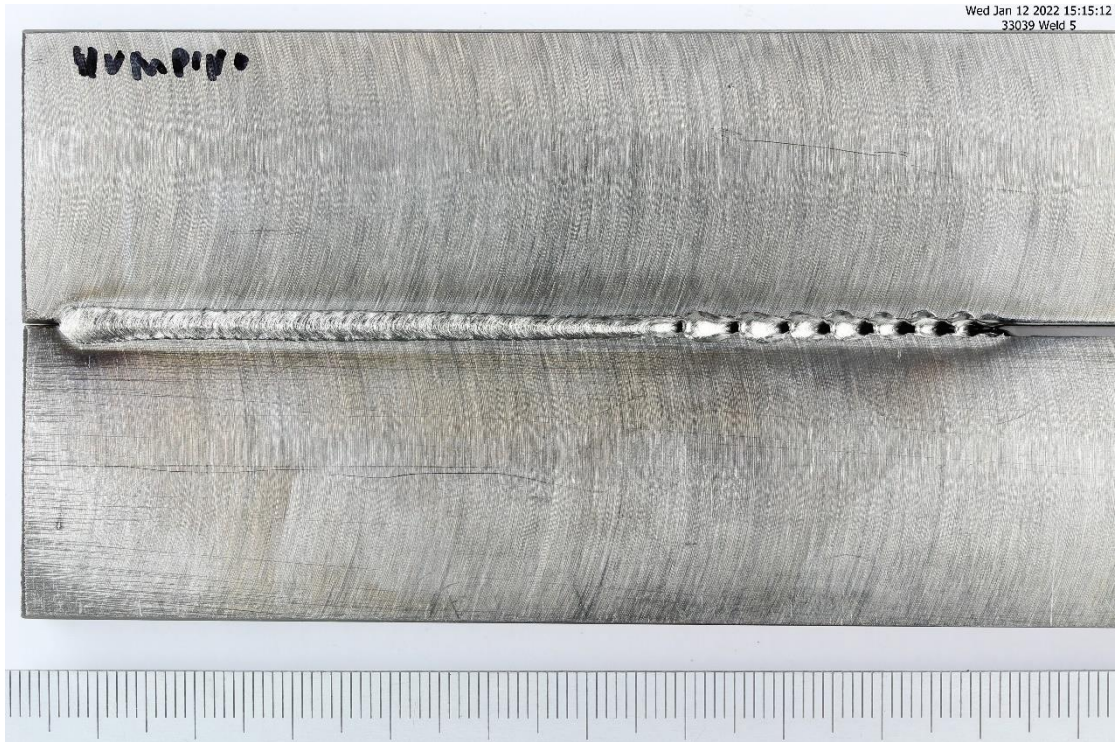
C)



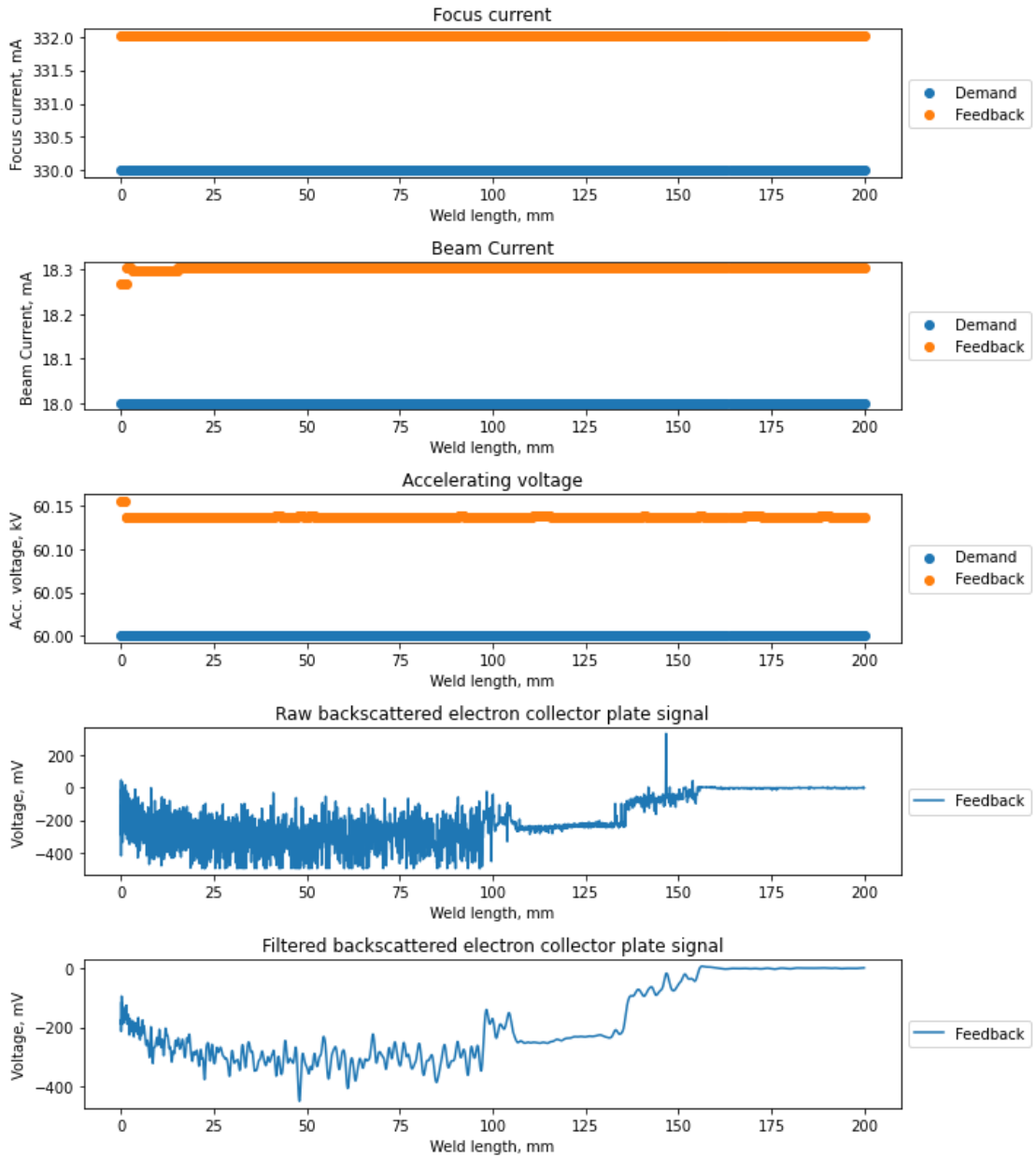
Handwritten markings on the samples are unrelated to the numeration in the thesis.



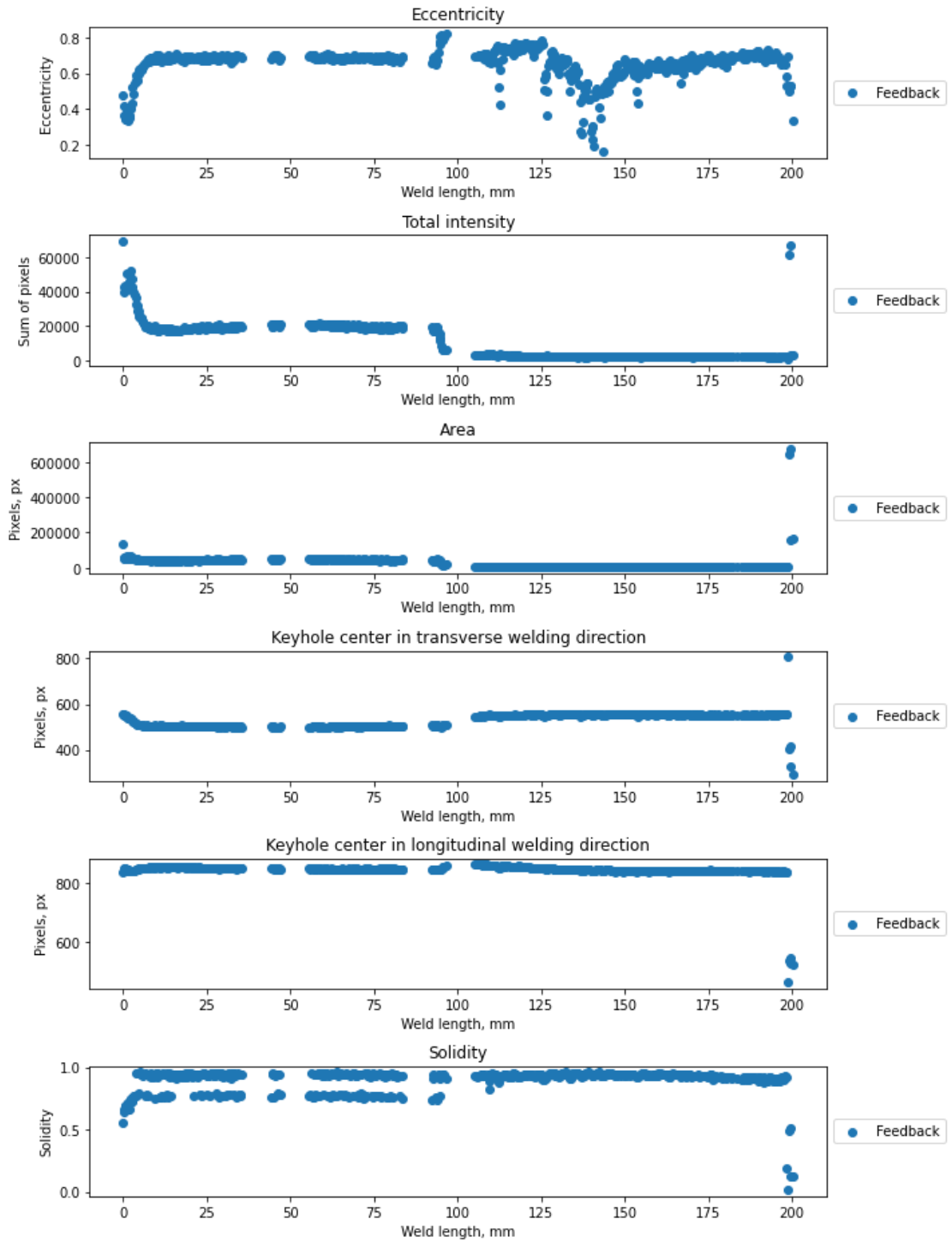
Chapter 8: Bibliography

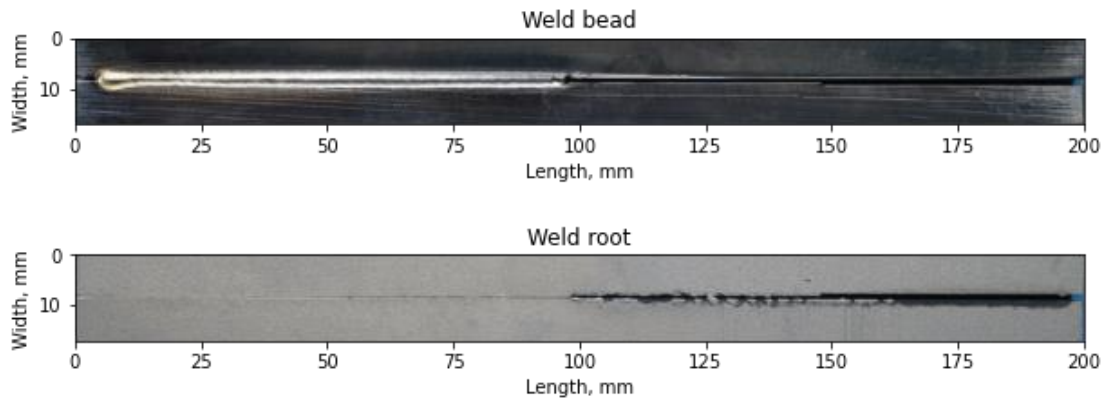


Appendix O. Weld 9

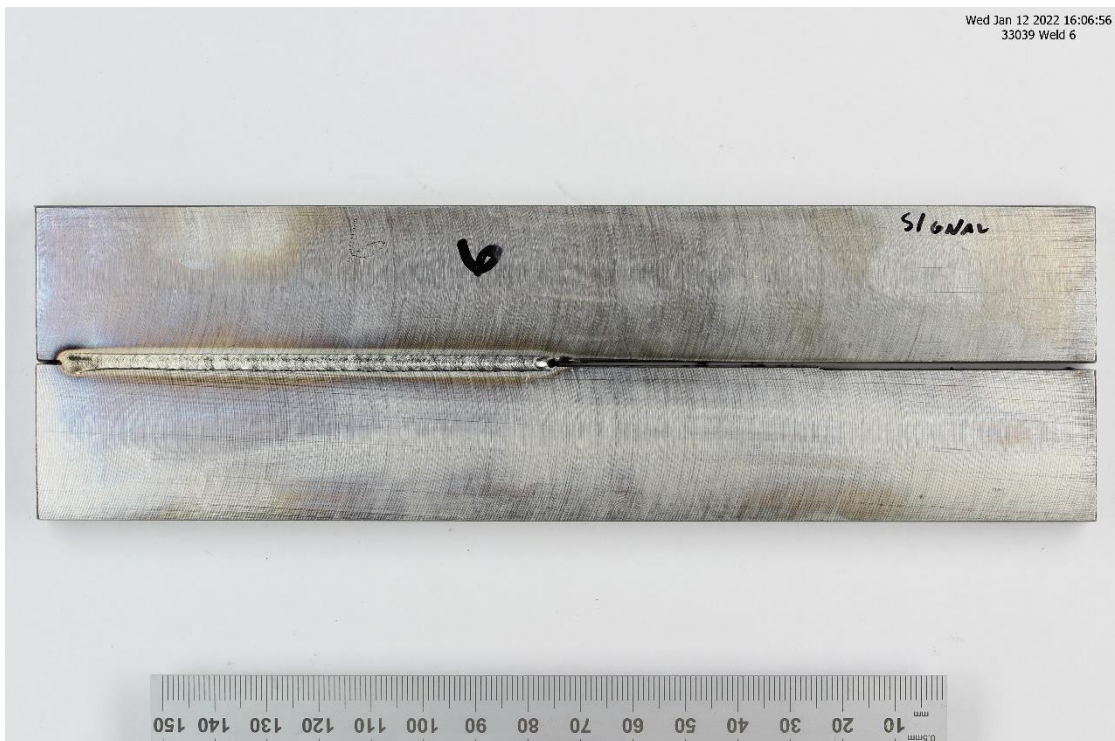


Chapter 8: Bibliography



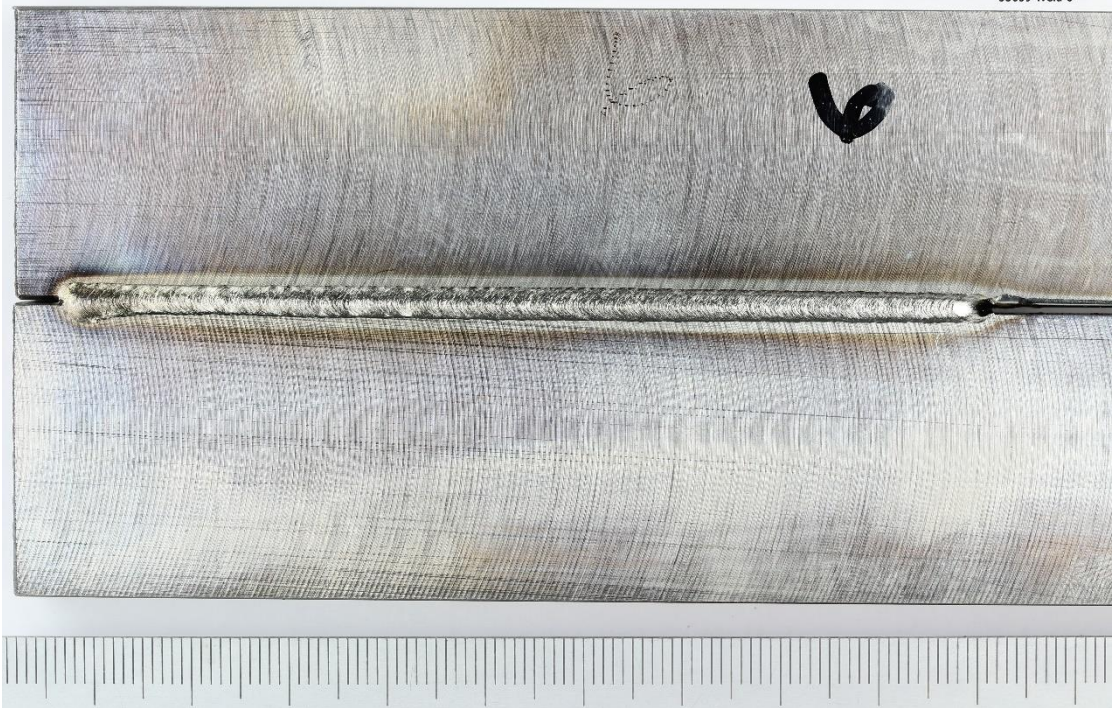


Handwritten markings on the samples are unrelated to the numeration in the thesis.

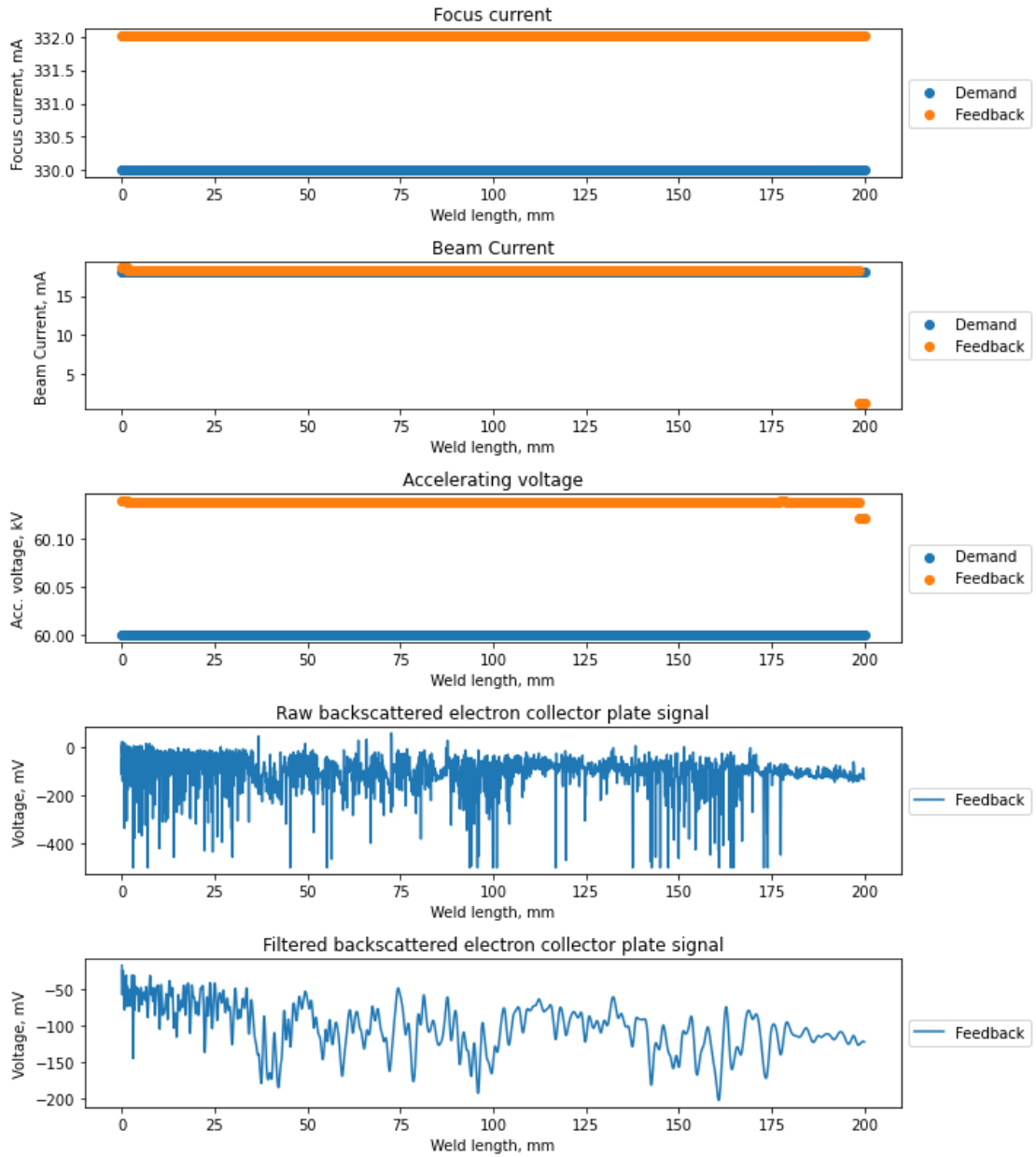


Chapter 8: Bibliography

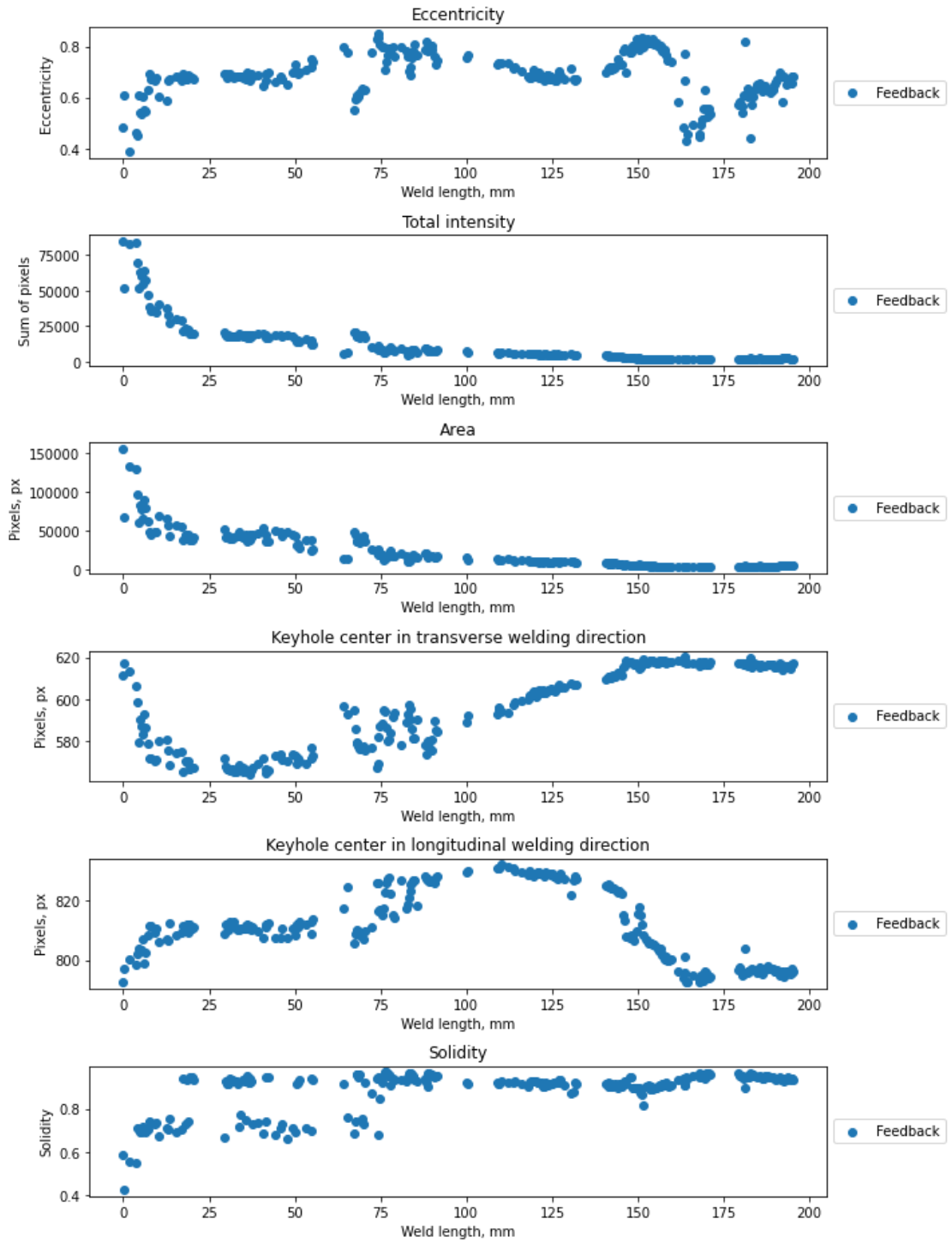
Wed Jan 12 2022 15:13:23
33039 Weld 6

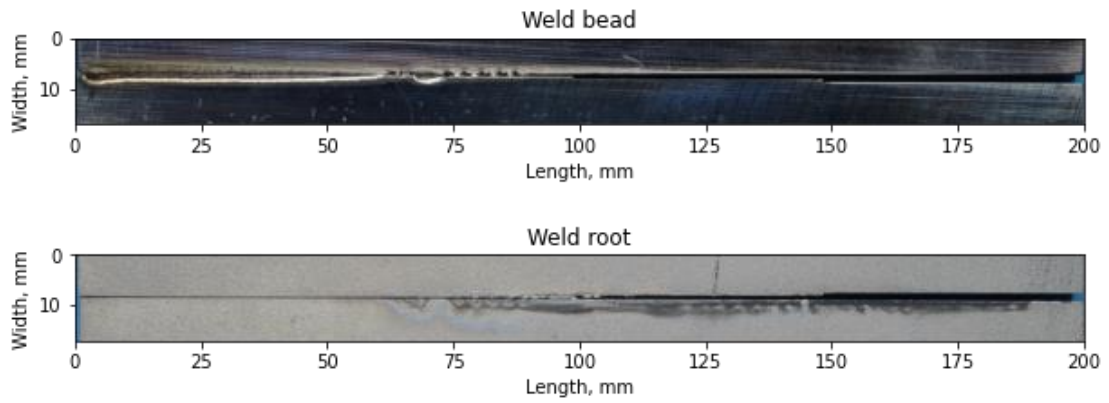


Appendix P. Weld 10

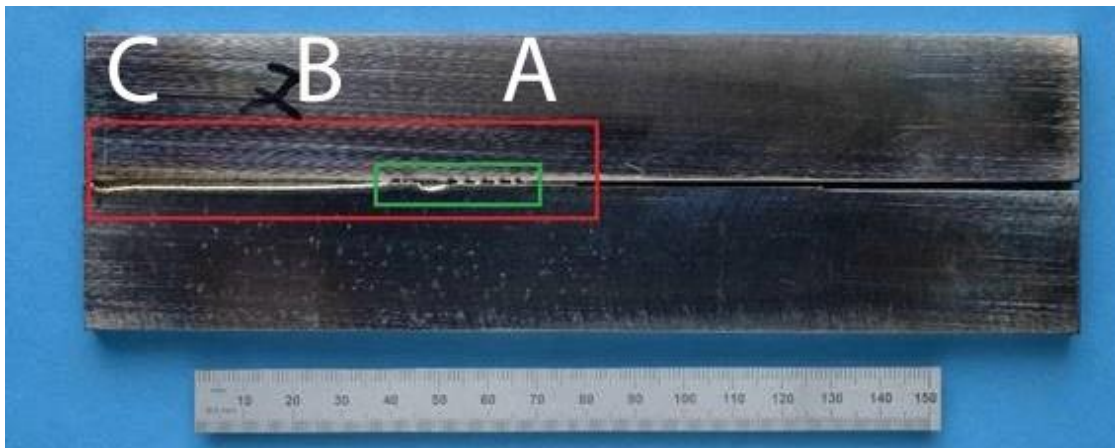


Chapter 8: Bibliography

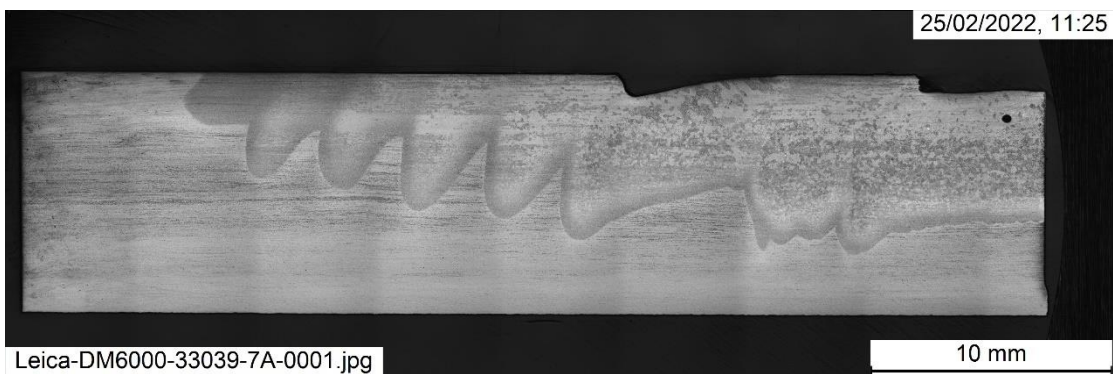




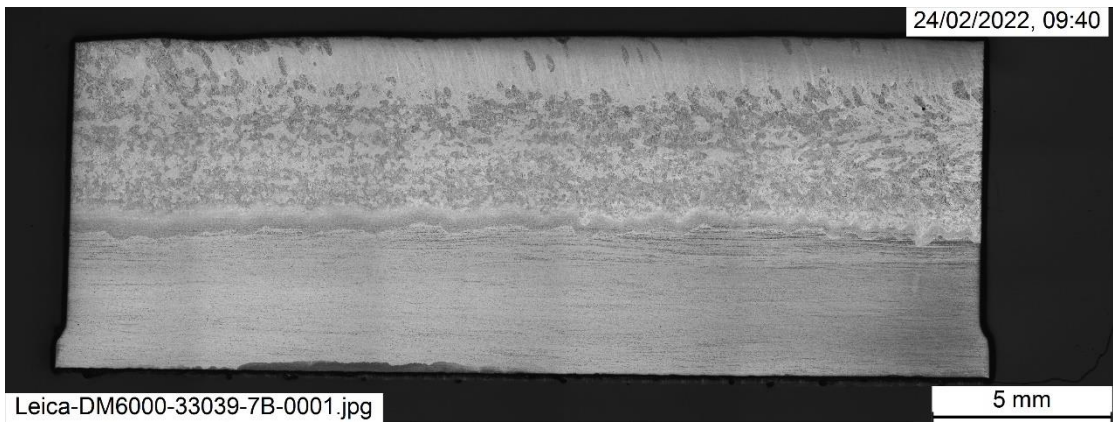
Longitudinal sections of weld 10. Due to the length of samples, only certain region of interest were selected for cutting (red square) and split in three parts (A, B, C). Some regions, due to the possible defects, were of particular interest and to ensure their continuity there were cut with greater care (green square).



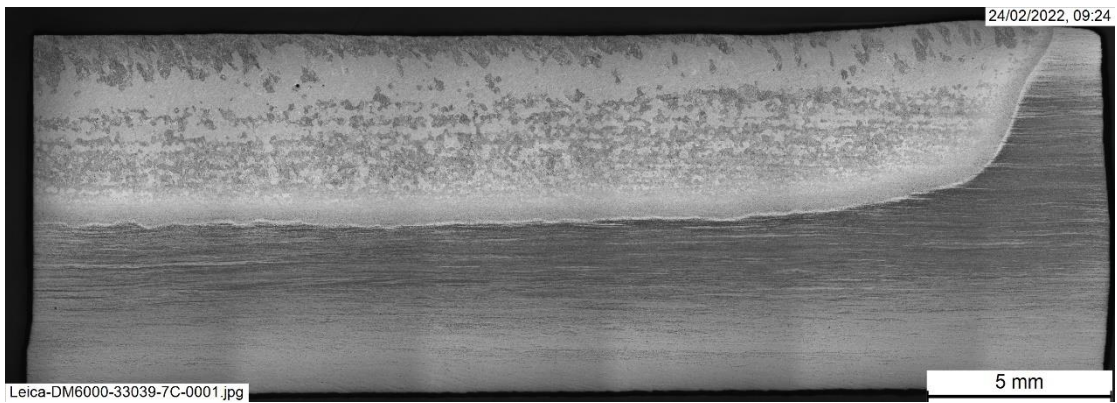
A)



B)



C)



Handwritten markings on the samples are unrelated to the numeration in the thesis.

